UNIVERSITÀ
DEGLI STUDI
DI BRESCIA

DOTTORATO DI RICERCA IN
DIPARTIMENTO DI INGEGNERIA MECCANICA E INDUSTRIALE

ICAR/08 Scienza Delle Costruzioni

CICLO
XXXVII

Modeling, Simulation, and Experiments Toward Next-Generation Li-Ion Cells

DOTTORANDO:
Erkin Yildiz

NOME DEL RELATORE:
Prof. Alberto Salvadori

COORDINATORE DEL DOTTORATO:
Prof. Pietro Poesio

Sommario

Nonostante la loro maturità, le batterie agli ioni di litio devono ancora affrontare sfide nelle applicazioni che richiedono contemporaneamente elevata potenza ed elevata capacità. Il loro funzionamento si basa sul meccanismo classico di intercalazione, in cui il litio viene inserito ed estratto dall'ospite elettrodico. Le variazioni volumetriche associate possono indurre danni meccanici, compromettere l'integrità strutturale e interrompere il contatto elettrico con i collettori di corrente. La progettazione di elettrodi nanostrutturati e compositi può contribuire ad attenuare questi meccanismi di degradazione.

Una cella elettrochimica è costituita da collettori di corrente, due elettrodi (anodo e catodo) e un separatore solido, permeato da un elettrolita liquido nelle batterie convenzionali. Il trasporto di carica è dipendente dalla fase: gli elettroni conducono all'interno degli elettrodi, mentre gli ioni trasportano carica attraverso l'elettrolita. Per sostenere le reazioni interfacciali, gli ioni devono attraversare l'elettrolita fino alle superfici degli elettrodi. Di conseguenza, il trasporto di massa nell'elettrolita è descritto dal moto degli ioni mobili, governato da diffusione (guidata da gradienti di concentrazione) e migrazione (guidata dal campo elettrico).

Gli studi teorici e computazionali approfondiscono la comprensione del comportamento delle batterie reali sia in condizioni operative sia in condizioni estreme e, insieme agli esperimenti, consentono di ottimizzare nuovi materiali e architetture. Di conseguenza, la modellazione rappresenta uno strumento potente per la progettazione di sistemi di accumulo energetico e per la previsione della loro vita utile.

Nel Capitolo 1 vengono introdotti la motivazione e il contesto del lavoro, vengono formulate le principali domande di ricerca e vengono delineati gli obiettivi complessivi, l'ambito e la struttura della tesi.

Nel Capitolo 2 vengono rivisti gli aspetti fondamentali delle batterie agli ioni di litio, inclusi i principi di funzionamento, i componenti di cella (anodi, catodi, elettroliti, separatori), i settori applicativi, i meccanismi di invecchiamento e degradazione, i concetti di stato di salute e vita utile residua, i processi produttivi, le vie di riciclo e le problematiche di sicurezza.

Nel Capitolo 3 viene presentata una rassegna critica e mirata degli approcci di modellazione per batterie agli ioni di litio allo stato solido. Piuttosto che passare in rassegna l'intera letteratura, vengono analizzati quattro modelli rappresentativi per la loro rilevanza concettuale e chiarezza metodologica. Da questi studi vengono spiegati i principali meccanismi elettro-chemo-meccanici che governano il comportamento della cella e vengono delineate le formulazioni matematiche utilizzate per rappresentarli, fornendo una visione chiara e aggiornata dello stato dell'arte.

Nel Capitolo 4 viene implementato un modello continuo termodinamicamente consistente, radicato nel quadro di Larché–Cahn, per predire la risposta della cella in una geometria tridimensionale realistica mediante l'accoppiamento di meccanica, elettrochimica e trasporto di massa. Il funzionamento della batteria è formulato come un problema

ai valori iniziali e al contorno; vengono derivate le equazioni di governo e le relative forme deboli per elettrolita, catodo, lamine e interfacce; il sistema risultante è risolto mediante uno schema agli elementi finiti di tipo Newton–Raphson, in un'implementazione ad alte prestazioni basata su deal.ii, utilizzando geometria e mesh che riflettono l'architettura completa a strati della cella (elettrolita/separatore, catodo, lamine e interfacce) e le condizioni operative. Tutti i costituenti solidi, ovvero il catodo in $LiCoO_2$ (LCO), l'elettrolita liquido incorporato nel separatore solido e le lamine, sono modellati assumendo elasticità lineare a piccole deformazioni, con la deformazione indotta dall'intercalazione rappresentata tramite deformazioni di rigonfiamento. Le condizioni al contorno sono applicate dove opportuno e le condizioni interfacciali sono imposte mediante relazioni di Butler–Volmer. La risposta elettro-chemo-meccanica accoppiata è stata investigata su un intervallo di C-rate e l'effetto dell'accoppiamento meccanico sul comportamento elettrochimico è stato esaminato. I risultati risultano coerenti con la letteratura consolidata, mostrando tensioni operative più basse e capacità ridotta all'aumentare del C-rate, nonché una chiara modifica della distribuzione di sovrapotenziale e dei campi di tensione dovuta all'accoppiamento meccanico.

Nel Capitolo 5 viene presentato uno studio elettrochimico comparativo svolto durante un periodo di ricerca in visita nel laboratorio della Professoressa Jennifer Schaefer presso il Dipartimento di Chemical and Biomolecular Engineering dell'Università di Notre Dame. Il metodo ibrido termochimico sviluppato dal Professore Khachatur Manukyan presso il Nuclear Science Laboratory, Dipartimento di Physics and Astronomy, Università di Notre Dame, è stato inizialmente testato su polvere commerciale di LCO; il processo è stato quindi ottimizzato passo dopo passo su tali campioni e, una volta ottenute prestazioni elettrochimiche coerenti con il riferimento commerciale, lo studio è stato esteso a precursori recuperati da pacchi batteria esausti. In questo quadro, le polveri di LCO rigenerate sono state confrontate con riferimenti commerciali da 0.1C a 5C utilizzando protocolli identici di preparazione degli elettrodi e di test in coin-cell. Sono stati analizzati la rate capability, i profili tensione–capacità e l'efficienza coulombica, e le prestazioni sono state correlate a microstruttura e contenuto di impurità. A causa della durata limitata del periodo di visita, non tutti i test pianificati hanno potuto essere completati e alcuni protocolli sono stati abbreviati; ciò si riflette nell'ambito dei risultati riportati. Per la stessa ragione, una validazione incrociata completa tra modello ed esperimento e una calibrazione dei parametri rispetto al modello continuo non hanno potuto essere intraprese e sono rimandate a lavori futuri. I risultati mostrano che la prestazione elettrochimica delle polveri rigenerate si avvicina a quella dei riferimenti commerciali e che il metodo sviluppato offre un percorso promettente per la rigenerazione dei catodi.

Infine, il Capitolo 6 riassume i principali risultati sia della parte di modellazione sia di quella sperimentale, discute i limiti del presente lavoro e delinea possibili direzioni per ricerche future.

Abstract

Despite their maturity, lithium-ion batteries still face challenges in applications that demand both high power and high capacity. Their operation hinges on classical intercalation, where lithium is inserted into and extracted from the electrode host. The associated volumetric changes can induce mechanical damage, undermine structural integrity, and break electrical contact with the current collectors. Designing nano-structured and composite electrodes can help mitigate these degradation mechanisms.

An electrochemical cell is made of current collectors, two electrodes (anode and cathode), and a solid separator, which is permeated by a liquid electrolyte in conventional batteries. Charge transport is phase-dependent: electrons conduct within the electrodes, while ions carry charge through the electrolyte. To sustain interfacial reactions, ions must traverse the electrolyte to the electrode surfaces. Consequently, mass transport in the electrolyte is described by the motion of mobile ions governed by diffusion (driven by concentration gradients) and migration (driven by the electric field).

Theoretical and computational studies deepen our understanding of how real batteries behave under both operational and extreme conditions and, alongside experiments, help tailor new materials and architectures. Consequently, modeling is a powerful tool for designing energy-storage systems and predicting their service life.

In Chapter 1, the motivation and context for this work are introduced, the main research questions are formulated, and the overall objectives, scope, and structure of the thesis are outlined.

In Chapter 2, the fundamental aspects of lithium-ion batteries are reviewed, including working principles, cell components (anodes, cathodes, electrolytes, separators), application domains, aging and degradation mechanisms, state-of-health and remaining useful life concepts, manufacturing processes, recycling routes, and safety issues.

In Chapter 3, a targeted, critical review of modelling approaches for all solid state lithium ion batteries is presented. Rather than surveying the entire literature, four representative models are examined for their conceptual significance and methodological clarity. From these studies, the key electro-chemo-mechanical mechanisms that govern cell behaviour are explained and the mathematical formulations used to represent them are outlined, providing a clear, up to date view of the state of the art.

In Chapter 4, a thermodynamically consistent continuum model, rooted in the Larche-Cahn framework, is implemented to predict battery cell response in three dimensional realistic geometry by coupling mechanics, electrochemistry, and mass transport. Battery operation is posed as an initial and boundary value problem, the governing equations and their weak forms for the electrolyte, cathode, foils, and interfaces are derived, and the resulting system is solved with a finite element Newton-Raphson scheme in a high performance computing implementation based on deal.ii, using geometry and meshing that reflect the complete multilayer cell-stack architecture (electrolyte/separator, cathode, foils, and interfaces) and operating conditions. All solid constituents, namely $LiCoO_2$ (LCO)

cathode, liquid electrolyte embedded in solid separator, and the foils, are modeled under the assumption of small strain linear elasticity, with intercalation induced deformation represented through swelling strains. Boundary conditions are applied where appropriate, and interface conditions are enforced through Butler-Volmer relations. The coupled electro-chemo-mechanical response was investigated across a range of C-rates, and the effect of mechanical coupling on electrochemical behavior was examined. The results aligned with established literature, showing lower operating voltage and reduced capacity at higher C-rates and a clear modification of the overpotential distribution and stress fields due to mechanical coupling.

In Chapter 5, a comparative electrochemical study conducted during a visiting research period in Professor Jennifer Schaefer's laboratory in the Department of Chemical and Biomolecular Engineering at the University of Notre Dame is presented. The hybrid thermochemical method developed by Professor Khachatur Manukyan at the Nuclear Science Laboratory, Department of Physics and Astronomy, University of Notre Dame, was first tested on commercial LCO powder; the process was then optimized step by step on these samples, and once electrochemical outputs consistent with the commercial reference were achieved, the study was extended to precursors recovered from spent battery packs. Within this framework, regenerated LCO powders were benchmarked against commercial references from 0.1 C to 5 C under identical electrode preparation and coin-cell testing protocols. Rate capability, voltage–capacity profiles, and Coulombic efficiency were analyzed, and performance was related to microstructure and impurity content. Owing to the limited duration of the visit, not all planned tests could be completed and some protocols were shortened; this is reflected in the scope of the reported results. For the same reason, comprehensive model–experiment cross validation and parameter calibration against the continuum model could not be undertaken and are deferred to future work. The findings show that the electrochemical performance of the regenerated powders approaches that of the commercial references and that the developed method offers a promising pathway for cathode regeneration.

Finally, Chapter 6 summarizes the main findings of both the modeling and experimental parts, discusses the limitations of the present work, and outlines directions for future research.

Acknowledgements

I would first like to express my deepest gratitude to my supervisor, Prof. Alberto Salvadori, for his constant support, supervision, and encouragement throughout my PhD, and for giving me the opportunity to pursue this work. His scientific guidance, trust, and patience have been invaluable for my development as a researcher.

I am also grateful to the University of Brescia and to the Department of Industrial and Mechanical Engineering for all the support provided during my doctoral studies.

I sincerely thank all current and former members of m4lab, both in the battery and mechanobiology teams, for their friendship and for creating such a stimulating and supportive environment. In particular, I am profoundly grateful to Dr. Mattia Serpelloni, who has always been like an older brother to me. I owe him much for everything he has taught me, for the many enjoyable moments we shared, and for his motivating presence during some of the most challenging periods of this journey.

I am sincerely grateful to Prof. Jennifer Schaefer for welcoming me into her laboratory in the Department of Chemical and Biomolecular Engineering at the University of Notre Dame, and for offering me the opportunity to carry out the experimental part of this work under her mentorship. I also wish to thank Prof. Khachatur Manukyan from the Nuclear Science Laboratory, Department of Physics and Astronomy at the University of Notre Dame, for generously sharing his expertise on hybrid thermochemical synthesis and for his continuous scientific guidance. My special thanks go to all the members of the Schaefer and Manukyan groups for their help in the laboratory, for the many discussions about batteries and materials, and for making my time at Notre Dame both highly productive and truly enjoyable.

I would like to express my deepest gratitude to Aysegul Dogan, my endless light. Without her, completing this work would probably have been impossible. I am deeply grateful for all her help, her support, and her tireless presence every time I fell, for always standing by my side and lifting me up, and for her love. I would not have come this far without her. I look forward with excitement to the future we will build together.

I would also like to express my deepest gratitude to my mother, Macide Girgin, the best parent I could ever wish for in this life. There are no words that can truly describe the love, gratitude, and appreciation I feel for you. I am endlessly thankful for your unwavering faith in me and for holding my hand from my very first steps, standing behind me at every stage of my life. Without you, I could not have done this.

Contents

Sommario i

Abstract iii

Acknowledgements v

Contents v

1 Introduction 1
1.1 Motivation and context . . . 1
1.2 Objectives and scope of the thesis . . . 3
1.3 Outline of the thesis . . . 5

2 Fundamentals of Li-ion Batteries 7
2.1 Working principle of lithium-ion batteries . . . 7
2.2 Main components of a lithium ion battery . . . 8
2.2.1 Anodes . . . 8
2.2.1.1 Carbon based materials . . . 8
2.2.1.1.1 Graphene . . . 9
2.2.1.1.2 One-dimensional carbon nanostructure . . . 9
2.2.1.1.3 Three-dimensional porous carbon nanostructures 10
2.2.1.2 Transition metal oxides . . . 10
2.2.1.3 Alloying anodes . . . 11
2.2.1.3.1 Silicon . . . 12
2.2.1.3.2 Germanium . . . 12
2.2.1.3.3 Tin . . . 13
2.2.2 Electrolytes . . . 14
2.2.2.1 Liquid electrolytes . . . 14
2.2.2.2 Solid electrolytes . . . 15
2.2.2.2.1 Inorganic solid electrolytes . . . 15
2.2.2.2.2 Solid polymer electrolytes . . . 15
2.2.2.3 Gel polymer electrolytes . . . 16
2.2.2.4 Hybrid electrolytes . . . 16
2.2.3 Cathodes . . . 16
2.2.3.1 Intercalation-type cathode materials . . . 17
2.2.3.1.1 Layered oxides . . . 18
2.2.3.1.2 Spinel oxides . . . 20
2.2.3.1.3 Polyanionic olivine phosphates . . . 21
2.2.3.2 Conversion-type cathode materials . . . 22

2.2.3.2.1 Transition-metal fluorides (FeF_3 and FeF_2) 22
2.2.3.2.2 Iron sulfide (FeS_2) 23
2.2.3.2.3 Sulfur-based cathodes 23
2.3 Application of lithium-ion batteries 24
2.3.1 Portable electronic devices 24
2.3.2 Electric vehicles 25
2.3.3 Grid energy storage 25
2.3.4 Medical applications 26
2.3.5 Renewable energy sources 26
2.4 Aging and performance degradation of lithium-ion batteries 27
2.4.1 Aging of lithium-ion batteries 28
2.4.2 State of health (SOH) and Remaining useful life (RUL) 28
2.4.2.1 Definition of SOH and RUL 29
2.4.2.2 Relationship between SOH and RUL 29
2.5 Fabrication process of lithium-ion batteries 29
2.6 Recyling of lithium-ion batteries 30
2.6.1 Methods of recycling 31
2.7 Lithium-ion battery safety issues 32
2.8 Conclusion 33

3 A Comparative Review for ASSLIBs 35
3.1 Introduction 35
3.2 Models and their governing equations. 36
3.2.1 One-dimensional single-ion conduction models [245] 39
3.2.2 An advanced framework for solid electrolyte intercalation batteries [246] 40
3.2.3 An advanced all-solid-state lithium-ion battery model [247] 42
3.2.4 Two-mechanisms model for all-solid-state lithium-ion batteries 45
3.3 Benchmark comparison 50
3.4 Final remarks and further developments 54
Appendix 3.A 59
Appendix 3.B 60

4 A 3D electro–chemo–mechanical continuum model for a Li/LCO half-cell 61
4.1 Introduction 61
4.2 Definition of the problem 63
4.2.1 Model geometry 64
4.3 The concept of balance laws in an abstract context 64
4.3.1 Conservation of moving species 64
4.3.2 Electro-quasistatic approximation of Maxwell's equations 65
4.3.3 Faraday's Law 66
4.3.4 Balance of momentum 67
4.4 Balance Laws 67
4.4.1 Balance equations for the electrolyte 67
4.4.2 Balance equations for the cathode 68
4.4.3 Balance equations for the foils 68
4.5 Thermodynamics 68
4.5.1 Thermodynamics: electrolyte 68

4.5.1.1 Energy balance . . . 68
4.5.1.2 Entropy imbalance . . . 70
4.5.1.3 Helmholtz free energy . . . 72
4.5.1.4 Thermodynamic restrictions . . . 72
4.5.2 Thermodynamics: cathode . . . 73
4.5.2.1 Energy balance . . . 73
4.5.2.2 Entropy imbalance . . . 74
4.5.2.3 Additive decomposition of strains . . . 74
4.5.2.4 Helmholtz free energy . . . 75
4.5.2.5 Thermodynamic restrictions . . . 75
4.5.3 Thermodynamics: foils . . . 76
4.6 Constitutive theory . . . 76
4.6.1 Constitutive theory: electrolyte . . . 76
4.6.2 Constitutive theory: cathode . . . 78
4.6.3 Constitutive theory: foils . . . 80
4.7 Interface Conditions . . . 80
4.7.1 Interface between the anode and the electrolyte . . . 81
4.7.2 Interface between the electrolyte and the cathode . . . 81
4.7.3 Interface between the cathode and the current collector . . . 83
4.8 Governing equations . . . 83
4.8.1 Electrolyte . . . 83
4.8.2 Cathode . . . 84
4.8.3 Foils . . . 85
4.9 Boundary and initial conditions . . . 85
4.10 Weak forms across all domains . . . 87
4.10.1 Electrolyte . . . 88
4.10.1.1 Weak form of the electrolyte . . . 88
4.10.1.2 Dimensionless weak form of the electrolyte . . . 88
4.10.2 Cathode . . . 90
4.10.2.1 Weak form of the cathode . . . 90
4.10.2.2 Dimensionless weak form of the cathode . . . 91
4.10.3 Foils . . . 93
4.10.3.1 Weak form of the foils . . . 93
4.10.3.2 Dimensionless weak form of the foils . . . 93
4.10.4 Interfaces . . . 94
4.10.4.1 Lithium foil-electrolyte interface . . . 94
4.10.4.1.1 Weak form of the lithium foil-electrolyte interface 94
4.10.4.1.2 Dimensionless weak form of the lithium foil - electrolyte interface . . . 95
4.10.4.2 Electrolyte-cathode interface . . . 96
4.10.4.2.1 Weak form of the electrolyte-cathode interface . . 96
4.10.4.2.2 Dimensionless weak form of the electrolyte - cathode interface . . . 97
4.11 Numerical example . . . 98
4.11.1 Description of computational domains . . . 99
4.11.2 Material parameters of the LIB cell . . . 100
4.11.3 Numerical outcomes and discussion . . . 101
4.11.3.1 Electro-chemo-mechanical response at 1C . . . 101

4.11.3.2 Electro-chemo-mechanical response at varying C-rates . . 114
4.12 Conclusions . . . 118
Appendix 4.A . . . 120
4.A.1 Finite element discretization in time and space for the electrolyte domain . . . 120
4.A.2 Newton-Raphson scheme in the electrolyte domain 123
4.A.3 Finite element discretization for the cathode domain . . . 125
4.A.4 Newton-Raphson scheme in the cathode domain . 128
4.A.5 Finite element discretization for the foil domains 129
4.A.6 Newton-Raphson scheme in the foils domain . . . 130
4.A.7 Finite element discretization for the lithium foil-electrolyte interface domain . . . 131
4.A.8 Newton-Raphson scheme in the lithium foil-electrolyte interface domain . . . 132
4.A.9 Finite element discretization for the electrolyte-cathode interface domain . . . 132
4.A.10 Newton-Raphson scheme in the electrolyte-cathode interface domain . . . 133

5 Commercial versus hybrid thermochemical regenerated $LiCoO_2$ cathodes: A comparative electrochemical study 136
5.1 Introduction . . . 136
5.2 Experimental procedures . . . 137
5.2.1 List of the samples . . . 137
5.2.2 Scanning electron microscopy images (SEM) . . . 138
5.2.3 Cathode preparation . . . 139
5.2.4 Determination of the mass loading . . . 140
5.2.4.1 Steps for determining mass loading . . . 140
5.2.5 Determination of porosity . . . 141
5.2.5.1 Steps for determining the porosity . . . 141
5.2.6 Coin cell assembly . . . 143
5.2.7 Half cell cycling performance . . . 144
5.3 Results and Discussion . . . 144
5.3.1 Cycling protocol and general rate trend . . . 144
5.3.2 Morphological comparison of commercial and regenerated LCO powders (SEM) . . . 144
5.3.3 Rate capability of LCO-C . . . 146
5.3.4 Rate capability of LCO-M . . . 146
5.3.5 Rate capability of LCO-R . . . 147
5.3.6 Rate capability of LCO-S . . . 149
5.3.7 Rate capability comparison of LCO materials . . . 150
5.3.8 Voltage-capacity profiles at different C-rates for each LCO material 152
5.3.9 Comparison of coulombic efficiency of LCO materials . . . 153
5.4 Conclusion . . . 155

6 Conclusions and outlook **157**
6.1 Summary of main contributions 157
6.1.1 Continuum electro-chemo-mechanical modeling 158
6.1.2 Comparative electrochemical study of commercial and regenerated $LiCoO_2$ cathodes 159
6.2 Limitations of the present work 161
6.3 Perspectives and future research directions 162
6.3.1 Model development and extensions 162
6.3.2 Strengthening the link between modeling and experiments 162
6.3.3 Implications for recycling and cathode regeneration 163
6.4 Final remarks 163

Bibliography **165**

Chapter 1

Introduction

1.1 Motivation and context

Modern society is increasingly dependent on technologies that require a continuous and reliable supply of electrical energy. From portable electronics to electric vehicles and grid-scale storage, the demand for high-performance energy-storage systems has grown dramatically over the past decades, driven by the global push for electrification and the integration of renewable energy sources into power systems [1, 2, 3]. At the same time, the environmental and geopolitical drawbacks of fossil-fuel–based energy systems – greenhouse gas emissions, air pollution, resource depletion, and supply-chain vulnerabilities – have made the transition toward low-carbon energy systems and renewable energy integration a central priority in both policy and research agendas [3, 4].

Lithium-ion batteries (LIBs) have emerged as the dominant technology enabling this transition. Their combination of high gravimetric and volumetric energy density, relatively long cycle life, and design flexibility has established LIBs as the state-of-the-art storage solution in consumer electronics, electric vehicles, and an increasing share of stationary storage installations [1, 5, 6].

In quantitative terms, global lithium-ion battery demand is projected to increase by more than an order of magnitude over the period 2010–2030, as illustrated in Figure 1.1. According to Bloomberg data compiled by Statista [7], demand rises from about 0.5 GWh in 2010 to 526 GWh in 2020 and is expected to reach approximately 9300 GWh in 2030. This dramatic growth underscores both the central role of LIBs in the energy transition and the urgency of addressing sustainability, resource availability, and end-of-life management.

However, this success also brings major challenges. The rapid growth in LIB deployment significantly increases the demand for critical raw materials such as lithium, cobalt, and nickel, raising concerns about long-term availability, supply-chain concentration, and associated environmental and social impacts [8, 9]. These issues are now widely recognized in critical raw-materials assessments and supply-risk studies for electrochemical energy storage technologies. At the same time, large volumes of end-of-life batteries must be managed in an environmentally sound manner, and questions of safety, durability, and accurate lifetime prediction have become central to the sustainable scaling of LIB technology [10].

At the cell level, LIB performance and degradation are governed by a complex interplay of electrochemical, transport, and mechanical processes. Lithium insertion and extraction cause volumetric changes in active materials; the resulting stress fields can induce

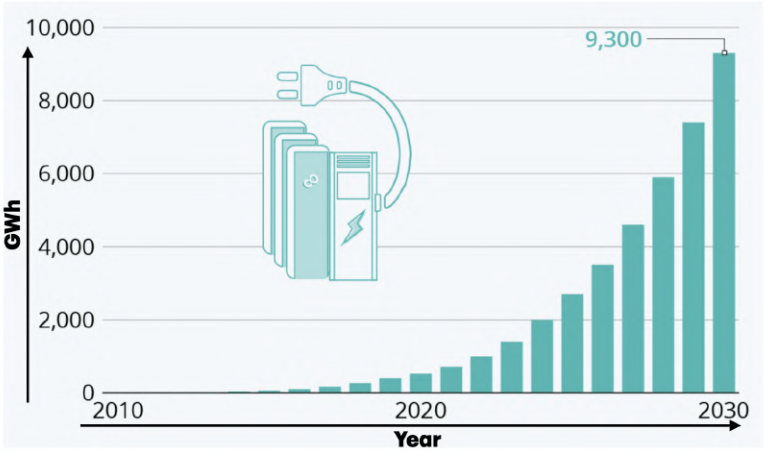

Figure 1.1: Projected trends in the rising demand for Li-ion batteries.

particle cracking, loss of electrical contact, interfacial delamination, and microstructural damage, ultimately degrading capacity and power capability [10, 11, 12]. Experimental and numerical studies have shown that mechanically driven damage in electrode microstructures is a key contributor to performance fade, particularly under high-rate or high-depth-of-discharge operation [11, 12]. Designing robust cells therefore requires not only improvements in materials and manufacturing but also a quantitative understanding of these coupled electro-chemo-mechanical phenomena at the electrode and cell scale.

The coupled interaction between lithium transport, electric potential, and mechanical deformation has been studied widely using continuum and finite-element models. At the electrode scale, finite-strain electro-chemo-mechanical formulations have been proposed to describe large lithiation-induced deformations and their feedback on diffusion and reaction kinetics [13, 14]. One such formulation [13] provides a thermodynamically consistent finite-strain theory for lithium-ion electrodes together with a monolithic, unconditionally stable finite-element scheme, which is particularly suited for high-volume-change materials such as silicon anodes. Another contribution [14] combines a phase-field description of two-phase intercalation with small-strain elasto-plasticity in microstructure-resolved simulations of lithium-iron-phosphate electrodes, thereby linking local stress fields to the effective electrode response. For solid-state batteries, several works have developed continuum electro-chemo-mechanical models that emphasize the role of space-charge layers, interfacial stresses and large deformation in solid electrolytes and composite cathodes. A general framework for all-solid-state cells is presented in [15], where space-charge layers and interfacial stresses at electrode–electrolyte interfaces are treated in a thermodynamically consistent manner. The work in [16] proposes a finite-strain electro-chemo-mechanical theory for ion transport in binary solid electrolytes, highlighting the coupling between swelling, stress and ionic conductivity in deformable solid conductors. A fully coupled phase-field finite-element model for composite all-solid-state cathodes is introduced in [17], capturing electro-chemo-mechanical interactions and damage within the composite microstructure. In addition, a three-dimensional finite-element formulation resolving the full microstructure of an all-solid-state cell and coupling nonlinear solid mechanics with electrochemistry in a monolithic fashion is developed in [18]. A substantial body of work has also focused on mechanically driven degradation. The work in [19] analyzes fracture in active materials using coupled electrochemical–mechanical and phase-field formulations to study crack initiation and propagation in electrode particles and composite electrodes. A gradient-

enhanced electro-chemo-mechanical framework with damage is proposed in [20] to investigate the nucleation and growth of lithium filaments and cracks in solid electrolytes. Beyond purely isothermal settings, [21] introduces a thermo–electro–chemo–mechanical model for lithium-ion cells and implements high-order transient finite-element simulations in two dimensions, illustrating how thermal, electrochemical and mechanical fields interact under dynamic operating conditions. Recent reviews [22] synthesize these developments and emphasize that electro-chemo-mechanical coupling has become a central design and degradation consideration, particularly in all-solid-state batteries where interfaces and mechanical constraints play a critical role. In contrast to most of these works, which either focus on individual particles, specific interfaces or solid-state architectures, the first part of the present thesis numerically solves a thermodynamically consistent, three-dimensional, multi-domain electro-chemo-mechanical model for a lithium-ion cell. The electrolyte, cathode and metal foils are treated as distinct but coupled mechanical and electrochemical domains and formulated together as a boundary-value problem with appropriate interface and boundary conditions. This problem is discretized within a finite-element framework and solved using a parallel implementation of the open-source C++ library deal.ii [23], enabling large-scale three-dimensional simulations on high-performance computing architectures.

In addition to understanding degradation at the cell and electrode scale, the sustainability of LIB technology depends on efficient recycling and regeneration strategies that close the loop for critical materials. In particular, $LiCoO_2$ (LCO) remains a widely used cathode material in consumer electronics due to its high energy density and reliable performance, despite the ongoing shift toward lower-cobalt chemistries in some applications [24]. Recovering and regenerating LCO from spent cells is essential to reduce the environmental footprint of LIBs, to mitigate critical-materials risks, and to enable circular-economy approaches in the battery value chain. Recent work has demonstrated that direct regeneration and advanced recycling routes can restore the electrochemical performance of spent LCO cathodes close to or comparable with commercial materials, provided that appropriate process conditions and impurity controls are used [25, 26, 27]. To be viable, regenerated cathodes must therefore be benchmarked against commercial references under controlled and comparable operating conditions.

Taken together, the modeling and experimental parts of this thesis address a common scientific problem: how the behavior and performance of LCO-based lithium-ion half-cells can be understood and evaluated by combining mechanistic continuum modeling with controlled electrochemical benchmarking. In this framework, the first part of the thesis develops a physics-based electro-chemo-mechanical description of an LCO-based half-cell, with the aim of identifying the coupled roles of lithium transport, electric potential, and mechanical deformation. The second part examines, under identical half-cell conditions, how regenerated LCO powders compare with commercial references in terms of short-term electrochemical response. Although these two parts are not combined here into a fully calibrated model–experiment workflow, they are conceived as complementary contributions to the same broader objective: improving the understanding and evaluation of LCO cathodes from both a mechanistic and a materials-performance perspective.

1.2 Objectives and scope of the thesis

This thesis is to contribute to a more quantitative and physically consistent understanding of the coupled electro–chemo–mechanical behavior of lithium-ion batteries, with

a specific focus on LCO-based cathodes and their regeneration from spent cells. The work combines continuum-scale modeling and numerical simulation of a Lithium-ion cell with an experimental study that benchmarks regenerated LCO powders against commercial cathode materials under controlled operating conditions.

More specifically, the thesis pursues the following objectives:

- To formulate a thermodynamically consistent, three-dimensional multi-domain continuum model for a lithium-ion cell that captures lithium transport, electric potential and mechanical deformation in the electrolyte, cathode and metal current collectors. The governing equations are expressed as a coupled boundary-value problem with appropriate interface and boundary conditions, and are subsequently non-dimensionalized to identify the dominant parameters and couplings.

- To discretize and solve this multi-domain boundary-value problem in a finite-element framework using a parallel implementation of the open-source C++ library deal.ii. The numerical framework is designed to perform fully three-dimensional simulations of the coupled electro-chemo-mechanical fields in realistic cell geometries, with several hundred thousand unknowns, on high-performance computing systems.

- To investigate LCO cathode materials from spent lithium-ion batteries using a hybrid thermo-chemical route developed by Prof.Khachatur Manukyan and coworkers [28], to prepare corresponding cathodes, and to carry out systematic electrochemical testing (rate capability and cycling) under defined conditions.

- To compare the electrochemical performance of regenerated LCO powders with that of commercial LCO, and to relate the observed behavior to differences in microstructure and possible impurity-related effects, thereby assessing the practical viability and limitations of the regeneration route.

The scope of the thesis is restricted in several ways. On the modeling side, attention is limited to isothermal conditions and small-strain linear elasticity with swelling in the active solid phases; fracture, interfacial delamination, solid–electrolyte interphases and detailed side-reaction kinetics are not modeled explicitly. The electro–chemo–mechanical analysis is carried out in a continuum framework using three-dimensional, idealized yet representative particle-resolved geometries based on randomly distributed cathode particles, rather than experimentally reconstructed, fully resolved electrode microstructures. On the experimental side, the work is restricted to LCO-based cathodes assembled into lithium-metal coin-cell half-cells and evaluated primarily by means of galvanostatic rate-capability tests and Coulombic-efficiency analysis over a limited number of cycles. This constraint is largely a consequence of the finite experimental window of the project: the electrochemical campaign could only be conducted within an approximately five-month period, which was not sufficient to design, assemble, and cycle a broader test matrix including long-term aging protocols. As a result, systematic cycle-life and degradation studies – such as extended high-cycle testing, calendar-aging experiments, or application-specific duty cycles – could not be implemented. Likewise, advanced electrochemical diagnostics (e.g. electrochemical impedance spectroscopy, cyclic voltammetry, or intermittent titration methods) were not pursued within this time frame. Therefore, the experimental section should be interpreted as a short-term, time-limited comparative evaluation of the synthesized cathode materials, and not as a full electrochemical validation of their long-term cycle life and durability. Within these boundaries, the thesis brings

together two distinct yet complementary contributions. The first is a continuum electro–chemo–mechanical modeling framework for lithium-ion cells, developed to provide mechanistic insight into the coupled roles of lithium transport, electric potential, and mechanical deformation in LCO-based systems. The second is an experimental benchmarking study of regenerated LCO cathode materials, designed to assess, under controlled and identical half-cell conditions, how close regenerated powders can come to commercial references in short-term electrochemical performance. These two parts are developed independently and do not constitute a fully coupled, calibrated model–experiment loop. Nevertheless, they address the same broader scientific question from two different but compatible perspectives: the first establishes a physics-based framework for interpreting coupled battery behavior, while the second provides comparative evidence on the practical viability of regenerated cathodes. In this sense, the thesis is not intended to present a complete validation workflow, but rather to place side by side two building blocks that can support future integration between continuum modeling and targeted electrochemical experiments.

1.3 Outline of the thesis

The remainder of this thesis is organized as follows.

Chapter 2 reviews the fundamental aspects of lithium-ion batteries, including working principles, cell components (anodes, cathodes, electrolytes, separators), application domains, aging and degradation mechanisms, state-of-health and remaining useful life concepts, manufacturing processes, recycling routes, and safety issues.

Chapter 3 presents a targeted critical review of modeling approaches for all-solid-state lithium-ion batteries (ASSLIBs). Rather than surveying the entire literature, four representative models are selected for their conceptual significance and methodological clarity. From these studies, the key electro-chemo-mechanical mechanisms that govern cell behavior are explained and the mathematical formulations used to represent them are outlined, providing a clear, up to date view of the state of the art.

Chapter 4 introduces a thermodynamically consistent continuum model, rooted in the Larche-Cahn framework, is implemented to predict battery cell response in three dimensional realistic geometry by coupling mechanics, electrochemistry, and mass transport. Battery operation is posed as an initial and boundary value problem, the governing equations and their weak forms for the electrolyte, cathode, foils, and interfaces are derived, and the resulting system is solved with a finite element Newton-Raphson scheme in a high performance computing implementation based on deal.ii, using geometry and meshing that reflect the full cell architecture and operating conditions. All solid constituents, namely LCO cathode, liquid electrolyte embedded in solid separator, and the foils, are modeled under the assumption of small strain linear elasticity, with intercalation induced deformation represented through swelling strains. Boundary conditions are applied where appropriate, and interface conditions are enforced through Butler-Volmer relations. The coupled electro-chemo-mechanical response was investigated across a range of C-rates, and the effect of mechanical coupling on electrochemical behavior was examined. The results aligned with established literature, showing lower operating voltage and reduced capacity at higher C-rates and a clear modification of the overpotential distribution and stress fields due to mechanical coupling.

Chapter 5 presents a comparative electrochemical study conducted during a visiting research period in Prof. Jennifer Schaefer's laboratory. Commercial LCO powders and

LCO materials regenerated from commercial and spent cells using a hybrid thermochemical method developed by Prof. Khachatur Manukyan and co-workers are benchmarked under identical electrode preparation and coin-cell cycling protocols. Rate capability, voltage–capacity profiles and Coulombic efficiency are analysed and compared, and performance is related to microstructure, porosity, and residual Li_2CO_3 originating from the regeneration process.

Finally, Chapter 6 summarizes the main findings of both the modeling and experimental parts, discusses the limitations of the present work, and outlines directions for future research.

Chapter 2

Fundamentals of lithium-ion batteries

Some part of this chapter is adopted from the publication [29].

2.1 Working principle of lithium-ion batteries

A conventional lithium-ion battery cell consists of five key components—electrolyte, anode, cathode, separator, and a pair of current collectors (positive and negative)—as illustrated in Figure 2.1. The anode and cathode both store lithium, while the separator acts as a barrier between the two electrodes and prevent electron flow within battery. Lithium ions move between the electrodes of a lithium-ion battery during charging and discharging, intercalating into the active materials. During discharge, lithium is deintercalated from the negative electrode (with copper acting as the current collector), releasing electrons. The positive electrode typically contains active materials like metal oxides, while the negative electrode is primarily made up of graphite and amorphous carbon compounds, into which lithium is intercalated. Figure 2.1 illustrates that, during discharge, lithium ions travel from the negative electrode via the electrolyte and separator to the positive electrode. Electrons at the same time move through from the negative electrode to the positive electrode via an external circuit, utilizing aluminum as the current collector. During charging, the process is inverted: lithium ions travel from the positive electrode, passing through the electrolyte and separator, to the negative electrode.

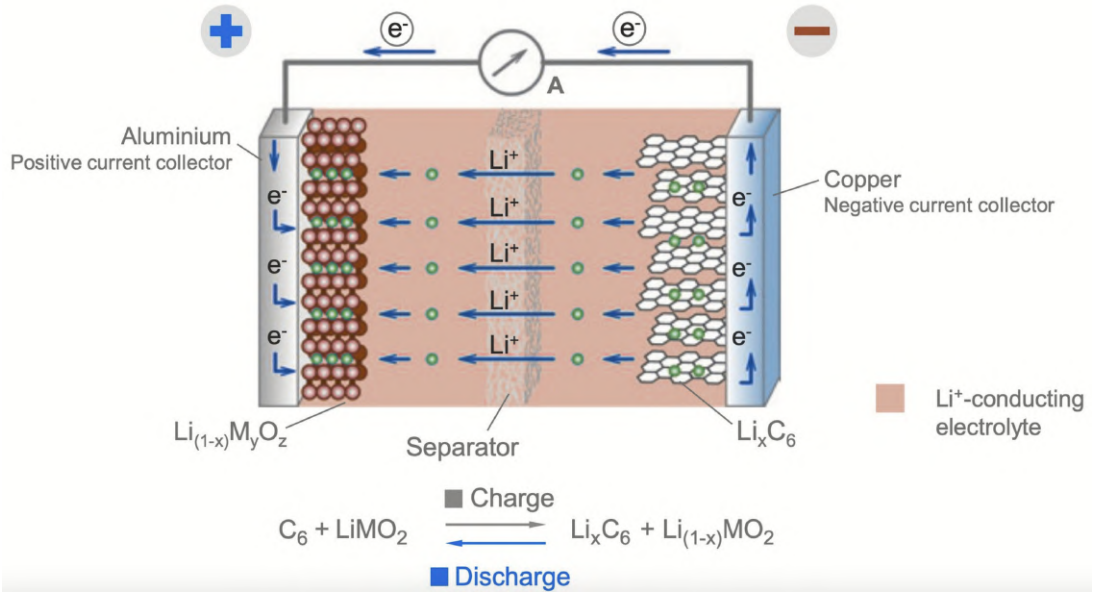

Figure 2.1: Typical configuration of a lithium-ion battery.

As mentioned in [30], the main reactions, expressed in a general form for a carbon anode, are represented in Equation (2.1) for the discharging process and in Equation (2.2) for the charging process.

$$\begin{aligned} &\text{Discharge reactions:} \\ &\text{At the anode:} \quad \mathrm{Li}_x\mathrm{C}_6 \rightarrow \mathrm{C}_6 + x\mathrm{Li}^+ + xe^- \\ &\text{At the cathode:} \quad \mathrm{Li}_{1-x}\mathrm{MO}_2 + x\mathrm{Li}^+ + xe^- \rightarrow \mathrm{LiMO}_2 \\ &\text{Global reaction:} \quad \mathrm{Li}_x\mathrm{C}_6 + \mathrm{Li}_{1-x}\mathrm{MO}_2 \rightarrow \mathrm{C}_6 + \mathrm{LiMO}_2 \end{aligned} \tag{2.1}$$

where MO_2 is the general formula for the cathode chemistry, denoting a metal (M = Co, Mn, Ni, etc.) oxide, and x signifies the stoichiometric coefficient of lithium participating in the process.

$$\begin{aligned} &\text{Charge reactions:} \\ &\text{At the anode:} \quad \mathrm{C}_6 + x\mathrm{Li}^+ + xe^- \rightarrow \mathrm{Li}_x\mathrm{C}_6 \\ &\text{At the cathode:} \quad \mathrm{LiMO}_2 \rightarrow \mathrm{Li}_{1-x}\mathrm{MO}_2 + x\mathrm{Li}^+ + xe^- \\ &\text{Global reaction:} \quad \mathrm{C}_6 + \mathrm{LiMO}_2 \rightarrow \mathrm{Li}_x\mathrm{C}_6 + \mathrm{Li}_{1-x}\mathrm{MO}_2. \end{aligned} \tag{2.2}$$

2.2 Main components of a lithium ion battery

2.2.1 Anodes

2.2.1.1 Carbon based materials

Carbon-based materials offer advantages such as low cost, ease of preparation, and variety in forms. Carbon-based materials are currently regarded as more realistic anode materials, operating as representatives of the lithium ion insertion/extraction mechanism. Graphite carbon, referred known as soft carbon, exhibits excellent crystallinity; nonetheless, lithium ions intercalate into graphite carbon in stages to produce LiC_6, resulting in a specific capacity of only 372 $mAhg^{-1}$.This limited theoretical specific capacity constrains the use

of graphitic carbon as a negative electrode material in hybrid and electric vehicles. Non-graphitic carbon, referred to as hard carbon, contains disordered internal crystallites. It has commendable stability; yet, it suffers from significant reversibility and capacity degradation issues. Research indicates that particle size, additives, and elevated porosity are the reasons of its high reversibility [31]. The nano size of carbon may effectively reduce the lithium ion diffusion length, enhance specific capacity, and the low-dimensional structure significantly contributes to structural stability. A considerable amount of research has focused on the synthesis of carbon materials, the optimization of their structures, and alteration of their properties [32].

2.2.1.1.1 Graphene

Theoretically, the thickness of a graphene sheet is merely one carbon atom, with a specific surface area reaching up to 2630 m^2g^{-1}. The hexagonal lattice structure gives favorable mechanical qualities to graphene, and both ends of the sheet may connect with lithium ions to form Li_3C, thereby attaining double the specific capacity of graphite [33]. Nonetheless, there are certain practical limitations regarding the utilization of graphene. The large specific surface area between graphene sheets will result in aggregation, and a decrease in the effective area will reduce the capacity. Additionally, graphene performs poorly as an anode material due to the restricted transport of electrons and Li^+ in the sheets [34].

2.2.1.1.2 One-dimensional carbon nanostructure

Carbon nanotubes (CNTs) are classified into single-wall carbon nanotubes (SWCNT) and multi-wall carbon nanotubes (MWCNT), depending on the quantity of graphene layers [35]. Single-walled carbon nanotubes (SWCNTs) possess a smaller diameter and exhibit fewer defects than multi-walled carbon nanotubes (MWCNTs), in which defects may arise between the layers. Many methods exist for synthesizing carbon nanotubes (CNTs), resulting in different morphologies, such as entangled and arrayed CNTs [36, 37]. Arrayed CNTs, due to their one-dimensional configuration, are particularly advantageous for electrode applications. The chirality of CNTs influences lithium ion diffusion and storage capacity, with SWCNTs demonstrating a greater diffusion barrier [38]. The carbon storage capacity of CNTs can exceed 1116 $mAhg^{-1}$ [39], although some lithium ions stored within the tubes are irreversible. The work [40] demonstrates that both the internal and external surfaces of CNTs can host lithium ions, with defects or openings in the tubes facilitating ion penetration. MWCNTs, having a 0.34 nm interlayer spacing, facilitate the accommodation of lithium ions. The curvature of the carbon nanotube walls enhances lithium storage via condensation processes, exhibiting a linear correlation between diameter and storage capacity [41]. Surface functionalization, particularly with NH_2 groups, can enhance lithium ion intercalation efficiency, hence improving the performance of CNTs as anode materials in lithium-ion batteries [42]. CNTs can also form free-standing conductive films that do not require binders, thanks to their ability to self-assemble [43, 44]. These free-standing films provide improved thermal resistance, flexibility, and may be formed into various geometries, making them appropriate for numerous applications. CNTs can serve as conductive additions when integrated into composite materials for developing high-capacity anode materials. As conductive additives, CNTs enhance electrical conductivity and cycling performance in composite materials by enabling powerful transfer of electrons through a "wire-to-point" conduction mechanism within electrodes [40]. CNTs can be modified using nanoparticles such as silver, which improves the adhesion between CNTs and metal substrates. This integration of CNTs with silver nanoparticles enhances

the conductivity and increases the power output of the electrode material. Zhao et al. [45] showed that this modification resulted in good conductivity due to the strong adhesion between CNTs and the metal substrate.

2.2.1.1.3 Three-dimensional porous carbon nanostructures

The porous carbon nanostructure is a conventional three-dimensional carbon material utilized as the negative electrode of lithium-ion batteries. These materials can be categorized into macroporous, mesoporous, and microporous types based on the size of their pores. The interconnected network structure of these materials offers excellent electrochemical performance, enhanced stability, and helps prevent irreversible capacity loss. As mentioned in [46], A three-dimensional porous nitrogen-doped graphite carbon framework infused with cobalt oxide ($CoO@N-GCs$) was fabricated through a simple polymer pyrolysis method. This material functions as an anode in lithium-ion batteries (LIBs), exhibiting outstanding electrochemical properties. Notably, the ($CoO@N-GC-400$) variant delivers an impressive initial capacity of 1628 mAh g^{-1} at 0.05 A g^{-1}, maintaining a robust capacity of 352.72 mAh g^{-1} even after 1000 cycles at 1 A g^{-1}. Throughout the pyrolysis process, the interconnected macroporous architecture is well preserved, with macropores forming in a direction perpendicular to the surface. This structural evolution primarily results from the high-temperature carbonization of polyvinylpyrrolidone (PVP) and the substantial pore generation caused by the thermal decomposition of cobalt nitrate ($Co(NO_3)_3$). Furthermore, the pore walls undergo a solid-to-hollow transformation as CoO nanoparticles are embedded within, reinforcing the material's stability and electrochemical efficiency. This innovative synthesis approach provides a promising route for engineering advanced anode materials in high-performance lithium-ion batteries. Three-dimensional graphene is a porous carbon nanomaterial. Its extensive production techniques encompass hydrothermal and chemical reduction procedures, capable of producing nanomaterials with submicron pore sizes. Nevertheless, the self-assembly procedure possesses inherent defects. The synthesized graphene network exhibits a significant number of defects and interlayer connections. Chemical vapor deposition (CVD) approach provides an efficient technique for synthesizing high-quality 3D graphene [47].

2.2.1.2 Transition metal oxides

Transition metal oxide (TMO) electrodes offer a high theoretical specific capacity (ranging from 500 to 1000 mAh g^{-1}), a tunable operating voltage, and outstanding cycling stability [48]. In comparison to commercially manufactured graphite anodes, TMO anode materials can prevent lithium dendrite formation and exhibit superior safety and specific capacity. The production cost is reduced in comparison to alloy anode materials. Nevertheless, the present commercial application remains not sufficiently developed, with numerous issues to address, such as inherent low conductivity, electrode degradation due to significant volume expansion, voltage hysteresis during charge and discharge cycles, and ongoing electrolyte decomposition. The voltage hysteresis issue arises from the reconfiguration of the anode material's structure during the lithiation and delithiation processes, which partially dissipates internal heat, hence minimizing the energy density efficiency of the charge and discharge cycle. Combining TMO with conductive carbon material is a method to solve the low conductivity of the TMO, therefore enhancing the conductivity of the material overal. The hierarchical structure, with its increased surface area, enhances the reaction rate, but this also leads to the persistent decomposition of the electrolyte and considerable loss of lithium. Two reaction mechanisms are applicable in the interaction

between TMO anode materials and lithium ions: the conversion reaction mechanism and the insertion/removal reaction mechanism. The conversion reaction mechanism described in [49] is fundamentally characterized as a redox process, which can be articulated in the following manner:

$$MO_x + 2x\ Li^+ + 2x\ e^- \rightarrow M + x\ Li_2O \tag{2.3}$$

where M refers to a nanoparticle of a transition metal element, which plays a crucial role in the aforementioned reaction reversibility. M demonstrates strong electrochemical activity and is employed to decompose Li_2O. Nonetheless, the high reactivity of nanoparticles may trigger electrolyte decomposition, compromising the overall performance of the battery. Research [50] indicates that the negative species influences the voltage lag issue. Different voltage delays are observed in nitrides, oxides, and sulfides of the same transition metal. Simultaneously, the potential of the negative electrode material that has been prepared is dependent upon the degree of strength of the ionic bond occurs between the oxygen ion and the transition metal cation [51]. The common transition metals involved in the conversion mechanism include cobalt, iron, and manganese. Titanium-based oxide exemplifies the insertion mechanism in transition metal oxides (TMO). The negative electrode materials in the insertion mechanism exhibits a smaller volume change compared to other types of material; nonetheless, it exhibits low conductivity and a specific capacity ranging from 175 to 330 mAh g^{-1}. Hematite (Fe_2O_3) and magnetite (Fe_3O_4) , with theoretical capacities of 1007 mAh g^{-1} and 926 mAh g^{-1}, respectively, are iron-based oxides extensively investigated as negative electrode materials. Researchers are concentrating on optimizing their structure and minimizing their dimensions, while simultaneously boosting their electrochemical performance through the integration of carbon materials or carbon coatings [52, 53]. Cobalt-based oxides, such as (CoO) and (Co_3O_4), are recognized for their high specific capacities. The dimensions and morphology of these oxides can be customized by modifying the synthesis techniques. In [54], CoO nanoclusters were successfully synthesized directly on copper foil, demonstrating a reversible capacity of 1516.2 mAh g^{-1} at a 1C current density, which underscores its potential as an attractive material for binder-free electrodes. Hydrothermal methods are commonly used to synthesize Co-based anode materials. Rui et al. [55] employed a hydrothermal technique to fabricate template-free, sea urchin-shaped hollow (Co_3O_4) nanoparticles. The material demonstrated remarkable rate performance, achieving a capacity of 433 mAh g^{-1} at a 10C current density. Mn-based oxides (comprising MnO, Mn_3O_4, Mn_2O_3, and MnO_2 [56]) have garnered significant interest owing to their elevated theoretical capacity and affordability. Nonetheless, they retain the intrinsic drawbacks associated with transition metal oxides. The 3D layered porous Mn_2O_3 single crystal synthesized in [57] shows a homogeneous parallelepiped arrangement and demonstrates a %95 Coulombic efficiency following the second cycle.

2.2.1.3 Alloying anodes

Negative electrode materials operating via an alloying mechanism form alloys between metallic lithium and metals or semimetals from Groups IV and V, such as Silicon (Si), Germanium (Ge), and Tin (Sn). The lithiation process of alloy-based materials can generally be categorized into addition and displacement reactions. In the case of pure active metals or inert metal composites, addition reactions occur, where only the active metal participates in lithiation, while inactive components remain electrochemically inert. The particle size of the active metal significantly influences battery performance, as it controls the lithium diffusion length and thus affects voltage behavior and capacity retention. El-

ements such as Fe, Co, and Ni are often incorporated to enhance electrical conductivity and improve mechanical stability. Carbon-containing composites can further improve rate capability. In displacement reactions involving binary alloys composed of electrochemically active and inactive elements, lithiation is driven by lithium insertion, which induces the separation of the inactive component while the active metal forms a lithium alloy. This process should not be interpreted as spontaneous self-decomposition of the alloy, but rather as a lithium-driven displacement–alloying mechanism. Compared to addition reactions, displacement reactions involve a single lithium-induced transformation step, and the resulting average voltage reflects both alloying and phase-separation energetics. Volume change remains a critical challenge for alloy-based negative electrode materials, as shown in Equation 2.4. The large volumetric expansion can lead to electrolyte decomposition, structural degradation of the electrode, and rapid capacity fading during cycling. Nevertheless, alloy anode materials offer exceptionally high specific capacities. Furthermore, elements such as Si, Ge, and Sn are abundant in nature. Their low lithium insertion potential contributes to higher cell voltage, while appropriate electrode design can mitigate lithium aggregation and enhance safety. For these reasons, alloy-based materials are considered promising candidates for next-generation lithium-ion battery anodes.

$$Sn_2Fe + 8.8Li \rightarrow 2Li_{4.4}Sn + Fe \tag{2.4}$$

2.2.1.3.1 Silicon

Silicon anode materials are seen as the most promising choices for the next generation of lithium-ion batteries owing to their significantly higher theoretical capacity in comparison to graphite [58, 59]. Si has a reduced working potential of 0.6 V relative to Li/Li+, hence expanding the operational voltage range of lithium-ion batteries [60]. An other significant benefit of utilizing Si anode materials is to their processing and fabrication, which involves very straightforward synthesis procedures [61]. Notwithstanding these benefits, significant disadvantages exist in its actual implementation, mostly because to the pronounced anode instability resulting from large volumetric changes. During repetitive charging and discharging cycles, the silicon anode can undergo significant volume expansion of up to % 300, leading to crack formation and total pulverization of the silicon anode. The pulverization causes a disruption of the electrical link among the active material and the current collector, leading to a fast decline in capacity [62].The phenomena of lithiation-induced deformation and stress have been thoroughly investigated over the past few years. Many researchers have conducted theoretical calculations to examine the swelling and stress generated by lithium intercalation induced swelling, offering or predicting the outcomes related to mechanical failure. For example, Christensen and Newman computed swelling and stress [63, 64], Cheng and colleagues computed the strain energy under both potentiostatic and galvanostatic processes for sphere-shaped particles [65, 66], and Sastry and colleagues simulated the stress generation throughout lithiation under galvano-static control [67]. Stress caused by lithiation in Si has been additionally computed [68]. Using electrochemical mechanics, lithiation-induced fracture has been documented in a number of recent publications [69, 70]. Furthermore, it leads to the development of a dense solid electrolyte interface (SEI) layer, which elevates internal resistance and diminishes battery capacity [61].

2.2.1.3.2 Germanium

Germanium is a prevalent semiconductor material. It is part of the same principal group as silicon and has analogous properties. In comparison to silicon, germanium exhibits

superior conductivity and lithium ion diffusion rates; its surface oxide layer is smaller, and the Coulomb efficiency of germanium-based anode materials is frequently higher. The volume expansion of Ge is isotropic, and the negative material is being subjected to uniform stress, thereby preventing anode material cracking due to stress concentration [71]. Germanium likewise encounters the same volumetric expansion issue as silicon. As a scarce metal, Ge has a comparatively high price. Throughout the battery cycle, germanium and lithium ions create a lithium-germanium alloy, resulting in a lithium-rich localized area that accounts for the superior lithium storage capacity of germanium-based anodes. Analogous to silicon, nanometerization and compounding are useful enhancement strategies to address its inherent limitations. Wang and colleagues employed Mg to decrease GeO_2, thereby synthesizing Ge nanoparticles approximately 30 nm in diameter, while eliminating the necessity for costly Ge compounds [72]. The synthesized nanoparticles exhibit a reversible battery capacity of 909 mAh g^{-1} at a current density of 3.2 A g^{-1}. Kim and coworkers [73] produced germanium nanowire (GeNW) with a diameter of 46 nm utilizing a gas-solid-liquid procedure and subsequently regulated the total number of graphene layers on the outermost layer by a catalyst-free CVD approach. The use of graphene markedly enhanced the electrochemical performance of GeNW. Following 200 cycles at a rates of 4.0 C, the capacity retention rate reached % 90. The thick Ge film possesses a substantial area capacity, effectively addressing the requirements of practical applications; however, the augmentation of film thickness results in a sharp decrease in capacity. Carbon coating can enhance the performance of Ge nanoparticles to a specific level. In the absence of a surfactant being used nanoparticle aggregation would make the coating ineffectual.

2.2.1.3.3 Tin

Tin (Sn) can serve as an anode material due to its high theoretical capacity of 993.4 mAh g^{-1} [74]. The lithiation/delithiation mechanism in tin-based anodes can be described as [75]:

$$x\mathrm{Li}^+ + xe^- + \mathrm{Sn} \rightleftharpoons \mathrm{Li}_x\mathrm{Sn} \quad (0 < x < 4.4) \tag{2.5}$$

Nonetheless, significant volume fluctuations and the agglomeration of Sn particles during the alloying/dealloying operation present primary challenges for applications in practice [76]. In order to overcome these difficulties and greatly improve the performance of Sn-based anode materials, carbonaceous substances and tin-based intermetallics are typically thought to be efficient [77]. Carbon materials, whether functioning as a support or a coating, can significantly mitigate volume fluctuations and accumulation of Sn particles while enhancing overall conductivity, particularly when utilizing graphene [78]. The graphene layer enhances electron mobility and inhibits the agglomeration of tin particles. Empty gaps can be incorporated between the graphene and tin nanostructures to facilitate the accommodation of volumetric fluctuations. The resultant composite exhibits a reversible battery capacity of 481 mAh g^{-1} with a current density of 100 mA g^{-1}. Certain Sn-based intermetallic compounds have been thought of as a viable option, including Sn-Sb, Sn-Bi, Sn-Se, Sn-Cu, Sn-Co, Sn-Fe, and Sn-Ni, among others [79, 80, 81, 82, 83]. Among all sorts of intermetallic materials, Sony's Nexelion, composed of Sn, Co, and C, is a commercially manufactured Sn-based anode, though its full composition remains undisclosed. Therefore, it is essential to further investigate the role and significance of cobalt in the Sn-Co intermetallic framework. Cobalt is generally considered an inactive element used to mitigate volume fluctuations. Moreover, cobalt does not generate Co carbides, hence preventing the loss of crystalline tin and enhancing the cyclic stability of the composite

[84, 85, 86]. The Sn-Cu alloy is a widely studied anode in lithium-ion batteries, particularly in the stable Cu_6Sn_5 intermetallic phase. Larcher and colleagues' [87] comprehensive in-situ X-ray investigation of Cu_6Sn_5 identifies two successive phase transformations of Cu_6Sn_5 in reaction with Li^+ in the following manner:

$$Cu_6Sn_5 + 10Li^+ + 10e^- \rightarrow 5Li_2CuSn + Cu \tag{2.6}$$

$$5Li_2CuSn + 12Li^+ + 12e^- \rightarrow Li_{22}Sn_5 + 5Cu \tag{2.7}$$

As the copper percentage in the copper-tin alloy grows, the resultant product will markedly enhance cyclability, as copper serves as an inactive buffering matrix to mitigate volume expansion. Nonetheless, it leads to a comparatively reduced discharge capacity; for instance, the theoretical specific discharge capacity of Cu_6Sn_5 in lithium-ion batteries is 584 mAh g^{-1} [88]. Conversely, certain Sn-based intermetallics containing electrochemically active metals such as Sb, Bi, and Ge exhibit superior initial capacities and enhanced electrochemical characteristics compared to the single active materials, attributable to the varying potentials relative to Li^+/Li of these active metals. The intermittent cycling process associated with these active materials ensures that tin and the active metals function electrochemically as mutually volume-releasing phases in succession [89].

2.2.2 Electrolytes

An inter-electrode medium, which includes the electrolyte, separates the electrodes [90, 91]. The purpose of this system is to grant ionic conduction while preventing the motion of electrons between electrodes, which would short-circuit the cell. Liquid electrolytes are the state-of-the-art in current cells but solid ones are a potential future substitute [92] and do not require the permeable membrane that accompanies liquid electrolytes. Alternative options, such as polymeric and hybrid electrolytes, lessen the disadvantages of both liquid and solid electrolytes by combining their benefits [93].

2.2.2.1 Liquid electrolytes

Liquid electrolytes (LEs) are usually made of a salt dissolved in a mixture of organic solvents, additives and co-solvents [94, 95, 96]. The salt dissolution provides the ionic species in the solvent, which dissociates the cations from the anions. Additives and co-solvents are added components that improve the performances of the electrolyte [97]. They reduce the viscosity of the electrolyte improving power performance or the wetting behavior, at the price of higher volatility [98]. Lithium hexafluorophosphate $LiPF_6$ is the most commonly used salt in lithium-ion batteries. It combines a strong ionic conductivity with chemical and electrochemical stability, being also able to passivate the aluminum current collector. Carbonate [99, 100] is a largely used organic solvent for lithium-ion batteries. The separator, a microporous polymer membrane, forms a multi-phase composite structure with the liquid electrolyte. Although the separator is not involved in the electro-chemical reactions, yet its porosity [101] and tortuosity [102] macroscopically influence the effective transport performances of the electrolyte. Tortuosity measures the degree to which the conductive pathways depart from the ideal state of a straight channel with a uniform cross section, while porosity quantifies the volume fraction occupied by the pores.

2.2.2.2 Solid electrolytes

Due to the absence of concentration polarization in the electrolyte, solid-state batteries (SSBs) have the potential to incorporate significantly thicker composite electrodes, thereby potentially augmenting their energy density. Solid-state electrolytes (SSEs) have the ability to limit the degradation processes that occur when different species diffuse between the electrodes of a battery. The community's fascination with electro-chemo-mechanics has been amplified by the increasing attention given to SSEs [103], which have been conventionally [104, 105, 106, 107, 108, 109, 110, 111, 112, 113, 114, 115] classified into two different groups based on their composition, i.e., inorganic (glasses [116], or ceramic [117] oxides or sulfides) and organic (mostly solid polymers [118]).

2.2.2.2.1 Inorganic solid electrolytes

It has just been ten years since *inorganic solid electrolytes* (ISEs) with high enough room-temperature conductivity became generally accessible for use in lithium-ion battery technology [119, 120]. *Ceramic* ISEs can be found in either a crystalline or glassy state. Oxides, sulfides, or phosphates-based compounds exhibit different crystalline structures, with ionic conduction due to diffusion in the lattice structure [120]. They include LISICON (lithium super-ionic conductor) [121], garnets (LLZO) [122], NASICON (sodium super-ionic conductor) [123]. Certain ISEs, such as lithium phosphorus oxynitride (LIPON) and lithium thiophosphates (Li_2S–P_2S_5), are notable examples of amorphous glass ceramics. All ISEs exhibit a brittle mechanical behavior, which results in an extensive network of micro-fractures accompanied with poor compatibility and stability towards the electrode. This effect rises significantly the interfacial resistance and poses challenges in scaling up from academic to industrial applications [124]. Numerous studies [125, 126, 127] have shown that several ceramics SSEs have reached levels of ionic conductivity comparable to liquid electrolytes. Other chemical and mechanical requirements must be met to put SSEs on the market, such as electro-chemical compatibility, electrode surface wetting, improved solid-solid interfacial contact between electrode and electrolyte interfaces, proper stiffness and fracture toughness, essential to ensure the structural integrity of the integrated system. Recently, research on ceramic ISEs indulged on gaining a comprehensive understanding of the complex properties of solid-solid interfaces, motivated by the considerable difficulties presented by the electrochemical and mechanical stability of SSEs at these interfaces [128]. Dendrite growth is a highly complex problem in SSBs, involving the interaction of mechanical and chemical forces. The infiltration of lithium dendrites into solid-state electrolytes (SSEs) has been extensively documented as a major cause of battery short-circuits across various SSE types [129, 130, 131]. In contrast to the dendrite growth mechanisms observed in liquid electrolyte systems, the growth of dendrites in SSBs is primarily influenced by the surface shape of the SSE. Li metal can be infiltrated and redistributed unequally in ISEs due to the existence of microstructural defects as pores, cracks, and grain boundaries [132]. Additionally, investigations were conducted to explore space-charge models in single-ion conductors, aiming to elucidate the phenomenon of Donnan potentials [133].

2.2.2.2.2 Solid polymer electrolytes

Solid Polymer Electrolytes (SPEs) are very relevant SSEs, with research efforts highly devoted to developing materials with high ionic conductivity. Dissolution of inorganic salts in polar polymer leads to SSEs with high conductivity. Several variables influence the electrostatic forces between metal ions and polar groups in polymers, such as the

type of the polar groups connected to the polymer backbone, the distance between polar groups, the degree of branching, the molecular weight, the type of metal cations, their charge and nature and charge of counterions. When cations are exposed to an electric field, they can move from one coordinated site to the other one. This is owing to the poor coordination of the cations to sites throughout the polymer chain [118]. Polyethers are considered the most popular polymer materials in SSEs. This is because of high electrochemical stability and good dissolution of lithium salts. The ether oxygens on polyethers creates binding to metal ions which facilitates the dissolution. PEO, is the most used solid solvent among polyethers, since it has ether oxygen atoms with high donor character (which leads to solvating cation ions), ethylene oxide segments which are flexible and the fact that it can be provided at an affordable price. Polypropylene oxide (PPO), polysiloxane (PSi), MEEP were among polymer materials with low Tg which have been explored by researchers, too [134].

2.2.2.3 Gel polymer electrolytes

Gel Polymer Electrolytes (GPEs) have received considerable attention because they combine the benefits of SSEs, as higher safety because the liquid content is kept inside a polymeric host matrix, and LEs, as high conductivity because the polymer matrix mainly serves as structural support. GPEs also show some drawbacks, as the emission of volatile compounds and reactivity with the metal electrode [118]. In terms of physical state, GPEs incorporate several states since amorphous, crystalline, and liquid regions co-exist [135].

2.2.2.4 Hybrid electrolytes

The purpose of developing hybrid electrolytes (HSE) is to improve the electrolyte performance using various ISEs-SPEs composites that ensure sufficiently high ionic conductivity, low interfacial impedance, and high electrode stability [136] overcoming the limited ionic conductivity and poor solid-solid interfacial contact between the electrode and electrolyte interface of SSEs. A hybrid electrolyte can be designed to have an inorganic filler in an SPE either active [137, 138] or passive (i.e., with no ionic carriers). The latter do not appreciably alter the ion-conduction mechanism, but ceramic fillers improve the mechanical properties of a polymer matrix: metal organic frameworks and clay minerals are examples of these materials, as are Al_2O_3, TiO_2, SiO_2, and ZrO_2. Active fillers boost ionic conductivity and directly participate in Li^+ (garnet, perovskite, sulfide, and oxy-nitride electrolytes fall into this category).

2.2.3 Cathodes

Most of the cyclable lithium inventory is stored in the cathode because the anode (graphite) is initially lithium-free. The characteristics of the cathode electrode fundamentally rely on its conductivity and structural stability. Like the anode, the cathode must also be able to facilitate reversible intercalation and deintercalation of Li^+ ions, as diffusivity is crucial in the cathode. The synthesis of materials that exhibit excellent performance, capacity, safety, and low cost will facilitate the widespread utilization of lithium-ion batteries (LIBs). The cathode electrode of lithium-ion batteries is the most heavy and most costly component when compared with the electrolyte and anode electrode [139].

2.2.3.1 Intercalation-type cathode materials

An intercalation cathode is a solid framework that allows for the insertion or extraction of a guest ion. Cathode development has historically lagged behind anode development in some aspects, particularly in terms of energy density and cost. From starting the next section concentration will be focused on several cathode materials. Li^+ ions serve as the guest ions, whereas the host network materials comprise transition metal complexes, oxides, metal chalcogenides, and polyanion compounds [140]. In intercalation reactions, electroneutrality is preserved because the host electrode material accommodates changes in the oxidation state of the transition-metal cations during during Li^+ intercalation/deintercalation. The layered structural oxide materials, which contain the formula $LiMO_2$ (where M is a 3D transition metal such as Co, Mn, Al, Ni, and the mixture, see section 1.2), have been the subject of numerous studies. The Li and M are organized in alternate layers, with M and Li enclosed by octahedral and tetrahedral arrangements of oxygen. Layered transition metal oxides ($LiNi_{1-x-y}Mn_yO_z$), manganese-based spinels ($LiMn_2O_4$), and polyanion materials are primarily utilized as cathode materials. These materials offer enhanced safety and reduced costs. Figure 2.2 compares the operating voltages and capacities of the several cathode materials currently employed in lithium-ion batteries (LIBs). The compounds predominantly utilized in Li^+ ion intercalation are

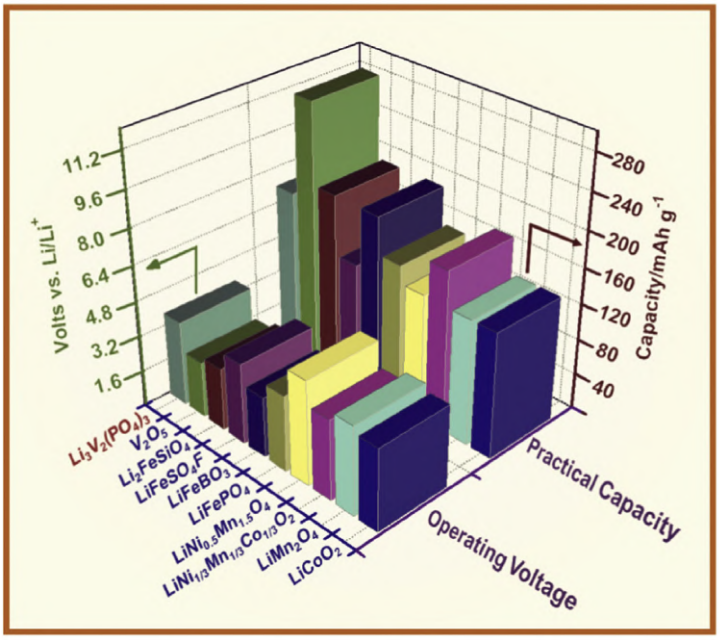

Figure 2.2: Comparative studies of various cathode materials in lithium-ion batteries (LIBs), focusing on their operating voltage and achievable practical capacity [141].

transition metal compounds featuring layered spinel and olivine crystal structures, as illustrated in Figure 2.3. The primary difficulty of the electrode is to improve energy density and maintain structural integrity at elevated energy densities. Layered materials are employed as cathodes in high energy systems, whereas olivine and spinel are utilized in high power lithium-ion batteries (LIBs) that offer longevity and cost-effectiveness, respectively. Researchers are persistently endeavoring to discover alternate materials for application. Several alternative materials have been extensively investigated (and in some cases demonstrated in prototype cells), including layered $LiNiO_2$ and $LiMnO_2$, together

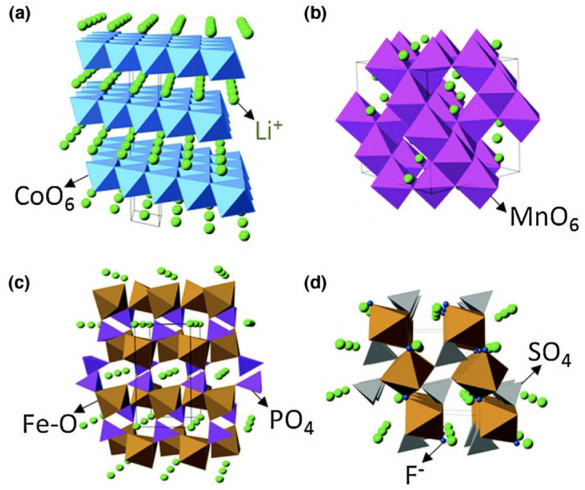

Figure 2.3: Crystal structures of (a) $LiCoO_2$ (layered), (b) $LiMn_2O_4$ (Spinel), (c) $LiFePO_4$ (olivine) and (d) $LiFeSO_4F$ [142]

.

with their derivatives ($LiNi_xCo_yO_2$, $LiCo_xNi_yMn_{1-x-y}O_2$), spinel-structured $LiMn_2O_4$, and olivine-structured $LiFePO_4$. The subsequent section presents a report on several cathode materials [143].

2.2.3.1.1 Layered oxides

Lithium cobalt oxide ($LiCoO_2$)

Since 1980, layered lithium cobalt oxide (LCO) has been the most common commercial cathode material utilized in rechargeable lithium-ion batteries (LIBs) and has attracted significant interest. They exhibit a structured layered arrangement with the space group R3m. The first-generation lithium-ion batteries (LIBs) have graphite as the anode, lithium cobalt oxide (LCO) as the cathode, and an organic liquid electrolyte consisting of dimethylene carbonate (DMC), ethylene carbonate (EC), and lithium hexafluorophosphate (LiPF6). During the electrochemical charging process, lithium ions depart from the cathode (LCO structure) and migrate via the solution of electrolyte to the graphite, while the corresponding electrons are conveyed by the power from the outside flowing from the cathode to the anode. During discharge, the electrons and Li^+ ions migrate in opposite directions. Despite the complete transfer of Li^+ions yielding a theoretical capacity of 274 mAh/g, the fundamental structure of LCO exhibits instability at high levels of delithiation, namely when the value of x exceeds one-half [144]. The limiting potential is approximately 4.2 V (versus. Li/Li+), corresponding to a practical capacity of about 140 mAh/g (approximately 0.5 Li per formula of LCO). The primary concern is the high cost and significant toxicity of cobalt, which is regrettable given its favorable electrochemical characteristics and straightforward production. The primary issues in lithium-ion batteries (LIBs) with increased energy density include structural instability and inadequate interface compatibility of lithium cobalt oxide (LCO) and other battery components. $LiCoO_2$ undergoes an irreversible change in phase at high potentials. Recent studies have employed doping or coating techniques to enhance the stability of $LiCoO_2$ at elevated potentials, resulting in a discharge capacity exceeding 200 mAh/g [145]. Several metals (including Al, Mn, Cr, Fe) were employed as dopants or partial alternatives for Co, exhibiting competent material properties but constrained performance [146, 147].

The application of several metal oxide coatings has enhanced the functionality and stability of LCO throughout extensive cycling. The stability of chemical and mechanical oxide materials minimizes structural alterations in LCO and mitigates side interactions with the electrolyte [148].

Lithium nickel oxide ($LiNiO_2$)

Dyer et al. [149] were the pioneers in introducing $LiNiO_2$ as a cathode material for rechargeable lithium-ion batteries. $LiNiO_2$ was deemed a more advantageous choice for cathode material compared to LCO because of its lower toxicity and cost-effectiveness. $LiNiO_2$ is synthesized by substituting Co^{3+} with Ni^{3+} in a structure analogous to that of LCO. The layered $LiNiO_2$ serves as an alternate cathode electrode material, characterized by an operating voltage of 4 V, a specific capacity of 250 mAh [150]. $LixNiO_2$ serves as the cathode in lithium-ion batteries, characterized by rhombohedral layered structures. The fundamental formula of lithium nickel oxide is $Li_{1-x}Ni_{1+x}O_2$, rather than $LixNiO_2$, where x ranges from 0.05 to 0.20. The rate capability of $LiNiO_2$ is exceptional and less prone to oxygen evolution [151]. A pure form of $LiNiO_2$ is not an advantageous cathode material since Ni^{2+} ions tend to substitute for Li^+ sites during manufacture and delithiation, obstructing the pathway for Li diffusion. $LiNiO_2$ exhibits more thermal instability than LCO due to the more facile reduction of Ni^{3+} relative to Co^{3+}. The actual application of $LiNiO_2$ is restricted by various factors, including restrictive cut-off voltages for optimal cycling, incomplete reversibility of the rhombohedral phase transition, and inadequate thermal stability, among others [152, 153]. The unadulterated form of $LiNiO_2$ exhibits significant lithium absence and cation disorder, which impairs electrochemical performance. The commercialization of pure $LiNiO_2$ was hindered solely by safety concerns. The breakdown of the cathode occurred following the exothermic oxidation of the electrolyte. $LiNiO_2$ was deemed the superior substitute for $LiCoO_2$. The limited lifespan of its electrochemical cycles and stability concerns are the primary issues. Consequently, $LiNiO_2$ is currently an unsuitable cathode material for lithium-ion batteries. Numerous endeavors were undertaken to resolve these issues. Other metals, including nickel (Ni), manganese (Mn), and aluminum (Al), have been partially substituted for cobalt in $LiNiO_2$ materials to enhance electrochemical performance.

Lithium manganese oxide ($LiMnO_2$)

Other layered oxide compounds, such as $LiMnO_2$ (LMO), have been intensively explored due to the more affordable price and reduced toxicity of manganese. The structure of LMO is more complicated than that of $LiCoO_2$ and $LiNiO_2$. LMO can be synthesized in several configurations. The fundamental structure of LMO comprises a zigzag-type orthorhombic LMO exhibiting Pmnm symmetry and a monoclinic LMO displaying C/2 m symmetry; both serve as electrochemically active materials, providing a theoretical capacity of 285 mAh/g. Anhydrous and stoichiometric layered LMO has been produced throughout the past two decades to enhance several features, including structural instability during cycling, inadequate crystallinity, and varying stoichiometry. The synthesis of pure $LiMnO_2$ and $LiNiO_2$ is challenging, and their structures exhibit instability relative to LCO during the charging process [154]. The cycling performance of LMO remains inadequate; during Li^+-ion extraction, the layered structure tends to transform into a spinel structure. ii) Manganese leaches from LMO during the cycle process. The theoretical capacity of LMO is 285 mAh/g, the practical capacity is 200 mAh/g, and the voltage range varies between 2.5 and 4.3 V [142]. The primary disadvantage of LMO is its rapid capacity degradation, leading to a transformation into the spinel structure [155]. The transfor-

mation of layered structures to spinel configurations impedes the specific capacity of the LMO cathode, as the electrochemical activity of the structure is partitioned into two domains: at 3 and 4 V vs. Li/Li+, interacting through phase transitions within these voltage ranges. The stabilization of LMO using cationic doping was conducted both theoretically and experimentally; nevertheless, the results indicated inadequate cycle stability at high temperatures [156]. Consequently, LMO has impeded extensive commercialization. Recent research has concentrated on transition metal oxide materials utilized in lithium-ion batteries (LIBs), such as $LiNi_{1/3}Mn_{1/3}Co_{1/3}O_2$ (NCM), $LiNi_{0.94}Co_{0.06}O_2$, tungsten-doped $LiNiO_2$, and nickel-rich layered oxide cathodes, among others.

Nickel based layered oxides ($LiNi_{1-x}Mn_xO_2$)
In order to enhance lithium consumption in the layered lattice and reduce material costs, substituting cobalt with nickel and other elements is a highly effective strategy. Nickel-based layered oxides ($LiNi_{1-x}M_xO_2$, where M = Co, Mn, and Al) have been produced and have achieved significant market success in recent times, including compounds such as $LiNi_{1/3}Co_{1/3}Mn_{1/3}O_2$, $LiNi_{0.5}Co_{0.2}Mn_{0.3}O_2$, and $LiNi_{0.8}Co_{0.15}Al_{0.05}O_2$. In comparison to $LiCoO_2$, this category of materials exhibits an identical α-$NaFeO_2$ structure as shown in Figure 2.2 (a), an equivalent average operating voltage (approximately 3.8 V vs. Li/Li^+), greater available reversible capacities ranging from 160 to 200 mAh g^{-1}, depending on the degree of nickel incorporation, and satisfactory long-term cycling stability, notwithstanding slightly elevated upper cut-off voltages (4.3–4.5 V vs. Li/Li^+). To enhance the gravimetric energy density of advanced rechargeable lithium-ion batteries to exceed 300 Wh kg^{-1} for electric vehicles with ranges above 300 miles, the advancement of Ni-rich layered oxides with a specific capacity of 200 mAh g^{-1} is essential. This has sparked significant research initiatives within the battery sector to reexamine Ni-rich layered oxides with elevated nickel content (Z0.8), including $LiNi_{0.8}Co_{0.1}Mn_{0.1}O_2$ [157, 158], $LiNi_{0.85}Co_{0.05}Mn_{0.1}O_2$ [159]. Simultaneously, increasing the operational voltage range of commercially recognized $LiNi_{1-x}M_xO_2$ above 4.5 V (e.g., $LiNi_{1/3}Co_{1/3}Mn_{1/3}O_2$ [160, 161], $LiNi_{0.4}Co_{0.2}Mn_{0.4}O_2$ [162, 163], etc.) is an alternative method to obtain greater capacities. Both systems provide difficulties, including challenges in sample processing and reduced battery safety and cycle longevity. The newly developed high-energy-density Ni-rich layered oxide cathodes require more optimization before they may achieve commercial viability in the coming years.

2.2.3.1.2 Spinel oxides

Spinel lithium manganese oxide ($LiMn_2O_4$)
The spinel lithium manganese oxide $LiMn_2O_4$ stands out as a promising cathode material due to its toxic-free and ecologically friendly properties, along with the high plentiful supply of manganese and its cost-effectiveness [164]. The spinel cathode provides a high discharge plateau, exceptional rate capability, and improved cycle performance. LiMn2O4 provides a cost-effective, non-toxic alternative with excellent thermal stability as well as high rate capability, featuring a potential of about 4 V (vs. Li/Li^+) and a theoretical capacity of 148 mAh g^{-1} [165]. A comprehensive examination of the electrical, thermal, and structural characteristics of $LiMn_2O_4$, along with the conduction mechanism for this material, is available in a different publication [166]. A number of studies [167, 168] examining the electrochemical properties of $LiMn_2O_4$ have reported discharge capacities ranging from 100 to 120 $mAhg^{-1}$, which corresponds to 67-81% of its theoretical capacity (148 $mAhg^{-1}$) [169]. A wide range of synthetic methods has been utilized to create spinel $LiMn_2O_4$, consisting of solid-state reaction [170], sol-gel technique

[171], hydrothermal synthesis [164], combustion synthesis, and templating approaches. In $LiMn_2O_4$, two strategies have frequently been suggested to enhance its structural integrity and electrochemical performance: cationic replacement and modification of the surface. Mn substituted spinels with the structural formula $LiM_xMn_2O_4$(where M represents Al, Co, Ni, or Zn) were the subject of extensive investigation by various research groups aimed at enhancing the cycling ability of $LiMn_2O_4$ [172, 173, 174, 175]. Between these compounds, $LiNi_xMn_{2-x}O_4$ demonstrated notable enhancement in the cycling performance of $LiMn_2O_4$. It was claimed that lithium substitution is utilized in the production of nearly all commercial spinel materials which contains manganese oxides (LMOs), as it enhances cycling behavior compared to $LiMn_2O_4$ [176]. Surface modification was proposed as an alternative method for enhancement, with materials such as Al_2O_3, $AlPO_4$, ZnO being investigated. Additional nanostructural alterations have been investigated, including the encapsulation of $LiMn_2O_4$ nanowires within ZnO [177] nanotubes by Liu et al. [178] and the uniform distribution of $LiMn_2O_4$ nanostructures in the structure of carbon nanotube (CNT) composite materials by Ding et al. [179] and the latter method exhibited a substantial enhancement in the cycling performance of $LiMn_2O_4$, nearing 100% after 100 cycles.

2.2.3.1.3 Polyanionic olivine phosphates

Lithium iron phosphate ($LiFePO_4$)

Polyanionic olivine $LiMPO_4$ (where M = Fe, Mn, Co, or Ni) is highly appealing as a cathode material for lithium-ion batteries. $LiMPO_4$ possesses an olivine structure, as illustrated in Figure 2.3. Lithium iron phosphate ($LiFePO_4$), presented as a cathode material by Goodenough in 1997, is among the most appealing commercially accessible positive electrode materials. Its popularity stems from its superior safety features, a large theoretical capacity of 170 mAh/g at low current densities, and a stable Fe^{3+}/Fe^{4+} redox potential of 3.5 V relative to Li^+/Li. $LiFePO_4$ provides a consistent voltage plateau, thermal stability at elevated temperatures, reliable electrochemical and chemical characteristics, exceptional cycling performance, affordability, and the plentiful availability of iron, rendering it a highly economical option. The crystal form of olivine $LiFePO_4$ has a polyanionic structure featuring octahedral LiO_6, octahedral FeO_6, and tetrahedral PO_4 units. The strong covalent bonds within the $(PO_4)_3^-$ polyanion help stabilize the oxygen at full charge, preventing O_2 release at high charge states, thus making $LiFePO_4$ a long-lasting, safe, and superior positive electrode material, as demonstrated in Figure 2.3(c). The configuration of the cation in $LiFePO_4$ is distinct from that found in $LiCoO_2$ (layered) and $LiMn_2O_4$ (spinel). The divalent ions of Fe^{2+} are positioned at the corners of the octahedral structure; P^{5+} is located in the tetrahedral sites, while Li^+ is found along the chain of shared edges with the octahedra. At first, a lag in capacity was noticed as a gradually reversible limit of insertion for Li_xFePO_4 at x = 0.06, and a capacity loss was recorded when the current density exceeded 0.05 mA/g. The decline in reversible capacity is linked to the sluggish diffusion kinetics of lithium ions, with the lost capacity being restored once the current density falls below 0.05 mA g^{-1}. The electronic conductivity of $LiFePO_4$ is notably limited because of the configuration of the ions in the crystal lattice framework [180]. The ionic and electronic conductivities are essential for the intercalation and deintercalation processes, facilitating the movement of charge-carrying ions within the electrode. Olivine exhibits limited electronic and ionic conductivity due to its low rate capacity. To address these challenges, different scientists have been investigating a range of techniques to improve the properties through different approaches. $LiFePO_4$ aims to

improve its electrochemical properties. Additional enhancement can be achieved through Fe doping of the material. The incorporation of ferrous metal can enhance ionic and electrical conductivity while offering extra support. Its thermally stable nature makes it extremely advantageous for use in electric vehicles (EVs). Among the several olivine materials, the most developed now under consideration is Olivine Lithium Phosphate [181]. In contrast to lithium transition metal oxides that incorporate hazardous and costly metals like cobalt and nickel, it utilizes more affordable and safer elements that include ferrous and phosphate.

2.2.3.2 Conversion-type cathode materials

Besides intercalation-type oxides and polyanionic compounds, a broad class of so-called conversion-type cathode materials has attracted increasing attention as candidates for next-generation high-energy lithium-based batteries [182, 183]. In these materials, lithium storage does not proceed via the reversible insertion of Li^+ into a pre-existing host lattice. Instead, the initial compound is fully transformed into new product phases upon lithiation and is ideally regenerated during delithiation through a multielectron redox process. A generic overall reaction for a conversion cathode may be written as

$$\mathrm{MX}_a + b\,\mathrm{Li}^+ + b\,e^- \rightleftharpoons \mathrm{M} + a\,\mathrm{Li}_{b/a}\mathrm{X}, \tag{2.8}$$

where M denotes a transition metal (e.g., Fe, Co, Cu) and X is typically a highly electronegative anion such as F^-, O^{2-}, S^{2-}, or a halide [184]. Here, a is the stoichiometric coefficient of X in MX_a and b is the number of electrons transferred (equal to the number of inserted Li^+); thus, b/a accounts for the anion valence (e.g., $b/a = 1$ for halides giving LiX and $b/a = 2$ for oxides/sulfides giving Li_2X). Because several electrons per transition-metal cation can participate in the redox reaction, conversion cathodes can, in principle, deliver significantly higher theoretical capacities and energy densities than conventional intercalation oxides such as $LiCoO_2$. However, these advantages are accompanied by considerable challenges, including low intrinsic electronic/ionic conductivity, large volume changes, complex reaction pathways and pronounced voltage hysteresis [182, 183]. Among the different conversion-type positive electrodes, transition-metal fluorides, sulfides and elemental sulfur (in Li–S cells) are the most intensively investigated representatives.

2.2.3.2.1 Transition-metal fluorides (FeF_3 and FeF_2)

Transition-metal fluorides (TMFs) are prototypical high-voltage conversion-type cathodes [185]. Iron fluorides, in particular FeF_3 and FeF_2, have received substantial attention due to the abundance and low toxicity of iron, in combination with the high electronegativity of fluorine, which yields relatively high reaction potentials (typically $\approx$ 2.7–2.8 V vs. Li/Li^+) [186, 187]. For FeF_3, the overall reaction

$$\mathrm{FeF_3} + 3\,\mathrm{Li}^+ + 3\,\mathrm{e}^- \rightleftharpoons \mathrm{Fe} + 3\,\mathrm{LiF} \tag{2.9}$$

involves a three-electron redox process per Fe center, corresponding to a theoretical capacity of approximately 712 mAh g^{-1}, i.e., about twice that of layered $LiCoO_2$ [188]. Early studies on bulk FeF_3 suffered from poor reversibility, sluggish kinetics and large voltage hysteresis, which were attributed to the insulating nature of the fluoride phases, the large structural rearrangements associated with the conversion reaction, and the growth of resistive interphases at the cathode–electrolyte interface [189]. To mitigate these issues,

recent research has focused on nanostructuring and composite design. Li et al [188] demonstrated high-capacity lithium-ion battery conversion cathodes based on networks of FeF_3 nanowires embedded in a conductive carbon matrix, reporting initial discharge capacities above 500 mAh g^{-1} and significantly improved cycling stability compared with microcrystalline FeF_3. Similar approaches using FeF_2 nanodomains confined in carbon nanopores, solid-polymer electrolytes to stabilize the cathode–electrolyte interphase, and oxyfluoride derivatives have further improved rate capability and cycling performance [190]. Nevertheless, TMF cathodes still suffer from voltage hysteresis and interfacial instability, and their practical use in commercial lithium-ion batteries remains at an early stage.

2.2.3.2.2 Iron sulfide (FeS_2)

Transition-metal sulfides constitute another important family of conversion-type positive electrodes. Pyrite-type iron disulfide (FeS_2) is widely studied as a model conversion cathode because it combines low cost, natural abundance and a very high theoretical capacity of approximately 894 mAh g^{-1}, based on a four-electron redox reaction: [191]

$$FeS_2 + 4\,Li^+ + 4\,e^- \rightleftharpoons Fe + 2\,Li_2S. \tag{2.10}$$

During discharge, FeS_2 typically undergoes an initial intercalation-like step at higher potentials, followed by a conversion reaction to form metallic Fe and Li_2S at lower potentials [192]. The coexistence of intercalation and conversion processes, the formation of nanoscale Fe/Li_2S mixtures and possible polysulfide intermediates makes the reaction pathway highly complex. Similar to fluorides, the FeS_2 cathode experiences large volume changes, mechanical degradation and severe interfacial side reactions with liquid electrolytes, which lead to rapid capacity fading and pronounced voltage hysteresis [191]. To address these limitations, recent work has explored FeS_2 embedded in mixed-conducting matrices, nanostructured FeS_2/carbon composites and solid-state configurations, which can better accommodate strain and suppress soluble intermediate species [191, 193]. For example, FeS_2 particles dispersed in a conductive porous matrix have shown markedly improved cycle life and rate performance in solid-state cells, indicating that careful control of particle size, morphology and electrode architecture is crucial for harnessing the high theoretical capacity of FeS_2 conversion cathodes.

2.2.3.2.3 Sulfur-based cathodes

Elemental sulfur is another archetypal conversion cathode material, mainly investigated in the context of lithium–sulfur (Li–S) batteries. The overall reaction

$$S_8 + 16\,Li^+ + 16\,e^- \rightleftharpoons 8\,Li_2S \tag{2.11}$$

corresponds to a very high theoretical capacity of 1672 mAh g^{-1} for sulfur and a moderate operating voltage of about 2.1 V vs. Li/Li^+ [194, 195, 196]. These characteristics make sulfur-based cathodes highly attractive for high-energy rechargeable batteries. However, Li–S cells are also conversion systems and face their own set of challenges, such as the insulating nature of sulfur and Li_2S, large volume changes and the dissolution and shuttling of lithium polysulfides in liquid electrolytes, which lead to self-discharge, low Coulombic efficiency and rapid capacity decay [183, 194, 197]. A wide range of strategies, including confining sulfur within conductive porous hosts, designing functional separators, and tailoring electrolytes, have been proposed to overcome these obstacles. Although Li–S batteries are typically considered as a separate beyond lithium-ion technology, they share

the same fundamental conversion-type reaction principles discussed above and therefore provide valuable insights into the design and optimisation of conversion-type cathode materials in general [182].

2.3 Application of lithium-ion batteries

Secondary lithium-ion batteries represent the fastest-growing high-energy storage solutions in the industry. The benefits of lithium-ion cells in comparison with other types of rechargeable electrochemical systems include the absence of a memory effect, a higher energy density per unit mass, and a self-discharge rate that is far lower than that of alternative options like NiCd and NiMH cells. Moreover, the lifespan of existing commercial lithium batteries exceeds 1000 cycles, and their shelf-life extends beyond 10 years [198]. While there are drawbacks, such as the fragility of lithium-ion battery materials that necessitate a protection circuit for safe operation, it is noteworthy that the newly developed Li-polymer cells offer improved handling and safety [199].

2.3.1 Portable electronic devices

Portable electronic devices, including mobile phones, laptops, and wearable devices, have experienced significant advancements in recent decades, propelled by the increasing need for efficient processing of data and real-time communication. The efficacy of these devices is significantly influenced by their energy storage systems, especially batteries. The ongoing advancement of battery technologies—from lead-acid to Ni-Cd, Ni-MH, and, most recently, lithium-ion batteries—has played a crucial role in the progression of portable electronic devices, facilitating compact designs and enhanced functionality. Nonetheless, current battery technologies still exhibit several limitations that affect the performance and sustainability of portable electronic devices. A significant challenge lies in the restricted energy storage capacity, which frequently does not satisfy the growing energy requirements of contemporary portable electronic devices, thereby constraining their capacity to deliver extended usage durations and enhanced functionalities. Furthermore, the limited cycle life continues to pose a considerable challenge, especially in high-temperature environments or with extended usage, impacting the durability and performance of portable electronic devices. Batteries like Ni-Cd exhibit significant self-discharge rates, making rapid charge loss when not actively utilized, presenting a challenge for devices that operate intermittently. Moreover, specific batteries, notably Ni-Cd, present environmental issues because of their toxic nature, particularly when not disposed of correctly. Ultimately, although lithium-ion batteries dominate the market because of their exceptional performance, the elevated manufacturing costs continue to hinder their accessibility for cost-effective portable electronic devices. To address the increasing demand for rechargeable batteries in portable electronic devices, considerable efforts are dedicated to enhancing current battery systems through the investigation of novel materials, innovative techniques, and cutting-edge energy chemistries. Innovative battery systems, including Li metal-based batteries, sodium-ion batteries, and rechargeable batteries featuring solid electrolytes, are under examination as potential alternatives to existing technologies. The anticipated advancements in these next-generation batteries are poised to fulfill the requirements for enhanced performance and safety in upcoming portable electronic devices. The incorporation of Artificial Intelligence (AI) into the science of materials is demonstrating significant potential for speeding up advancements in battery development. The

utilization of AI enhances data analysis efficiency, facilitates the prediction of new compositions, and enables the identification of potential materials with customized properties for targeted applications. This method has the potential to greatly improve the efficiency, safety, and economic viability of upcoming battery technologies. In conclusion, although battery technologies have significantly contributed to the advancement of portable electronic devices, there are still challenges to address, including limited energy storage capacity, short cycle life, elevated self-discharge rates, environmental issues, and high costs. Continuing to explore and innovate in these areas will be essential for developing the next generation of portable electronic devices and satisfying the growing energy requirements of future technologies [200].

2.3.2 Electric vehicles

In the near future, gasoline-powered vehicles are expected to be largely substituted by electric vehicles. The core component of an electric vehicle is its rechargeable battery, which requires outstanding performance. The lithium-ion battery is widely utilized in consumer electronics due to its high energy and power density, extended service life, and comparatively eco-friendly nature when assessed against other commonly used rechargeable batteries such as Ni-Cd, Ni-MH, and Lead-acid batteries. In order to assemble a battery pack, it is essential to configure multiple batteries in both parallel and series arrangements, particularly for high-power applications such as electric vehicles and energy storage systems. This raises concerns regarding cost, stability, consistency, and safety issues. The range of applications for lithium-ion batteries is limited by these challenges. The charge rate, temperature, and voltage range significantly influence the safety and reliability of lithium-ion battery usage. Exceeding these limits can lead to a rapid decline in battery performance and may pose potential safety concerns. Furthermore, it is essential to evaluate the capacity of lithium-ion batteries and estimate the remaining useful life of the electric vehicle throughout the battery's service life to ensure dependable performance of lithium-ion batteries. Additionally, techniques for cell sorting are crucial to guarantee the reliability and safety of cells [201]. The external environment and internal factors influencing lithium-ion batteries lead to battery aging and performance decline, which must be considered when evaluating their state of health. In battery electric vehicles, precise state of health prediction is essential for extending battery lifespan and ensuring safe functionality. Numerous algorithms for predicting state of health currently exist; however, most are primarily utilized in simulated environments due to their complexity in real industrial applications [202].

2.3.3 Grid energy storage

The grid energy storage system is essential for electricity utilization, offering electrical energy for a range of broad applications. The variation in electrical power demand occurs on a daily, seasonal, and even urgent basis. Furthermore, a significant difference between the highest and lowest values from day to night can be noted. Consequently, it is essential to store the generated power and supply available power during peak load through peak shaving and load leveling. Furthermore, renewable energy sources are influenced by geological, and seasonal conditions. The periodic features result in irregular variations in output power, resulting in it unsuitable for direct application to the electrical grid. Consequently, it is essential for the power grid system to stabilize the variable output

power produced by renewable energy sources and mitigate the fluctuations associated with these sources, including wind and solar energy, through the adjustment of their output profiles. Due to its remarkable benefits, such as a relatively high specific energy (up to 200 Wh/kg), impressive energy efficiency (exceeding 95 %), and a long cycle life (3,000 cycles at significant depletion of 80 %), lithium-ion batteries have received considerable interest as backup systems in grid storage. The significance of lithium-ion batteries in the market is underscored by the statistic that 77 % of the electrical power storage devices currently employed to support the grid in the USA rely on this technology. Moreover, lithium-ion batteries present a highly favorable choice for integration with solar and wind energy within grid energy storage systems, owing to their impressive energy density. Peak trimming and load leveling are essential for storing the generated electricity and supplying it during peak demand periods. Storage systems maintain a constant level of voltage and frequency in the supply of electricity during instances of imbalance among power generation and consumption [203].

2.3.4 Medical applications

Recent advances have led to the development of medical applications utilizing lithium-ion batteries that might be recharged whereas remaining inside the body. While the specific performance requirements of the device may vary, there are several common criteria that remain consistent. These include high levels of protection, reliability, volumetric energy density, extended service life, and indicators for state of discharge. The advancement of biomedical implanted devices for the treatment of human diseases has been made feasible through the effective development and application of various battery types, particularly lithium-ion batteries [204, 205]. In the context of using a lithium ion battery as an energy source for an implantable medical instrument, it is essential to track the battery's capacity decline and assess its remaining useful life as time progresses. This can provide guidance to the patient and their healthcare provider regarding the necessity and timing of a potential device substitution. The types of implantable healthcare devices that may be powered by a lithium-ion battery include neurological stimulators, cardiac stimulators such as pacemakers and defibrillators, as well as diagnostic equipments such as heart rhythm monitors [204].

2.3.5 Renewable energy sources

Batteries play a vital role in the functioning of renewable energy systems, acting as the primary medium for energy storage. lithium-ion batteries demonstrate significant potential owing to their exceptional performance and consistently decreasing costs [50]. Conversely, the availability of energy from renewable sources often fluctuates due to factors such as insufficient wind or sunlight. Consequently, it is crucial to oversee the power fluctuations within a power system that integrates various renewable energy sources, such as solar and wind [206, 207]. Wind power generation stands out as a significant source of renewable energy. Wind energy generation experiences considerable challenges due to its inherent intermittency, which is heavily influenced by seasonal variations and geographic factors. Moreover, it is typical to observe a difference between the peak power generation and consumption. A highly effective approach involves utilizing lithium-ion batteries to capture surplus energy generated by wind turbines, thereby providing electrical energy during peak consumption periods [203, 207]. Figure 2.4 demonstrates a schematic illustration of

utilizing a lithium ion battery bank for the storage of extra energy generated by a wind power generator system. The integrated lithium-ion packs enhance solar photovoltaic

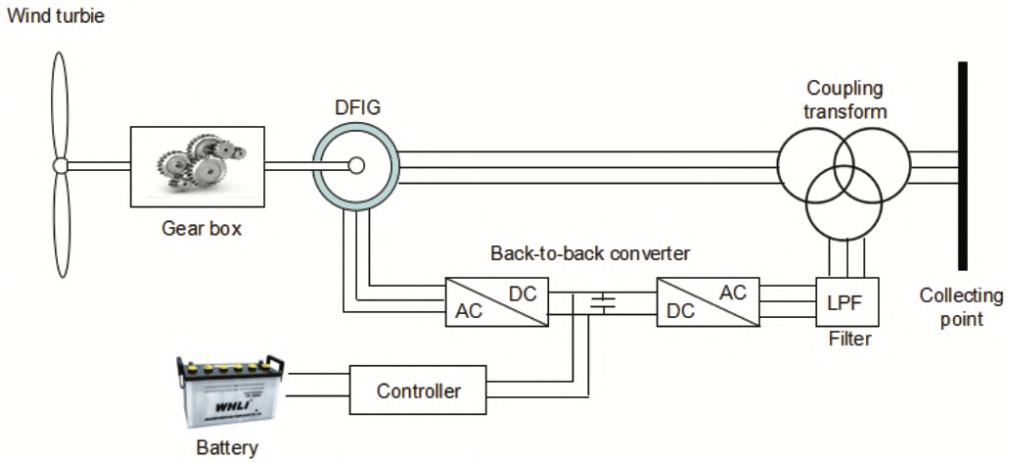

Figure 2.4: Schematic represantation of battery energy storage system integration with wind energy conversion system [208].

(PV) power plants by optimizing electrical energy storage and effectively managing output power. One of the significant challenges is that solar photovoltaic systems cannot generate energy at night or when sunlight is blocked. The integration of batteries creates an optimal operational system capable of handling both consistent power demands and significant power peaks. The implementation of battery packs in a solar photovoltaic farm has demonstrated consistent power generation [203, 209]. A schematic diagram of a photovoltaic power plant and battery storage system is presented in Figure 2.5.

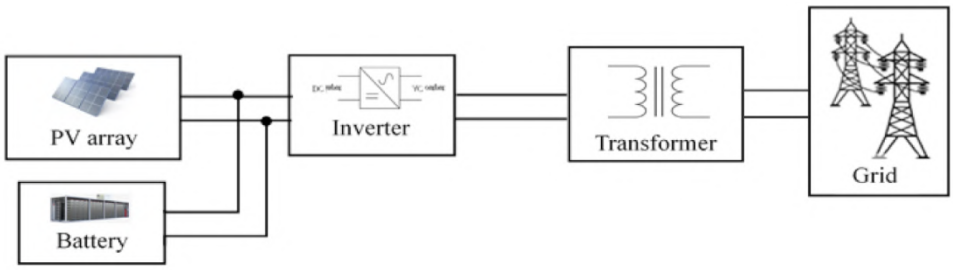

Figure 2.5: A block Diagram of a PV and battery storage system [210].

2.4 Aging and performance degradation of lithium-ion batteries

The performance of lithium-ion batteries is notably influenced by aging and improper usage. Battery leakage, insulation degradation, and partial short-circuit issues are significant challenges that may result in severe accidents once the battery's performance deteriorates beyond a critical threshold. Studies have discovered a link between these incidents and the aging of lithium-ion batteries. Consequently, it is essential to investigate

the state of health (SOH) of lithium-ion batteries in order to avoid catastrophic failures. At present, certain individuals assess battery performance and degradation by examining the battery's remaining useful life (RUL). Consequently, SOH and RUL exhibit a strong correlation and can effectively characterize battery functionality [202, 211].

2.4.1 Aging of lithium-ion batteries

The aging of lithium-ion batteries is the primary factor that impacts their health and lifespan. The internal chemical reactions within the battery are highly complex, and explaining the exact causes of aging is not simple. However, recent studies have explored and attempted to clarify the dynamics of battery aging. According to current research, aging is mainly driven by both external environmental factors and internal mechanisms. External factors include the battery's location and operating conditions, such as temperature, charge and discharge rates, depth of discharge (DOD), and the charging cut-off voltage. Internal factors are primarily related to three mechanisms: loss of lithium inventory (LLI), loss of active material (LAM), and conductivity loss (CL). LLI includes the formation of the solid electrolyte interphase (SEI) layer, the growth of lithium dendrites, and battery self-discharge. LAM refers to the breakdown of the cathode and anode materials, as well as electrolyte decomposition. CL pertains to aging caused by degradation of the current collector and adhesive materials within the battery [202]. Figure 2.6 presents an explanation of these aging mechanisms.

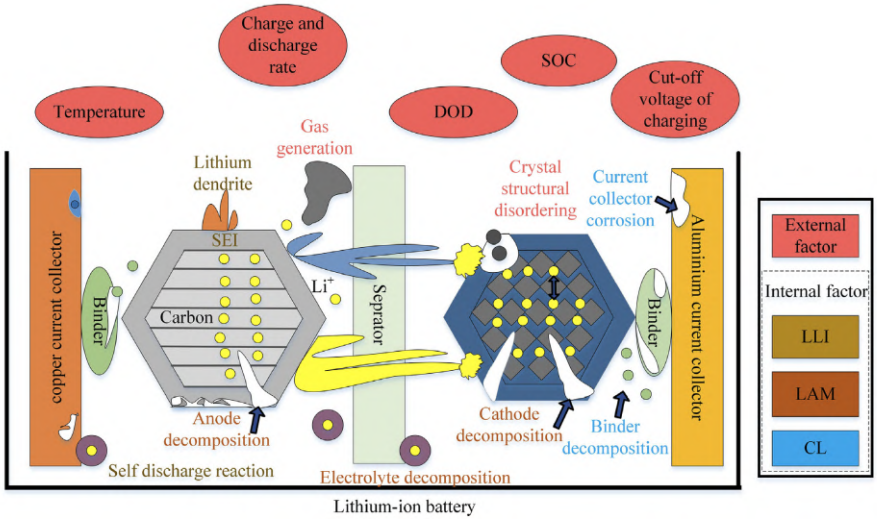

Figure 2.6: Schematic representation illustrating the factors contributing to battery aging [202].

2.4.2 State of health (SOH) and Remaining useful life (RUL)

Concentrating on enhancing battery lifespan, the forecasting of state of health and remaining useful life has become a crucial field of study. Different sources perceive them as either the same or completely separate variables. Alongside the distinctions, shared characteristics, and connections between the two that have sometimes been overlooked, there are also cases of misunderstandings or incorrect definitions linked to these terms. This section aims to elucidate the discussion by providing complete explanations for the terms and examining the relationships between them.

2.4.2.1 Definition of SOH and RUL

The state of health (SOH) of the battery is a measure of its dynamic condition in relation to its starting condition. At moment of production, this original condition is usually regarded as SOH = 100 %. Battery aging is the term used to describe the irreversible internal physical and chemical mechanisms that cause the SoH reduce with time and usage. The battery must be replaced when its capacity to store and deliver energy falls below a certain level, indicating that it is exhausted yet still useful. At this point, 0 % is the definition of the SOH. The remaining useful life (RUL) is a significant metric, categorized alongside another dynamic battery status indicators. This is closely associated with the state of health, typically characterized by the number of charge and discharge cycles or the remaining time until the battery's SOH reaches 0% [211].

2.4.2.2 Relationship between SOH and RUL

According to their description, a significant relationship exists between SOH and RUL, as the aging parameter serves to characterize both concepts. As a result, the estimation of SOH and RUL can be conducted employing the same methodologies from this perspective [202]. A range of techniques, such as traditional methodologies, model-driven approaches, and innovative algorithms, are employed to evaluate the state of health and remaining useful life of the battery. Nonetheless, the strength of the approach is diminished by uncertainties in the model. Nevertheless the calculations inherent in these methodologies are challenging and demand huge amounts of training data [212].

2.5 Fabrication process of lithium-ion batteries

Figure 2.7 illustrates the contemporary advanced battery fabrication process, which consists of three main stages: electrode preparation, cell assembly, and electrochemical activation of the battery. Initially, the active material, conductive additives, and binder are mixed with a solvent to form a uniform slurry. N-methyl pyrrolidone (NMP) is commonly employed to dissolve the binder, polyvinylidene fluoride (PVDF), in the cathode, while the binder in the anode, styrene-butadiene rubber (SBR), is dissolved in water along with carboxymethyl cellulose (CMC). The slurry is subsequently applied to each sides of the current collector (aluminum foil for the cathode and copper foil for the anode) utilizing a slot die, prior to being transferred to a drying system to remove the solvent [213]. NMP, a prevalent organic solvent for cathode slurry, is hazardous and subject to stringent emission laws. The solvent recovery process is essential in cathode manufacturing, wherein recovered NMP is repurposed for battery fabrication, resulting in a loss of 20 % to 30 % [214]. The nontoxic vapor from the water-based anode slurry can be released directly into the surrounding environment. The subsequent calendering operation can modify the physical characteristics of the electrodes. Following to these operations, the completed electrodes undergo stamping and slitted to the required dimensions to conform to the cell design. The electrodes are subsequently placed in the vacuum oven to eliminate the surplus water. The moisture content of the electrodes will be assessed post-drying to mitigate side reactions and corrosion within the cell. Upon adequate preparation of the electrodes, they are relocated to a dry room alongside separators for cell construction. The electrodes and separators are either coiled or arranged in layers to form the inner structure of the cell. Aluminum and copper tabs are subsequently welded onto the cathode and anode cur-

rent collectors, accordingly. Ultrasonic welding is the predominant method employed for this operation; however, many manufacturers choose resistance welding according to their particular cell design specifications. The constructed cell stack is subsequently positioned within a tailored enclosure, which differs among manufacturers due to the absence of a global standard. The selection of enclosure design frequently relies on the cell's intended application. The container is ultimately filled with electrolyte, sealed, and the cell fabrication procedure is finalized [213]. Prior to supplying the cells to the final product producers, electrochemical activation procedures are performed to ensure operational stability. In addition to preventing irreversible electrolyte utilization, a stable solid-electrolyte interface (SEI) layer can shield the anode from overpotential throughout rapid charging, which may cause Li dendrites to develop [215]. The production and aging process starts by charging the cells to a low voltage (e.g., 1.5V) to avert corrosion of the copper current collector, succeeded by a resting phase for electrolyte soaking. The cells are subsequently charged and discharged at a low current rate (e.g., C/20), progressively increasing the rate for stabilizing solid electrolyte interphase layer on the anode [216]. Gas produced during the forming process is released for safety purposes. Post-formation, the cells are stored on aging shelves to facilitate thorough electrolyte soaking and SEI stabilization, followed by an additional degassing phase prior to final sealing. This process generally endures for several weeks, contingent upon the methodology and aging temperatures.

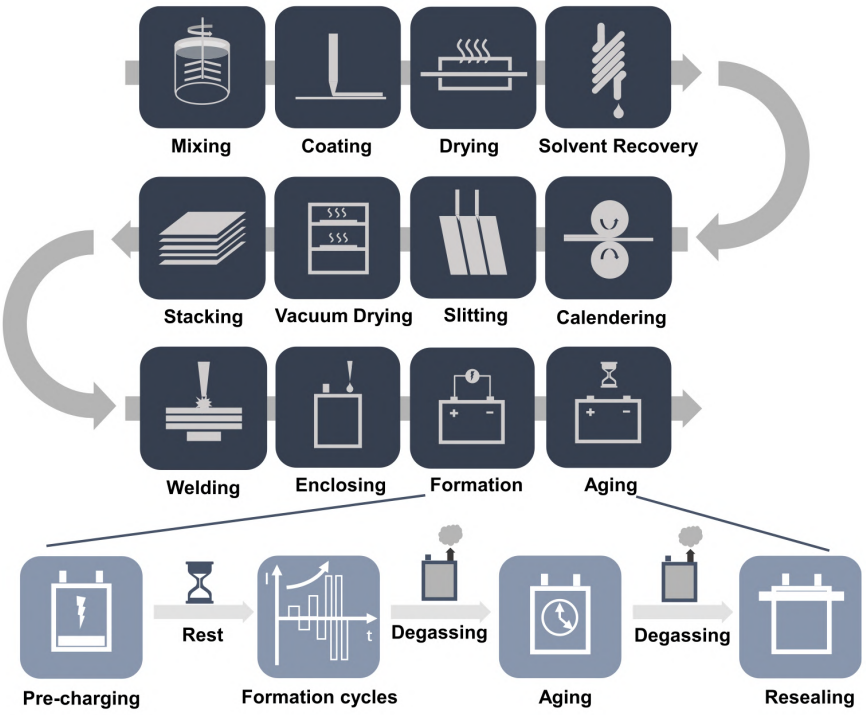

Figure 2.7: Schematic representation of lithium ion battery fabrication process [213].

2.6 Recyling of lithium-ion batteries

The widespread dependence on the power and convenience offered by LIBs has made their production and disposal key areas of political and environmental concerns [217]. Limited resources and supply are critical considerations due to the limited lifespan of

devices, which may result from design obsolescence, upgrades to newer cellphone models, or frequently, the lithium ion battery approaching the end of its life cycle. According to prevalent assessments, the majority of discarded lithium-ion batteries are ultimately disposed of in landfills or accumulated, resulting in soil contamination and the wasting of energy and natural resources that are not renewable. By February 2019, the global electric car number exceeded 5.6 million, reflecting a 64 % rise from 2018. By 2040, it is projected that 58 % of all automobiles sold globally will be electric vehicles [218]. The rapid increase in electric vehicle quantities will result in substantial lithium-ion battery waste annually, which, if not recycled and used again, will have severe environmental consequences and exacerbate the depletion of mineral sources.

2.6.1 Methods of recycling

Owing to the intricate composition and diversity of elements in lithium-ion batteries they require a series of treatments before reuse or recycling. The cathode materials of LIBs are recycled through pyrometallurgy, hydrometallurgy, and direct methods, as seen in Figure 2.8. Direct recycling is a cost-effective method for lithium ion battery recycling

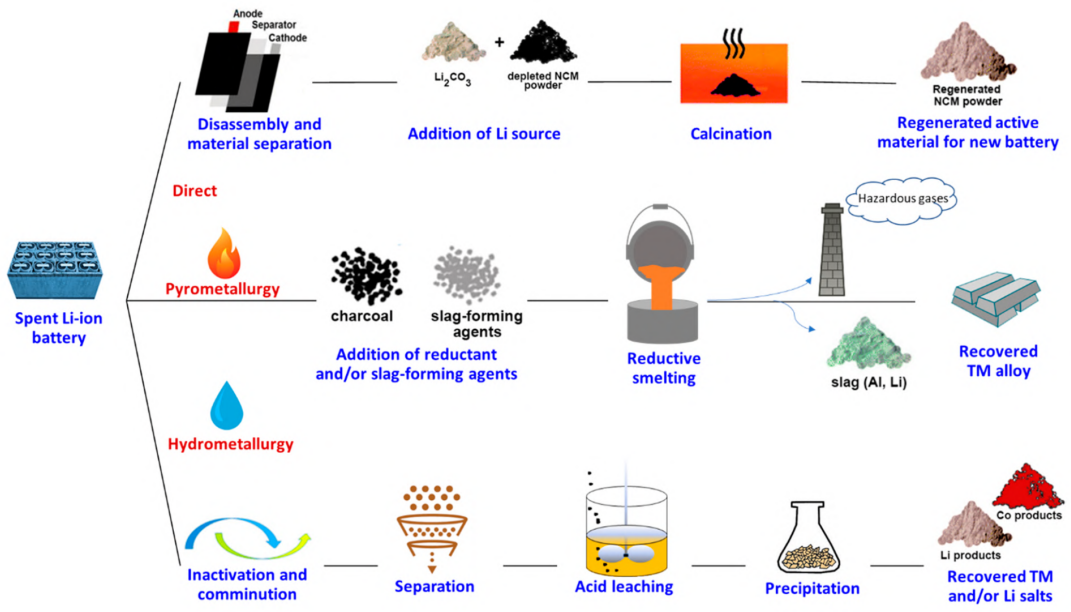

Figure 2.8: The methods for recycling and recovering active materials from lithium-ion batteries can be divided into three primary categories: direct, pyrometallurgical, and hydrometallurgical [218].

that has been investigated alongside other traditional techniques. Relithiation is utilized in direct lithium-ion battery recycling, facilitating the maximal preservation of component elements. The active materials remain unbroken and are not disassembled into their components. Because of this preservation, recyclers can avoid the expensive parts of the remanufacturing process, which uses metals that are recycled from cathode materials. Electrochemical, mechanical, and cathode-to-cathode techniques are all examples of direct recycling. The ability to reactivate the cathode material without breaking it down into its component elements or compounds is a commonality among these approaches [219]. Unlike direct recycling, which retrieves and refreshes electrode materials for laboratory-scale battery production, pyrometallurgical and hydrometallurgical recycling methods are

commercialized by extracting the precious metals and salts [220]. Despite pyrometallurgical recycling (also known as smelting) of lithium-ion batteries retrieves rich transition metals, lithium and aluminum remain in the slag, making their recovery difficult. All organic components, alongside aluminum, undergo oxidation to supply process heat and reduce transition metals. Lithium iron phosphate cathodes are incapable of generating any valuable products. A substantial capital expenditure is also necessary for an effective industrial-scale smelting operation. The primary advantage of smelting is its ability to treat batteries containing heterogeneous cathode compositions; but, before to reuse, the components must ultimately be separated through leaching. Since they operate at lower temperatures and require less initial investment, direct recycling and hydrometallurgical recycling might be more financially feasible on a more personal level. It is possible to quickly recover the copper and aluminum foils as pure metals even though separation is required. The primary goal of hydrometallurgy is to recover lithium and transition metals from the cathode; direct recycling helps to accomplish this goal by attempting to recover cathode materials in the proper form. This technique is especially attractive for LFP and LMO cathodes since it is the only one generated to restore their significant value [221].

2.7 Lithium-ion battery safety issues

Numerous cases of lithium ion battery fires and explosions in the past few years have led to property damage and harm to people [222]. Conversely, the rapid advancement of electronic products and the increasing prevalence of electric vehicles have elevated the safety of batteries to a global concern. Mechanical, electrical, and thermal abuse are the primary aspects that lead to battery fires and explosions. The issue of mechanical abuse is considerable among these underlying causes. When a lithium ion battery experiences mechanical abuse, the battery pack first undergoes mechanical deformation. The mechanical distortion of the separator or electrodes can lead to short circuits, elevated temperatures, gas generation, and increased pressure. The formation of an internal short circuit results in a rapid temperature rise, known as thermal runaway. Under extreme conditions, thermal runaway can lead to a fire due to the elevated temperatures [223]. In order to enhance battery safety, steps must be implemented to prevent detrimental internal processes. A wide range of studies has been conducted to enhance the thermal performance of cathodes. The two primary approaches employed are protective coating and element replacement. Element replacement can markedly improve the thermal performance of layered oxide materials by preserving the crystal structure. Cationic metals, such as cobalt, manganese, and magnesium, can partly substitute nickel or manganese to enhance thermal stability. Most applications that require significant power necessitate the efficient aggregation of many batteries inside a small space. Nevertheless, these batteries comprise reactive components, rendering the prevention of fire start and thermal runaway impossible. This fire can subsequently propagate and inflict significant damage on adjacent batteries. Researchers have proposed many strategies to mitigate the propagation of thermal runaway from a malfunctioning battery to adjacent cells. Five strategies for mitigating the propagation of thermal runaway were proposed, including minimizing the likelihood of a battery's steel casing bursting, ensuring sufficient spacing and effective heat dissipation among batteries, individually splicing parallel-connected batteries, protecting adjacent batteries from hot ejecta, and stopping flames and sparks from escaping the battery enclosures [224]. The most efficient approach to address the safety issues associated with lithium-ion batteries may involve the identification of safer materials. Alongside

materials, the notable rise of supplementary devices will yield critical insights into the advancement and safer utilization of next-generation lithium-ion batteries. Enhancements in battery safety will necessitate the adoption of novel technologies for batteries. Further comprehension of the thermal properties of lithium-ion batteries in cold regions and marine environments is still required. Information regarding the fire hazards associated with lithium-ion batteries, including ignition time, safety venting, air pressure, humidity, gas concentration, and similar factors, is rare [223, 224, 225].

2.8 Conclusion

Lithium-ion batteries (LIBs) have emerged as the cornerstone of modern energy storage systems, driven by their high energy density, longevity, and adaptability across diverse applications. This section underscores their pivotal role in enabling the transition from fossil fuels to renewable energy systems, powering portable electronics, electric vehicles (EVs), grid storage, and medical devices. The evolution of LIB technology has been marked by significant advancements in electrode materials, electrolytes, and fabrication processes. Carbon-based anodes, such as graphite and graphene, remain dominant due to their stability and cost-effectiveness, though challenges like limited capacity persist. Transition metal oxides (TMOs) and alloying materials (e.g., Si, Ge, Sn) offer higher theoretical capacities but face hurdles such as volume expansion and structural degradation. Innovations in nanostructuring, composite materials, and surface coatings have partially mitigated these issues, enhancing cyclability and conductivity. Cathode materials, including layered oxides ($LiCoO_2$, $LiNiO_2$), spinels ($LiMn_2O_4$), and polyanion compounds ($LiFePO_4$), have been optimized for energy density and safety. However, their reliance on scarce metals like cobalt and nickel raises economic and environmental concerns, necessitating research into low-cost, abundant alternatives. Electrolyte development has shifted toward solid-state systems to address flammability risks, though trade-offs in ionic conductivity and interfacial stability remain unresolved. Hybrid and gel polymer electrolytes present promising compromises, balancing safety and performance. The applications of LIBs highlight their transformative impact, particularly in EVs and renewable energy integration, where their ability to buffer intermittent power generation is critical. However, aging mechanisms—loss of lithium inventory (LLI), active material degradation (LAM), and conductivity loss (CL)—pose persistent challenges, necessitating advanced state-of-health (SOH) monitoring and predictive models for remaining useful life (RUL). Fabrication processes, while mature, face environmental scrutiny due to toxic solvents like NMP, emphasizing the need for greener manufacturing and efficient recycling. Current recycling methods (pyrometallurgy, hydrometallurgy, direct recycling) struggle with cost and material recovery efficiency, underscoring the urgency of closed-loop systems to reclaim critical metals and reduce ecological footprints. Safety remains a paramount concern, with thermal runaway triggered by mechanical, electrical, or thermal abuse posing significant risks. Mitigation strategies, including advanced thermal management, material coatings, and structural safeguards, are essential to prevent catastrophic failures. Future advancements hinge on interdisciplinary innovation: solid-state electrolytes, silicon-anode commercialization, AI-driven material discovery, and sustainable recycling protocols. Addressing these challenges will require concerted efforts from academia, industry, and policymakers to ensure LIBs meet the escalating demands of a decarbonized global economy while minimizing environmental harm. In summary, LIBs have revolutionized energy storage; their

future evolution must prioritize sustainability, safety, and scalability to cement their role in a cleaner, electrified world.

Chapter 3

A comparative review of models for all-solid-state lithium-ion batteries

This chapter is adapted from the publication [226].

3.1 Introduction

Numerous instances demonstrate that traditional lithium-ion batteries, which rely on liquid organic electrolytes and porous electrodes, are susceptible to chemo-mechanical degradation. They also face environmental and safety concerns, due to the flammability of the toxic liquid electrolytes. Hazardous leaks do not occur in all-solid-state batteries (ASSBs) [227, 228], since they exploit solid electrolytes, broadly categorized in polymer, inorganic, and organic-inorganic composite [229]. In this note we will restrict our focus on thin films ASSB, equipped either with Lithium phosphorous oxy-nitride "LiPON" or with Lithium lanthanum zirconium oxide "LLZO" ($Li_7La_3Zr_2O_{12}$) electrolytes.

Largely funded international projects [230] and strategic action plans (as for the European battery 2030+ initiative) assess how the scientific community trusts and supports the development of storage systems to meet the social quest for decarbonization. ASSBs are among the best next-generation candidates, provided that they achieve ultra-high-performance while meeting sustainability and safety. Among the shortcomings of solid electrolytes cells, the technical ones that currently limit the industrialization of ASSBs appear to be (i) achieving a substantial ionic conductivity at ambient temperature; (ii) reducing the resistance at the interface between the active material and electrolyte [231, 232]; (iii) eliminating the mechanical damage [233, 234] and the dendritic growth from anodic lithium foils [235, 236, 237]. Experimental investigations are presently mainly focused on key materials and structures [238, 239, 240], such as composite electrolyte/electrode morphologies [241] or thin film glass layers [242].

Computational modeling and simulations, which operate at different scales and complement experimental research, allow a profound understanding of the interconnected physics that rule the response of ASSBs. Digital twins enable the comprehension of processes and the identification of limiting factors. Several advanced mathematical models have been documented in the literature. Unlike previous studies [227, 228, 243, 244], a broad screening of the existing literature is not the goal of this review. It does not consist in a brief and cursory summary of various pieces of work in the literature, because it would fail to give the reader a physical and quantitative insight into the functioning principles of ASSBs. Although we realize that it is always hard, if not even impossible, to categorize

the whole bibliography on a subject and undoubtedly identify those cornerstone papers that changed the flow of the subject itself, in this review we detail and compare four different approaches [245, 246, 247, 248] because of their significant ideas. A pictorial view of the mathematical framework that characterize each of those approaches is portrayed in Fig. 3.1.

Fabre et al. [245] developed a one-dimensional model of a Li/LiPON thin-film micro battery, described in section 3.2.1. The ionic transfer is modeled via a single-ion conduction within the solid electrolyte. This results in a uniform distribution of lithium ions (Li^+) throughout the solid electrolyte, with concentrations determined by the initial conditions and established by the overall electroneutrality in the electrolyte (electroneutrality is extensively discussed in [249] (see also [250])). In single-ion conduction, the negative vacant positions in the lattice are tightly bound and do not flow. Since ionic mobility isn't governed by a concentration gradient, the model's main goal is to identify the potential drop, which is primarily determined by Ohm's law.

An advanced model framework for ASSBs was further proposed by Landstorfer and coworkers in [246] and will be analyzed in section 3.2.2. While using a single-ion conduction ionic transport model as in [245], the authors enriched the formulation of the interface mechanisms. Standing from a rigorous thermodynamic setting, the interface conditions ultimately lead to non-Butler-Volmer type equations. Capacitance within interfaces was captured also in the third paper accounted for in this review, authored by Raijmakers and co-workers in [247]. Their key contribution lies in an innovative two-mechanisms conduction model, wherein both interstitial lithium and negative vacancies move autonomously. This results in establishing a concentration gradient at a steady state, resembling the distribution seen in liquid electrolytes [251, 252].

The double mechanism in ionic transport has been further developed in the last contribution discussed here, authored by Cabras et al. [248]. Since the unbalanced negative charges associated with a vacancy in the LiPON lattice cannot flow, the model proposed in [247] appears to be unphysical. Rather, Cabras et al. [248] assume that some positive ions hop to occupy neighboring empty vacancies, while the rest of the Li+ ions transition into a meta-stable interstitial phase of the same kind as described in [247]. The complex explanation of interfaces has also been incorporated from [247].

This review is organized as follows. A brief theoretical summary of models and their governing equations for ASSBs is proposed in section 3.2. An experimental benchmark, taken from [253], is devised in section 3.3. The finite element solution scheme provides numerical approximations for the electric potential profiles, interface currents, fluxes, and concentration profiles. These quantities of interest were used to compare the more recent model in [248] against the antecedent published in [247]. In the section 3.4, the article provides an overview of the objectives pursued. It also outlines the future plans that are intended to be implemented. Final remarks that summarize the key points discussed conclude the paper.

3.2 Models and their governing equations.

Several mathematical formulations, some of which examined in [243, 244], concern the battery microstructure, which simplistically can be categorized into two types, i.e., thin films and porous electrodes. Electrodes made of porous materials have been scrutinized by a broad set of models, including pseudo-2-D [254, 255], multiscale [256, 257] and fine-

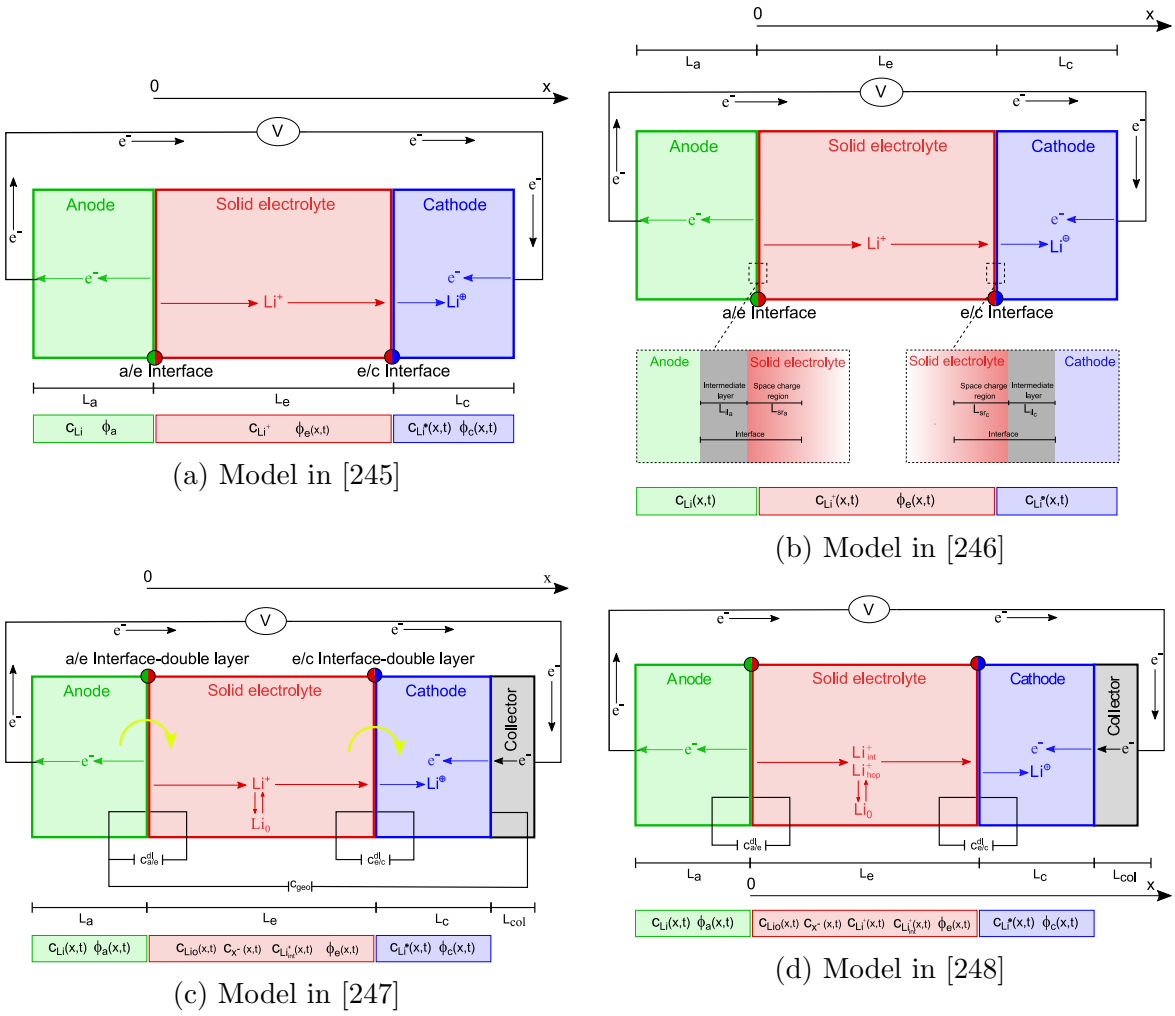

(a) Model in [245]

(b) Model in [246]

(c) Model in [247]

(d) Model in [248]

Figure 3.1: *Schematics of the ASSBs models proposed in the selected literature. The unknown fields, under discharge conditions, are highlighted. The yellow arrows in (c) point out the charge-transfer reactions at both interfaces. For the sake of generality, the lithium concentration in the anode is listed in the unknown fields.*

grained [258], accounting for the different phases and attempting at capturing realism either in liquid [259] or solid electrolytes [241].

In thin film batteries, a planar geometry is commonly employed. This is because the ratio between the lateral dimension and the thickness is sufficiently large to treat the lateral dimension as infinite, as illustrated in Figure 3.1. Additionally, electrodes and electrolytes can be adequately represented as homogeneous planar materials. As a result, one-dimensional mathematical models are typically used to describe thin-film batteries.

An all-solid-state electrochemical cell incorporates two electrodes and a solid electrolyte, as depicted schematically in Figure3.1. Lithium-ions are extracted from the cathode (positive electrode) during charge and inserted back during discharge. The opposite holds for the anode (negative electrode). Assuming $LiCoO_2$ to be the cathode material, the fundamental electrochemical charge-transfer reaction is written as

$$\mathrm{LiCoO_2} \underset{k_{-1}}{\overset{k_1}{\rightleftarrows}} \mathrm{Li_{1-x}CoO_2} + x\mathrm{Li^+} + x\mathrm{e^-} \quad 0 \leq x \leq \frac{1}{2}\,. \tag{3.1}$$

Since the anode is a lithium foil, the deposition and extraction processes at the negative

surface are described by the following reaction:

$$\mathrm{Li} \underset{k_{-2}}{\overset{k_2}{\rightleftarrows}} \mathrm{Li}^+ + \mathrm{e}^- \,. \tag{3.2}$$

Figure 3.2 depicts the structure of the solid electrolyte: LiO is the lithium bound to the non-bridging oxygen atoms, Li^+ ions have motion capabilities (either transferred to the meta-stable interstitial state or hopping). The uncompensated negative charges n^- are associated with vacancies formed in the LiPON matrix. The saturation concentration c_0 of host sites is determined by the stoichiometric composition of the electrolyte material. This concentration is attained in the ideal scenario of zero absolute temperature, as vanishing conductivity results from immobile ions. On the contrary, under standard conditions, some of the Li ions are thermally excited, and the chemical ionization reaction

$$\mathrm{LiO} \underset{k_b^{\mathrm{ion}}}{\overset{k_f^{\mathrm{ion}}}{\rightleftarrows}} \mathrm{Li}^+ + \mathrm{n}^- \tag{3.3}$$

occurs, k_f^{ion} and k_b^{ion} being the forward and backward rate constants for the ionization and recombination reaction, respectively.

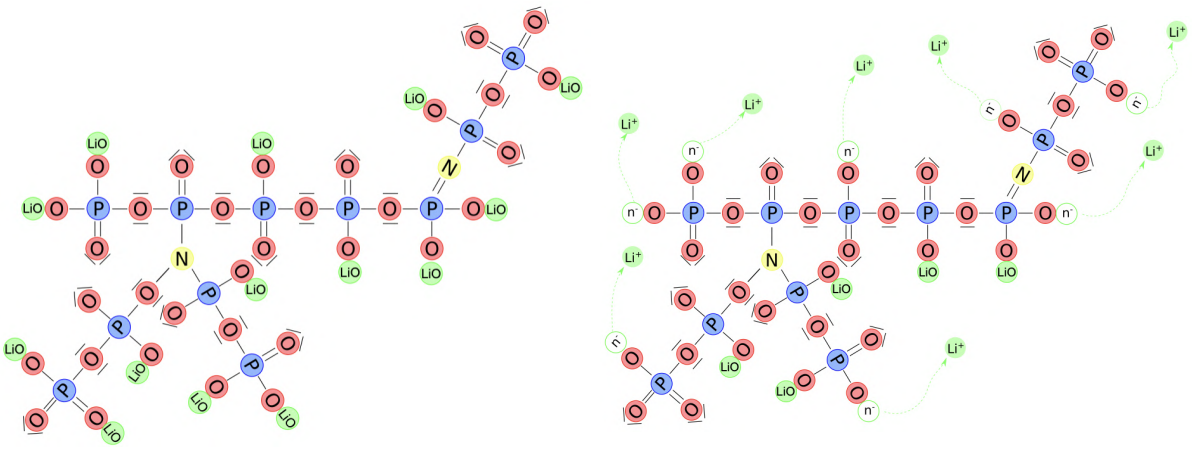

(a) (b)

Figure 3.2: *LiPON matrix contains nitrogen, which has triple and double coordination (a). Ionic conductivity in LiPON is achieved through the displacement of charged particles, either by hopping and vacancies filling or by interstitial motion (b).*

A quantitative determination of the kinetics of mobile ionic species allows prediction of the response of electrochemical cells. A $\mathrm{LiCoO_2}$ electrode contains lithium oxide, and the lithium is an ion as part of a lithium salt. Li is intercalated in the cathode as an ion "shielded" by its own electron. It will be denoted with $\mathrm{Li}^{\oplus}$ to stress its ionic nature, while distinguishing it from mobile charges Li^+ in the electrolyte.

In the following, we give an overview of four electrochemical models proposed in the literature, showcasing numerical results covering electric potential profiles, interfacial currents, fluxes, and concentration profiles. In terms of notation, T stands for the absolute temperature, F for Faraday's constant, $\mathbb{D}_\alpha$ for the diffusivity of species α; symbol $\mathbb{1}$ denotes the identity matrix.

3.2.1 One-dimensional single-ion conduction models [245]

A one-dimensional model of a Li/LiPON thin-film micro battery was developed by Fabre et al. [245] and is depicted schematically in Figure 3.1a. The x-axis, which points out the characteristic lengths of the model is directed from the negative towards the positive electrode; the interface between the negative electrode and the solid electrolyte hosts its origin.

The authors aimed at keeping their model as simple as possible, by introducing proper assumptions in order to come up with a reduced set of input parameters that can be measured from purposely designed experiments. The model is isothermal with no self-heating, neglects volume alterations during charge/discharge, and assumes that redox activities occur solely on the surface area, which remains unchanged throughout cycling. The negative electrode is a metallic film of lithium with negligible Ohmic losses. The ionic transfer in the solid electrolyte is described by a single ion conduction model; as such, the concentration of lithium ions across the solid electrolyte Li^+ is uniform. This property straightforwardly comes out as long as electro-neutrality approximation holds, a property of the governing equations largely discussed in [249, 251, 252].

Accordingly, the model traces lithium $Li^{\oplus}$ diffusion and electron e^- migration in the positive electrode, single Li^+ ions' migration in the solid electrolyte, and charge-transfer kinetics at the electrode/electrolyte interfaces. Three unknown fields are required, the concentration of lithium in the positive electrode $c_{Li^{\oplus}}(x,t)$, the electric potentials $\phi_e(x,t)$ and $\phi_c(x,t)$ in the solid electrolyte and in cathode, respectively.

The electric potentials in the positive electrode ϕ_c and in the solid electrolyte ϕ_e are related to the current densities $\vec{i}_c(x,t)$ and $\vec{i}_e(x,t)$ by means of Ohm's law, through the electrical k_c and ionic k_e conductivities, respectively:

$$\vec{i}_e(x,t) = -k_e \nabla \phi_e(x,t) \qquad 0 \leq x \leq L_e \;, \tag{3.4a}$$

$$\vec{i}_c(x,t) = -k_c \nabla \phi_c(x,t) \qquad L_e \leq x \leq L_e + L_c \;. \tag{3.4b}$$

The third governing equation in the positive electrode is a planar solid-state diffusion equation, which describes the (neutral, in the sense detailed beforehand of shielded positive ion) transport of lithium $Li^{\oplus}$ in the electrode:

$$\frac{\partial c_{Li^{\oplus}}(x,t)}{\partial t} = \nabla \cdot \left[\mathbb{D}_{Li^{\oplus}} \nabla c_{Li^{\oplus}}(x,t) \right] \qquad L_e \leq x \leq L_e + L_c \;, \tag{3.4c}$$

with diffusion coefficient $\mathbb{D}_{Li^{\oplus}}$. A concentration-dependent ionic diffusion coefficient was studied in [245], which resulted in more accurate outcomes.

Denoting with $\vec{n}$ the outward normal to the surface at boundary, the two *boundary conditions* required for Equation (3.4c) are the lithium flux density at the reaction surface and the zero-flux condition for lithium $Li^{\oplus}$ at the electrode/collector interface:

$$\mathbb{D}_{Li^{\oplus}} \nabla c_{Li^{\oplus}}(x,t) \cdot \vec{n} = \frac{-i_{e/c}(t)}{F} \qquad x = L_e \;, \tag{3.5a}$$

$$\mathbb{D}_{Li^{\oplus}} \nabla c_{Li^{\oplus}}(x,t) \cdot \vec{n} = 0 \qquad x = L_e + L_c \;. \tag{3.5b}$$

The conditions for ϕ_e and ϕ_c, either at the anode-electrolyte (a/e) or at the electrolyte-cathode (e/c) interfaces

$$\vec{i}_e(0,t) \cdot \vec{n} = -i_{a/e}(t) \;, \qquad \vec{i}_e(L_e,t) \cdot \vec{n} = -i_{e/c}(t) \;, \qquad \vec{i}_c(L_c,t) \cdot \vec{n} = i_{e/c}(t) \tag{3.6}$$

are modeled via Butler-Volmer equations in Fabre et al. [245], in the form

$$i_s(t) = i_s^0(t) \left(e^{\frac{\alpha F}{RT}\eta(t)} - e^{-\frac{(1-\alpha)F}{RT}\eta(t)} \right) \tag{3.7}$$

with s either a/e or e/c and α the so-called anodic (cathodic) charge transfer coefficient, usually both taken to be equal to 0.5. The overpotential

$$\eta(t) = [\![\phi]\!] - OCP \tag{3.8}$$

is the difference between $[\![\phi]\!] = \phi_{electrode} - \phi_{electrolyte}$, i.e. the electric potential jump at the electrolyte/electrode interface, and the open circuit potential (OCP). The latter can either be measured experimentally or calculated theoretically as in [260]. The exchange current $i_{a/e}^0$ is given by:

$$i_{a/e}^0(t) = F\, k_2\, k_{-2} \left(c_{\mathrm{Li^+}}^{sat} - c_{\mathrm{Li^+}}(0,t) \right)^{\alpha} c_{\mathrm{Li^+}}(0,t)^{1-\alpha}, \tag{3.9}$$

where k_2 and k_{-2} are the forward and backward reaction rate constants for the reaction (3.2), $c_{\mathrm{Li^+}}^{sat}$ is the saturation concentration of lithium in the electrolyte. The exchange current $i_{e/c}^0$ is given by:

$$i_{e/c}^0(t) = F\, k_1\, k_{-1} \left(c_{\mathrm{Li^+}}^{sat} - c_{\mathrm{Li^+}}(0,t) \right)^{\alpha} c_{\mathrm{Li^+}}(0,t)^{1-\alpha} \left(c_{\mathrm{Li^\oplus}}^{sat} - c_{\mathrm{Li^\oplus}}(0,t) \right)^{\alpha} c_{\mathrm{Li^\oplus}}(0,t)^{1-\alpha}, \tag{3.10}$$

where k_1 and k_{-1} are the forward and backward reaction rate constants for the reaction (3.1) and $c_{\mathrm{Li^\oplus}}^{sat}$ represents the saturation lithium concentration within the cathode. Replacing $c_{\mathrm{Li^+}}(0,t)$ with the initial, uniform concentration of lithium in the electrolyte, the exchange current densities $i_{a/e}^0(t)$ and $i_{e/c}^0(t)$ simplify as

$$i_{a/e}^0(t) = F\, k_-^{app}\,, \qquad i_{e/c}^0(t) = F\, k_+^{app} \left(c_{\mathrm{Li^\oplus}}^{sat} - c_{\mathrm{Li^\oplus}}(0,t) \right)^{\alpha} c_{\mathrm{Li^\oplus}}(0,t)^{1-\alpha}. \tag{3.11}$$

where k_-^{app} and k_+^{app} are apparent rate constant for negative electrode and defined as the multiplication of the terms in Equations (3.9) and (3.10).

Galvanostatic boundary conditions are eventually imposed,

$$\vec{i_c}(L_e + L_c, t) \cdot \vec{n} = i_{bat}(t), \tag{3.12}$$

where i_{bat} is the given galvanostatic current flowing across the 1D battery. The potential is set arbitrarily to $\phi_e(0,t) = 0$.

3.2.2 An advanced framework for solid electrolyte intercalation batteries [246]

Landstorfer and coworkers studied in [246] a non-porous electrode and a crystalline solid electrolyte. As in [245], they assumed a solid electrolyte with one mobile species (Li^+) and a uniform concentration of vacancies $c_{\mathrm{n^-}}$ that remains unaltered in time. The model entails a novel view of the electrode/solid electrolyte interface, which consisted of an intermediate layer and a space charge region within the electrolyte. A visual representation of the model is given in Figure 3.1b.

Once ions randomly intercalated in the lattice structure of graphite or $LiCoO_2$, a simple Fickian law diffusion analogous to Equation (3.4c) accounts for ionic transport. The electric potential ϕ_c is considered to be uniform within the electrodes, neglecting the

ohmic loss (depicted in [245] via Equation (3.4b)), while ϕ_e influences the ionic transport in the electrolyte, ruled by non-equilibrium thermodynamics. The mass balance law relates the concentration of lithium $c_{\mathrm{Li^+}}(x,t)$ to the actual flux of cations $\vec{h}_{\mathrm{Li^+}}(x,t)$

$$\frac{\partial c_{\mathrm{Li^+}}(x,t)}{\partial t} = -\nabla \cdot \left[\vec{h}_{\mathrm{Li^+}}(x,t)\right] \qquad 0 \le x \le L_e \ . \tag{3.13}$$

Using the standard linear relationship of Onsager type (Here

$$\boldsymbol{M}(x,t) = \frac{\mathbb{D}_{\mathrm{Li^+}}}{RT} c_{\mathrm{Li^+}}(x,t)\ \mathbb{1} \tag{3.14}$$

is the expression taken in [246] for the mobility tensor. Note that Equation (3.14) differs a little from the choice made in [261, 262]. This remark also gives a justification for the different outcomes on the final form of the mass balance equation.)

$$\vec{h}_{\mathrm{Li^+}}(x,t) = -\boldsymbol{M}(x,t)\,\nabla\overline{\mu}_{\mathrm{Li^+}}(x,t) \qquad 0 \le x \le L_e \ , \tag{3.15}$$

between the flux $\vec{h}_{\mathrm{Li^+}}$ and the gradient of the electrochemical potential $\overline{\mu}_{\mathrm{Li^+}}$, the Clausis-Duhem inequality is satisfied a priori and thermodynamic consistency is granted, as largely discussed in [251, 252]. The chemical potential is the functional derivative of the Gibbs free energy (or Helmholtz free energy according to [251, 252]) with respect to the ionic concentration $c_{\mathrm{Li^+}}(x,t)$. The splitting of chemical and electrical potentials used in [246] is classical, as it is the free energy of mobile guest atoms interacting with a host medium, described by a regular solution model [263, 264]. The electrochemical potential is eventually derived as the sum of the chemical and electrostatic potential as follows,

$$\overline{\mu}_{\mathrm{Li^+}}(x,t) = \mu_{\mathrm{Li^+}}(x,t) + F\phi_e(x,t) \qquad 0 \le x \le L_e\,, \tag{3.16a}$$

$$\mu_{\mathrm{Li^+}}(x,t) = \mu^0_{\mathrm{Li^+}} + RT\ \ln\frac{\theta_{\mathrm{Li^+}}(x,t)}{1-\theta_{\mathrm{Li^+}}(x,t)} + RT\ \chi[\,1-2\theta_{\mathrm{Li^+}}(x,t)\,] \qquad 0 \le x \le L_e\,, \tag{3.16b}$$

with $\theta_{\mathrm{Li^+}} = c_{\mathrm{Li^+}}/c^{sat}_{\mathrm{Li^+}}$. The chemical potential in (3.16b) collects the entropy of mixing and the energetic interactions. The term $\mu^0_{\mathrm{Li^+}}$ is the reference value of the chemical potential in the absence of interaction and entropic contributions. The energy of interaction between insertion sites and mobile guest species is characterized via the real valued constant χ (see Equation (3.16b)), also called the exchange parameter [265]. $\chi = 0$ means that mixing is purely entropic. The contribution $RT\ \chi[\,1-2\theta_{\mathrm{Li^+}}(x,t)\,]$, emanating from the excess Gibbs energy [261, 262], may lead to phase segregation [266, 267, 268]. The mass flux to be inserted into the mass balance law (3.13) eventually holds:

$$\vec{h}_{\mathrm{Li^+}}(x,t) = \left(2\chi\,\theta_{\mathrm{Li^+}} - \frac{1}{1-\theta_{\mathrm{Li^+}}}\right)\ \mathbb{D}_{\mathrm{Li^+}}\ \nabla c_{\mathrm{Li^+}} - \frac{\mathbb{D}_{\mathrm{Li^+}}\,F}{RT}\ c_{\mathrm{Li^+}}\ \nabla\phi_e \qquad 0 \le x \le L_e\,. \tag{3.17}$$

The classical Nernst-Planck flux (z_α is the valency of ion α, equal to +1 for $\mathrm{Li^+}$ cations)

$$\vec{h}_\alpha(x,t) = -\mathbb{D}_\alpha \nabla c_\alpha(x,t) - \frac{z_\alpha F}{RT}\mathbb{D}_\alpha c_\alpha(x,t)\nabla\phi_e(x,t)\ , \tag{3.18}$$

is attained in the dilute limit assumed $1-\theta_{\mathrm{Li^+}} \sim 1$ when the energy of interaction vanishes $\chi = 0$.

The whole electrolyte is thought as consist of a space charge region and a bulk region, as shown in Figure 3.1b. In the bulk region electroneutrality is imposed a priori, $c_{\mathrm{Li^+}}$

is defined by the (given and uniform) concentration of vacancies, and Ohm's law (3.4a) allows recovery of the electric potential. On the contrary, in proximity of the interfaces, where the concentrations of cations and anions differ, the electric potential is obtained by Gauss's law, which provides, after constitutive prescriptions, the following Poisson equations:

$$-\nabla^2\phi_e(x,t) = \frac{F}{\varepsilon_r\varepsilon_0}(c_{\mathrm{Li}^+}(x,t) - c_{\mathrm{Li}}) \qquad 0 \le x \le L_{sr_a}\ , \tag{3.19a}$$

$$-\nabla^2\phi_e(x,t) = \frac{F}{\varepsilon_r\varepsilon_0}(c_{\mathrm{Li}^+}(x,t) - c_{\mathrm{Li}^\oplus}) \qquad L_e - L_{sr_c} \le x \le L_e\ , \tag{3.19b}$$

where ε_r denotes the relative permittivity of the electrolyte and ε_0 the vacuum permittivity. Local electroneutrality is not enforced in the space charge region [246], rather a weak (i.e. global) electroneutrality is prescribed in the whole electrolyte

$$F\int_V (c_{\mathrm{Li}^+}(x,t) - c_{\mathrm{n}^-})\,dV = 0\ , \qquad F\int_V (c_{\mathrm{Li}^+}(x,t) - c_{\mathrm{n}^-})\,dV = 0\ , \tag{3.20}$$

thus allowing local deviations between cation and anion concentrations while keeping the overall number of cations and anions equal.

The interface between the electrodes and the solid electrolyte was modelled as two intermediate layers, treated as plate capacitors in terms of potential jumps and flux continuity. The authors borrowed from [269] the constitutive equation for potential jumps (defined as the potential at an electrode minus the one at the electrolyte) as

$$[\![\,\phi\,]\!]_{anode} = \frac{\varepsilon_a}{C_a}\,\nabla\phi_e(0,t)\cdot\vec{n}\ , \qquad [\![\,\phi\,]\!]_{cathode} = \frac{\varepsilon_c}{C_c}\,\nabla\phi_e(L_e,t)\cdot\vec{n}\ , \tag{3.21}$$

with given surface capacitances C_a, C_c and permittivities ε_a, ε_c.

The boundary conditions on fluxes at electrode - solid electrolyte interfaces resemble Butler-Volmer equations (3.7) in a form originally presented in [270] and named generalized Frumkin-Butler-Volmer equations. They read:

$$\vec{h}_{\mathrm{Li}^+}(0,t)\cdot\vec{n} = -\tilde{k}_2\, e^{\frac{\triangle G_1 - \beta F(\phi_a - \phi_e(0,t))}{RT}} c_{\mathrm{Li}}(0,t) + \tilde{k}_{-2}\, e^{\frac{\triangle G_{-1} - (1-\beta)F(\phi_a - \phi_e(0,t)}{RT}} c_{\mathrm{Li}^+}(0,t)\ , \tag{3.22a}$$

$$\vec{h}_{\mathrm{Li}^+}(L_e,t)\cdot\vec{n} = -\tilde{k}_1\, e^{\frac{\triangle G_2 - \beta F(\phi_c - \phi_e(L_e,t))}{RT}} c_{\mathrm{Li}^\oplus}(L_e,t) + \tilde{k}_{-1}\, e^{\frac{\triangle G_{-2} - (1-\beta)F(\phi_c - \phi_e(L_e,t)}{RT}} c_{\mathrm{Li}^+}(L_e,t), \tag{3.22b}$$

where the reaction rate constants defined in reactions (3.1) and (3.2) are taken to be of Arrhenius type, i.e., $k_n = \tilde{k}_n\, e^{E_n/RT}$, $n = 1, 2$. The Gibbs energies of activation $\triangle G_n$ are further parameters of the model and relate to the OCP in Butler-Volmer equations.

3.2.3 An advanced all-solid-state lithium-ion battery model [247]

More complex one-dimensional mathematical models were proposed in a series of publications from Notten's group [253, 271, 272] for a micro-battery $Li/LiPON/LiCoO_2$. In these studies, ionic transport in the solid electrolyte involved the ionization reaction (3.3) of immobile, oxygen-bound lithium LiO to mobile Li^+ ions and negatively charged vacancies. The transport of Li^+ ions in the electrolyte and of $Li^\oplus$ in the positive electrode were accounted for, as well as charge-transfer kinetics at both electrode/electrolyte

interfaces. In their recent work, [247], additional features were introduced, such as: (i) a mixed ionic/electronic conductivity in the positive electrode; (ii) electrical double layers occurring at both electrode/electrolyte interfaces; and (iii) variable ionic and electronic diffusion coefficients that depend on the lithium concentration inside the positive electrode.

Figure 3.1c displays a discharge process. The anode consists of a lithium Li foil, the cathode of a $LiCoO_2$ film, while LiPON is used as the electrolyte material. The current collector is tied from the top of the $LiCoO_2$. As for [245] and [246], also this model is also isothermal (no self-heating). Redox processes exclusively take place at the interfaces between the electrolyte and the electrode layers. Volume expansion or shrinking in the electrolyte are disregarded, and it is assumed that the active surface area remains constant throughout cycling.

As a distinctive feature of this class of models, the ionic transfer in the solid electrolyte is not described by a single ion conduction model and the concentration of lithium ions through the solid electrolyte is generally not uniform even though electro-neutrality approximation holds. Defining with δ the fraction of Li at equilibrium, concentrations are denoted as follows: $c_{\mathrm{Li^+}}$ refers to mobile $\mathrm{Li^+}$ ions; c_{LiO} to immobile lithium; $c_{\mathrm{n^-}}$ to uncompensated negative charges; $c^{eq}_{\mathrm{Li^+}} = c^{eq}_{\mathrm{n^-}} = \delta c_0$ is the equilibrium concentration of the charge carriers; $c^{eq}_{\mathrm{LiO}} = (1-\delta)c_0$ refers to the remaining immobile lithium. The overall rate of the charge carrier generation according to reaction (3.3) is

$$w^{(3.3)} = k^{\mathrm{ion}}_f \, c_{\mathrm{LiO}} - k^{\mathrm{ion}}_b \, c_{\mathrm{Li^+}} \, c_{\mathrm{n^-}} \ . \tag{3.23}$$

The ratio

$$K^{\mathrm{ion}}_{\mathrm{eq}} = k^{\mathrm{ion}}_f / k^{\mathrm{ion}}_b \tag{3.24}$$

is the equilibrium constant of reaction (3.3) and is related to the fraction of Li at equilibrium δ, see [247]. In addition to earlier models, two electrical double-layer capacitances $C^{dl}_{a/e}$ and $C^{dl}_{e/c}$ and a geometric capacitance C_{geo} were introduced in [247]. As in [246], double-layer capacitances attempt to capture the response of the space charge's very narrow layers as for electric capacitors. Whereas the concept resembles [246], the implementation is different. Capacitors in [246] are described "in series", whereas in [247] "in parallel" (compare Figures 3.1b and 3.1c). In view of this assumption, the current at electrode/electrolyte interfaces splits into two terms, the faradaic contribution that drives the reduction/oxidation charge-transfer reactions (3.1)-(3.2) (i^{ct}_s) and the non-faradaic contribution that feeds the double layer (i^{dl}_s), with s either a/e or e/c.

During charging, the $\mathrm{Li^+}$ ions released from the positive surface must cross the solid electrolyte and are reduced into metallic Li at anode. Electrons, generated by the charge-transfer reactions (3.1) and (3.2), flow across the Li foils and the electronic collector, with potential drops that follow Ohm's law, similar to Equation (3.4a). The transport of ionic concentrations (this description of transport of vacancies, in a form analogous to liquid electrolytes, appears to be questionable and is replaced by a different formulation in the novel approach to be presented in Section 3.2.4) $c_{\mathrm{Li^+}}$ and $c_{\mathrm{n^-}}$ in the solid electrolyte is ruled by the mass continuity Equation (3.13), properly extended as

$$\frac{\partial c_{\mathrm{Li^+}}(x,t)}{\partial t} = -\nabla \cdot \left[\vec{h}_{\mathrm{Li^+}}(x,t)\right] + w^{(3.3)}(x,t) \qquad 0 \le x \le L_e \ , \tag{3.25a}$$

$$\frac{\partial c_{\mathrm{n^-}}(x,t)}{\partial t} = -\nabla \cdot \left[\vec{h}_{\mathrm{n^-}}(x,t)\right] + w^{(3.3)}(x,t) \qquad 0 \le x \le L_e \ , \tag{3.25b}$$

in order to account for the reaction rate $w^{(3.3)}$ (see Equation (3.23)). The generic mass flux $\vec{h}_\alpha$, with $\alpha = \mathrm{Li}^+, \mathrm{n}^-$, is constitutively described by the Nernst-Planck law (3.18), which carries the electric potential as a further unknown field. Coupling with an additional relation is thus mandatory to model the migration process. The most common selection for such an additional relation in battery modeling is the electroneutrality condition

$$c_{\mathrm{Li}^+}(x,t) = c_{\mathrm{n}^-}(x,t)\ . \tag{3.26}$$

By substituting Equation (3.18) into Equations (3.25) and subtracting Equation (3.25a) from Equation (3.25b), two independent partial differential equations eventually arise:

$$\frac{\partial c_{\mathrm{Li}^+}(x,t)}{\partial t} = \nabla\cdot\left[\mathbb{D}_{\mathrm{Li}^+}\,\nabla c_{\mathrm{Li}^+}(x,t) + \frac{F\mathbb{D}_{\mathrm{Li}^+}}{RT}c_{\mathrm{Li}^+}(x,t)\nabla\phi_e(x,t)\right] + w^{(3.3)}(x,t) \tag{3.27a}$$

$$\nabla\cdot[(\mathbb{D}_{\mathrm{n}^-} - \mathbb{D}_{\mathrm{Li}^+})\nabla c_{\mathrm{Li}^+}(x,t)] - \nabla\cdot\left[(\mathbb{D}_{\mathrm{n}^-} + \mathbb{D}_{\mathrm{Li}^+})\frac{F}{RT}c_{\mathrm{Li}^+}(x,t)\nabla\phi_e(x,t)\right] = 0. \tag{3.27b}$$

To be solved they require the initial concentrations for c_{Li^+}

$$c_{\mathrm{Li}^+}(x,0) = c^{eq}_{\mathrm{Li}^+} = \delta c_0 \tag{3.28}$$

and the Neumann conditions on fluxes at the left and right boundaries of the electrolyte

$$\vec{h}_{\mathrm{Li}^+}(0,t)\cdot\vec{n} = -\frac{i^{ct}_{a/e}(t) + i^{dl}_{a/e}(t)}{F}, \qquad \vec{h}_{\mathrm{Li}^+}(L_e,t)\cdot\vec{n} = -\frac{i^{ct}_{e/c}(t) + i^{dl}_{e/c}(t)}{F}\ . \tag{3.29}$$

In the positive electrode a mixed ionic/electronic conductivity is considered. The mass balance equations that characterize the transport of $\mathrm{Li}^\oplus$ ions and electrons e^- are similar to Equations (3.25) for the solid electrolyte and is written as

$$\frac{\partial c_{\mathrm{Li}^\oplus}(x,t)}{\partial t} = -\nabla\cdot\left[\vec{h}_{\mathrm{Li}^\oplus}(x,t)\right] \qquad L_e \le x \le L_e + L_c\ , \tag{3.30a}$$

$$\frac{\partial c_{\mathrm{e}^-}(x,t)}{\partial t} = -\nabla\cdot\left[\vec{h}_{\mathrm{e}^-}(x,t)\right] \qquad L_e \le x \le L_e + L_c\ . \tag{3.30b}$$

The generic mass flux $\vec{h}_\alpha$, $\alpha = \{\mathrm{Li}^\oplus, \mathrm{e}^-\}$ is constitutively described by the Nernst-Planck law (3.18). This choice of independent motion of electrons and ionic intercalated lithium makes the governing equations different from Fabre's [245] ((3.4c) to be compared with (3.30a)).

Additionally, the model from [247] makes the positive electrode's diffusion coefficients dependent on the concentration of ions. Experimental results show that the local electrochemical environment has a major impact on solid-state diffusion. The model further exploits the electroneutrality approximation inside the cathode, implying $c_{\mathrm{Li}^\oplus}(x,t) = c_{\mathrm{e}^-}(x,t)$, and a space-time proportionality of the diffusion coefficients for $\mathrm{Li}^\oplus$ and e^-. Classical mathematical derivations allow one to retrieve Equation (3.4c) as the single PDE required to model the mass transport in the electrode, provided that the diffusivity $\mathbb{D}_{\mathrm{Li}^\oplus}$ is replaced by a suitable combination of electron and ionic diffusivities.

The initial concentration of the charge carrier at $t = 0$, when no concentration profile developed yet, is equal to its equilibrium concentration

$$c_{\mathrm{Li}^\oplus}(x,0) = c^{eq}_{\mathrm{Li}^\oplus}. \tag{3.31}$$

Neglecting the impact of geometric capacitance, the Neumann boundary conditions related to fluxes at both the left and right boundaries of the electrolyte result in:

$$\vec{h}_{\mathrm{Li}^{\oplus}}(L_e,t)\cdot\vec{n} = \frac{i^{ct}_{e/c}(t)+i^{dl}_{e/c}(t)}{F} \tag{3.32a}$$

$$\vec{h}_{\mathrm{Li}^{\oplus}}(L_e+L_c,t)\cdot\vec{n} = 0 \tag{3.32b}$$

$$\vec{h}_{\mathrm{e}^{-}}(L_e,t)\cdot\vec{n} = 0 \tag{3.32c}$$

$$\vec{h}_{\mathrm{e}^{-}}(L_e+L_c,t)\cdot\vec{n} = -\frac{i_{bat}(t)}{F} \tag{3.32d}$$

with $i_{bat}(t)$ the given galvanostatic current flowing across the 1D battery, defined in Equation (3.12).

Non-faradaic current $i^{dl}_{\alpha}(t)$ can be defined as

$$i^{dl}_{\alpha}(t) = C^{dl}_{\alpha}\,\frac{\partial[\![\,\phi\,]\!]}{\partial t}, \tag{3.33}$$

where $\alpha = a/e, e/c$. The jump $[\![\,\phi\,]\!]$ is defined as the electrode potential minus the electrolyte potential. Equation (3.33) shall be compared with (3.21) in [246].

The faradaic current, as proposed in [247], arises from charge transfer kinetics. It takes a form that extends the Butler-Volmer Equation (3.7) to conditions influenced by mass transfer [273]. The expression of $i^{ct}_{a/e}$ at the metallic lithium electrode interface reads

$$i^{ct}_{a/e} = i^{0}_{a/e}\,\left(\frac{c_{\mathrm{Li}}(0,t)}{\overline{c}_{\mathrm{Li}}}\exp\left[\,\frac{\alpha_a F}{RT}\,\eta_a(t)\right] - \frac{c_{\mathrm{Li}^{+}}(0,t)}{\overline{c}_{\mathrm{Li}^{+}}}\exp\left[-\,\frac{(1-\alpha_a)F}{RT}\,\eta_a(t)\right]\right)\ , \tag{3.34a}$$

where $\overline{c}_{\mathrm{Li}^{+}}$ is the average bulk concentration of species Li^{+}, $\overline{c}_{Li}$ is the bulk activity of the metallic Li, α_a is the charge transfer coefficient for reaction Equation (3.2), η_a is the overpotential (3.8) of the charge transfer reaction at the negative electrode, and the exchange current $i^{0}_{a/e}$ is given by:

$$i^{0}_{a/e} = F\,k_2\,(\overline{c}_{\mathrm{Li}^{+}})^{\alpha_a}\,(\overline{c}_{\mathrm{Li}})^{1-\alpha_a}\ , \tag{3.34b}$$

with k_2 the standard rate constant for reaction Equation (3.2). The expression of $i_{e/c}$ at the positive electrode interface is given by the Butler-Volmer Equation (3.7), with the exchange current density

$$i^{0}_{e/c} = F\,k_1\,c^{sat}_{\mathrm{Li}^{\oplus}}\,\left(1-\frac{\overline{c}_{\mathrm{Li}^{\oplus}}}{c^{sat}_{Li^{\oplus}}}\right)^{\alpha_c}\,\left(\frac{\overline{c}_{\mathrm{Li}^{\oplus}}}{c^{sat}_{Li^{\oplus}}}\right)^{1-\alpha_c}\,(\,\overline{c}_{\mathrm{Li}^{+}}\,)^{\alpha_c}\ , \tag{3.34c}$$

with k_1 the standard rate constant for reaction Equation (3.1).

3.2.4 Two-mechanisms model for all-solid-state lithium-ion batteries

A model that accounts for two mechanisms of ionic conduction was recently published in [248]. Rooted in the thermo-mechanics of continua, the model builds upon the work of Raijmakers et al. [247] to enhance the description of vacancy replenishment in a LiPON solid electrolyte and applies to LLZO as well, according to [274]. The equations that depict

ionic transfer in [248] are multi-scale compatible. This feature seems to be particularly pertinent for composite cathodes, as indicated in [241].

As eloquently detailed in [247], some of the Li ions within a solid electrolyte undergo thermal excitation at standard conditions. This activates the chemical ionization reaction (3.3), resulting in the generation of uncompensated negative charges associated with vacancies in the LiPON matrix at the sites previously occupied by lithium. Raijmakers et al. depicted vacancies as capable of movement within the solid material (as for the motion of anions in liquid electrolytes) driven by entropic Brownian motion and migration within an electric field, as described in equation (3.25b). This vision is thermodynamically encapsulated in the constitutive law (3.18).

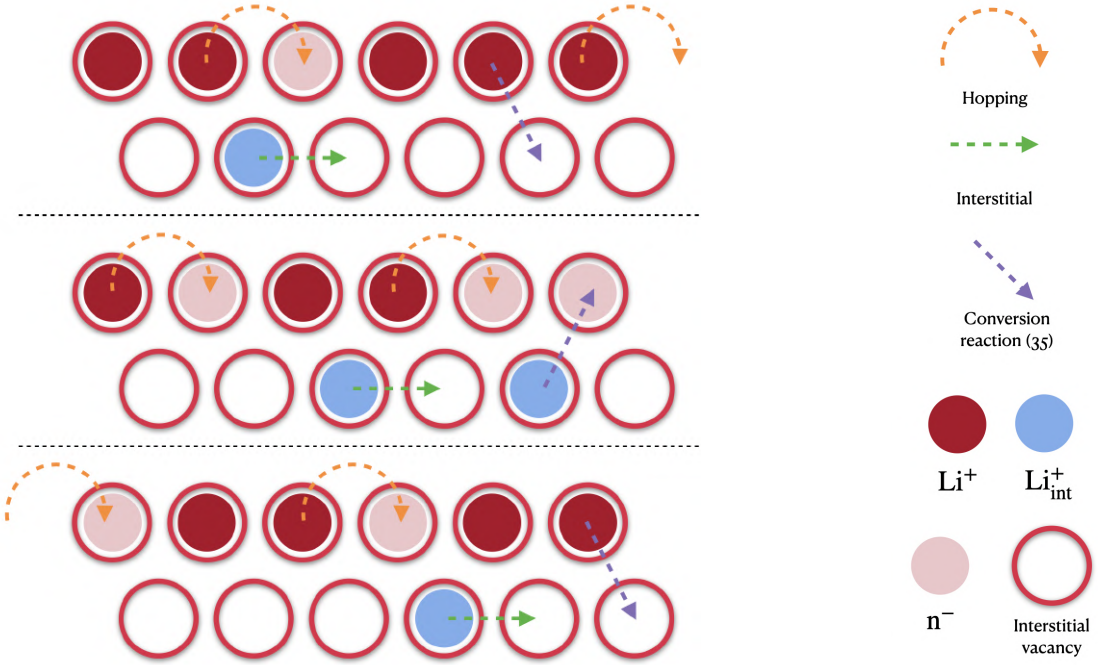

Figure 3.3: *Cation migration mechanisms: hopping into uncompensated negative charges associated with vacancies in the LiPON matrix, direct interstitial and conversion after reaction* (3.35). *(a) A sequence of three ionic distribution snapshots in time; (b) Legend.*

The filling of vacancies was modeled in [248, 275] following the pictorial view in Figure 3.3. Some ions, denoted henceforth with $\mathrm{Li}^+_{\mathrm{int}}$ and depicted in blue in Figure 3.3, move in a meta-stable interstitial state, whereas other ions, depicted in red in Figure 3.3, hop and fill neighboring vacancies. This dynamic behavior thus entails a differentiation among the Li^+ ions after the chemical ionization reaction (3.3) occurs. It is described by a further reaction

$$\mathrm{Li}^+ \underset{k_b^{\mathrm{int}}}{\overset{k_f^{\mathrm{int}}}{\rightleftarrows}} \mathrm{Li}^+_{\mathrm{int}} \,, \tag{3.35}$$

where k_f^{int} and k_b^{int} are the rate constants for reaction (3.35). When $k_f^{\mathrm{int}} = 0$, no interstitial mechanism is accounted for and the model becomes to a classical single-ion conducting solid electrolyte [245].

In essence, reaction (3.3) enables lithium ions to depart from the host sites and flow across the intricate amorphous LiPON structure, either by occupying neighboring vacancies or interstitially. The ratio of ions engaging in these two mechanisms is governed by

reaction (3.35). Within this framework, only positive ions are mobile species, with the vacancies lacking inherent mobility. Consequently, there exists no direct flow $\vec{h}_{\mathrm{n}^-}(x,t)$ of negative charges, in contrast to Equation (3.25b), and the local vacancy concentration is modified solely by the chemical ionization reaction (3.35).

This conceptual picture frames into the following set of mass balance equations, which characterize the immobile lithium LiO, the negative charges n^-, the transport of the lithium ions $\mathrm{Li}^+_{\mathrm{int}}$ that go interstitial, and the remaining Li^+ that hop:

$$\frac{\partial c_{\mathrm{LiO}}}{\partial t} = -w^{(3.3)} \qquad 0 \le x \le L_e \,, \tag{3.36a}$$

$$\frac{\partial c_{\mathrm{n}^-}}{\partial t} = w^{(3.3)} \qquad 0 \le x \le L_e \,, \tag{3.36b}$$

$$\frac{\partial c_{\mathrm{Li}^+}}{\partial t} + \nabla \cdot \left[\vec{h}_{\mathrm{Li}^+}\right] = w^{(3.3)} - w^{(3.35)} \qquad 0 \le x \le L_e \,, \tag{3.36c}$$

$$\frac{\partial c_{\mathrm{Li}^+_{\mathrm{int}}}}{\partial t} + \nabla \cdot \left[\vec{h}_{\mathrm{Li}^+_{\mathrm{int}}}\right] = w^{(3.35)} \qquad 0 \le x \le L_e. \tag{3.36d}$$

having set

$$w^{(3.35)} = k_f^{\mathrm{int}} c_{\mathrm{Li}^+} - k_b^{\mathrm{int}} c_{\mathrm{Li}^+_{\mathrm{int}}} \tag{3.36e}$$

according to reaction (3.35). The ratio

$$K_{\mathrm{eq}}^{\mathrm{int}} = k_f^{\mathrm{int}} / k_b^{\mathrm{int}}$$

provides the equilibrium constant of reaction (3.35). Five unknown fields, i.e., the concentrations c_{LiO}, c_{n^-}, c_{Li^+}, and $c_{\mathrm{Li}^+_{\mathrm{int}}}$ and the electric potential ϕ, are accompanied by the set of four mass balance Equations (3.36a)-(3.36d). The additional required equation is Ampère's law (with Maxwell's correction, because the electroneutrality condition $c_{\mathrm{Li}^+} + c_{\mathrm{Li}^+_{\mathrm{int}}} = c_{\mathrm{n}^-}$ is not used as a fundamental law). To conclude the set of balance equations, the usual balance of forces in small strains was accounted for in [275]

$$\nabla \cdot [\boldsymbol{\sigma}] + \vec{b} = \vec{0} \,. \tag{3.36f}$$

An additive decomposition of the strain tensor $\boldsymbol{\varepsilon}$ in an elastic recoverable after unloading ($\boldsymbol{\varepsilon}^{el}$) and a swelling contribution related to the insertion of species in the host material ($\boldsymbol{\varepsilon}^{sw}$) were considered:

$$\boldsymbol{\varepsilon} = \boldsymbol{\varepsilon}^{el} + \boldsymbol{\varepsilon}^{sw} \,. \tag{3.37}$$

The swelling contribution

$$\boldsymbol{\varepsilon}^{sw} = \sum_{\alpha} \omega_\alpha \left(c_\alpha - c_\alpha^0\right) \mathbb{1}, \quad \text{with} \quad \alpha = \mathrm{Li}^+, \mathrm{Li}^+_{\mathrm{int}} \,, \tag{3.38}$$

was assumed to be volumetric and proportional to the deviation $c_\alpha - c_\alpha^0$ from the reference concentration c_α^0 by means of the chemical expansion coefficients ω_α of species α. They equal one third of the partial molar volumes at a given temperature.

To derive *governing equations* from the balance Equation (3.36), constitutive laws were derived from a rigorous thermodynamic setting. The interstitial motion differs thermodynamically from the hopping mechanism. Therefore, using the same thermodynamic

approach for both mechanisms might be disputable. Aware of this limitation and inspired by [16, 276, 277] restricted to small strains, elaborating the electromagnetic contribution in the Helmholtz free energy ψ from [251, 252], the chemical potential (3.16b) of species $\alpha = \mathrm{Li}^+, \mathrm{Li}^+_{\mathrm{int}}$ was extended to

$$\mu_\alpha = \mu^0_\alpha + RT \ln[\frac{\theta_\alpha}{1-\theta_\alpha}] + RT \not{\chi}(1-2\theta_\alpha) + \frac{\partial \psi_{el}}{\partial c_\alpha} , \tag{3.39}$$

as detailed in [261, 262]. A standard quadratic form for the elastic part of the free energy density ψ_{el}, in the small strains regime, can be adopted

$$\psi_{el}(\boldsymbol{\varepsilon}, c_\alpha) = \frac{1}{2} K(c_\alpha) \,\mathrm{tr}\,[\,\boldsymbol{\varepsilon} - \boldsymbol{\varepsilon}^{sw}\,]^2 + \; G(c_\alpha)\, \mathrm{dev}\,[\,\boldsymbol{\varepsilon} - \boldsymbol{\varepsilon}^{sw}\,]^{\,2} , \tag{3.40}$$

where K, G are the bulk and shear modulus respectively and they are made dependent on species concentrations. The stress tensor $\boldsymbol{\sigma}^e(\boldsymbol{\varepsilon}, c_\alpha)$ descends from thermodynamic restrictions (see [261] for details and extension to temperature dependency)

$$\boldsymbol{\sigma}^e = \frac{\partial \psi_{el}}{\partial \boldsymbol{\varepsilon}} = 2\,G\,\mathrm{dev}\,[\,\boldsymbol{\varepsilon}\,] + \; K \;(\,\mathrm{tr}\,[\,\boldsymbol{\varepsilon} - \boldsymbol{\varepsilon}^{sw}\,]\,)\;\mathbb{1} \; . \tag{3.41}$$

Note that the derivative $\partial\psi_{el}/\partial c_\alpha$, in Equation (3.39) is the sum of two contributions

$$\frac{\partial \psi_{el}}{\partial c_\alpha} = -\omega_\alpha \,\mathrm{tr}\,[\,\boldsymbol{\sigma}^e\,] + \frac{1}{2}\frac{\partial K}{\partial c_\alpha}\,\mathrm{tr}\,[\,\boldsymbol{\varepsilon} - \boldsymbol{\varepsilon}^{sw}\,]^2 + \; \frac{\partial G}{\partial c_\alpha}\,\mathrm{dev}\,[\,\boldsymbol{\varepsilon} - \boldsymbol{\varepsilon}^{sw}\,]^{\,2} . \tag{3.42}$$

The first emanates from the swelling part of the strain, and is present even if the material parameters are made independent on concentration of species. Nernst-Planck Equation (3.18) is extended as follows

$$\begin{aligned} \vec{h}_\alpha(x,t) = &- \mathbb{D}_\alpha \;[1 - 2\not{\chi}\,\theta_\alpha\,(1-\theta_\alpha)]\;\nabla c_\alpha(x,t) \\ &- 3\,\boldsymbol{M}(c_\alpha)\;K\;\omega_\alpha\;[3\,\omega_\alpha\,\nabla c_\alpha - \nabla \mathrm{tr}\,[\,\boldsymbol{\varepsilon}\,]] \\ &- \frac{\mathbb{D}_\alpha F}{RT} c_\alpha(x,t)\;\nabla\phi_e(x,t) \; , \end{aligned} \tag{3.43}$$

with $\alpha = \mathrm{Li}^+, \mathrm{Li}^+_{\mathrm{int}}$. By defining with $\theta_\alpha = c_\alpha / c^{sat}_\alpha$, the mobility tensor reads [263]

$$\boldsymbol{M}(c_\alpha) = \frac{\mathbb{D}_\alpha}{RT}\, c^{sat}_\alpha\;\theta_\alpha\;(1-\theta_\alpha)\;\mathbb{1} \; . \tag{3.44}$$

It accounts for saturation and in this differs from Equation (3.14). The energetic and entropic contributions in the constitutive law (3.43) have already been described in Equation (3.17). The mechanical contribution to the mass flux is driven by the chemical expansion coefficient and derives from thermodynamic consistency.

The mass balance equations, after inserting (3.43) into Equations (3.36c)-(3.36d), do not form a complete set, because ionic transport entails a movement of mass and charge. In order to build a multiscale compatible theory, the generally accepted electroneutrality assumption cannot be taken, since it prevents one from imposing the conservation of energy across the scales: this concept was illustrated with great detail in [256, 251] and is not further elaborated here. Multiscale compatibility is granted by using Ampere's law (with Maxwell's correction in the realm of small strains)

$$\nabla \cdot \left[-\varepsilon\,\nabla\frac{\partial \phi_e}{\partial t} + F\,\left(\vec{h}_{\mathrm{Li}^+} + \vec{h}_{\mathrm{Li}^+_{\mathrm{int}}}\right)\right] = 0 \qquad\qquad 0 \le x \le L_e \; . \tag{3.45}$$

When multiscale is not invoked, the electroneutrality assumption

$$c_{\mathrm{Li^+}}(x,t) + c_{\mathrm{Li^+_{int}}}(x,t) = c_{\mathrm{n^-}}(x,t) \tag{3.46}$$

can be called for.

A widespread choice for the initial conditions for concentrations and electric potential enforces equilibrium conditions. They hold

$$\phi_e(x,0) = 0 \,, \tag{3.47a}$$
$$c_{\mathrm{LiO}}(x,0) = c^{eq}_{\mathrm{LiO}} = (1-\delta)c_0 \,, \tag{3.47b}$$
$$c_{\mathrm{n^-}}(x,0) = c^{eq}_{\mathrm{n^-}} = \delta c_0 \,, \tag{3.47c}$$
$$c_{\mathrm{Li^+}}(x,0) = c^{eq}_{\mathrm{Li^+}} = \frac{\delta c_0}{1+K^{\mathrm{int}}_{\mathrm{eq}}} = K^{\mathrm{ion}}_{\mathrm{eq}}\left(\frac{1}{\delta}-1\right) \,, \tag{3.47d}$$
$$c_{\mathrm{Li^+_{int}}}(x,0) = c^{eq}_{\mathrm{Li^+_{int}}} = K^{\mathrm{int}}_{\mathrm{eq}}\,\frac{\delta c_0}{1+K^{\mathrm{int}}_{\mathrm{eq}}} = \delta\, c_0 + K^{\mathrm{ion}}_{\mathrm{eq}}\left(1-\frac{1}{\delta}\right) \,. \tag{3.47e}$$

Three independet factors influence the equilibrium concentrations within the system: c_0 and the equilibrium constants for reactions (3.3) and (3.35). While c_0 can be determined with precision, estimating $K^{\mathrm{ion}}_{\mathrm{eq}}$ and $K^{\mathrm{int}}_{\mathrm{eq}}$ through experiments is fraught with substantial uncertainties. These three parameters are interrelated and play a role in defining the fraction of lithium existing in a mobile state at equilibrium, which is referred to as δ, as detailed in reference [247]. δ holds,

$$\delta = \frac{2}{1+\sqrt{1+4\frac{c_0}{K^{\mathrm{ion}}_{\mathrm{eq}}}\frac{1}{1+K^{\mathrm{int}}_{\mathrm{eq}}}-1}} \,. \tag{3.48}$$

Equation (3.49) can be readily transformed to express $K^{\mathrm{int}}_{\mathrm{eq}}$ in terms of both δ and $K^{\mathrm{ion}}_{\mathrm{eq}}$ as follows,

$$K^{\mathrm{int}}_{\mathrm{eq}} = \frac{-c_0\delta^2 + (1-\delta)K^{\mathrm{ion}}_{\mathrm{eq}}}{(\delta-1)K^{\mathrm{ion}}_{\mathrm{eq}}} \,. \tag{3.49}$$

The interface conditions for this advanced model are Equations (3.29) and (3.33). The faradaic current originates from charge transfer kinetics, as proposed in [247]. Because of the interstitial and hopping classification of lithium flux, faradaic interface conditions split:

$$i^{ct}_{a/e} = i^{ct}_{a/e_{\mathrm{Li^+}}} + i^{ct}_{a/e_{\mathrm{Li^+_{int}}}} \,, \qquad\qquad i^{ct}_{e/c} = i^{ct}_{e/c_{\mathrm{Li^+}}} + i^{ct}_{e/c_{\mathrm{Li^+_{int}}}} \,. \tag{3.50}$$

The charge transfer current is the sum of interstitial and hopping contributions, inferred from Butler-Volmer Equation (3.7) or (3.34). The exchange current reads:

$$i^0_{a/e_{\mathrm{Li^+}}} = F\,k_2\,(\overline{c}_{\mathrm{Li^+}})^{\alpha}\,(\overline{c}_{\mathrm{Li}})^{1-\alpha} \,, \quad i^0_{e/c_{\mathrm{Li^+}}} = F\,k_1\,c^{sat}_{\mathrm{Li^\oplus}}\,\left(1-\frac{\overline{c}_{\mathrm{Li^\oplus}}}{c^{sat}_{\mathrm{Li^\oplus}}}\right)^{\alpha}\left(\frac{\overline{c}_{\mathrm{Li^\oplus}}}{c^{sat}_{\mathrm{Li^\oplus}}}\right)^{1-\alpha}(\overline{c}_{\mathrm{Li^+}})^{\alpha} \tag{3.51a}$$

$$i^0_{a/e_{\mathrm{Li^+_{int}}}} = i^0_{a/e_{\mathrm{Li^+}}}\,\left(\frac{\overline{c}_{\mathrm{Li^+_{int}}}}{\overline{c}_{\mathrm{Li^+}}}\right)^{\alpha} \,, \quad i^0_{e/c_{\mathrm{Li^+_{int}}}} = i^0_{e/c_{\mathrm{Li^+}}}\,\left(\frac{\overline{c}_{\mathrm{Li^+_{int}}}}{\overline{c}_{\mathrm{Li^+}}}\right)^{\alpha} \,. \tag{3.51b}$$

Here, $\overline{c}_{\mathrm{Li^+}}$ and $\overline{c}_{\mathrm{Li^+int}}$ represent the average bulk concentrations of the species $\mathrm{Li^+}$ and $\mathrm{Li^+int}$, respectively. Unlike in [247], these averages are not time-independent. In the absence of a clearer understanding, we make the assumption that the non-faradaic current $i_\alpha^{dl}(t)$, as described in Equation (3.33), is proportional to the faradaic splitting, i.e.

$$i_s^{dl} = i_{s\ \mathrm{Li^+}}^{dl} + i_{s\ \mathrm{Li^+_{int}}}^{dl}\ , \text{with} \quad i_{s\ \mathrm{Li^+}}^{dl} = \frac{i_{s\ \mathrm{Li^+}}^{ct}}{i_s^{ct}}\ c_s^{dl}\ \frac{\partial [\![\, \phi \,]\!]}{\partial t} \quad \text{and} \quad i_{s\ \mathrm{Li^+_{int}}}^{dl} = \frac{i_{s\ \mathrm{Li^+_{int}}}^{ct}}{i_s^{ct}}\ c_s^{dl}\ \frac{\partial [\![\, \phi \,]\!]}{\partial t}\ . \tag{3.52}$$

where $s = a/e, e/c$. The Neumann conditions on fluxes at the boundaries of the electrolyte read:

$$\vec{h}_{\mathrm{Li^+}}(0,t)\cdot\vec{n} = -(i_{a/e_{\mathrm{Li^+}}}^{ct} + i_{a/e_{\mathrm{Li^+}}}^{dl})/F\ , \qquad \vec{h}_{\mathrm{Li^+}}(L_e,t)\cdot\vec{n} = -(i_{e/c_{\mathrm{Li^+}}}^{ct} + i_{e/c_{\mathrm{Li^+}}}^{dl})/F\ , \tag{3.53a}$$

$$\vec{h}_{\mathrm{Li^+_{int}}}(0,t)\cdot\vec{n} = -(i_{a/e_{\mathrm{Li^+_{int}}}}^{ct} + i_{a/e_{\mathrm{Li^+_{int}}}}^{dl})/F\ , \quad \vec{h}_{\mathrm{Li^+_{int}}}(L_e,t)\cdot\vec{n} = -(i_{e/c_{\mathrm{Li^+_{int}}}}^{ct} + i_{e/c_{\mathrm{Li^+_{int}}}}^{dl})/F\ . \tag{3.53b}$$

The continuity of displacements and normal tractions are interface conditions for the mechanical governing Equation (3.36f). The electrodes governing equations and boundary conditions do not differ from section 3.2.3.

In this section, the main features of the four models depicted in [245, 246, 247, 248] have been recapitulated, highlighting the main features as well as the mathematical structure of each formulation. In the following section the two most advanced theories, proposed in [247] and [248], are compared numerically. The experimental outcomes described in [253] will be used for validation. Material and geometrical parameters have been collected in Table 3.1 in Appendix 2.2.

3.3 Benchmark comparison

We considered a layer of $\mathrm{LiCoO_2}$ with thickness $\mathrm{L_c} = 0.32\mu\mathrm{m}$ deposited on a platinum substrate as the positive electrode. A Lithium metal foil with thickness $\mathrm{L_a} = 0.50\mu\mathrm{m}$ was used as a negative electrode. The solid electrolyte was a one-micron-thick ($\mathrm{L_e} = 1.00\mu\mathrm{m}$) layer of LiPON. The surface area of the deposited electrodes was $A = 10^{-4}\mathrm{m}^2$ and the theoretical storage capacity of the battery was $10^{-5}\mathrm{Ah}$.

It should be emphasized that the benchmark configuration considered in this section corresponds to a thin-film all-solid-state battery architecture taken from the reference benchmark and is used here to compare the predictions of the models discussed in this chapter under a common and well-defined set of conditions, rather than to represent the dimensions of conventional lithium-ion battery electrodes. In particular, the cathode and lithium foil thicknesses adopted in the benchmark are much smaller than those typically encountered in practical composite electrodes, which are commonly on the order of several tens of micrometers. The purpose of this section is therefore not to establish direct quantitative correspondence with commercial-format electrodes, but to assess how the selected modeling approaches behave within the same benchmark framework. Accordingly, care must be taken when extrapolating these benchmark results to realistic battery systems with much thicker electrodes and more complex microstructures.

The electrochemical cell was subject to a galvanostatic process of discharge at different $C-rates$, under a temperature-controlled condition of 25°C. Symbol I_{nC} denotes the current corresponding to $C-rate = n$. For $C-rate = 1$, I_{1C} was $10^{-5}A$. Initial and boundary conditions were made compatible with a thermodynamic equilibrium at $t = 0$, tuning the density current $i_{bat}(t)$ in time as:

$$i_{bat}(t) = (1 - e^{-t}) \frac{I_{nC}}{A} , \tag{3.54}$$

with t in seconds. In view of Equation (3.54), the concentrations of ions across all battery components were uniform and at equilibrium at $t = 0$, since no profiles had been established yet. By enforcing the fraction of mobile lithium in the electrolyte $\delta = 0.18$ and a maximum concentration of lithium host sites in the electrolyte $c_0 = 6.01 \cdot 10^4\,\mathrm{mol/m^3}$, Equation (3.47) provided

$$c_{\mathrm{Li}}(x,0) = 7.60 \cdot 10^4 \quad \mathrm{mol/m^3} \quad -L_a \le x \le 0, \tag{3.55a}$$
$$c_{\mathrm{LiO}}(x,0) = 4.93 \cdot 10^4 \quad \mathrm{mol/m^3} \quad 0 \le x \le L_e, \tag{3.55b}$$
$$c_{\mathrm{n^-}}(x,0) = 1.08 \cdot 10^4 \quad \mathrm{mol/m^3} \quad 0 \le x \le L_e, \tag{3.55c}$$
$$c_{\mathrm{Li^+}}(x,0) = 5.68 \cdot 10^3 \quad \mathrm{mol/m^3} \quad 0 \le x \le L_e, \tag{3.55d}$$
$$c_{\mathrm{Li^+_{int}}}(x,0) = 5.12 \cdot 10^3 \quad \mathrm{mol/m^3} \quad 0 \le x \le L_e, \tag{3.55e}$$
$$c_{\mathrm{Li^\oplus}}(x,0) = c^{\mathrm{eq}}_{\mathrm{Li^\oplus}} = 1.20 \cdot 10^4 \quad \mathrm{mol/m^3} \quad L_e \le x \le L_e + L_c\,. \tag{3.55f}$$

The electric potential at the interface between the anode and the solid electrolyte was fixed as:

$$\phi(0,t) = 0\ [V] \quad \forall t. \tag{3.56}$$

All material parameters used in the simulation are listed in Table 3.1. The equilibrium constants read

$$K^{\mathrm{ion}}_{\mathrm{eq}} = \frac{1.125 \cdot 10^{-5}}{0.90 \cdot 10^{-8}} = 1250\,, \qquad K^{\mathrm{int}}_{\mathrm{eq}} = \frac{8.10 \cdot 10^{-9}}{0.90 \cdot 10^{-8}} = 0.9\,. \tag{3.57}$$

for this benchmark comparison.

The solution of the governing equations was approximated using the finite element method, implemented with custom weak forms in MATLAB. The unknown fields (refer to Figures 3.1c, 3.1d) and the geometry were tesselled with 61 linear elements. Only one element is necessary for the anode, as the lithium concentration was uniform and the electric potential was linear. The results were based on a mesh consisting of 40 finite elements covering the electrolyte and 20 panels discretizing the cathode. In both cases, the mesh was locally refined around the electrode/electrolyte interface. Integration in time was performed using the backward Euler method, with constant time increments of $\Delta t = 1.0, \mathrm{s}$.

The OCP was reconstructed from experimental data presented in [253] using interpolatory splines derived in the simulations. Alternatively, the OCP could have been analytically calculated following the approach outlined in [260]. Results obtained with the analytically determined OCP are reported in Appendix 2.1.

The simulations covered a wide set of rates, from 1.0 to 51.2. Experimental results are plotted with dots in Figure 3.4b as a function of time, while continuous lines reproduce

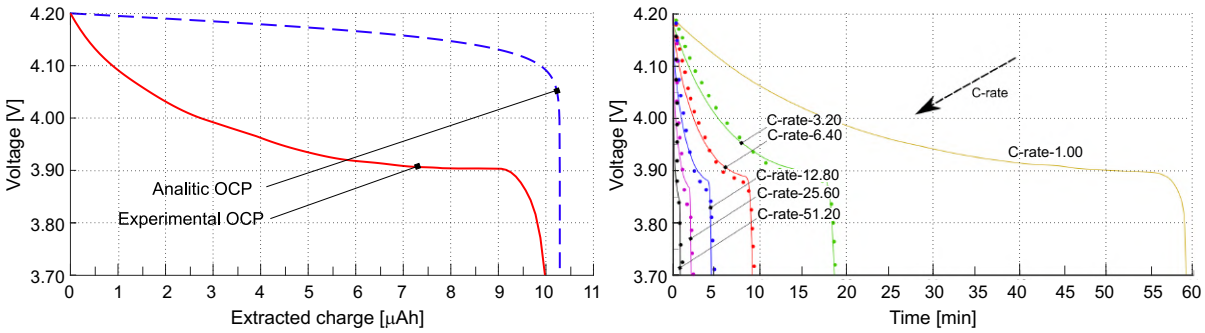

Figure 3.4: *(a) The open circuit potential (OCP) is depicted as a function of extracted charge. The OCP obtained from experimental tests is represented by the red line, while the OCP evaluated using the approach in [260] is illustrated by the blue line. (b) Discharge curves plotting voltage against time for various C−rates, from [248]. Different C−rates are shown by coloured lines, and the experimental values are indicated by dots. Reprinted with permission from [248] Copyright 2022 Elsevier.*

simulated outcomes. Experimental evidences and simulations show good agreement for all investigated C-rates. As expected, the extracted charge decreases with increasing C-rate due to higher over-potentials. Lower discharge rates imply a slower insertion, hence a more uniform allocation, of lithium in the positive electrode.

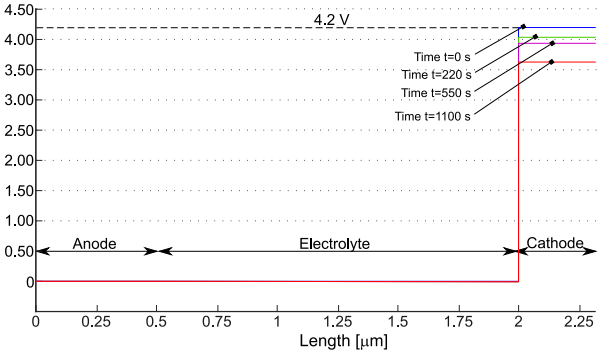

(a) $C\text{–}rate = 3.20$ for [248]

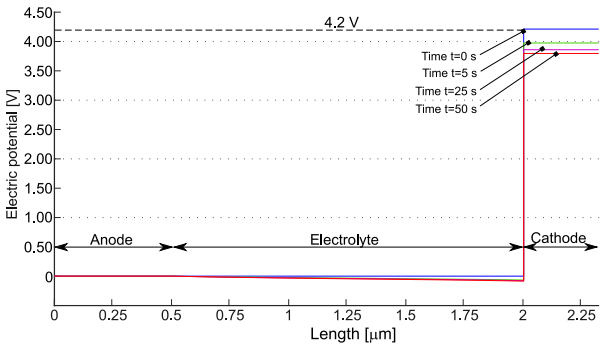

(b) $C\text{–}rate = 51.2$ for [248]

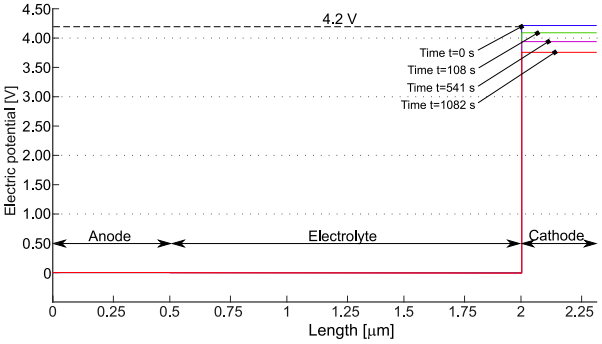

(c) $C\text{–}rate = 3.20$ for [247]

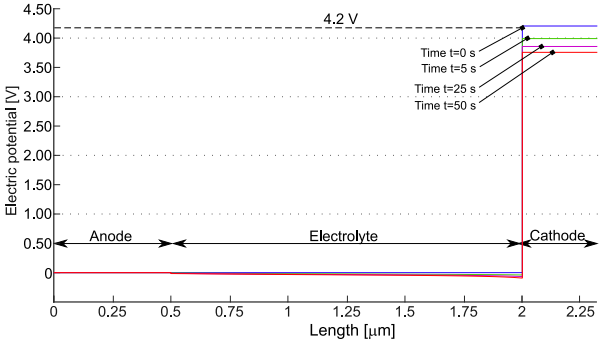

(d) $C\text{–}rate = 51.2$ for [247]

Figure 3.5: *The electric potential profile for the models published in [248] ((a) and (b)) and [247] ((c) and (d)) at various times for two different C–rates. The simulations quit when the concentration of lithium* $\mathrm{Li}^{\oplus}$ *within the positive electrode reaches its saturation* $c^{\mathrm{sat}}_{\mathrm{Li}^{\oplus}}$*. Reprinted partially with permission from [248] Copyright 2022 Elsevier.*

For two different discharge rates, Figure 3.5 plots the profile of the electric potential $\phi(x)$ at various times. At C-rate = 3.20, the battery is allowed to discharge in 1125s. At C-rate = 51.2, the battery ideally completes the discharge process in 70s. Simulations terminate when the concentration of lithium $\mathrm{Li}^{\oplus}$ inside the cathode reaches the saturation limit $c^{sat}_{\mathrm{Li}^{\oplus}}$, occurring after 1085s and 50s, respectively. Cathodic saturation is the limiting factor for battery operation. An extensive discussion on limiting factor induced by materials and architectures is reported in [278].

At the initial time the electric potential discontinuity at the interfaces make Butler-Volmer currents vanishing. Based on the measured battery OCP, at full charge state $\Delta\phi{=}4.2V$, as highlighted in Figure 3.5. During the discharge, the potential drops in the anode and in the electrolyte. However, the major changes in the potential profile occur at interface between electrolyte and cathode: the battery voltage decreases significantly during discharge as depicted in Figure 3.5a,b and it becomes almost uniform within the cathode. A similar behavior is observed for the model in [247] (see fig. 3.5 c,d).

Figure 3.6 depicts the evolution of lithium concentration $c_{\mathrm{Li}^{\oplus}}(x)$ in the cathode and in the solid electrolyte for the model in [248] ((a),(b)) as well as for the one proposed in [247] ((c),(d)). Since two ionic concentrations are concurrently present in the electrolyte, only their sum $(c_{\mathrm{Li}^{+}}+c_{\mathrm{Li}^{+}_{\mathrm{int}}})$ is plotted in Figure 3.6a,b.

The anodic foil of lithium remains unaffected by the charge/discharge processes and is considered as an unlimited reservoir of lithium. After intercalation, the lithium ions accumulate near the electrolyte/cathode interface. The discharge process ends when the lithium concentration in the cathode reaches its saturation limit $c^{sat}_{\mathrm{Li}^{\oplus}} = 23400, \mathrm{mol}, \mathrm{m}^{-3}$. Therefore, saturation at the interface between the electrolyte and the cathode is the limiting factor for the performance of this battery.

The concentration of $(c_{\mathrm{Li}^{+}}+c_{\mathrm{Li}^{+}_{\mathrm{int}}})$ in [247], initially uniform, increases near the anode interface, while decreasing at the cathode interface. This "liquid electrolyte" kind of behavior is justified since in [247], negative charges are allowed to move. This type of electrolyte-side concentration polarization is therefore model-dependent: it arises when both positive and negative charge carriers are allowed to redistribute (as in [247]), similarly to liquid and many polymer electrolytes. It should not be interpreted as a universal feature of all ASSBs, since in several solid electrolytes the counter-charge is effectively immobile or not described as a mobile species, leading to a different (often much weaker) concentration-polarization behavior. In the formulation proposed in [248], negative charges are filled by hopping lithium, which in turn is allowed to be intercalated. The time evolution of negative charges and total lithium is driven by the ionization reaction rates $w^{(3.3)}$ and $w^{(3.35)}$, as already discussed, and is very small in Figure 3.6a,b.

Figure 3.8 displays the total lithium concentration for the model from [248] (panels (a) and (b)) and for the model from [247] (panels (c) and (d)). The concentrations are depicted at the anode/electrolyte interface with a blue line and at the electrolyte/cathode interface with a red line. According to [248], the tangent disappears at $t = 0$. Such behavior is attributed to the electroneutrality coupled with the equilibrium condition $w = 0$ imposed at $t = 0$ in Equation (3.36b). The concentrations at the two electrodes evolve in accordance with the mass balance Equations (3.36c) and (3.36d). Over time, fluxes tend to converge to a uniform value across the electrolyte, diminishing the significance of the divergence contribution, and thus the evolution of concentrations is primarily driven by the evolution of $w^{(3.3)}$ and $w^{(3.35)}$. It is expected that, at the same equilibrium constant, increasing the reaction constant (i.e., making the reaction faster) would lead to reaching

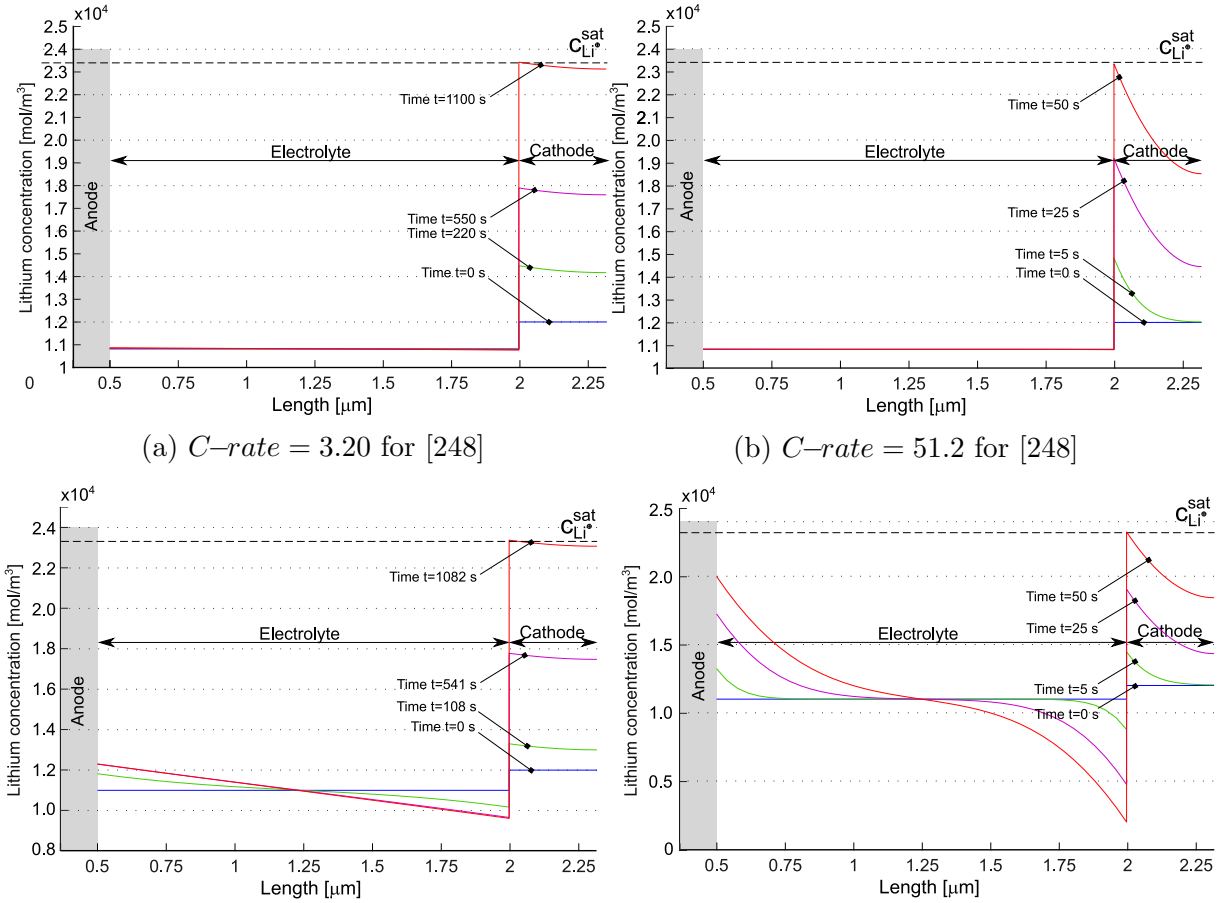

(a) $C\text{–}rate = 3.20$ for [248]

(b) $C\text{–}rate = 51.2$ for [248]

(c) $C\text{–}rate = 3.20$ for [247]

(d) $C\text{–}rate = 51.2$ for [247]

Figure 3.6: *Lithium concentration profiles within the battery for two different C–rates at different time steps for the models published in [248] ((a) and (b)) and in [247] ((c) and (d)). The blue lines refer to the starting time, when the battery is in thermodynamic equilibrium. The red line depicts the last time step, when the amount of lithium* $\mathrm{Li}^{\oplus}$ *in the positive electrode has reached the saturation limit* $c^{\mathrm{sat}}_{\mathrm{Li}^{\oplus}}$*. Reprinted partially with permission from [248] Copyright 2022 Elsevier.*

the steady state more rapidly. This numerical response is observed in Figure 3.8 (panels (a) and (b)), where higher values of k_f^{ion} and k_b^{ion}, while keeping $K_{\mathrm{eq}}^{\mathrm{ion}} = 1250$, result in reaching the concentration plateau faster. For the model by [247], the concentration response resembles that of liquid electrolytes [251, 252], as expected. It's noteworthy that steady state is achieved only at low C-rates in this case.

3.4 Final remarks and further developments

This note had the purpose of highlighting the main features, the fundamental assumptions, and the most relevant limitations of four ASSBs models of particular relvance in the literature. All formulations have been comprehensively examined from a theoretical perspective, whereas the model in [248] and its predecessor [247] have also been compared from a computational standpoint. Such an assessment was achieved via the finite element method, validating and comparing interface currents, electric potentials, flux patterns, and concentration profiles.

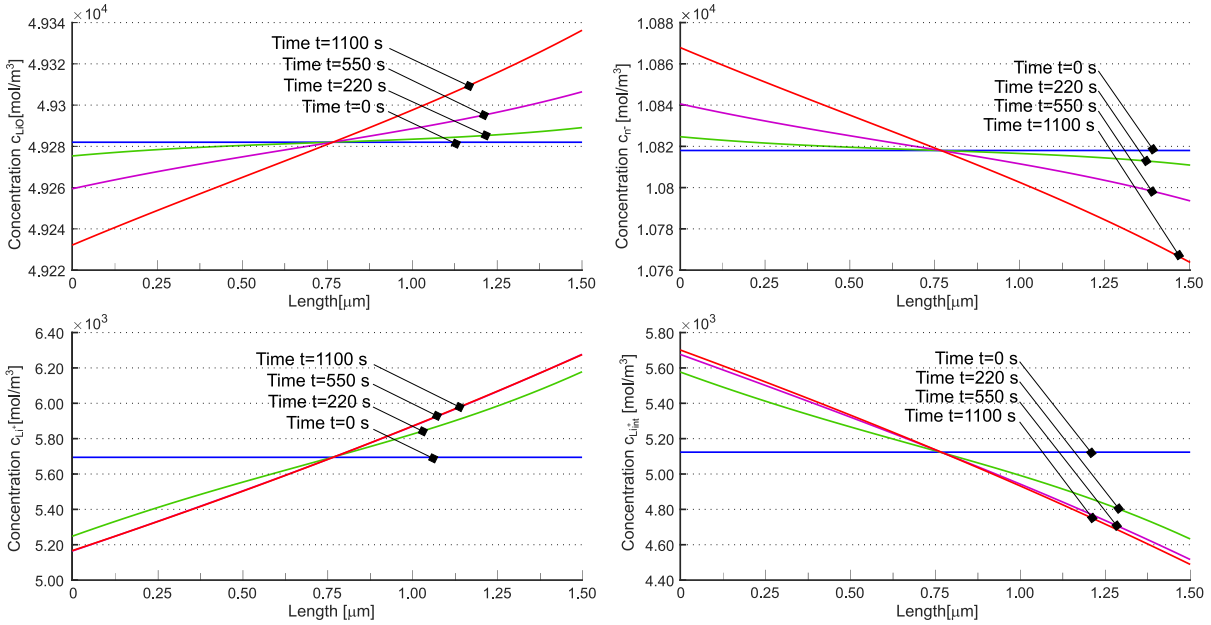

(a) $C\text{–}rate = 3.20$

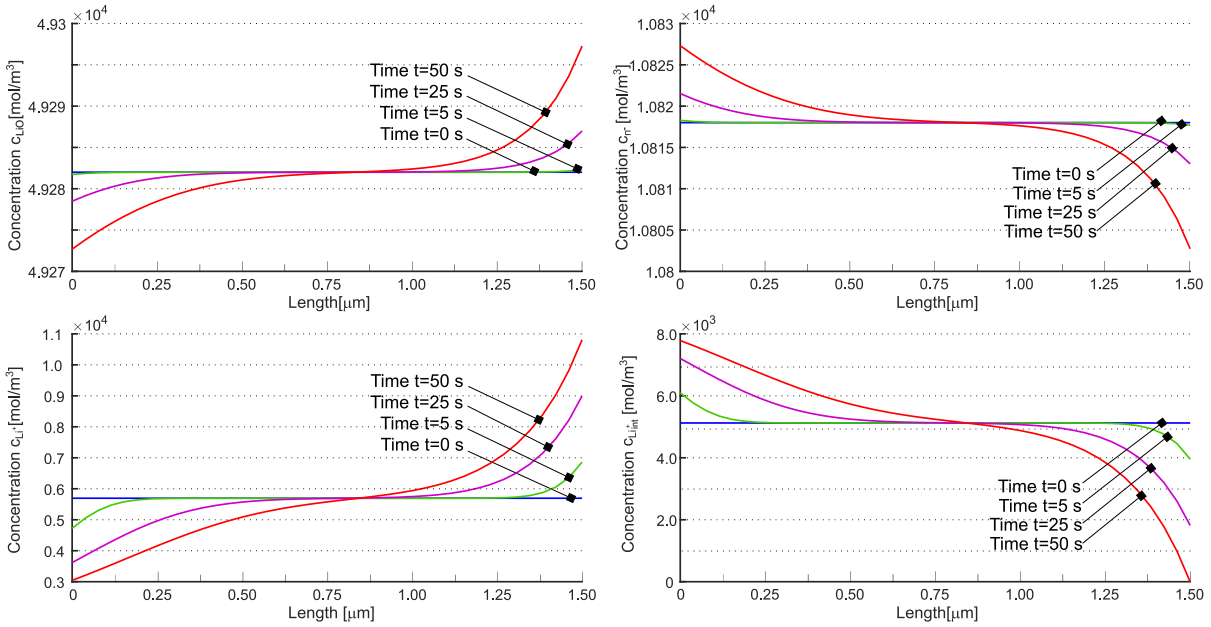

(b) $C\text{–}rate = 51.2$

Figure 3.7: Concentrations c_{LiO}, c_{n^-}, c_{Li^+} and $c_{Li^+_{int}}$ in the solid electrolyte at different times for a $C\text{–}rate = 3.2$ (a) and a $C\text{–}rate = 51.2$ (b). Reprinted with permission from [248] Copyright 2022 Elsevier.

Corresponding to the chronological order of publication, models' degree of complexity increased. All-solid-state Li/LiPON/$LiCoO_2$ micro-batteries were modelled by Fabre et al. [245] in one dimension, addressing the kinetics involved in charge-transfer at the interfaces between the electrodes and the electrolyte, as well as the diffusion of neutral lithium within the cathode and the migration of lithium ions throughout the solid electrolyte. A modified Poisson-Nernst-Planck system of equations for the solid electrolyte was established in [246]. Besides modeling diffusion and migration of mobile lithium ions in the solid electrolyte, the model in [247] accounted for the kinetics of the charge transfer

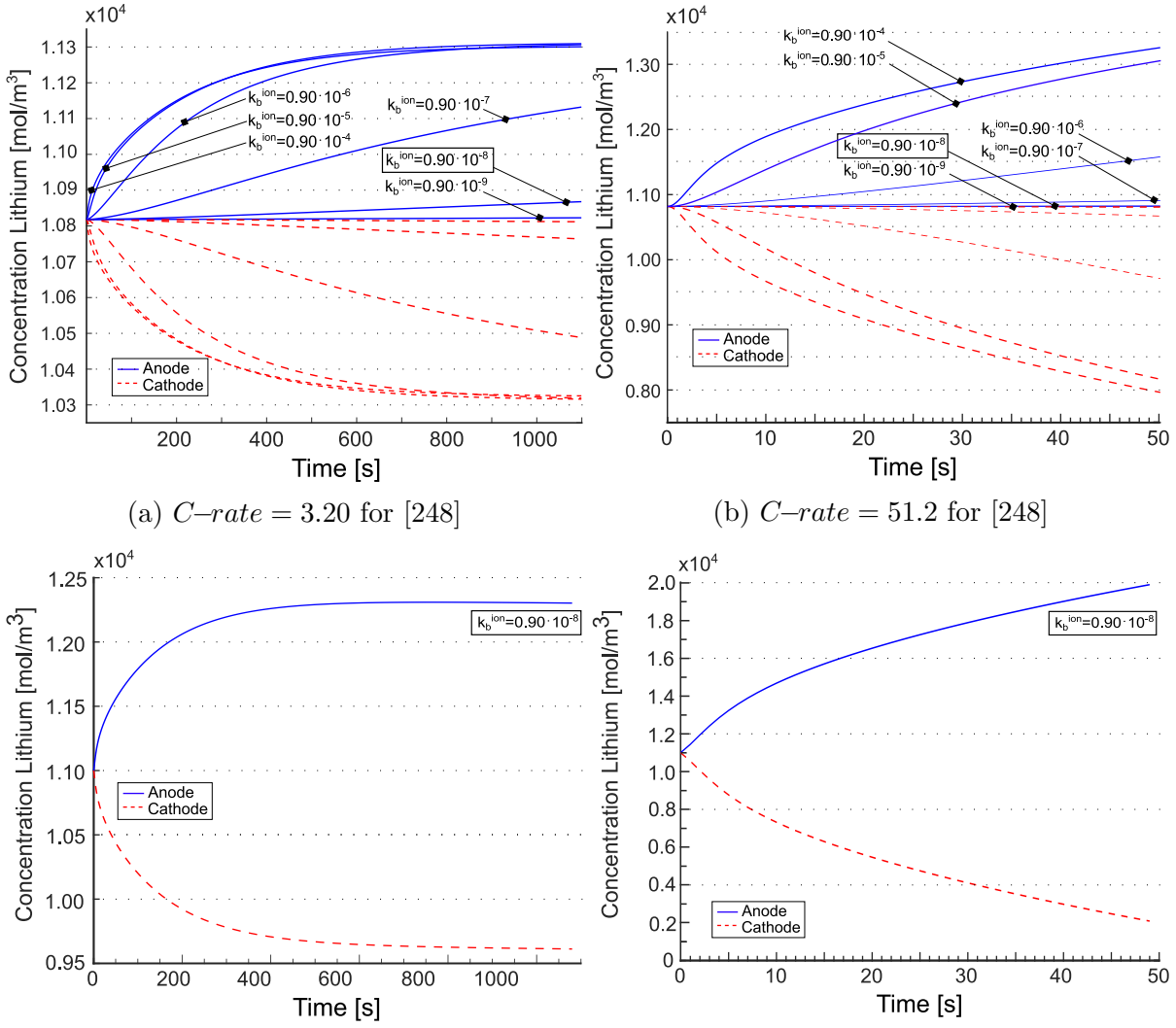

(a) $C\text{–}rate = 3.20$ for [248]

(b) $C\text{–}rate = 51.2$ for [248]

(c) $C\text{–}rate = 3.20$ for [247]

(d) $C\text{–}rate = 51.2$ for [247]

Figure 3.8: *Concentration of lithium at the interfaces with the positive and the negative electrodes for the two different C−rates. The values recorded at the anode/electrolyte interface are represented by the blue lines, while the red line illustrates the values at the electrolyte/cathode interface. Tangents at* $t = 0$ *vanish in Figures (a) and (b) due to the electroneutrality and the equilibrium condition* $w = 0$ *set at* $t = 0$ *in Equation* (3.36b). *Reprinted partially with permission from [248]Copyright 2022 Elsevier.*

at the interfaces between electrodes and electrolyte. To capture the space-charge effect, double-layer capacitors were positioned at the electrode/electrolyte interfaces. Ionic mobility in [248] resulted from hopping and interstitial diffusion, i.e., two mechanisms of ionic conduction in the solid electrolyte were devised.

The reviewed models share some common assumptions. They are: (i) thin-film based: the first model encapsulates this assumption in the constitutive equations, while the others are in principle fully three-dimensional and hence also applicable to composite electrode/electrolyte systems; (ii) isothermal (no self-heating), although it is quite well known that temperature affects the response of the battery [279]. Those assumptions shall be removed in further publications aiming at realistically replicate the response of batteries. The research focus should escape the limiting scenario of thin-film ASSBs and incorporate polymer solid electrolytes, inorganic solid electrolytes, and organic-inorganic

composite solid electrolytes [229, 280].

Polymer electrolytes show desirable characteristics such as exceptional flexibility, low weight, easy processing, and favorable compatibility with electrodes [281]. Their vulnerability to flammability underscores the urgent need for models that account for flame-retardant additives [282].

Inorganic solid electrolytes show high energy density and inherent safety [283, 274], but they suffer from a few major issues that might be mitigated by a proper design, facilitated by computational strategies [280]. Oxide solid electrolytes demonstrate exceptional electrochemical stability and ionic conductivity, yet they show inadequate electrode contact [284, 285]. Halide electrolytes exhibit exceptional compatibility with electrodes, although they are vulnerable to moisture [286]. Sulfide electrolytes exhibit notable ionic conductivity and commendable mechanical flexibility; however, they are characterized by a lack of stability of the electrode/electrolyte interface [287]. The presence of a lithium-depleted layer at the interface between an oxide cathode and sulfide electrolyte has been elucidated through the utilization of first-principle molecular dynamics simulations. Moreover, density functional theory (DFT) electronic structure calculations provide compelling evidence that the charge current specifically eliminates lithium ions from the sulfide electrolyte part of the interface, resulting in the depletion of lithium ions in that specific region. The obtained calculations align with experimental outcomes [288, 289, 290]. In recent years, the utilization of high-throughput density functional theory calculations and machine learning predictions has emerged as formidable methodologies for the exploration and identification of innovative materials [291, 292, 293]. Comprehensive calculations on a dataset of 740,000 lithium compounds have been published in [293], allowing the discovery of new solid electrolytes (SEs) .

Xi et al [294] conducted a comprehensive investigation into the physical contact and chemical/electrochemical properties of interfaces in ASSBs, offering a comprehensive summary of recent progress in interface modification techniques. In a recent work of Tian et al. [234], the effect of imperfect contact area was incorporated into a 1D Newman battery model, assuming that the current and Li concentration will be localized at the contacted area of the interfaces.

An electrochemical model for ASSBs with a composite positive electrode was developed in [295] by incorporating an imperfect solid-solid contact interface and an electrical double layer at the electrode-electrolyte interface. To enhance the accuracy of the battery model, diffusion coefficients dependent upon the lithium concentration were implemented. The simulations suggested that the primary factors restricting the performance of batteries were overpotentials that arose from concentration polarization within positively charged particles and interface reactions. Moreover, the size of the particles and the area of contact within the composite positive electrode had a significant impact on the performance of the battery.

Further phenomena should be included in the list of processes to be modeled towards achieving a realistic digital twin of energy storage systems. A change in volume due to repeated insertion and removal of Li atoms may lead to contact breakdown and degradation of the solid electrolyte lattice. Among the four reviewed publications, only [248] does not neglect volume changes during charge/discharge but the active surface area remained unaltered over cycling. The volumetric changes in composite electrodes increase the likelihood of crack formation and internal short circuits [296]. Hence, there is an urgent requirement to create innovative models of crack propagation and arrest in solid state electrolytes [297]. It is recommended to handle the mechanical problem in a three

dimensional setting, with large strain mechanics as in [16, 298, 299, 300].

Modeling ASSBs should also account for the solid electrolyte interface (SEI) formation. It occurs as a result of the reduction of the electrolyte, leading to the development of a thin and heterogeneous layer at the interface between the anode and electrolyte [301, 259]. The SEI progresses gradually over time, depleting active electrons and electrolyte species, resulting in an overall loss in capacity and ultimately the death of the battery [302, 303]. An effective modeling of the SEI has not been achieved yet, despite attempts in molecular modeling methods, including DFT, force fields, and machine learning potentials [304, 305].

Appendix

3.A Analytical OCP simulations

An approach to calculate the open circuit over-potential analytically is described in [260], based on the ideal chemical potential μ_{Li} , as reported in Figure 3.4a with blue dashed line. The discharge curves as a function of the extracted charge, obtained following this analytical approach, are given in Figure 3.9 a,b. The difference between the results

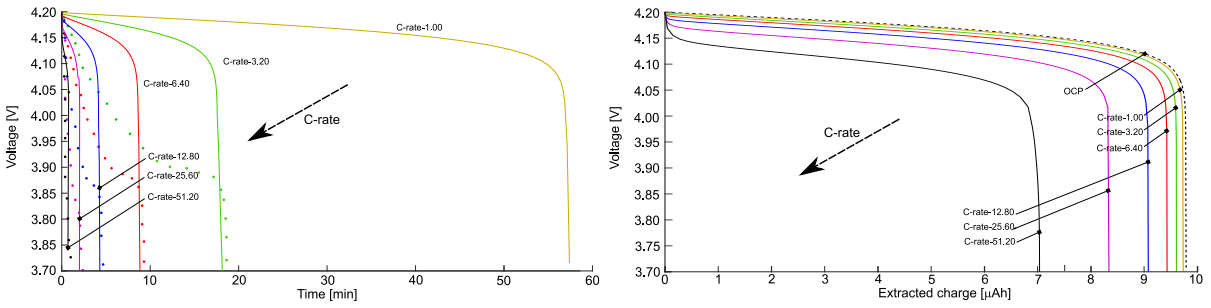

(a) (b)

Figure 3.9: *Discharge curves as a function of time (a), and the extracted charge (b) for different C–rates, obtained following the analytical approach to evaluate the OCP as given in [260].*

obtained considering the OCP evaluated from experimental tests and from the analytical approach are not negligible for this kind of battery meaning that more complex forms of the chemical potential shall be used as in [306].

3.B Material and geometrical parameters used for model validation

Parameter	Unit	Value	Description
T	298.5	K	Temperature
L_a	$0.50 \cdot 10^{-6}$	m	Thickness of the anode
L_e	$1.50 \cdot 10^{-6}$	m	Thickness of the electrolyte
L_c	$0.32 \cdot 10^{-6}$	m	Thickness of the cathode
L_{col}	$0.10 \cdot 10^{-6}$	m	Thickness of the positive collector
A	$1.00 \cdot 10^{-4}$	m^2	Geometrical surface area
$c_{\mathrm{Li}^{\oplus}}^{sat}$	$2.34 \cdot 10^{4}$	mol/m^3	Maximum concentration of $Li^{\oplus}$ ions in the electrode
k_a	$1.08 \cdot 10^{7}$	S/m	Electrical conductivities in the lithium anode
k_{col}	10.0	S/m	Electrical conductivities in the current collector
k_f^{ion}	$1.125 \cdot 10^{-5}$ ($1.80 \cdot 10^{-5}$)	1/s	Lithium ion generation reaction rate constant for Equation (3.3)
k_b^{ion}	$0.90 \cdot 10^{-8}$	$m^3/(mols)$	Lithium ion recombination reaction rate constant for Equation (3.3)
k_f^{int}	$8.10 \cdot 10^{-9}$ ($1.69 \cdot 10^{-9}$)	1/s	Lithium ion generation reaction rate constant for Equation (3.35)
k_b^{int}	$0.90 \cdot 10^{-8}$	m^3 (mols)	Lithium ion recombination reaction rate constant for Equation (3.35)
c_a^{dl}	$1.74 \cdot 10^{-4}$	F/m^2	Double layer capacity per unit area of anode
c_c^{dl}	$5.30 \cdot 10^{-3}$	F/m^2	Double layer capacity per unit area of cathode
α_n	0.6	-	Charge transfer coefficient for the negative electrode
α_p	0.6	-	Charge transfer coefficient for the positive electrode
$\mathbb{D}_{\mathrm{Li}^+}$	$5.10 \cdot 10^{-15}$	m^2/s	Diffusion coefficient for Li^+ ions in the electrolyte
$\mathbb{D}_{\mathrm{Li}_{\mathrm{int}}^+}$	$0.90 \cdot 10^{-15}$	m^2/s	Diffusion coefficient for Li_{int}^+ ions in the electrolyte
$\mathbb{D}_{\mathrm{Li}^{\oplus}}$	$1.76 \cdot 10^{-15}$	m^2/s	Diffusion coefficient for $Li^{\oplus}$ ions in the cathode
k_1	$5.10 \cdot 10^{-6}$	$m^{2.5}\ mol^{-0.5}/s$	Standard reaction rate constant for forward reaction in Equation (3.1)
k_2	$1.09 \cdot 10^{-5}$	m/s	Standard reaction rate constant for forward reaction in Equation (3.2)
δ	0.18	-	Fraction of mobile ions in the electrolyte in equilibrium
c_0	$6.01 \cdot 10^{4}$	mol/m^3	Maximal lithium concentration in the electrolyte
ε_r	2.25	–	Relative permittivity in the electrolyte

Table 3.1: A list of the parameters used in the simulations

Chapter 4

A 3D electro–chemo–mechanical continuum model for a Li/LCO half-cell

4.1 Introduction

In the study of lithium-ion battery systems (LIBs), modeling is essential for predicting behavior under given operating conditions. Over the past decades, LIBs have become central to portable electronics and electric vehicles, driving intense academic and industrial research worldwide [307, 308]. Because experimental testing is costly and time-consuming, a sound theoretical framework is needed to guide the design of more efficient and environmentally friendly batteries [309]. Physical models interpret experimental observations and help identify promising materials and cell architectures, while experiments provide the data required to validate and refine models. Together, theory and experiment underpin progress in the battery industry.

Mathematical models express the physics of LIBs through systems of equations. They clarify the mechanisms governing existing cells and predict the performance of new designs. When combined with uncertainty quantification and careful validation, computational simulations can optimize energy-storage devices, tailor architectures, and accelerate the discovery of high-capacity, high-power materials [310]. Modeling also allows safe exploration of operating regimes that are difficult or expensive to reproduce experimentally. Nevertheless, theoretical models must be grounded in realistic conditions and systematically compared with experiments; only consistent agreement can justify their predictive use. Since simulations are often cheaper and faster than dedicated experiments, reliable models can significantly shorten development cycles and time-to-market. Battery modeling thus spans methodologies from empirical and equivalent-circuit approaches that reproduce global discharge characteristics to fully physics-based formulations [311, 312, 313].

Over the last forty years, computational modeling of LIBs has advanced considerably, both in the description of material behavior and in the understanding of full-cell operation. Different levels of resolution are used depending on the quantities of interest. Atomistic models such as molecular dynamics (MD) probe the structure of electrolytes and active materials, while kinetic Monte Carlo (kMC) methods resolve interface reactions [314, 315]. Electronic-structure models provide local energy landscapes in the electrolyte, and continuum porous-electrode models describe charge/discharge behavior at the cell scale by

solving coupled partial differential equations for species concentrations, electric potential, temperature, and stress [316]. Multiscale, multiphysics continuum formulations link these descriptions across scales, enabling optimal cell design and robust lifetime predictions [317, 318]. A clear understanding of the physical processes active during cell operation is therefore crucial.

Comprehensive physical models rest on a common set of principles: balance laws, thermodynamics, constitutive theory, and frame-indifference. Balance equations enforce mass, charge, and momentum conservation; the first and second laws of thermodynamics constrain energy and entropy evolution; and constitutive relations must satisfy these restrictions while remaining objective, especially at finite strains. The governing equations follow systematically from this hierarchy [319, 320, 321, 322]. However, such rigor is not always respected in the battery-modeling literature, and violations of the second law may compromise the consistency of proposed constitutive models.

Figures 4.1 and 4.2 summarize the main processes and models relevant to LIB operation. Process 1 indicates the intercalation of Li^+ into the active particles. The process is modeled using the Butler-Volmer equation and the Gouy-Chapman hypothesis. Mass transfer involves the characterization of the motion of mobile ionic species. When convection does not exist, which is typically assumed during operation, the motion of species is determined by diffusion, which is induced by gradients in the concentration or by migration, which is controlled by an electric field [273, 323].

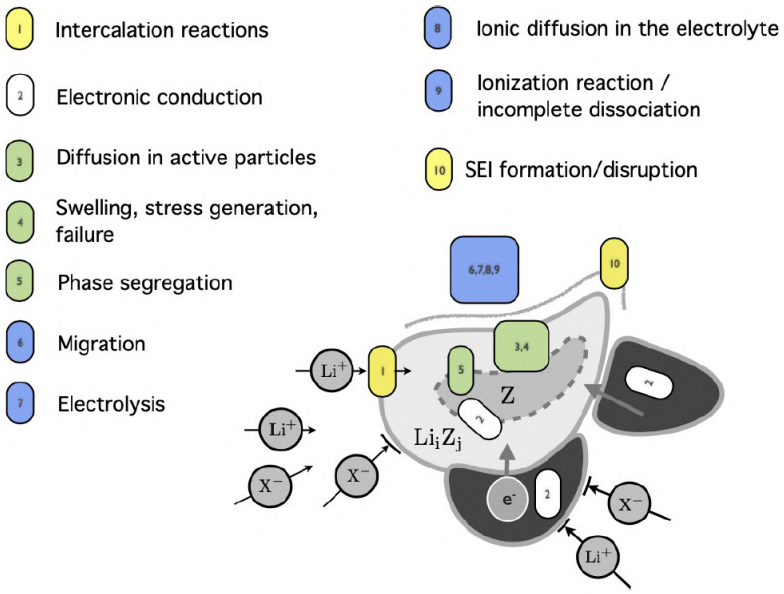

Figure 4.1: The set of processes that occur in a battery during its normal operation. The light grey phase represents the active cathode particles, whereas the dark grey phase corresponds to the conductive additive. The ions Li^+ and X^- denote the mobile species dissolved from the binary salt LiX in the electrolyte [243].

In this study, the behavior of a half cell during its operation is simulated as an initial/boundary value problem by coupling mechanics, electro-chemistry, and transport. The governing partial differential equations are derived from a thermodynamically consistent continuum multi-physics model [249, 278] which is based on the theory of Larche-Cahn [261]. The governing equations have been formulated in weak form, discretized,

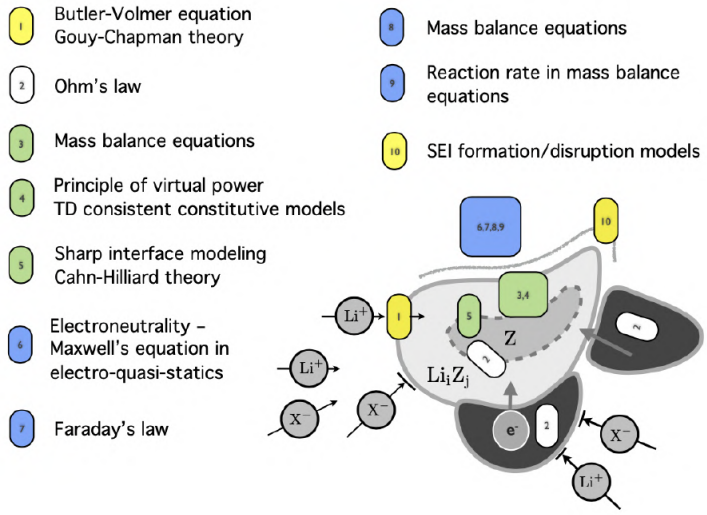

Figure 4.2: The set of models that occur in a battery during its normal operation [243].

and then implemented into a High-Performance Computing (HPC) algorithm using the Finite Element Method (FEM) library deal.ii [23]. The proposed formulation accounts for the elastic constitutive response of the foils and electrolyte for the expansion/contraction of the active particles of $LiCoO_2$ during intercalation and extraction. Finally, boundary conditions and interface conditions, the latter in the form of Butler Volmer equations, have been adopted. A brief methodological remark is in order regarding the numerical discretization adopted in this chapter. Although both the finite element method (FEM) and the finite volume method (FVM) are widely used in electrochemical energy modeling [324], the choice of discretization depends on the mathematical structure of the problem. In the present work, FEM was adopted because the governing equations are formulated in weak form and the model involves the coupled treatment of transport, electrochemistry, mechanics, and interfacial Butler–Volmer kinetics in a three-dimensional multi-domain setting. FEM is therefore a convenient choice for the present formulation and is consistent with the deal.ii-based implementation used in this chapter.

4.2 Definition of the problem

The interplay between solid mechanics and electrochemical fields is particularly significant in lithium-ion batteries (LIBs), as outlined in the introduction. In the following sections, we present the governing conservation laws—specifically, the conservation of linear and angular momentum for the mechanical domain, and the conservation of charge and mass for the electrochemical domain. Furthermore, we detail the coupling mechanisms between these fields and discuss interfacial phenomena that arise between different material domains. To begin, we define the relevant domains, interfaces, and boundaries within a typical lithium-ion battery (LIB) cell.

4.2.1 Model geometry

Figure 4.3 shows a simplified 2D cross-section of the 3D computational geometry of the LIB cell, included here solely to illustrate the main geometric features for clarity. In the

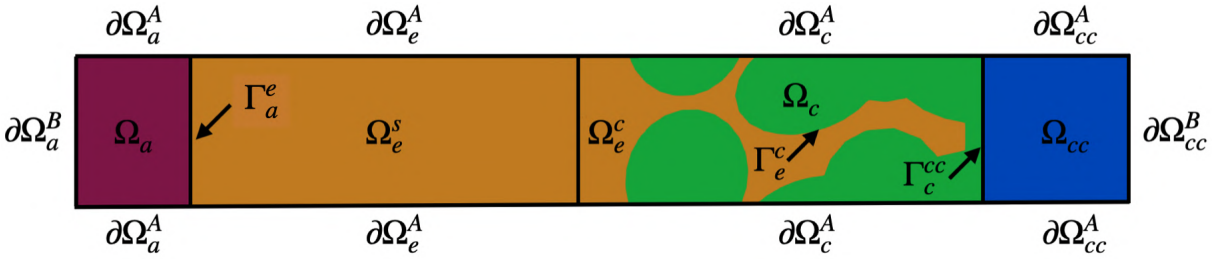

Figure 4.3: Schematic representation of computational domain

simplified 2D geometry, Ω_a denotes the anode region of the lithium-ion battery cell, which is modeled as a lithium metal foil. The cathode region, denoted by Ω_c, corresponds to a porous $LiCoO_2$ (LCO) cathode , where the phases corresponding to binder and carbon black are not considered for the sake of modeling simplicity. The electrolyte domain is split into two subregions: Ω_e^s refers to the electrolyte embedded in the polymer separator, and Ω_e^c corresponds to the electrolyte within the porous cathode. The current collector is made of aluminum foil which is represented as Ω_{cc}, and the overall computational domain is defined as $\Omega = \Omega_a \cup \Omega_e^s \cup \Omega_e^c \cup \Omega_c \cup \Omega_{cc}$. The interface between the anode and the electrolyte is denoted by Γ_a^e, while Γ_e^c represents the interface between the cathode and the electrolyte, and Γ_c^{cc} denotes the interface between the cathode and the current collector. The boundary of the anode domain is given by $\partial\Omega_a = \partial\Omega_a^A \cup \partial\Omega_a^B \cup \Gamma_a^e$; similarly, the boundaries of the electrolyte, cathode, and current collector domains are given by $\partial\Omega_e = \partial\Omega_e^A \cup \Gamma_a^e \cup \Gamma_e^c$, $\partial\Omega_c = \partial\Omega_c^A \cup \Gamma_e^c \cup \Gamma_c^{cc}$, and $\partial\Omega_{cc} = \partial\Omega_{cc}^A \cup \partial\Omega_{cc}^B \cup \Gamma_c^{cc}$, respectively, as illustrated in Figure 4.3. Although the modeling framework allows for a distinction between electrolyte regions such as the separator and the porous cathode, a single electrolyte phase is considered in this study—defined as $\Omega_e = \Omega_e^s \cup \Omega_e^c$—to avoid unnecessary notational complexity without significant gain in physical insight.

4.3 The concept of balance laws in an abstract context

The concept of balance laws is presented in an abstract context. The problem at hand will be specifically addressed in Section 4.4. As customary for multi-component systems, we consider an abstract entity embedded in the solid or liquid, called network, which allows the definitions of displacements and strains [325]. In the context of this work, the small displacement theory is deemed to be adequate.

4.3.1 Conservation of moving species

We consider a mobile species α, characterized by its molar concentration, $c_\alpha\ (\vec{x}, t)$,which gives the number of moles per unit volume at position $\vec{x}$ and time t. For any subregion $\mathcal{V} \subset \mathcal{B}$, where $\mathcal{B}$ denotes the body under consideration, the amount of this species may change in time due to (i) transport across the boundary $\partial\mathcal{V}$ and (ii) volumetric production (or consumption) within $\mathcal{V}$. The initial contribution entails the projection of a flux

vector, $\vec{h}_\alpha(x,t)$,taken positive in the direction of the outward unit normal $\vec{n}$ on $\partial\mathcal{V}$. The subsequent addition introduces a species supply rate, $s_\alpha(x,t)$, indicating the quantity of moles per unit volume per unit time. The conservation laws of species exist in both global and local forms as follows:

$$\frac{d}{dt}\int_{\mathcal{V}} c_\alpha \,\mathrm{d}\Omega = -\int_{\partial\mathcal{V}} \vec{h}_\alpha \cdot \vec{n}\,\mathrm{d}\Gamma + \int_{\mathcal{V}} s_\alpha \,\mathrm{d}\Omega \tag{4.1}$$

and

$$\frac{\partial c_\alpha}{\partial t} + \nabla \cdot \left[\vec{h}_\alpha\right] = s_\alpha. \tag{4.2}$$

4.3.2 Electro-quasistatic approximation of Maxwell's equations

The problem at hand pertains to the application of Maxwell's equations in relation to charged species. In this context, we will use the electro-quasistatic (EQS) model instead of the complete set of Maxwell's equations [249]. This decision offers the main advantage of substituting the hyperbolic representation of Maxwell's equations with a more straightforward parabolic problem, as highlighted in [326]. Obtaining the EQS model is a straightforward process that involves disregarding the time derivative of the magnetic field $\vec{B}(\vec{x},t)$ in Maxwell's equations, resulting in the expression [326], as follows:

$$\nabla \cdot \left[\vec{D}\right] = \xi, \tag{4.3a}$$

$$\mathrm{curl}\left[\vec{H}\right] = \frac{\partial \vec{D}}{\partial t} + \vec{i}, \tag{4.3b}$$

$$\nabla \cdot \left[\vec{B}\right] = 0, \tag{4.3c}$$

$$\mathrm{curl}\left[\vec{E}\right] = \vec{0}. \tag{4.3d}$$

where $\vec{D}$ electric displacement field, ξ the charge density, $\vec{H}$ magnetizing field, $\vec{i}$ current density, $\vec{B}$ magnetic field, and $\vec{E}$ electric fields was presented. Equations (4.3a), and (4.3b) align with the initial set of Maxwell's equations [327], indicating that the local form of charge conservation remains applicable within the EQS model

$$\frac{\partial \xi}{\partial t} = -\nabla \cdot \left[\vec{i}\right]. \tag{4.4}$$

On the other hand, equations (4.3c) and (4.3d) deviate from Maxwell's equations as they do not take into account electromagnetic induction. The magnetic field remains solenoidal, whereas the electric field has transitioned to an irrotational state. The latter enables the representation of the electromagnetic field to be written in terms of an electric potential $\phi(\vec{x},t)$, as opposed to the simultaneous consideration of both electric and magnetic potentials $\vec{A}(\vec{x},t)$, as observed in the genuine electromagnetic problem.

$$\vec{E} = -\nabla\left[\phi\right]. \tag{4.5}$$

The relationship between the first and second sets of the EQS approximation is established through the constitutive laws,

$$\vec{D} = \text{ɬ}_0\vec{E} + \vec{P}, \tag{4.6a}$$

$$\vec{H} = \text{ɬ}_0^{-1}\vec{B} - \vec{M}. \tag{4.6b}$$

wherein $\vec{P}$ and $\vec{M}$ represent the polarization and magnetization fields, accordingly. Additionally, $\not{\epsilon}_0$ and $\not{\mu}_0$ denote universal constants which are not negative [327]. Utilizing the Helmholtz decomposition theorem enables the analysis of the divergence of the electric field, facilitating the determination of its evolution. The differential equation derived from (4.6a) can be computed by applying the divergence operator to (4.3b) in the following manner:

$$\nabla \cdot \left[\frac{\partial \vec{D}}{\partial t} + \vec{i} \right] = 0, \tag{4.7}$$

It is important to note that the EQS approximation does not take into account the magnetic contribution to the Lorentz, as explained in [326]. Consequently, the Lorentz force per unit of volume is measured as follows:

$$\vec{b}_\xi = \xi \vec{E}. \tag{4.8}$$

Based on equations (4.6a), (4.7), (4.8) and, it can be concluded that the magnetic field does not have an impact on the development of the electric field and the Lorentz force, provided that $\vec{P}$ is independent of $\vec{B}$. This pertains to linear, isotropic, homogeneous dielectric materials, wherein the expression for $\vec{P}$ is commonly denoted as

$$\vec{P} = \not{\epsilon}_0 \, \lambda \, \vec{E}. \tag{4.9}$$

where λ is a constant and represents electric susceptibility. By employing this approach, the constitutive description of the electric displacement is obtained as follows:

$$\vec{D} = \not{\epsilon}_0 \not{\epsilon}_r \, \vec{E}, \tag{4.10}$$

where

$$\not{\epsilon}_r = (1 + \lambda), \tag{4.11}$$

and it is called relative permittivity. Equation (4.10) will serve as the constitutive relation for the electric displacement field in the electrolyte solution in Section 4.6.1. In the present scenario, the existence of a magnetic field is acknowledged, yet its impact is negligible.

4.3.3 Faraday's Law

Ions that have dissolved are responsible for the transportation of charges in the electrolyte solution. Hence, the charge density ξ is directly linked to the ion concentration through the given equation

$$\xi = F \sum_\alpha z_\alpha c_\alpha \tag{4.12}$$

The value of F is 96485.3383. Faraday's constant, denoted as C mol^{-1}, represents the magnitude of electric charge per mole. The valency of ion α, symbolised as z_α, is commonly $+1$ for Li^+ ions and -1 for X^- ions. The flux of mass in balance of species (4.2) incorporates to an electric current density in the electrolyte $\vec{i}$ according to Faraday's law of electrolysis

$$\vec{i} = F \sum_\alpha z_\alpha h_\alpha. \tag{4.13}$$

4.3.4 Balance of momentum

The local forms of the balance laws for linear and angular momentum are summarized here. In line with the standard treatment in the literature [328], the balance of linear momentum is adopted in its quasistatic form, because electro-diffusive processes evolve on a much slower time scale than the mechanical deformation of the body,

$$\nabla \cdot [\boldsymbol{\sigma}] + \vec{b} = \vec{0}, \qquad \boldsymbol{\sigma} = \boldsymbol{\sigma}^T. \tag{4.14}$$

Here $\boldsymbol{\sigma}(\vec{x}, t)$ denotes the Cauchy stress tensor and $\vec{b}(\vec{x}, t)$ represents the body force per unit current volume, collecting contact forces and non-local (action-at-a-distance) contributions such as gravity and electromagnetic forces. As argued in [249], the Lorentz contribution $\vec{b}_\xi = (\vec{E} + \vec{v} \times \vec{B})$, is negligible with respect to other mechanical effects, because charge separation in both the active particles and the electrolyte can be ignored. Under the electroneutrality assumption, the mechanical and electrical fields therefore decouple in the momentum balance (4.14), which reduces to a homogeneous equation when mechanical body forces are absent.

4.4 Balance Laws

4.4.1 Balance equations for the electrolyte

In the context of generality, it is assumed that the battery cell consists of a binary electrolyte, wherein a binary salt, such as LiX, is dissolved in an organic solvent, such as a polymer. Once the binary salt LiX has fully dissociated, the electrolyte is identified by the existence of ionic species Li^+ and X^-. It is important to note that balance laws remain unchanged regardless of saturation levels. This implies a complete dissociation of the binary salt in solution, without any additional supply of species. As a result of that, s_α is taken equal to zero. In the electrolyte, Equation (4.2) is applicable to ions Li^+ and X^-, meaning that it is relevant and valid for those specific ions as follows

$$\frac{\partial c_{\mathrm{Li}^+}}{\partial t} + \nabla \cdot \left[\vec{h}_{\mathrm{Li}^+}\right] = 0, \tag{4.15a}$$

$$\frac{\partial c_{\mathrm{X}^-}}{\partial t} + \nabla \cdot \left[\vec{h}_{\mathrm{X}^-}\right] = 0. \tag{4.15b}$$

In accordance with the EQS approximation, the electric displacement field (referred to as $\vec{D}_e$ in the electrolyte) is governed by the following rate equation

$$\nabla \cdot \left[\frac{\partial \vec{D}_e}{\partial t} + \vec{i}_e\right] = 0. \tag{4.16}$$

Inertia effects and non-electrostatic bulk forces are not taken into consideration. Based on the electroneutrality, it can be deduced that electrostatic forces possess a secondary order. Therefore, the overall balance of momentum given in Equation (4.14) is defined for the electrolyte as

$$\nabla \cdot [\boldsymbol{\sigma}_e] = \vec{0}, \qquad \boldsymbol{\sigma_e} = \boldsymbol{\sigma_e}^T. \tag{4.17}$$

4.4.2 Balance equations for the cathode

Electrode particles are classified as either active or storage, depending on whether lithium ions can be inserted into or extracted from the particle. In our model, we neglect conductive additives (e.g., carbon black) and polymeric binders, and represent the cathode exclusively by active particles. Conservation of moving lithium ions in the cathode is guaranteed by following equation [1]

$$\frac{\partial c_{\mathrm{Li}^{\oplus}}}{\partial t} + \nabla \cdot \left[\vec{h}_{\mathrm{Li}^{\oplus}}\right] = 0. \tag{4.18}$$

In order to represent the movement of electrons within the cathode, Ohm's law is employed in various publications [254, 260]. In alignment with previous studies, it is also incorporated into the current model, resulting in the following expression:

$$\nabla \cdot \left[\vec{i}_c\right] = 0. \tag{4.19}$$

The expression of the balance of momentum for the cathode is identical to that of the electrolyte and it is given as

$$\nabla \cdot [\boldsymbol{\sigma}_c] = \vec{0}, \qquad \boldsymbol{\sigma}_c = \boldsymbol{\sigma}_c^T. \tag{4.20}$$

where $\boldsymbol{\sigma}_c$ denotes the Cauchy stress at the cathode.

4.4.3 Balance equations for the foils

A unified notation is adopted for the metallic foils, namely the lithium foil anode (a) and the aluminum foil current collector (cc), collectively denoted by $f \in \{a, cc\}$ is used here to avoid repetition. When a specific foil is intended, we write $f = a$ for the anode and $f = cc$ for the current collector. A similar procedure to that formulated for the cathode is followed, so two balance equations which are the local form of charge conservation and balance of momentum derived for the foils in the absence of concentration change are written as follows: The local form of charge conservation yields,

$$\nabla \cdot \left[\vec{i}_f\right] = 0. \tag{4.21}$$

where $\vec{i}_f$ denotes the current density in the foils. The expression of the balance of momentum for the foils is identical way to that of the electrolyte and the cathode and it is given as

$$\nabla \cdot [\boldsymbol{\sigma}_f] = \vec{0}, \qquad \boldsymbol{\sigma}_f = \boldsymbol{\sigma}_f^T. \tag{4.22}$$

where $\boldsymbol{\sigma}_f$ indicates the Cauchy stress at the foils.

4.5 Thermodynamics

4.5.1 Thermodynamics: electrolyte

4.5.1.1 Energy balance

The relationship between the internal energy $\mathcal{U}$ of a material region $\mathcal{V}$, the external mechanical power $\mathcal{W}_r$ applied to $\mathcal{V}$, the heat transmitted $\mathcal{Q}_r$ in $\mathcal{V}$, and the power resulting

[1] To avoid notational confusion, lithium ions dissolved in the cathode active particles are denoted by the symbol $\mathrm{Li}^{\oplus}$ instead of Li^{+}.

from mass $\mathcal{T}_r$ and electromagnetic $\mathcal{E}_r$ interactions exchanged in $\mathcal{V}$ for the given situation, which involves quasistatic interactions, is as follows,

$$\frac{d\mathcal{U}}{dt}(\mathcal{V}) = \mathcal{W}_r(\mathcal{V}) + \mathcal{Q}_r(\mathcal{V}) + \mathcal{T}_r(\mathcal{V}) + \mathcal{E}_r(\mathcal{V}), \tag{4.23}$$

These processes are believed to occur independently and make unique contributions to the overall balance. Specifically, the energy resulting from charges and mass transfer are treated as separate processes and added together. The specific contributions made by each individual are:
i) There is a mechanical contribution caused by the body forces $\vec{b}$ and surface forces $\vec{p}$ that exert power against velocities $\vec{v}$,

$$\mathcal{W}_r(\mathcal{V}) = \int_{\mathcal{V}} \vec{b} \cdot \vec{v}\, \mathrm{d}\Omega_e + \int_{\partial\mathcal{V}} \vec{p} \cdot \vec{v}\, \mathrm{d}\Gamma, \tag{4.24}$$

ii) the heat contrubiton in which the scalar s_q denotes the heat provided by external sources and $\vec{q}$ denotes the heat flux vector:

$$\mathcal{Q}_r(\mathcal{V}) = \int_{\mathcal{V}} s_q\, \mathrm{d}\Omega_e - \int_{\partial\mathcal{V}} \vec{q} \cdot \vec{n}\, \mathrm{d}\Gamma, \tag{4.25}$$

iii) The mass flux contribution is represented by the scalar ${}^r\mu_\alpha$, which denotes the chemical potential. The scalar s_α represents the supply of species ($\alpha = \mathrm{Li}^+, \mathrm{X}^-$), and $\vec{h}_\alpha$ denotes the mass flux vector;

$$\mathcal{T}_r(\mathcal{V}) = \sum_\alpha \left(\int_{\mathcal{V}} {}^r\mu_\alpha\, s_\alpha\, \mathrm{d}\Omega_e - \int_{\partial\mathcal{V}} {}^r\mu_\alpha\, \vec{h}_\alpha \cdot \vec{n}\, \mathrm{d}\Gamma \right) \tag{4.26}$$

iv) The electric and magnetizing fields yield an electromagnetic contribution with the energy flux vector $\vec{E}_e \times \vec{H}_e$. The vector product of $\vec{E}_e$ and $\vec{H}_e$ represents an energy flux vector that arises from Poynting's theorem (see to [319], [327] for more information). Poynting's theorem is derived by replacing the curls in Maxwell's equations.

$$\mathcal{E}_r(\mathcal{V}) = -\int_{\partial\mathcal{V}} (\vec{E}_e \times \vec{H}_e) \cdot \vec{n}\, \mathrm{d}\Gamma = \int_{\mathcal{V}} \vec{H}_e \cdot \mathrm{curl}\left[\vec{E}_e\right] - \mathrm{curl}\left[\vec{H}_e\right] \cdot \vec{E}_e\, \mathrm{d}\Omega_\mathrm{e} \tag{4.27}$$

An internal energy r, which is specified per unit volume in the reference body (refer to [320]), is commonly defined as

$$\mathcal{U}(\mathcal{V}) = \int_{\mathcal{V}} r\, \mathrm{d}\Omega_\mathrm{e}, \tag{4.28}$$

to express the first law of thermodynamics in its local form. By using the divergence theorem and mass balances (4.2), the following outcome in equations can be derived (4.24) to (4.27):

$$\mathcal{W}_r(\mathcal{V}) = \int_{\mathcal{V}} \boldsymbol{\sigma}_e : \frac{\partial \boldsymbol{\varepsilon}_e}{\partial t}\, \mathrm{d}\Omega_\mathrm{e}, \tag{4.29a}$$

$$\mathcal{Q}_r(\mathcal{V}) = \int_{\mathcal{V}} s_q - \nabla \cdot [\vec{q}]\, \mathrm{d}\Omega_\mathrm{e}, \tag{4.29b}$$

$$\mathcal{T}_r(\mathcal{V}) = \sum_\alpha \int_{\mathcal{V}} {}^r\mu_\alpha \frac{\partial c_\alpha}{\partial t} - \vec{h}_\alpha \cdot \nabla[{}^r\mu_\alpha]\, \mathrm{d}\Omega_\mathrm{e}, \tag{4.29c}$$

$$\mathcal{E}_r(\mathcal{V}) = \int_{\mathcal{V}} \left(\frac{\partial \vec{D}_e}{\partial t} + \vec{i}_e \right) \cdot \vec{E}_e\, \mathrm{d}\Omega_\mathrm{e} \tag{4.29d}$$

In accordance with the principles of electro-quasistatics and Ampere-Maxwell's law (4.3b), the electromagnetic contribution (4.29d) is derived. The first law of thermodynamics can therefore be expressed as follows:

$$\int_{\mathcal{V}} \frac{\mathrm{d}r}{\mathrm{d}t}\,\mathrm{d}\Omega_\mathrm{e} = \int_{\mathcal{V}} \boldsymbol{\sigma_e} : \frac{\partial \boldsymbol{\varepsilon}_e}{\partial t} + s_q - \nabla\cdot[\vec{q}] + \left(\frac{\partial \vec{D}_e}{\partial t} + \vec{i}_e\right)\cdot\vec{E}_e + \sum_\alpha {}^r\mu_\alpha \frac{\partial c_\alpha}{\partial t} - \vec{h}_\alpha\cdot\nabla[{}^r\mu_\alpha]\,\mathrm{d}\Omega_\mathrm{e} \tag{4.30}$$

Since the region $\mathcal{V}$ is arbitrary, the relation must be valid for any such domain. The local form of the first law can therefore be written as:

$$\frac{\mathrm{d}r}{\mathrm{d}t} = \boldsymbol{\sigma_e} : \frac{\partial \boldsymbol{\varepsilon}_e}{\partial t} + s_q - \nabla\cdot[\vec{q}] + \left(\frac{\partial \vec{D}_e}{\partial t} + \vec{i}_e\right)\cdot\vec{E}_e + \sum_\alpha {}^r\mu_\alpha \frac{\partial c_\alpha}{\partial t} - \vec{h}_\alpha\cdot\nabla[{}^r\mu_\alpha] \tag{4.31}$$

The internal energy is expressed as a function of the state variables. These state variables include the concentrations c_α, the electric displacement field $\vec{D}_e$, and the kinematic variables represented by the small strain tensor $\boldsymbol{\varepsilon}_e$.

4.5.1.2 Entropy imbalance

The second law of thermodynamics concerns the equilibrium between the internal entropy of a system $\mathcal{V}$ and the entropy changes resulting from mass and heat transfer within $\mathcal{V}$. When considering quasistatic interactions, the entropy balance equation for the problem in hand is formulated as follows:

$$\frac{d\mathcal{S}}{dt}(\mathcal{V}) - \frac{d\mathcal{S}_{int}}{dt}(\mathcal{V}) = \mathcal{Q}_\eta + \mathcal{T}_\eta, \tag{4.32}$$

where $\mathcal{S}$ represents the net internal entropy of system $\mathcal{V}$, S_{int} denotes the entropy originating from internal processes within $\mathcal{V}$, $\mathcal{Q}_\eta$ represents the rate of entropy production due to heat transfer per unit time, and $\mathcal{T}_\eta$ signifies the rate of entropy generation per unit time due to mass transfer. The assertion that equation (4.32) arises from the non-trivial assumption implies that mechanics does not play a direct role in determining the overall entropy flow within the entropy balance equation. $\mathcal{Q}_\eta$ and $\mathcal{T}_\eta$ are defined as follows:

$$\mathcal{Q}_\eta(\mathcal{V}) = \int_{\mathcal{V}} \frac{s_q}{T}\,\mathrm{d}\Omega_\mathrm{e} - \int_{\partial\mathcal{V}} \frac{\vec{q}}{T}\cdot\vec{n}\,\mathrm{d}\Gamma, \tag{4.33a}$$

$$\mathcal{T}_\eta(\mathcal{V}) = \sum_\alpha \int_{\mathcal{V}} {}^\eta\mu_\alpha \frac{\partial c_\alpha}{\partial t} - \vec{h}_\alpha\cdot\nabla[{}^\eta\mu_\alpha]\,\mathrm{d}\Omega_\mathrm{e}, \tag{4.33b}$$

The symbol ${}^\eta\mu_\alpha$ represents the variation in specific entropy resulting from the providing of a unit quantity of moles of species $\alpha = \mathrm{Li}^+$, and X^-. The second principle of thermodynamics declares that

$$\frac{\mathrm{d}\mathcal{S}_\mathrm{int}}{\mathrm{d}t}(\mathcal{V}) \geq 0, \tag{4.34}$$

The specific internal entropy can be employed on a per-unit-volume basis, and denoted as η as follows:

$$\mathcal{S}(\mathcal{V}) = \int_{\mathcal{V}} \eta\,\mathrm{d}\Omega_\mathrm{e}. \tag{4.35}$$

During small displacements, it is possible to define specific internal entropy either per unit mass or per unit volume, as neither mass nor volume undergo changes throughout

the process. Here, the decision is made to define it on a per-unit-volume basis. In the absence of supply of species, standard application of the divergence theorem on local form of mass balances (4.2) leads from (4.33) to

$$\frac{\mathrm{d}}{\mathrm{d}t}\int_{\mathcal{V}} \eta \, d\Omega_e + \int_{\mathcal{V}} -\frac{s_q}{T} + \nabla\cdot\left[\frac{\vec{q}}{T}\right] - \sum_{\alpha} {}^{\eta}\mu_{\alpha}\frac{\partial c_{\alpha}}{\partial t} + \vec{h}_{\alpha}\cdot\nabla\left[{}^{\eta}\mu_{\alpha}\right]\mathrm{d}\Omega_{\mathrm{e}} \geq 0. \tag{4.36}$$

By acknowledging that

$$\nabla\cdot\left[\frac{\vec{q}}{T}\right] = \frac{1}{T}\nabla\cdot[\vec{q}] - \frac{1}{T^2}\vec{q}\cdot\nabla\left[T\right], \tag{4.37}$$

After multiplying by temperature T, the entropy imbalance can be reformulated in terms of internal energy by leveraging the properties of identity (4.31) and the sign definiteness of temperature

$$\begin{aligned}\int_{\mathcal{V}} T\frac{\mathrm{d}\eta}{\mathrm{d}t} - \frac{1}{T}\vec{q}\cdot\nabla\left[T\right] \; - T\sum_{\alpha} \; {}^{\eta}\mu_{\alpha}\frac{\partial c_{\alpha}}{\partial t} + T\sum_{\alpha}\vec{h}_{\alpha}\cdot\nabla\left[{}^{\eta}\mu_{\alpha}\right] \; \mathrm{d}\Omega_{\mathrm{e}} + \\ -\int_{\mathcal{V}} \frac{\mathrm{d}r}{\mathrm{d}t} - \boldsymbol{\sigma_e} : \frac{\partial \boldsymbol{\varepsilon}_e}{\partial t} + \left(\frac{\partial \vec{D}_e}{\partial t} + \vec{i}_e\right)\cdot\vec{E}_e - \sum_{\alpha} {}^{r}\mu_{\alpha}\frac{\partial c_{\alpha}}{\partial t} + \sum_{\alpha}\vec{h}_{\alpha}\cdot\nabla\left[{}^{r}\mu_{\alpha}\right] \; \mathrm{d}\Omega_{\mathrm{e}} \geq 0\end{aligned} \tag{4.38}$$

Knowing that the chemical potential of the species Li^+, and X^- are denoted μ_{α}, the quantity becomes

$$\mu_{\alpha} = {}^{r}\mu_{\alpha} - T\,{}^{\eta}\mu_{\alpha}, \tag{4.39}$$

in order to write the entropy imbalance as

$$\begin{aligned}\int_{\mathcal{V}} T\frac{\mathrm{d}\eta}{\mathrm{d}t} - \frac{\mathrm{d}r}{dt} - \frac{1}{T}\vec{q}\cdot\nabla\left[T\right] \; + \sum_{\alpha}\mu_{\alpha}\frac{\partial c_{\alpha}}{\partial t} + \boldsymbol{\sigma_e} : \frac{\partial \boldsymbol{\varepsilon}_e}{\partial t} + \left(\frac{\partial \vec{D}_e}{\partial t} + \vec{i}_e\right)\cdot\vec{E}_e \\ -\sum_{\alpha}\vec{h}_{\alpha}\cdot\nabla\left[\mu_{\alpha}\right] - \sum_{\alpha} {}^{\eta}\mu_{\alpha}\,\vec{h}_{\alpha}\cdot\nabla\left[T\right] \; \mathrm{d}\Omega_e \geq 0.\end{aligned} \tag{4.40}$$

In accordance with the framework proposed in [319], a redefined heat flux is introduced as

$$\vec{\bar{q}} = \vec{q} + T\sum_{\alpha} {}^{\eta}\mu_{\alpha}\,\vec{h}_{\alpha}, \tag{4.41}$$

can be defined, where the term $T\sum_{\alpha}{}^{\eta}\mu_{\alpha}\vec{h}_{\alpha}$ accounts for the heat transported by the diffusion of species such as Li^+, X^- in the electrolyte. The modified heat flux $\vec{\bar{q}}$ thus serves as the thermodynamic force conjugate to the temperature gradient, i.e.

$$\begin{aligned}\int_{\mathcal{V}} T\frac{\mathrm{d}\eta}{\mathrm{d}t} - \frac{\mathrm{d}r}{\mathrm{d}t} + \sum_{\alpha}\mu_{\alpha}\frac{\partial c_{\alpha}}{\partial t} + \boldsymbol{\sigma_e} : \frac{\partial \boldsymbol{\varepsilon}_e}{\partial t} + \left(\frac{\partial \vec{D}_e}{\partial t} + \vec{i}_e\right)\cdot\vec{E}_e \; \mathrm{d}\Omega_e + \\ + \int_{\mathcal{V}} -\frac{1}{T}\vec{\bar{q}}\cdot\nabla\left[T\right] \; - \sum_{\alpha}\vec{h}_{\alpha}\cdot\nabla\left[\mu_{\alpha}\right] \; \mathrm{d}\Omega_e \geq 0.\end{aligned} \tag{4.42}$$

4.5.1.3 Helmholtz free energy

Alternative thermodynamic potentials beyond internal energy u can be explored. The specific Helmholtz free energy that is denoted as ψ_e for the electrolyte, is defined as follows and will be employed from this point forward.

$$\psi_e = r - T\eta. \tag{4.43}$$

Consequently, by incorporating following equation,

$$T\frac{\mathrm{d}\eta}{\mathrm{d}t} - \frac{\mathrm{d}r}{\mathrm{d}t} = -\frac{\mathrm{d}\psi_e}{\mathrm{d}t} - \eta\frac{\partial T}{\partial t} \tag{4.44}$$

into equation (4.42), the entropy imbalance can be derived in its final form

$$\begin{aligned}\int_{\mathcal{V}} -\frac{\mathrm{d}\psi_e}{\mathrm{d}t} - \eta\frac{\partial T}{\partial t} + \sum_\alpha \mu_\alpha \frac{\partial c_\alpha}{\partial t} + \boldsymbol{\sigma_e} : \frac{\partial \boldsymbol{\varepsilon}_e}{\partial t} + \left(\frac{\partial \vec{D}_e}{\partial t} + \vec{i}_e\right)\cdot\vec{E}_e + \\ -\frac{1}{T}\vec{q}\cdot\nabla\left[T\right] - \sum_\alpha \vec{h}_\alpha\cdot\nabla\left[\mu_\alpha\right]\mathrm{d}\Omega_e \geq 0.\end{aligned} \tag{4.45}$$

Considering the functional dependence of the free energy as stated, its total derivative with respect to time is expressed as follows:

$$\frac{\mathrm{d}\psi_e}{\mathrm{d}t} = \frac{\partial\psi_e}{\partial T}\frac{\partial T}{\partial t} + \frac{\partial\psi_e}{\partial\boldsymbol{\varepsilon}_e} : \frac{\partial\boldsymbol{\varepsilon}_e}{\partial t} + \frac{\partial\psi_e}{\partial\vec{D}_e}\cdot\frac{\partial\vec{D}_e}{\partial t} + \sum_\alpha \frac{\partial\psi_e}{\partial c_\alpha}\frac{\partial c_\alpha}{\partial t}. \tag{4.46}$$

4.5.1.4 Thermodynamic restrictions

The inequality (4.45) becomes

$$\begin{aligned}\int_{\mathcal{V}} -\frac{\partial\psi_e}{\partial T}\frac{\partial T}{\partial t} - \frac{\partial\psi_e}{\partial\boldsymbol{\varepsilon}_e} : \frac{\partial\boldsymbol{\varepsilon}_e}{\partial t} - \frac{\partial\psi_e}{\partial\vec{D}_e}\cdot\frac{\partial\vec{D}_e}{\partial t} - \frac{\partial\psi_e}{\partial c_\alpha}\frac{\partial c_\alpha}{\partial t} - \eta\frac{\partial T}{\partial t} + \sum_\alpha \mu_\alpha\frac{\partial c_\alpha}{\partial t} + \\ \boldsymbol{\sigma_e} : \frac{\partial\boldsymbol{\varepsilon}_e}{\partial t} + \left(\frac{\partial\vec{D}_e}{\partial t} + \vec{i}_e\right)\cdot\vec{E}_e - \sum_\alpha \vec{h}_\alpha\cdot\nabla\left[\mu_\alpha\right] - \frac{1}{T}\vec{q}\cdot\nabla\left[T\right]d\Omega \geq 0,\end{aligned} \tag{4.47}$$

and must hold for any region $\mathcal{V}$, since the latter was arbitrarily chosen. Hence, the following local entropy imbalance, commonly referred to as the Clausius-Duhem inequality, yields

$$\begin{aligned}\frac{\partial T}{\partial t}\left(-\eta - \frac{\partial\psi_e}{\partial T}\right) + \frac{\partial\boldsymbol{\varepsilon}_e}{\partial t} : \left(\boldsymbol{\sigma}_e - \frac{\partial\psi_e}{\partial\boldsymbol{\varepsilon}_e}\right) + \sum_\alpha \frac{\partial c_\alpha}{\partial t}\left(\mu_\alpha - \frac{\partial\psi_e}{\partial c_\alpha}\right) + \\ \frac{\partial\vec{D}_e}{\partial t}\left(\vec{E}_e - \frac{\partial\psi_e}{\partial\vec{D}_e}\right) + \vec{i}_e\cdot\vec{E}_e - \frac{1}{T}\vec{q}\cdot\nabla\left[T\right] - \sum_\alpha \vec{h}_\alpha\cdot\nabla\left[\mu_\alpha\right] \geq 0.\end{aligned} \tag{4.48}$$

Clausius-Duhem ineqeuality given in equation (4.48) is expressed in terms of the electrochemical potential, which is defined as:

$$\overline{\mu}_\alpha = \mu_\alpha + F z_\alpha \phi_e \tag{4.49}$$

The term $\vec{i}_e \cdot \vec{E}_e$ represents the Joule effect. Based on Faraday's law, straightforward algebraic manipulation yields:

$$\vec{i}_e \cdot \vec{E}_e - \sum_\alpha \vec{h}_\alpha \cdot \nabla [\mu_\alpha] = -\sum_\alpha \vec{h}_\alpha \cdot \nabla [\overline{\mu}_\alpha] \tag{4.50}$$

taking equation (4.49) into account. By reformulating the equation (4.48) for the speicies ($\alpha = \mathrm{Li}^+, \mathrm{X}^-$), the final form of the Clauisus-Duhem inequality for the electrolyte is obtained as follows:

$$\begin{aligned}\frac{\partial T}{\partial t}\left(-\eta - \frac{\partial \psi_e}{\partial T}\right) + \frac{\partial \boldsymbol{\varepsilon}_e}{\partial t} : \left(\boldsymbol{\sigma}_e - \frac{\partial \psi_e}{\partial \boldsymbol{\varepsilon}_e}\right) + \frac{\partial c_{\mathrm{Li}^+}}{\partial t}\left(\mu_{\mathrm{Li}^+} - \frac{\partial \psi_e}{\partial c_{\mathrm{Li}^+}}\right) + \frac{\partial c_{\mathrm{X}^-}}{\partial t}\left(\mu_{\mathrm{X}^-} - \frac{\partial \psi_e}{\partial c_{\mathrm{X}^-}}\right) \\ + \frac{\partial \vec{D}_e}{\partial t} \cdot \left(\vec{E}_e - \frac{\partial \psi_e}{\partial \vec{D}_e}\right) - \frac{1}{T}\vec{q} \cdot \nabla [T] - \vec{h}_{\mathrm{Li}^+} \cdot \nabla [\overline{\mu}_{\mathrm{Li}^+}] - \vec{h}_{\mathrm{X}^-} \cdot \nabla [\overline{\mu}_{\mathrm{X}^-}] \geq 0\end{aligned} \tag{4.51}$$

The inequality is required to remain valid regardless of the values taken by the time derivative of temperature T, concentrations c_{Li^+} and c_{X^-}, strain tensor $\boldsymbol{\varepsilon}$, and electric field $\vec{E}$. Given their linear representation within the inequality, the coefficients accompanying them must be set to zero. Failure to do so would potentially allow for the identification of time derivative values that result in a violation of the stated inequality. Through the application of the Coleman-Noll procedure, it is imperative that inequality (4.51) maintains validity across all constitutive processes [320, 322], thereby imposing the subsequent thermodynamic constraints.

$$\begin{aligned}\eta + \frac{\partial \psi_e}{\partial T} = 0,\ \boldsymbol{\sigma}_e - \frac{\partial \psi_e}{\partial \boldsymbol{\varepsilon}_e} = 0,\ \mu_{\mathrm{Li}^+} - \frac{\partial \psi_e}{\partial c_{\mathrm{Li}^+}} = 0,\ \mu_{\mathrm{X}^-} - \frac{\partial \psi_e}{\partial c_{\mathrm{X}^-}} = 0,\ \vec{E}_e - \frac{\partial \psi_e}{\partial \vec{D}_e} = 0, \\ \frac{1}{T}\vec{q} \cdot \nabla [T] \leq 0,\ \vec{h}_{\mathrm{Li}^+} \cdot \nabla [\overline{\mu}_{\mathrm{Li}^+}] \leq 0,\ \vec{h}_{\mathrm{X}^-} \cdot \nabla [\overline{\mu}_{\mathrm{X}^-}] \leq 0.\end{aligned} \tag{4.52}$$

Given the state of thermodynamic equilibrium, the consideration of entropy as a function of temperature is omitted. The thermodynamic restrictions are outlined as follows:

$$\begin{aligned}\boldsymbol{\sigma}_e - \frac{\partial \psi_e}{\partial \boldsymbol{\varepsilon}_e} = 0,\ \mu_{\mathrm{Li}^+} - \frac{\partial \psi_e}{\partial c_{\mathrm{Li}^+}} = 0,\ \mu_{\mathrm{X}^-} - \frac{\partial \psi_e}{\partial c_{\mathrm{X}^-}} = 0, \\ \vec{E}_e - \frac{\partial \psi_e}{\partial \vec{D}_e} = 0,\ \vec{h}_{\mathrm{Li}^+} \cdot \nabla [\overline{\mu}_{\mathrm{Li}^+}] \leq 0,\ \vec{h}_{\mathrm{X}^-} \cdot \nabla [\overline{\mu}_{\mathrm{X}^-}] \leq 0.\end{aligned} \tag{4.53}$$

4.5.2 Thermodynamics: cathode

4.5.2.1 Energy balance

Energy balance equation (4.23) described for the electrolyte is also applicable to the cathode with minor changes. In the context of cathode, material region $\mathcal{V}$ now specifically denotes the active materials. Consequently, it continues to investigate the interactions that are energetically characterized by equations (4.29a), (4.29b), (4.29c), and (4.29d). Power $\mathcal{T}_r(\mathcal{V})$ arises from the mass transfer of neutral Lithium under reduction at the interface prior to intercalation. The power $\mathcal{E}_r(\mathcal{V})$ generated by electromagnetic interactions is a result of the movement of electrons in the active particles, which are assumed to be conductive materials. Hence, The essential distinction, therefore, is that mass transport

and charge transport are carried by two different species. The equation (4.29c) pertains to an only one species

$$\mathcal{T}_r(\mathcal{V}) = \int_{\mathcal{V}} {}^r\mu_{\mathrm{Li}^\oplus} \frac{\partial c_{\mathrm{Li}^\oplus}}{\partial t} - \vec{h}_{\mathrm{Li}^\oplus} \cdot \nabla \left[{}^r\mu_{\mathrm{Li}^\oplus} \right] \, \mathrm{d}\Omega_\mathrm{c} \tag{4.54}$$

and Ampère's-Maxwell's law (4.29d) can be simplified as

$$\mathcal{E}_r(\mathcal{V}) = \int_{\mathcal{V}} \vec{i}_c \cdot \vec{E}_c \, \mathrm{d}\Omega_\mathrm{c} \tag{4.55}$$

which leads to the following form of the first law of thermodynamics

$$\int_{\mathcal{V}} \frac{\mathrm{d}r}{\mathrm{d}t} \, \mathrm{d}\Omega_\mathrm{c} = \int_{\mathcal{V}} \boldsymbol{\sigma_c} : \frac{\partial \boldsymbol{\varepsilon}_c}{\partial t} + s_q - \nabla \cdot [\vec{q}] + \vec{i}_c \cdot \vec{E}_c + {}^r\mu_{\mathrm{Li}^\oplus} \frac{\partial c_{\mathrm{Li}^\oplus}}{\partial t} - \vec{h}_{\mathrm{Li}^\oplus} \cdot \nabla [{}^r\mu_{\mathrm{Li}^\oplus}] \, \mathrm{d}\Omega_\mathrm{c}. \tag{4.56}$$

This yields the following local form of the energy balance equation in the cathode:

$$\frac{\mathrm{d}r}{\mathrm{d}t} = \boldsymbol{\sigma_c} : \frac{\partial \boldsymbol{\varepsilon}_c}{\partial t} + s_q - \nabla \cdot [\vec{q}] + \vec{i}_c \cdot \vec{E}_c + {}^r\mu_{\mathrm{Li}^\oplus} \frac{\partial c_{\mathrm{Li}^\oplus}}{\partial t} - \vec{h}_{\mathrm{Li}^\oplus} \cdot \nabla [{}^r\mu_{\mathrm{Li}^\oplus}]. \tag{4.57}$$

4.5.2.2 Entropy imbalance

The entropy balance relation given in equation (3.51) is also applicable to the cathode domain, where the terms $\mathcal{Q}_\eta$ and $\mathcal{T}_\eta$ are defined in accordance with the form presented in equation (4.32). The expressions for the cathode are given below:

$$\mathcal{Q}_\eta(\mathcal{V}) = \int_{\mathcal{V}} \frac{s_q}{T} \, d\Omega_c - \int_{\partial\mathcal{V}} \frac{\vec{q}}{T} \cdot \vec{n} \, d\Gamma, \tag{4.58a}$$

$$\mathcal{T}_\eta(\mathcal{V}) = \int_{\mathcal{V}} {}^\eta\mu_{\mathrm{Li}^\oplus} \frac{\partial c_{\mathrm{Li}^\oplus}}{\partial t} - \vec{h}_{\mathrm{Li}^\oplus} \cdot \nabla [{}^\eta\mu_{\mathrm{Li}^\oplus}] \, \mathrm{d}\Omega_\mathrm{c}. \tag{4.58b}$$

Proceeding analogously to equations (4.34)–(4.37), the entropy imbalance for the cathode can be written as:

$$\begin{aligned} &\int_{\mathcal{V}} T \frac{\mathrm{d}\eta}{\mathrm{d}t} - \frac{1}{T} \vec{q} \cdot \nabla [T] \; - T \, {}^\eta\mu_{\mathrm{Li}^\oplus} \frac{\partial c_{\mathrm{Li}^\oplus}}{\partial t} + T \, \vec{h}_{\mathrm{Li}^\oplus} \cdot \nabla [{}^\eta\mu_{\mathrm{Li}^\oplus}] \, \mathrm{d}\Omega_\mathrm{c} + \\ &- \int_{\mathcal{V}} \frac{\mathrm{d}r}{\mathrm{d}t} - \boldsymbol{\sigma_c} : \frac{\partial \boldsymbol{\varepsilon}_c}{\partial t} + \vec{i}_c \cdot \vec{E}_c - {}^r\mu_{\mathrm{Li}^\oplus} \frac{\partial c_{\mathrm{Li}^\oplus}}{\partial t} + \vec{h}_{\mathrm{Li}^\oplus} \cdot \nabla \left[{}^r\mu_{\mathrm{Li}^\oplus} \right] \, \mathrm{d}\Omega_\mathrm{c} \geq 0. \end{aligned} \tag{4.59}$$

Following the definition of the chemical potential equation (4.39) as expressed in the equation (4.38), and considering of the heat flux equation (4.41) in the electrolyte, the entropy imbalance for the cathode is reformulated as follows:

$$\begin{aligned} \int_{\mathcal{V}} T \frac{\mathrm{d}\eta}{dt} - \frac{\mathrm{d}r}{\mathrm{d}t} + \mu_{\mathrm{Li}^\oplus} \frac{\partial c_{\mathrm{Li}^\oplus}}{\partial t} + \boldsymbol{\sigma}_c : \frac{\partial \boldsymbol{\varepsilon}_c}{\partial t} + \vec{i}_c \cdot \vec{E}_c + \\ - \frac{1}{T} \vec{q} \cdot \nabla [T] - \vec{h}_{\mathrm{Li}^\oplus} \cdot \nabla \left[\mu_{\mathrm{Li}^\oplus} \right] \mathrm{d}\Omega_\mathrm{c} \geq 0. \end{aligned} \tag{4.60}$$

4.5.2.3 Additive decomposition of strains

Within our model, the cathode total strain $\boldsymbol{\varepsilon}_c$ is defined, following Equation (3.38) (see Section 3.2.4), as:

$$\boldsymbol{\varepsilon}_c = \frac{1}{2} \left(\nabla [\vec{u}_c] + \nabla [\vec{u}_c]^T \right). \tag{4.61}$$

It is additively decomposed into an elastic, recoverable part after unloading, $\boldsymbol{\varepsilon}_c^{el}$, and a swelling contribution, $\boldsymbol{\varepsilon}_c^{sw}$, caused by lithium intercalation in the cathode active material:

$$\boldsymbol{\varepsilon}_c = \boldsymbol{\varepsilon}_c^{el} + \boldsymbol{\varepsilon}_c^{sw}. \tag{4.62}$$

The swelling strain $\boldsymbol{\varepsilon}_c^{sw}$ is assumed to be volumetric and linearly proportional to the deviation $c_{\mathrm{Li}^\oplus} - c_{\mathrm{Li}^\oplus}^0$ from a reference concentration $c_{\mathrm{Li}^\oplus}^0$, through the chemical expansion coefficient $\omega_{\mathrm{Li}^\oplus}$ of species $\mathrm{Li}^\oplus$:

$$\boldsymbol{\varepsilon}_c^{sw} = \omega_{\mathrm{Li}^\oplus}(c_{\mathrm{Li}^\oplus} - c_{\mathrm{Li}^\oplus}^0)\mathbb{I}. \tag{4.63}$$

where $\mathbb{I}$ denotes the identity tensor.

4.5.2.4 Helmholtz free energy

Extending equations (4.43) and (4.44) to the cathode, the entropy imbalance can be written in terms of the Helmholtz free energy ψ_c as:

$$\begin{aligned}\int_{\mathcal{V}} -\frac{\mathrm{d}\psi_\mathrm{c}}{\mathrm{d}t} - \eta\frac{\partial T}{\partial t} + \mu_{\mathrm{Li}^\oplus}\frac{\partial c_{\mathrm{Li}^\oplus}}{\partial t} + \boldsymbol{\sigma_c} : \frac{\partial \boldsymbol{\varepsilon}_c}{\partial t} + \vec{i}_c \cdot \vec{E}_c + \\ -\frac{1}{T}\vec{q}\cdot\nabla\left[T\right] - \vec{h}_{\mathrm{Li}^\oplus}\cdot\nabla\left[\mu_{\mathrm{Li}^\oplus}\right]\mathrm{d}\Omega_\mathrm{c} \geq 0.\end{aligned} \tag{4.64}$$

Based on the specified functional dependence of the free energy, the total derivative with respect to time is given by

$$\frac{\mathrm{d}\psi_\mathrm{c}}{\mathrm{d}t} = \frac{\partial \psi_c}{\partial T}\frac{\partial T}{\partial t} + \frac{\partial \psi_c}{\partial \boldsymbol{\varepsilon}_c} : \frac{\partial \boldsymbol{\varepsilon}_c}{\partial t} + \frac{\partial \psi_c}{\partial c_{\mathrm{Li}^\oplus}}\frac{\partial c_{\mathrm{Li}^\oplus}}{\partial t}. \tag{4.65}$$

4.5.2.5 Thermodynamic restrictions

Considering equation (4.65), the entropy inequality for the cathode can thus be written as:

$$\begin{aligned}\int_{\mathcal{V}} -\frac{\partial \psi_c}{\partial T}\frac{\partial T}{\partial t} - \frac{\partial \psi_c}{\partial \boldsymbol{\varepsilon}_c} : \frac{\partial \boldsymbol{\varepsilon}_c}{\partial t} - \frac{\partial \psi_c}{\partial c_{\mathrm{Li}^\oplus}}\frac{\partial c_{\mathrm{Li}^\oplus}}{\partial t} - \eta\frac{\partial T}{\partial t} + \mu_{\mathrm{Li}^\oplus}\frac{\partial c_{\mathrm{Li}^\oplus}}{\partial t} + \\ \boldsymbol{\sigma_c} : \frac{\partial \boldsymbol{\varepsilon}_c}{\partial t} + \vec{i}_c\cdot\vec{E}_c - \vec{h}_{\mathrm{Li}^\oplus}\cdot\nabla\left[\mu_{\mathrm{Li}^\oplus}\right] - \frac{1}{T}\vec{q}\cdot\nabla\left[T\right]\ \mathrm{d}\Omega_\mathrm{c} \geq 0,\end{aligned} \tag{4.66}$$

and the Clausius-Duhem inequality for the cathode written as follows:

$$\begin{aligned}\frac{\partial T}{\partial t}\left(-\eta - \frac{\partial \psi_c}{\partial T}\right) + \frac{\partial \boldsymbol{\varepsilon}_c}{\partial t} : \left(\boldsymbol{\sigma}_c - \frac{\partial \psi_c}{\partial \boldsymbol{\varepsilon}_c}\right) + \frac{\partial c_{\mathrm{Li}^\oplus}}{\partial t}\left(\mu_{\mathrm{Li}^\oplus} - \frac{\partial \psi_c}{\partial c_{\mathrm{Li}^\oplus}}\right) + \\ +\vec{i}_c\cdot\vec{E}_c - \frac{1}{T}\vec{q}\cdot\nabla\left[T\right] - \vec{h}_{\mathrm{Li}^\oplus}\cdot\nabla\left[\mu_{\mathrm{Li}^\oplus}\right] \geq 0.\end{aligned} \tag{4.67}$$

By applying the Coleman–Noll procedure, inequality (4.67) must be satisfied. This leads to the following thermodynamic restrictions under the assumption of thermodynamic equilibrium and neglecting temperature variations:

$$\boldsymbol{\sigma}_c - \frac{\partial \psi_c}{\partial \boldsymbol{\varepsilon}_c} = 0, \quad \mu_{\mathrm{Li}^\oplus} - \frac{\partial \psi_c}{\partial c_{\mathrm{Li}^\oplus}} = 0, \quad \vec{i}_c\cdot\vec{E}_c \geq 0, \quad \vec{h}_{\mathrm{Li}^\oplus}\cdot\nabla\mu_{\mathrm{Li}^\oplus} \leq 0 \tag{4.68}$$

4.5.3 Thermodynamics: foils

Under the isothermal assumption applied to the entire system, the temperature of the foils is time-invariant. Consequently, akin to the electrolyte and cathode, the influence of temperature T as given in equation (4.48) is disregarded in formulating the Clausius-Duhem inequality [2]. The resulting inequality for the foils is expressed as follows

$$\frac{\partial \boldsymbol{\varepsilon}_f}{\partial t} : \left(\boldsymbol{\sigma}_f - \frac{\partial \psi_f}{\partial \boldsymbol{\varepsilon}_f} \right) + \vec{i_f} \cdot \vec{E}_f \geq 0 \tag{4.69}$$

where $\vec{i}_f \cdot \vec{E}_f$ denotes the Joule-Effect for the foils, in conjuction with the electrostatic approach in the absence of the time variation of the electric displacement field in the foils, i.e. $\frac{\partial \vec{D}_f}{\partial t} = 0$. Upon implementing the Coleman-Noll procedure, the thermodynamic constraints produce the following results:

$$\boldsymbol{\sigma}_f - \frac{\partial \psi_f}{\partial \boldsymbol{\varepsilon}_f} = 0, \ \vec{i}_f \cdot \vec{E}_f \geq 0. \tag{4.70}$$

4.6 Constitutive theory

4.6.1 Constitutive theory: electrolyte

The thermodynamic uncoupling of the processes is assumed, and the Helmholtz free energy density is decomposed into three distinct components

$$\psi_e \left(\boldsymbol{\varepsilon}_e, c_\alpha, \vec{D}_e \right) = \psi_e^{diff}(c_\alpha) + \psi_e^{es}(\vec{D}_e) + \psi_e^{el}(\boldsymbol{\varepsilon}_e). \tag{4.71}$$

Given that species concentrations c_α are used as the state variables, the mass transport process can be described using the ψ_e^{diff} notation. The electro-quasistatic interactions are modeled by the contribution ψ_e^{es}, which is expressed in terms of the electric displacement field $\vec{D}_e$. Lastly, the mechanical energy density, denoted by ψ_e^{el} is a function of the deformation that is solely determined by the history of the small strain tensor locally. Electro-quasistatic energy is defined as a function of the electric displacement field as follows:

$$\psi_e^{es}(\vec{D}_e) = \frac{1}{2\epsilon} \vec{D}_e \cdot \vec{D}_e. \tag{4.72}$$

A linear relationship is assumed between the electric displacement field $\vec{D}_e$ and the electric field $\vec{E}_e$, where $\epsilon > 0$ denotes the constant electrical permittivity of the material:

$$\vec{D}_e = \epsilon \vec{E}_e = -\epsilon \nabla \left[\phi_e \right]. \tag{4.73}$$

The electrostatic potential ϕ arises from idealized electric charges transitioning between electrodes, a process depicted by Fickian diffusion as follows:

$$\vec{h}_\alpha = -\boldsymbol{M}_\alpha \nabla \left[\overline{\mu}_\alpha \right] \tag{4.74}$$

This diffusion linearly connects the mass flux of species α to the gradient of its electrochemical potential, as denoted in equation (4.53), utilizing a positively defined mobility

[2] The thermodynamic steps—energy balance, entropy imbalance, Helmholtz free energy, and the Coleman–Noll restrictions—have already been derived for the electrolyte (Sections 4.5.1.1– 4.5.1.4) and the cathode (Sections 4.5.2.1– 4.5.2.5). To avoid repetition, they are not restated for the foils.

tensor $\boldsymbol{M}_\alpha$. The identity in (4.74) is consistent with the thermodynamic restrictions stated in Section (4.5.1.4). The isotropic non linear case [263] is a representative example of a traditional specialization of the mobility tensor $\boldsymbol{M}_\alpha$ for dilute solutions that takes saturation into account

$$\boldsymbol{M}_\alpha\left(c_{\mathrm{Li}^+}, c_{\mathrm{X}^-}\right) = \mathbb{\mu}_\alpha c_\alpha \left(1 - \theta_{\mathrm{Li}^+} - \theta_{\mathrm{X}^-}\right) \mathbb{I}. \tag{4.75}$$

where $\alpha = \mathrm{Li}^+, \mathrm{X}^-$. The quantity $\mathbb{\mu}_\alpha$ defines the ion mobility of species. Regardless of where the force is coming from, it is a representation of the average velocity of species α in the solution when it is subjected to a force of 1 N/mol. θ_α is the ratio given by $\frac{c}{c^{sat}}$, where c^{sat} represents the maximum saturation limit for ions Li^+ and X^- in the solution, under the principles of electroneutrality. Equation (4.75) denotes the physical condition wherein the pure phase ($c_\alpha = 0$) and the saturated phase ($\theta_{\mathrm{Li}^+} + \theta_{\mathrm{X}^-} = 1$) exhibit zero mobilities within the electrolyte. Utilizing the state of electroneutrality

$$\left(c_{\mathrm{Li}^+} - c_{\mathrm{X}^-}\right) = 0, \tag{4.76}$$

as described in the study conducted [251], the specialization for the mobility tensor can be simplified to

$$\boldsymbol{M}_\alpha(c_\alpha) = \mathbb{\mu}_\alpha c_\alpha \left(1 - 2\frac{c_\alpha}{c^{sat}}\right) \mathbb{I}. \tag{4.77}$$

The free energy $\psi_e^{diff}(c_\alpha)$ within a mixture is determined by the mixture's composition. The subsequent analysis will focus on diluted solutions, as defined in [319]. Based on the numerical analyses conducted in [329, 251], which revealed that concentration peaks reach approximately %50 of the saturation limit, the modeling assumption made here is that concentrations are far enough from saturation to ignore energetic interactions in the solution, yet not so small as to dismiss the saturation contribution. Consequently, the free energy is expressed in explicitly as follows:

$$\begin{aligned}\psi_e^{diff}(c_{\mathrm{Li}^+}, c_{\mathrm{X}^-}) = \mu^0_{\mathrm{Li}^+} c_{\mathrm{Li}^+} + \mu^0_{\mathrm{X}^-} c_{\mathrm{X}^-} + RTc^{sat}(\theta_{Li^+}\ln[\theta_{\mathrm{Li}^+}] + \theta_{\mathrm{X}^-}\ln[\theta_{\mathrm{X}^-}]) \\ + RTc^{sat}(1 - \theta_{\mathrm{Li}^+} - \theta_{\mathrm{X}^-})\ln[(1 - \theta_{\mathrm{Li}^+} - \theta_{\mathrm{X}^-})].\end{aligned} \tag{4.78}$$

In the aforementioned formula, R represents the universal gas constant, while $\mu^0_{\mathrm{Li}^+}$ and $\mu^0_{\mathrm{X}^-}$ serve as reference values for the chemical potential of diffusing species. Enforcing electroneutrality via Equation (4.76), the chemical potential can be written in the following general form:

$$\mu_\alpha = \mu^0_\alpha + RT \ln\left[\frac{c_\alpha}{c^{sat} - 2c_\alpha}\right], \tag{4.79}$$

For the two species, we obtain

$$\mu_{\mathrm{Li}^+} = \mu^0_{\mathrm{Li}^+} + RT \ln\left[\frac{c_{\mathrm{Li}^+}}{c^{sat} - 2c_{\mathrm{Li}^+}}\right], \tag{4.80a}$$

$$\mu_{\mathrm{X}^-} = \mu^0_{\mathrm{X}^-} + RT \ln\left[\frac{c_{\mathrm{X}^-}}{c^{sat} - 2c_{\mathrm{X}^-}}\right]. \tag{4.80b}$$

These expressions for the chemical potentials yield the following mathematical representation for the mass flux:

$$\vec{h}_\alpha = -\mathbb{D}_\alpha \nabla[c_\alpha] - z_\alpha F \mathbb{\mu}_\alpha c_\alpha \left(1 - 2\frac{c_\alpha}{c^{sat}}\right) \nabla\left[\phi_e\right]. \tag{4.81}$$

Mass fluxes of Li^+ and X^- ions are defined as follows:

$$\vec{h}_{\mathrm{Li^+}} = -\mathbb{D}_{\mathrm{Li^+}} \nabla[c_{\mathrm{Li^+}}] - F \mathbb{\mu}_{\mathrm{Li^+}} c_{\mathrm{Li^+}} \left(1 - 2\frac{c_{\mathrm{Li^+}}}{c^{sat}}\right) \nabla\left[\phi_e\right], \tag{4.82a}$$

$$\vec{h}_{\mathrm{X^-}} = -\mathbb{D}_{\mathrm{X^-}} \nabla[c_{\mathrm{X^-}}] + F \mathbb{\mu}_{\mathrm{X^-}} c_{\mathrm{X^-}} \left(1 - 2\frac{c_{\mathrm{X^-}}}{c^{sat}}\right) \nabla\left[\phi_e\right], \tag{4.82b}$$

where $\mathbb{D}_\alpha$ denotes the diffusivity of species α, which is related to its mobility through the Nernst–Einstein relation

$$\mathbb{D}_\alpha = \mathbb{\mu} RT, \tag{4.83}$$

often referred to as the Nernst-Einstein equation. By incorporating the Nernst-Einstein equation into the mass flux of each ion, fluxes are rearranged respectively

$$\vec{h}_{\mathrm{Li^+}} = -\mathbb{D}_{\mathrm{Li^+}} \nabla[c_{\mathrm{Li^+}}] - \frac{\mathbb{D}_{\mathrm{Li^+}} F}{RT} c_{\mathrm{Li^+}} \left(1 - 2\frac{c_{\mathrm{Li^+}}}{c^{sat}}\right) \nabla[\phi_e], \tag{4.84a}$$

$$\vec{h}_{\mathrm{X^-}} = -\mathbb{D}_{\mathrm{X^-}} \nabla[c_{\mathrm{X^-}}] + \frac{\mathbb{D}_{\mathrm{X^-}} F}{RT} c_{\mathrm{X^-}} \left(1 - 2\frac{c_{\mathrm{X^-}}}{c^{sat}}\right) \nabla[\phi_e]. \tag{4.84b}$$

In this study, the mechanical constitutive model of the electrolyte is assumed as isotropic, linear-elastic

$$\psi_e^{el}(\boldsymbol{\varepsilon}_e) = \frac{1}{2}\boldsymbol{\varepsilon}_e : \mathbb{C}_e : \boldsymbol{\varepsilon}_e = \frac{1}{2}\left(K_e \mathrm{tr}[\boldsymbol{\varepsilon}_\mathrm{e}]^2 + 2G_\mathrm{e} || \operatorname{dev}\left[\boldsymbol{\varepsilon}_\mathrm{e}\right] ||^2\right) \tag{4.85}$$

where K_e, G_e are the bulk and shear modulus of the electrolyte respectively. Symbol $\mathbb{C}_e$ denotes fourth-order stiffness tensor of the elastic material. The symbol $\mathrm{tr}[\boldsymbol{\varepsilon}_\mathrm{e}]$ represents the trace operator of the strain tensor, while $\operatorname{dev}[\boldsymbol{\varepsilon}_\mathrm{e}]$ signifies the deviator operator of the strain tensor. After applying the Coleman-Noll procedure, the thermodynamics restrictions (4.53) suggest,

$$\boldsymbol{\sigma}_e = K_e \,\mathrm{tr}[\boldsymbol{\varepsilon}_e]\,\mathbb{I} + 2G_e \operatorname{dev}[\boldsymbol{\varepsilon}_e]. \tag{4.86}$$

4.6.2 Constitutive theory: cathode

The choice of the free energy density is a reflection of the assumptions used to model the lithiation process in the cathodes. Since the system is isothermal, in the absence of the temperature, the Helmholtz free energy density is decomposed into two components in the cathode as follows:

$$\psi_c\left(\boldsymbol{\varepsilon}_c, c_{\mathrm{Li}^\oplus}\right) = \psi_c^{el}(c_{\mathrm{Li}^\oplus}, \boldsymbol{\varepsilon}_c) + \psi_c^{diff}(c_{\mathrm{Li}^\oplus}). \tag{4.87}$$

The electronic current density is assumed to follow a linear Ohmic law, consistent with the Joule-effect restriction in (4.68), and is characterized by the electrical conductivity $\kappa_c > 0$:

$$\vec{i_c} = \kappa_c \vec{E} = -\kappa_c \nabla[\phi_c]\,. \tag{4.88}$$

In order to satisfy restriction (4.68), a linear Fickian-diffusion law is established for the diffusion of Lithium in the cathode using a positive definite mobility tensor $\boldsymbol{M}_{\mathrm{Li}^\oplus}$

$$\vec{h}_{\mathrm{Li}^\oplus} = -\boldsymbol{M}_{\mathrm{Li}^\oplus} \nabla\left[\mu_{\mathrm{Li}^\oplus}\right]. \tag{4.89}$$

When high C-rates are present, as is typical in real batteries, the Lithium concentration within the electrodes generally exhibits localized high values. It is necessary to use saturation specialization of the mobility tensor $\boldsymbol{M}_{\mathrm{Li}^{\oplus}}$ in the form $\boldsymbol{M}_{\mathrm{Li}^{\oplus}} = \Vdash_{\mathrm{Li}^{\oplus}} \mathbb{M}_{\mathrm{Li}^{\oplus}} \mathbb{I}$, which is still isotropic but non linear, where

$$\mathbb{M}_{\mathrm{Li}^{\oplus}} = c_{\mathrm{Li}^{\oplus}} \left(1 - \frac{c_{\mathrm{Li}^{\oplus}}}{c^{sat}_{\mathrm{Li}^{\oplus}}}\right). \tag{4.90}$$

By recalling the equation (4.62), elastic strain can be written as

$$\boldsymbol{\varepsilon}^{el}_c = \boldsymbol{\varepsilon}_c - \boldsymbol{\varepsilon}^{sw}_c. \tag{4.91}$$

In the small-strain regime, the elastic contribution to the free energy density $\psi^{el}_c(c_{\mathrm{Li}^{\oplus}}, \boldsymbol{\varepsilon}_c)$ is taken in the standard quadratic form

$$\psi^{el}_c\left(\boldsymbol{\varepsilon}_c, c_{\mathrm{Li}^{\oplus}}\right) = \frac{1}{2}\left(K_c \mathrm{tr}[\boldsymbol{\varepsilon}_{\mathrm{c}} - \boldsymbol{\varepsilon}^{\mathrm{sw}}_{\mathrm{c}}]^2 + 2G_{\mathrm{c}}\ \mathrm{dev}||\left[\boldsymbol{\varepsilon}_{\mathrm{c}} - \boldsymbol{\varepsilon}^{\mathrm{sw}}_{\mathrm{c}}\right]||^2\right) \tag{4.92}$$

where K_c and G_c denote the bulk and shear moduli, respectively. From the thermodynamic restrictions (4.68), the stress tensor is obtained as:

$$\frac{\partial \psi^{el}_c}{\partial \boldsymbol{\varepsilon}_c} = \boldsymbol{\sigma}_c = K_c \mathrm{tr}\left[\boldsymbol{\varepsilon}_{\mathrm{c}}\right]\mathbb{I} + 2G_{\mathrm{c}}\ \mathrm{dev}\left[\boldsymbol{\varepsilon}_{\mathrm{c}}\right] - 3K_{\mathrm{c}}\omega_{\mathrm{Li}^{\oplus}}\left(\mathrm{c}_{\mathrm{Li}^{\oplus}} - \mathrm{c}^{0}_{\mathrm{Li}^{\oplus}}\right)\mathbb{I}. \tag{4.93}$$

It is worth noting that the derivative $\partial\psi^{el}_c/\partial c_{\mathrm{Li}^{\oplus}}$ takes the following form:

$$\frac{\partial \psi^{el}_c}{\partial c_{\mathrm{Li}^{\oplus}}} = \frac{\partial \psi^{el}_c}{\partial \boldsymbol{\varepsilon}^{el}_c} : \frac{\partial \boldsymbol{\varepsilon}^{el}_c}{\partial c_{\mathrm{Li}^{\oplus}}} = \boldsymbol{\sigma}_c : (-\omega_{\mathrm{Li}^{\oplus}}\mathbb{I}) = -\omega_{\mathrm{Li}^{\oplus}} \mathrm{tr}\left[\boldsymbol{\sigma}_{\mathrm{c}}\right] \tag{4.94}$$

which emanates from the swelling part of the strain. The diffusive part of the free energy ψ^{diff}_c, characterizes mass transport, with the neutral lithium concentration as the state variable. According to the regular-solution model [263, 264], the free-energy density includes an exchange (interaction) parameter χ. In this work we set $\chi = 0$ (ideal mixing), so the mixing contribution is purely entropic. Accordingly

$$\psi^{diff}_c(c_{\mathrm{Li}^{\oplus}}) = \mu^{0}_{\mathrm{Li}^{\oplus}} c_{\mathrm{Li}^{\oplus}} + RT c^{sat}_{\mathrm{Li}^{\oplus}}\left[\theta_{\mathrm{Li}^{\oplus}} \ln[\theta_{\mathrm{Li}^{\oplus}}] + (1 - \theta_{\mathrm{Li}^{\oplus}}) \ln\left[(1 - \theta_{\mathrm{Li}^{\oplus}})\right]\right] \tag{4.95}$$

where $\theta_{\mathrm{Li}^{\oplus}} = \frac{c_{\mathrm{Li}^{\oplus}}}{c^{sat}_{\mathrm{Li}^{\oplus}}}$ and $c^{sat}_{\mathrm{Li}^{\oplus}}$ are the saturation limits for $c_{\mathrm{Li}^{\oplus}}$. Even within the scope of this basic theory, the chemical potential is highly intricate and comprises two distinct components. From Equation (4.68) we derive the chemical potential of as a function concentration $c_{\mathrm{Li}^{\oplus}}$ as

$$\mu_{\mathrm{Li}^{\oplus}} = \frac{\partial \psi_c\left(\boldsymbol{\varepsilon}_c, c_{\mathrm{Li}^{\oplus}}\right)}{\partial c_{\mathrm{Li}^{\oplus}}} = \left(\frac{\partial \psi^{diff}_c}{\partial c_{\mathrm{Li}^{\oplus}}} + \frac{\partial \psi^{el}_c}{\partial c_{\mathrm{Li}^{\oplus}}}\right). \tag{4.96}$$

The chemical potential thus reads

$$\mu_{\mathrm{Li}^{\oplus}} = \mu^{0}_{\mathrm{Li}^{\oplus}} + RT \ln\left(\frac{c_{\mathrm{Li}^{\oplus}}}{c^{\mathrm{sat}}_{\mathrm{Li}^{\oplus}} - c_{\mathrm{Li}^{\oplus}}}\right) - \omega_{\mathrm{Li}^{\oplus}}\ \mathrm{tr}\left[\boldsymbol{\sigma}_c\right]. \tag{4.97}$$

The first emerges from the differential $\frac{\partial \psi^{diff}_c}{\partial c_{\mathrm{Li}^{\oplus}}}$, is generally non-convex, and originates only from transport. Second contribution arises from $\frac{\partial \psi^{el}_c}{\partial c_{\mathrm{Li}^{\oplus}}}$, and evaluates the impact of swelling deformation caused by swelling strain on the chemical potential as given in equation (4.94). By expressing diffusivity in the usual manner as $\mathbb{D}_{\mathrm{Li}^{\oplus}} = \Vdash_{\mathrm{Li}^{\oplus}} RT$, Fick's law (4.89) can be rewritten as follows:

$$\vec{h}_{\mathrm{Li}^{\oplus}} = -\mathbb{D}_{\mathrm{Li}^{\oplus}} \nabla\left[c_{\mathrm{Li}^{\oplus}}\right] + \frac{\mathbb{D}_{\mathrm{Li}^{\oplus}}}{RT} c_{\mathrm{Li}^{\oplus}} \left(1 - \frac{c_{\mathrm{Li}^{\oplus}}}{c^{sat}_{\mathrm{Li}^{\oplus}}}\right) \omega_{\mathrm{Li}^{\oplus}} \nabla\left[\mathrm{tr}\left[\boldsymbol{\sigma}_{\mathrm{c}}\right]\right]. \tag{4.98}$$

4.6.3 Constitutive theory: foils

The Helmholtz free energy is expressed for the foils as:

$$\psi_f\left(\boldsymbol{\varepsilon}_f\right) = \psi_f^{el}(\boldsymbol{\varepsilon}_f), \tag{4.99}$$

where $\boldsymbol{\varepsilon}_f$ represents the strain tensor. Assuming the both foils behave isotropically and exhibit linear elastic properties, the free energy is defined as:

$$\psi_f(\boldsymbol{\varepsilon}_f) = \frac{1}{2}\boldsymbol{\varepsilon}_f : \mathbb{C} : \boldsymbol{\varepsilon}_f = \frac{1}{2}\left(K_f \mathrm{tr}[\boldsymbol{\varepsilon}_\mathrm{f}]^2 + 2G_\mathrm{f}|| \operatorname{dev}[\boldsymbol{\varepsilon}_\mathrm{f}] \ ||^2\right). \tag{4.100}$$

Here K_f and G_f denote the bulk modulus and shear modulus respectively. Thermodynamic constraints (4.70) lead to the stress tensor being:

$$\boldsymbol{\sigma}_f = \frac{\partial \psi_f}{\partial \boldsymbol{\varepsilon}_f} = K_f \ \mathrm{tr}\left[\boldsymbol{\varepsilon}_\mathrm{f}\right]\mathbb{I} + 2G_\mathrm{f} \operatorname{dev}\left[\boldsymbol{\varepsilon}_\mathrm{f}\right]. \tag{4.101}$$

The current density, proportional to the gradient of the electric potential ϕ_f, which is given by:

$$\vec{i}_f = \kappa_f \vec{E}_f = -\kappa_f \nabla\left[\phi_f\right] \tag{4.102}$$

where $\kappa_f > 0$ represents electrical conductivity of the foils. The material parameters are taken constant within each foil but will differ between foils. Accordingly, in the anode Ω_a we use $K_f = K_a$, $G_f = G_a$, and $\kappa_f = \kappa_a$; in the current collector Ω_{cc} we use $K_f = K_{cc}$, $G_f = G_{cc}$, and $\kappa_f = \kappa_{cc}$. The numerical values of the materials parameters will be reported in Table 4.1. For brevity, we keep the compact notation K_f, G_f, and κ_f; the intended value is understood from the foil.

4.7 Interface Conditions

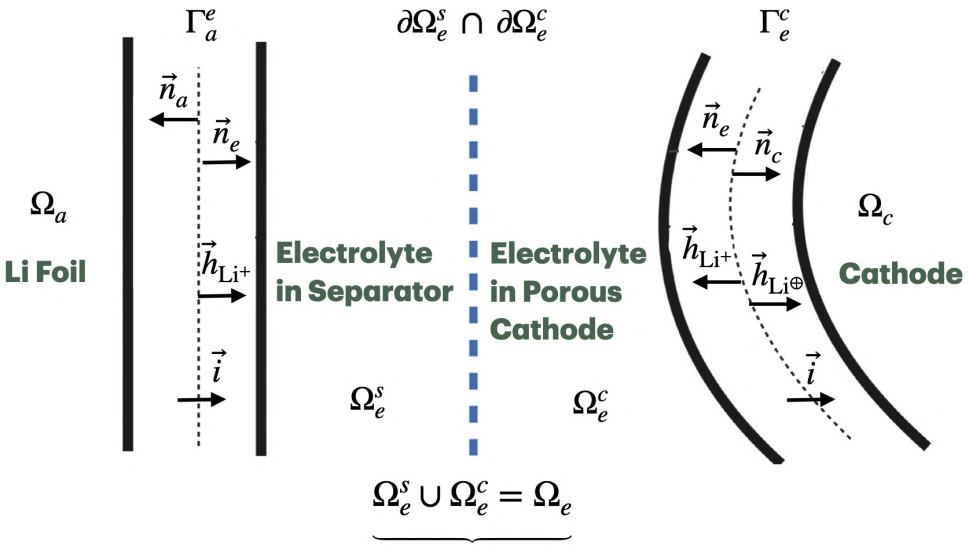

Figure 4.4: Schematic representation of interfaces

4.7.1 Interface between the anode and the electrolyte

Li dissolution into the electrolyte is characterized by the following electrochemical oxidation reaction:

$$\mathrm{Li} \rightleftharpoons \mathrm{Li}^+ + \mathrm{e}^- \tag{4.103}$$

which takes place at the Li-metal-foil/electrolyte interface at Γ_a^e in Figure 4.4. The Butler–Volmer equation is used to model the redox reaction process at a zero-thickness interface, as described in [245, 260]. This equation incorporates the exchange current density, denoted by $i_{a/e}^0$:

$$i_{BV}^a = i_{a/e}^0 \left\{ \exp\left[\frac{\alpha_A F \eta_s^a}{RT}\right] - \exp\left[\frac{-\alpha_C F \eta_s^a}{RT}\right] \right\}. \tag{4.104}$$

The exchange current density for the anode–electrolyte interface is given by [330]:

$$i_{a/e}^0 = k_R^a F \left(c_{\mathrm{Li}^+}\right)^{\alpha_A} \left(c_{\mathrm{Li}}\right)^{\alpha_C}, \tag{4.105}$$

where k_R^a denotes the standard rate constant for the anode–electrolyte interface, and c_{Li} represents the concentration of pure metallic lithium species in the anode. The surface overpotential at the negative electrode interface, denoted by η_s^a, is defined based on the electric potential jump across the interface:

$$\eta_s^a = [\![\phi]\!] - U_{\mathrm{Li}} = (\phi_e - \phi_a) - U_{\mathrm{Li}}. \tag{4.106}$$

Here, U_{Li} is the open circuit potential (OCP) of the lithium metal and it is zero, since the lithium metal anode is used as the reference point in experimental analyses of the open-circuit potential (OCP) [245, 260]. As a result, the corresponding electric potential jump across the interface is defined as:

$$[\![\phi]\!] = \phi_e - \phi_a. \tag{4.107}$$

Given the lack of intercalation of X^- ions between the anode and electrolyte, the interface conditions can be written as:

$$\vec{h}_{\mathrm{Li}^+} \cdot \vec{n}_e = h_{BV}^a \quad \text{on } \Gamma_a^e, \tag{4.108a}$$

$$\vec{h}_{\mathrm{X}^-} \cdot \vec{n}_e = 0 \quad \text{on } \Gamma_a^e, \tag{4.108b}$$

$$-\vec{i}_a \cdot \vec{n}_a = \vec{i}_e \cdot \vec{n}_e = i_{BV}^a = F h_{BV}^a \quad \text{on } \Gamma_a^e, \tag{4.108c}$$

where $\vec{n}_e = -\vec{n}_a$ denotes the outward normal on the interface Γ_a^e shown in Figure 4.4. In addition to the electrochemical interface conditions described above, mechanical continuity is also imposed at the interface between the anode and the electrolyte. Since cohesive behavior, damage, or delamination at this interface is not considered in the present model, the mechanical contact is assumed to be perfectly bonded. Therefore, the displacement field is continuous across the interface:

$$\vec{u}_a = \vec{u}_e \quad \text{on } \Gamma_a^e. \tag{4.109}$$

4.7.2 Interface between the electrolyte and the cathode

The electrochemical reduction reaction for intercalation:

$$\mathrm{Li}^+ + \mathrm{e}^- \rightleftharpoons \mathrm{Li} \tag{4.110}$$

taking place at the surface of the cathode is represented in this study using the Butler-Volmer equation at Γ_e^c in Figure 4.4, without considering the double-layer capacitance as mentioned in [330]. Instead of directly addressing the boundary layers between the cathode and the electrolyte, the phenomena concerned are integrated into an interface without the thickness. Therefore, the electric potential may exhibit discontinuity at the interface as presented in [331]. By applying the Butler-Volmer equation, the following definition of surface current density is obtained and denoted as i_{BV}^c. Butler-Volmer equation yields

$$i_{BV}^c = i_{e/c}^0 \left\{ exp\left[\frac{\alpha_A F \eta_s^c}{RT}\right] - exp\left[\frac{-\alpha_C F \eta_s^c}{RT}\right] \right\} \tag{4.111}$$

where $i_{e/c}^0$ referred to as exchanged current density, η_s^c denotes surface overpotential, α_A and α_C symbolize anodic charge transfer coefficient and cathodic charge transfer coefficient respectively. The exchange current density is contingent upon the lithium concentration existing at the interface is identified as in [332]:

$$i_{e/c}^0 = k_R^c F \left(c_{\mathrm{Li}^+}\right)^{\alpha_A} \left(c_{\mathrm{Li}^\oplus}^{max} - c_{\mathrm{Li}^\oplus}\right)^{\alpha_A} \left(c_{\mathrm{Li}^\oplus}\right)^{\alpha_C} \tag{4.112}$$

where k_R^c denotes the standart rate constant. The surface overpotential η_S^c is delineated as the difference between the electric potential jump at the interface where $[\![\phi]\!] = \phi_c - \phi_e$, and the surface open-circuit potential (OCP) U_s, as formally expressed in the following equation

$$\eta_S^c = [\![\phi]\!] - U_s = (\phi_c - \phi_e) - U_s. \tag{4.113}$$

In this work, we do not utilize the experimentally measured open-circuit potential (OCP) of cathode active particles. Instead, we adopt an idealized surface OCP expression, previously developed in the literature [260, 333], which relates the potential to the ideal chemical potential of lithium ions, $\mu_{\mathrm{Li}^\oplus}$, within a storage particle. This surface OCP, denoted with $U^s(t)$, is expressed by the following two equations:

$$F U^s(t) = \tilde{\mu}_{\mathrm{Li}} - \mu_{\mathrm{Li}^\oplus}(t), \tag{4.114}$$

$$U^s = -\frac{\mu_{\mathrm{Li}^\oplus}}{F} = -\frac{\mu_{\mathrm{Li}^\oplus}^0}{F} - \frac{RT}{F} \ln\left(\frac{c_{\mathrm{Li}^\oplus}}{c_{\mathrm{Li}^\oplus}^{\mathrm{sat}} - c_{\mathrm{Li}^\oplus}}\right) + \frac{\omega_{\mathrm{Li}^\oplus}}{F} \operatorname{tr}[\boldsymbol{\sigma}_c], \tag{4.115}$$

where $\mu_{\mathrm{Li}^\oplus}$ is defined in Equation (4.97). As customary, the reference lithium chemical potential $\tilde{\mu}_{\mathrm{Li}}$ in the metallic electrode is set to zero. The reference chemical potential $\mu_{\mathrm{Li}^\oplus}^0$ is selected as

$$\frac{\mu_{\mathrm{Li}^\oplus}^0}{F} = -4.2\,\mathrm{V} \tag{4.116}$$

to reflect the typical OCP of lithium cobalt oxide at the composition $\mathrm{Li}_{0.5}\mathrm{CoO}_2$, under the assumption of a stress-free electrode, that is, with $c_{\mathrm{Li}^\oplus} = c_{\mathrm{Li}^\oplus}^{\mathrm{sat}}/2$ and $\operatorname{tr}[\sigma_c] = 0$. The primary motivation for employing Equation (4.115) instead of using experimentally measured OCP data is as follows: experimental OCP values correspond to full-cell configurations, whereas the Butler–Volmer Equations (4.104), and (4.111) apply locally at each point along the lithium metal–electrolyte and electrolyte–cathode interfaces respectively. After the circuit is opened, state variables, such as lithium concentration and mechanical stress become spatially dependent, particularly in the presence of phase transformations within active particles [260, 333], even if no explicit phase transformation is considered in the present analysis. The symbol h_{BV}^c will denote the Butler–Volmer mass flux at the cathode–electrolyte interface. It is used to describe the rate of mass transfer occurring on

the surface of cathode particles in normal direction. The surface current density i_{BV}^{c} at a given point is directly linked to Faraday's law when it flows in the same direction

$$i_{BV}^{c} = F h_{BV}^{c}. \tag{4.117}$$

Since X anions do not intercalate into the cathode particle during the discharge, the mass flux of X anions will be equal to zero. As a consequence, interface conditions between electrolyte and cathode are summarized in terms of the electro-chemical perspective through the following equations

$$\vec{h}_{\mathrm{Li}^{\oplus}} \cdot \vec{n}_c = -\vec{h}_{\mathrm{Li}^{+}} \cdot \vec{n}_e = h_{BV}^{c} \quad \text{on } \Gamma_e^c, \tag{4.118a}$$

$$\vec{h}_{\mathrm{X}^{-}} \cdot \vec{n}_e = 0 \quad \text{on } \Gamma_e^c, \tag{4.118b}$$

$$\vec{i}_{\mathrm{c}} \cdot \vec{n}_c = -\vec{i}_{\mathrm{e}} \cdot \vec{n}_e = i_{BV}^{c} = F h_{BV}^{c} \quad \text{on } \Gamma_e^c. \tag{4.118c}$$

Here $\vec{n}_c = -\vec{n}_e$ denotes the outward normal on the interface Γ_e^c shown in Figure 4.4. Following the same reasoning applied at the anode–electrolyte interface, the displacement field is assumed to be continuous across the cathode–electrolyte interface, and it is expressed as:

$$\vec{u}_c = \vec{u}_e \quad \text{on } \Gamma_e^c. \tag{4.119}$$

This interface condition ensures that the mechanical interaction between the cathode and the electrolyte is correctly captured within the multiphysics framework.

4.7.3 Interface between the cathode and the current collector

At the interface between the cathode and the current collector, no electrochemical reaction is considered, and a perfectly bonded mechanical contact is assumed. Under this assumption, the displacement field remains continuous across the interface and is expressed as

$$\vec{u}_c = \vec{u}_{cc} \quad \text{on } \Gamma_c^{cc}. \tag{4.120}$$

This assumption ensures proper mechanical coupling between the cathode and the current collector, allowing for consistent stress transfer across the interface. From the electrical perspective, since both the cathode and the aluminum current collector support only electron conduction and no charge-transfer reaction occurs at the interface, the electric potential remains continuous across the interface, and is given by:

$$\phi_c = \phi_{cc} \quad \text{on } \Gamma_c^{cc}. \tag{4.121}$$

This condition enforces perfect electronic coupling and guarantees the absence of any potential drop across the interface.

4.8 Governing equations

4.8.1 Electrolyte

At the boundary between an electronic conductor and a liquid electrolyte, polarization develops and gives rise to a thin region with a steep electric-potential gradient [306]. Beyond this interfacial zone, strong electrostatic interactions suppress counter-ion separation during diffusion; thus, electroneutrality is typically preserved in the bulk of the

porous phase [249, 251]. Accordingly, in the electrolyte we adopt the electroneutrality assumption given in Equation (4.76),

$$c_{\mathrm{Li}^+} = c_{\mathrm{X}^-},$$

which is used in the following EQS formulation. Within the EQS framework, Maxwell's equations (4.3a)–(4.3d) reduce, under electroneutrality, to the local charge-balance condition

$$\nabla \cdot \vec{i}_e = 0, \tag{4.122}$$

which, combined with Faraday's law of electrolysis (4.13), yields

$$\nabla \cdot \left[\vec{h}_{\mathrm{X}^-} - \vec{h}_{\mathrm{Li}^+}\right] = 0. \tag{4.123}$$

By inserting the Nernst–Einstein fluxes (4.84a)–(4.84b) and the mechanical constitutive law (4.86) into the species mass balances (4.15a)–(4.15b) and the mechanical equilibrium equation (4.17), and enforcing (4.76), the following set of governing equations is obtained:

$$\frac{\partial c_{\mathrm{Li}^+}}{\partial t} + \nabla \cdot \left[-\mathbb{D}_{\mathrm{Li}^+} \nabla[c_{\mathrm{Li}^+}] - \frac{\mathbb{D}_{\mathrm{Li}^+} F}{RT}\, c_{\mathrm{Li}^+} \left(1 - 2\frac{c_{\mathrm{Li}^+}}{c^{sat}}\right) \nabla[\phi_e] \right] = 0, \tag{4.124a}$$

$$\nabla \cdot \left[(\mathbb{D}_{\mathrm{Li}^+} - \mathbb{D}_{\mathrm{X}^-}) \nabla[c_{\mathrm{Li}^+}] + \frac{(\mathbb{D}_{\mathrm{Li}^+} + \mathbb{D}_{\mathrm{X}^-}) F}{RT}\, c_{\mathrm{Li}^+} \left(1 - 2\frac{c_{\mathrm{Li}^+}}{c^{sat}}\right) \nabla[\phi_e] \right] = 0, \tag{4.124b}$$

$$\nabla \cdot \left[K_e \,\mathrm{tr}\,[\boldsymbol{\varepsilon}_e]\, \mathbb{I} + 2G_e \,\mathrm{dev}\,[\boldsymbol{\varepsilon}_e] \right] = \vec{0}. \tag{4.124c}$$

The variable fields governing the problem, determined by the thermodynamic prescriptions adopted, encompass the concentrations denoted as c_{Li^+}, the electric potential designated as ϕ_e, and the displacements referred to as $\vec{u}_e$. The governing equations are valid for all points $\vec{x} \in \Omega_e$ and a time $t \in [0, t_{end}]$.

4.8.2 Cathode

Phase segregation is not accounted for in the numerical simulations carried out in this thesis. Consequently, the analysis is restricted to the ideal-mixing regime, corresponding to $\chi = 0$, in which the material parameters are independent of $c_{\mathrm{Li}^\oplus}$. In the cathode domain, the governing equations are formulated by incorporating the constitutive equations (4.88), (4.93), and (4.98) into the balance equations for the cathode (4.18), (4.19), and (4.20). We write the equations using a new field,

$$\bar{\mu}^{\mathrm{m}}_{\mathrm{Li}^\oplus}(\mathrm{c}_{\mathrm{Li}^\oplus}, \boldsymbol{\varepsilon}_{\mathrm{c}}) = -\omega_{\mathrm{Li}^\oplus} \,\mathrm{tr}[\boldsymbol{\sigma}_{\mathrm{c}}] = -3K_{\mathrm{c}}\omega_{\mathrm{Li}^\oplus} \left(\mathrm{tr}[\boldsymbol{\varepsilon}_{\mathrm{c}}] - 3\omega_{\mathrm{Li}^\oplus} \left(\mathrm{c}_{\mathrm{Li}^\oplus} - \mathrm{c}^0_{\mathrm{Li}^\oplus}\right)\right). \tag{4.125}$$

This field captures how the chemical potential (4.97) varies with mechanical effects. The variable fields governing the problem, determined by the thermodynamic prescriptions adopted, encompass the concentrations denoted as $c_{\mathrm{Li}^\oplus}$, the electric potential designated as ϕ_c, and the displacement referred to as $\vec{u}_c$, and $\mu^m_{\mathrm{Li}^\oplus}$. The governing equations are valid

for all points $\vec{x} \in \Omega_c$ and a time $t \in [0, t_{end}]$,

$$\frac{\partial c_{\mathrm{Li}^\oplus}}{\partial t} + \nabla \cdot \left[- \mathbb{D}_{\mathrm{Li}^\oplus} \nabla \left[c_{\mathrm{Li}^\oplus} \right] - \frac{\mathbb{D}_{\mathrm{Li}^\oplus}}{RT} c_{\mathrm{Li}^\oplus} \left(1 - \frac{c_{\mathrm{Li}^\oplus}}{c^{sat}_{\mathrm{Li}^\oplus}} \right) \nabla \left[\mu^m_{\mathrm{Li}^\oplus} \right] \right] = 0, \tag{4.126a}$$

$$\nabla \cdot \left[-\kappa_c \nabla \left[\phi_c \right] \right] = 0, \tag{4.126b}$$

$$\nabla \cdot \left[K_c \mathrm{tr}[\boldsymbol{\varepsilon}_\mathrm{c}] \mathbb{I} + 2 G_\mathrm{c} \, \mathrm{dev}[\boldsymbol{\varepsilon}_\mathrm{c}] \; - 3 K_\mathrm{c} \omega_{\mathrm{Li}^\oplus} \left(\mathrm{c}_{\mathrm{Li}^\oplus} - \mathrm{c}^0_{\mathrm{Li}^\oplus} \right) \mathbb{I} \right] = \vec{0}. \tag{4.126c}$$

$$\mu^m_{\mathrm{Li}^\oplus} - \bar{\mu}^\mathrm{m}_{\mathrm{Li}^\oplus}(\mathrm{c}_{\mathrm{Li}^\oplus}, \boldsymbol{\varepsilon}_\mathrm{c}) = 0. \tag{4.126d}$$

Equation (4.126d) is introduced as an additional governing equation alongside equations (4.126a), (4.126b), and (4.126c) to facilitate the numerical solution of the system.

4.8.3 Foils

On the foil domains, the governing equations are obtained by substituting the constitutive relations (4.101), (4.102) into the balance laws (4.21), and (4.22). The primary unknown fields are the electric potential and the displacement, denoted ϕ_f and $\vec{u}_f$ with $f \in \{a, cc\}$. The system is posed for all $\vec{x} \in \Omega_f$ and a time $t \in [0, t_\mathrm{end}]$.

$$\nabla \cdot \left[-\kappa_f \nabla \left[\phi_f \right] \right] = 0, \tag{4.127a}$$

$$\nabla \cdot \left[K_f \, \mathrm{tr} \left[\boldsymbol{\varepsilon}_f \right] \mathbb{I} + 2 G_f \, \mathrm{dev} \left[\boldsymbol{\varepsilon}_f \right] \right] = \vec{0}. \tag{4.127b}$$

4.9 Boundary and initial conditions

In this section, suitable boundary and initial conditions are imposed as illustrated in Figure 4.3. A constant discharge current is applied on the boundary $\partial\Omega^B_{cc}$, while a referential potential ϕ_a is set to zero on $\partial\Omega^B_a$:

$$\vec{i}_{cc} \cdot \vec{n}_{cc} = \vec{i}_\mathrm{bat} = \frac{I(t)}{A} \quad \text{on} \quad \partial\Omega^B_{cc}, \quad \phi_a = 0 \quad \text{on} \quad \partial\Omega^B_a \tag{4.128}$$

Here, A denotes the cross-sectional area, and $\vec{i}_\mathrm{bat}$ represents the current density flowing through the battery. To ensure compatibility of the boundary and initial conditions with thermodynamic equilibrium at $t = 0$, the total current I is modulated over time as

$$I(t) = \left(1 - e^{-t} \right) \, I_{nC}, \tag{4.129}$$

where I_{nC} denotes the steady current corresponding to an nC-rate. The theoretical current density at 1C for the 3D half-cell is estimated as $\vec{i}_\mathrm{bat} = 6.29 \, \mathrm{A/m^2}$. Higher or lower current rates for any nC-rate can be computed as $(n \times 6.29 \, \mathrm{A/m^2})$. On the other hand the flux of current is zero on the remaining part of the boundary for reasons of the symmetry, thus the following boundary conditions arise

$$\vec{i}_a \cdot \vec{n}_a = 0 \quad \text{on} \quad \partial\Omega^A_a, \tag{4.130a}$$

$$\vec{i}_e \cdot \vec{n}_e = 0 \quad \text{on} \quad \partial\Omega^A_e, \tag{4.130b}$$

$$\vec{i}_c \cdot \vec{n}_c = 0 \quad \text{on} \quad \partial\Omega^A_c. \tag{4.130c}$$

Neither neutral lithium $Li^{\oplus}$ nor ionic species Li^{+} and X^{-} can flow through the external surfaces so that boundary conditons are written as:

$$\vec{h}_{\mathrm{Li^+}} \cdot \vec{n}_e = \vec{h}_{\mathrm{X^-}} \cdot \vec{n}_e = 0 \quad \text{on} \quad \partial\Omega_e^A, \tag{4.131a}$$

$$\vec{h}_{\mathrm{Li^{\oplus}}} \cdot \vec{n}_c = 0 \quad \text{on} \quad \partial\Omega_c^A. \tag{4.131b}$$

Moreover, following mechanical boundary conditions are imposed on the external surfaces for preventing the battery cell expansion and contraction:

$$\vec{u}_a = \vec{u}_{cc} = \vec{0} \quad \text{on} \quad \partial\Omega_a^B \cup \partial\Omega_{cc}^B. \tag{4.132}$$

For the external boundaries, homogeneous Neumann (traction-free) boundary conditions are imposed:

$$\boldsymbol{\sigma}_a \cdot \vec{n}_a = \vec{\bar{p}}_a = \vec{0} \quad \text{on} \quad \partial\Omega_a^A, \tag{4.133a}$$

$$\boldsymbol{\sigma}_e \cdot \vec{n}_e = \vec{\bar{p}}_e = \vec{0} \quad \text{on} \quad \partial\Omega_e^A, \tag{4.133b}$$

$$\boldsymbol{\sigma}_c \cdot \vec{n}_c = \vec{\bar{p}}_c = \vec{0} \quad \text{on} \quad \partial\Omega_c^A, \tag{4.133c}$$

$$\boldsymbol{\sigma}_{cc} \cdot \vec{n}_{cc} = \vec{\bar{p}}_{cc} = \vec{0} \quad \text{on} \quad \partial\Omega_{cc}^A. \tag{4.133d}$$

No external (stack) pressure is applied in the present model. Accordingly, the external mechanical boundaries are modeled as traction-free, i.e., $\vec{\bar{p}} = \vec{0}$ in Equations (4.133a–d). Initial conditions for the species concentrations are prescribed at $t = 0$ for each domain of the battery. In the lithium metal anode, the initial concentration is set to

$$c_{\mathrm{Li}}(\vec{x}, 0) = 7.64 \times 10^4 \quad \mathrm{mol/m^3} \quad \text{in } \Omega_{\mathrm{a}}, \tag{4.134}$$

as reported in [247]. For the electrolyte domain, the initial ionic species concentrations are taken from [252] and are assumed to be identical in order to satisfy the electroneutrality condition. Accordingly, we introduce the positive constant c_{bulk}, defined as

$$c_{bulk} = c_{\mathrm{Li^+}}(\vec{x}, 0) = c_{\mathrm{X^-}}(\vec{x}, 0) = 1.5 \times 10^3 \quad \mathrm{mol/m^3} \quad \text{in } \Omega_{\mathrm{e}}. \tag{4.135}$$

which will be used as a reference value to scale the concentration variables in the weak forms. The initial concentration in the cathode was set to half of the saturation limit to reflect typical operating conditions, as discussed in [334]. In practice, only a portion of the theoretical capacity of $LiCoO_2$ is utilized in order to maintain structural stability and avoid undesirable phase transitions during cycling. The specific initial concentration of $Li^{\oplus}$ in the cathode is taken from [335], i.e.

$$c_{\mathrm{Li^{\oplus}}}(\vec{x}, 0) = 1.195 \times 10^4 \quad \mathrm{mol/m^3} \quad \text{in } \Omega_{\mathrm{c}}. \tag{4.136}$$

The initial electric potentials are prescribed at $t = 0$ for each domain of the battery. In the lithium metal anode and the electrolyte domains, the potentials are set to the zero:

$$\phi_{\mathrm{a}}(\vec{x}, 0) = \phi_{\mathrm{e}}(\vec{x}, 0) = 0 \text{ V} \quad \text{in} \quad \Omega_{\mathrm{a}} \cup \Omega_{\mathrm{e}}. \tag{4.137}$$

In contrast, the potentials in the cathode and the current collector domains are initialized to 4.2 V, corresponding to a fully charged state:

$$\phi_{\mathrm{c}}(\vec{x}, 0) = \phi_{\mathrm{cc}}(\vec{x}, 0) = 4.2 \text{ V} \quad \text{in} \quad \Omega_{\mathrm{c}} \cup \Omega_{\mathrm{cc}}. \tag{4.138}$$

4.10 Weak forms across all domains

The evolution problem can be reformulated in a weak form by projecting the governing Equations (4.124a), (4.124b), (4.124c), (4.126a), (4.126b), (4.126c), (4.126d), (4.127a), and (4.127b) onto a set of test functions and integrating them over the computational domain. By applying Green's theorem (or integration by parts), the differentiation order is reduced, shifting derivatives onto the test functions. Within the Galerkin framework, these test functions—also referred to as variational quantities—are denoted by a hat symbol ($\hat{\cdot}$), and are introduced for each primary unknown field, such as the lithium-ion concentrations (c_{Li^+}, $c_{\mathrm{Li}^\oplus}$), the displacement fields ($\vec{u}_e$, $\vec{u}_c$, $\vec{u}_a$, $\vec{u}_{cc}$), electric potentials (ϕ_e, ϕ_c, ϕ_a, ϕ_{cc}), and $\mu^m_{\mathrm{Li}^\oplus}$. Accordingly, the associated variational quantities are written as ($\hat{c}_{\mathrm{Li}^+}$, $\hat{c}_{\mathrm{Li}^\oplus}$, $\hat{\vec{u}}_e$, $\hat{\vec{u}}_c$, $\hat{\vec{u}}_a$, $\hat{\vec{u}}_{cc}$, $\hat{\phi}_e$, $\hat{\phi}_c$, $\hat{\phi}_a$, $\hat{\phi}_{cc}$, $\hat{\mu}^m_{\mathrm{Li}^\oplus}$) respectively.

4.10.1 Electrolyte

4.10.1.1 Weak form of the electrolyte

A weak form of governing equations (4.124a), (4.124b), and (4.124c) in the electrolyte can be written as follows :
From the governing equation (4.124a) regarding the mass balance the weak form is obtained

$$\begin{aligned}
&\frac{RT}{c_{bulk}}\int_{\Omega_e}\hat{c}_{\mathrm{Li^+}}\left\{\frac{\partial c_{\mathrm{Li^+}}}{\partial t}+\nabla\cdot\left[-\mathbb{D}_{\mathrm{Li^+}}\nabla[c_{\mathrm{Li^+}}]-\frac{\mathbb{D}_{\mathrm{Li^+}}F}{RT}c_{\mathrm{Li^+}}\left(1-2\frac{c_{\mathrm{Li^+}}}{c^{sat}}\right)\nabla\left[\phi_e\right]\right]\right\}\mathrm{d}\Omega_e\\
&=\frac{RT}{c_{bulk}}\int_{\Omega_e}\hat{c}_{\mathrm{Li^+}}\frac{\partial c_{\mathrm{Li^+}}}{\partial t}+\mathbb{D}_{\mathrm{Li^+}}\int_{V_e}\nabla[\hat{c}_{\mathrm{Li^+}}]\cdot\nabla[c_{\mathrm{Li^+}}]\mathrm{d}\Omega_e\\
&+\frac{RT}{c_{bulk}}\int_{\Omega_e}\frac{\mathbb{D}_{\mathrm{Li^+}}F}{RT}c_{\mathrm{Li^+}}\left(1-2\frac{c_{\mathrm{Li^+}}}{c^{sat}}\right)\nabla[\hat{c}_{\mathrm{Li^+}}]\cdot\nabla\left[\phi_e\right]\mathrm{d}\Omega_e\\
&+\frac{RT}{c_{bulk}}\int_{\partial\Omega_e}\hat{c}_{\mathrm{Li^+}}\left\{\vec{h}_{\mathrm{Li^+}}\cdot\vec{n}_e\right\}\mathrm{d}\Gamma=0.
\end{aligned}\tag{4.139}$$

The equation (4.124b) can be expressed in a weak form as follows:

$$\begin{aligned}
&F\int_{\Omega_e}\hat{\phi}_e\nabla\cdot\left[(\mathbb{D}_{\mathrm{Li^+}}-\mathbb{D}_{\mathrm{X^-}})\nabla[c_{\mathrm{Li^+}}]+\frac{(\mathbb{D}_{\mathrm{Li^+}}+\mathbb{D}_{\mathrm{X^-}})F}{RT}c_{\mathrm{Li^+}}\left(1-2\frac{c_{\mathrm{Li^+}}}{c^{sat}}\right)\nabla\left[\phi_e\right]\right]\mathrm{d}\Omega_e\\
&=F\int_{\Omega_e}(\mathbb{D}_{\mathrm{Li^+}}-\mathbb{D}_{\mathrm{X^-}})\nabla[\hat{\phi}_e]\cdot\nabla[c_{\mathrm{Li^+}}]\mathrm{d}\Omega_e\\
&-F\int_{\Omega_e}\frac{(\mathbb{D}_{\mathrm{Li^+}}+\mathbb{D}_{\mathrm{X^-}})F}{RT}c_{\mathrm{Li^+}}\left(1-2\frac{c_{\mathrm{Li^+}}}{c^{sat}}\right)\nabla[\hat{\phi}_e]\cdot\nabla\left[\phi_e\right]\mathrm{d}\Omega_e\\
&+F\int_{\partial\Omega_e}\hat{\phi}_e\left\{\vec{h}_{\mathrm{X^-}}\cdot\vec{n}_e\right\}\mathrm{d}\Gamma-F\int_{\partial\Omega_e}\hat{\phi}_e\left\{\vec{h}_{\mathrm{Li^+}}\cdot\vec{n}_e\right\}\mathrm{d}\Gamma=0.
\end{aligned}\tag{4.140}$$

The weak form of the equation (4.124c) is obtained

$$\begin{aligned}
&\frac{1}{\bar{t}}\int_{\Omega_e}\hat{\vec{u}}_e\cdot\nabla\cdot[\boldsymbol{\sigma}_e]\ \mathrm{d}\Omega_e=-\frac{2G_e}{\bar{t}}\int_{\Omega_e}\nabla^s\left[\hat{\vec{u}}_e\right]:\nabla^s\left[\vec{u}_e\right]\ \mathrm{d}\Omega_e\\
&+\frac{\left(\frac{2G_e}{3}-K_e\right)}{\bar{t}}\int_{\Omega_e}\nabla\cdot\left[\hat{\vec{u}}_e\right]\ \nabla\cdot[\vec{u}_e]\ \mathrm{d}\Omega_e+\frac{1}{\bar{t}}\int_{\partial\Omega_e}\hat{\vec{u}}_e\cdot\vec{p}_e\ \mathrm{d}\Gamma=0
\end{aligned}\tag{4.141}$$

where the symbol ∇^{s} represents the symmetric gradient operator. In order to preserve the physical consistency of power expenditure in the weak form, the mass balance equation (4.139), is appropriately scaled using the coefficient $\frac{RT}{c_{bulk}}$ derived from the constitutive relation (4.79), the electroneutrality equation (4.140) is scaled by the Faraday constant F, and the mechanical equilibrium equation (4.141) is divided by reference time scale $\bar{t}$ to convert stored elastic energy into a rate (i.e., mechanical power) consistent with Joules per second ($\frac{J}{s}$). These scalings ensure that all terms in the coupled weak form equations are dimensionally consistent and represent comparable forms of energy or power.

4.10.1.2 Dimensionless weak form of the electrolyte

It is useful to express equations (4.139), (4.140), and (4.141) in a dimensionless form. To achieve this, the governing fields are rescaled to have unit dimensions, indicated by

starred superscripts, using appropriate scaling factors as follows:

$$
\begin{aligned}
&\vec{x}^* = \frac{\vec{x}}{L}, \quad t^* = \frac{t}{\bar{t}}, \quad \nabla^* = L\,\nabla, \quad \mathrm{d}\Omega^* = \frac{\mathrm{d}\Omega_e}{L^3}, \quad \mathrm{d}\Gamma^* = \frac{\mathrm{d}\Gamma}{L^2},\\
&c^*_{\mathrm{Li^+}} = \frac{c_{\mathrm{Li^+}}}{c_{\mathrm{bulk}}}, \quad \hat{c}^*_{\mathrm{Li^+}} = \frac{\hat{c}_{\mathrm{Li^+}}}{c_{\mathrm{bulk}}}, \quad c^{sat*} = \frac{c^{sat}}{c_{\mathrm{bulk}}}, \quad \mathbb{D}^*_\alpha = \frac{\mathbb{D}_\alpha \bar{t}}{L^2},\\
&\phi^*_e = \frac{F}{RT}\,\phi_e, \quad \hat{\phi}^*_e = \frac{F}{RT}\,\hat{\phi}_e, \quad \vec{u}^*_e = \frac{\vec{u}_e}{L}, \quad \hat{\vec{u}}^*_e = \frac{\hat{\vec{u}}_e}{L}, \quad \vec{h}^*_\alpha = \frac{\vec{h}_\alpha \bar{t}}{c_{\mathrm{bulk}}\,L}\\
&\boldsymbol{\sigma}^*_e = \frac{\boldsymbol{\sigma}_e}{RTc_{\mathrm{bulk}}}, \quad \vec{\bar{p}}^*_e = \frac{\vec{\bar{p}}_e}{RTc_{\mathrm{bulk}}}, \quad G^*_e = \frac{G_e}{RTc_{\mathrm{bulk}}}, \quad K^*_e = \frac{K_e}{RTc_{\mathrm{bulk}}}.
\end{aligned}
$$

where L, $\bar{t}$, and c_{bulk} represents the characteristic length, time, and concentration. The weak forms of Equations (4.139), (4.140), and (4.141) are expressed in following form over the time interval $[0, t_{\mathrm{end}}]$, respectively:

$$
\begin{aligned}
&\frac{RTc_{\mathrm{bulk}}\,L^3}{\bar{t}} \int_{\Omega_e} \hat{c}^*_{\mathrm{Li^+}}\, \frac{\partial c^*_{\mathrm{Li^+}}}{\partial t^*}\, \mathrm{d}\Omega^*_e\\
&+ \frac{RTc_{\mathrm{bulk}}\,L^3}{\bar{t}} \int_{\Omega_e} \mathbb{D}^*_{\mathrm{Li^+}} \nabla^*[\hat{c}^*_{\mathrm{Li^+}}] \cdot \nabla^*[c^*_{\mathrm{Li^+}}]\, \mathrm{d}\Omega^*_e\\
&+ \frac{RTc_{\mathrm{bulk}}\,L^3}{\bar{t}} \int_{\Omega_e} \mathbb{D}^*_{\mathrm{Li^+}}\, c^*_{\mathrm{Li^+}} \left(1 - 2\frac{c^*_{\mathrm{Li^+}}}{c^{sat*}}\right) \nabla^*[\hat{c}^*_{\mathrm{Li^+}}] \cdot \nabla^*[\phi^*_e]\, \mathrm{d}\Omega^*_e\\
&+ \frac{RTc_{\mathrm{bulk}}\,L^3}{\bar{t}} \int_{\partial\Omega_e} \hat{c}^*_{\mathrm{Li^+}} \left\{\vec{h}^*_{\mathrm{Li^+}} \cdot \vec{n}_e\right\} \mathrm{d}\Gamma^* = 0.
\end{aligned}
\tag{4.142}
$$

$$
\begin{aligned}
&- \frac{RTc_{\mathrm{bulk}}\,L^3}{\bar{t}} \int_{\Omega_e} (\mathbb{D}^*_{\mathrm{Li^+}} - \mathbb{D}^*_{\mathrm{X^-}})\, \nabla^*[\hat{\phi}^*_e] \cdot \nabla^*[c^*_{\mathrm{Li^+}}]\, \mathrm{d}\Omega^*_e\\
&- \frac{RTc_{\mathrm{bulk}}\,L^3}{\bar{t}} \int_{\Omega_e} (\mathbb{D}^*_{\mathrm{Li^+}} + \mathbb{D}^*_{\mathrm{X^-}})\, c^*_{\mathrm{Li^+}} \left(1 - 2\frac{c^*_{\mathrm{Li^+}}}{c^{sat*}}\right) \nabla^*[\hat{\phi}^*_e] \cdot \nabla^*\,[\phi^*_e]\;\mathrm{d}\Omega^*_e\\
&+ \frac{RTc_{\mathrm{bulk}}\,L^3}{\bar{t}} \int_{\partial\Omega_e} \hat{\phi}^*_e \left\{\vec{h}^*_{\mathrm{X^-}} \cdot \vec{n}_e\right\} \mathrm{d}\Gamma^* - \frac{RTc_{\mathrm{bulk}}\,L^3}{\bar{t}} \int_{\partial\Omega_e} \hat{\phi}^*_e \left\{\vec{h}^*_{\mathrm{Li^+}} \cdot \vec{n}_e\right\} \mathrm{d}\Gamma^* = 0.
\end{aligned}
\tag{4.143}
$$

$$
\begin{aligned}
&- \frac{2G^*_e\; RTc_{\mathrm{bulk}}\,L^3}{\bar{t}} \int_{\Omega_e} \nabla^{*s} \left[\hat{\vec{u}}^*_e\right] : \nabla^{*s}\,[\vec{u}^*_e]\;\mathrm{d}\Omega^*_e\\
&+ \frac{\left(\frac{2G^*_e}{3} - K^*_e\right) RTc_{\mathrm{bulk}}\,L^3}{\bar{t}} \int_{\Omega_e} \nabla^* \cdot \left[\hat{\vec{u}}^*_e\right]\; \nabla^* \cdot [\vec{u}^*_e]\;\mathrm{d}\Omega^*_e\\
&+ \frac{RTc_{\mathrm{bulk}}\,L^3}{\bar{t}} \int_{\partial\Omega_e} \hat{\vec{u}}^*_e \cdot \vec{\bar{p}}^*_e\, \mathrm{d}\Gamma^* = 0.
\end{aligned}
\tag{4.144}
$$

To obtain the dimensionless weak forms, both sides of Equations (4.142), (4.143), and (4.144) are divided by the characteristic power unit $\frac{RTc_{\mathrm{bulk}}\,L^3}{\bar{t}}$. This scaling factor, which carry units of $(\frac{J}{s})$ is dropped from the final expressions to yield the fully dimensionless forms.

The dimensionless weak form of the mass balance equation is given by:

$$\begin{aligned}
&\int_{\Omega_e} \hat{c}^*_{\mathrm{Li^+}} \, \frac{\partial c^*_{\mathrm{Li^+}}}{\partial t^*} \, \mathrm{d}\Omega^*_e \\
&+ \int_{\Omega_e} \mathbb{D}^*_{\mathrm{Li^+}} \nabla^*[\hat{c}^*_{\mathrm{Li^+}}] \cdot \nabla^*[c^*_{\mathrm{Li^+}}] \, \mathrm{d}\Omega^*_e \\
&+ \int_{\Omega_e} \mathbb{D}^*_{\mathrm{Li^+}} \, c^*_{\mathrm{Li^+}} \left(1 - 2\frac{c^*_{\mathrm{Li^+}}}{c^{sat*}}\right) \nabla^*[\hat{c}^*_{\mathrm{Li^+}}] \cdot \nabla^*[\phi^*_e] \, \mathrm{d}\Omega^*_e \\
&+ \int_{\partial\Omega_e} \hat{c}^*_{\mathrm{Li^+}} \left\{\vec{h}^*_{\mathrm{Li^+}} \cdot \vec{n}_e\right\} \mathrm{d}\Gamma^* = 0.
\end{aligned} \tag{4.145}$$

The dimensionless weak form regarding electroneutrality reads:

$$\begin{aligned}
&- \int_{\Omega_e} (\mathbb{D}^*_{\mathrm{Li^+}} - \mathbb{D}^*_{\mathrm{X^-}}) \, \nabla^*[\hat{\phi}^*_e] \cdot \nabla^*[c^*_{\mathrm{Li^+}}] \, \mathrm{d}\Omega^*_e \\
&- \int_{\Omega_e} (\mathbb{D}^*_{\mathrm{Li^+}} + \mathbb{D}^*_{\mathrm{X^-}}) \, c^*_{\mathrm{Li^+}} \left(1 - 2\frac{c^*_{\mathrm{Li^+}}}{c^{sat*}}\right) \nabla^*[\hat{\phi}^*_e] \cdot \nabla^* \left[\phi^*_e\right] \, \mathrm{d}\Omega^*_e \\
&+ \int_{\partial\Omega_e} \hat{\phi}^*_e \left\{\vec{h}^*_{\mathrm{X^-}} \cdot \vec{n}_e\right\} \mathrm{d}\Gamma^* - \int_{\partial\Omega_e} \hat{\phi}^*_e \left\{\vec{h}^*_{\mathrm{Li^+}} \cdot \vec{n}_e\right\} \mathrm{d}\Gamma^* = 0.
\end{aligned} \tag{4.146}$$

The dimensionless mechanical equilibrium equation becomes:

$$\begin{aligned}
&- 2G^*_e \int_{\Omega_e} \nabla^{*s} \left[\hat{\vec{u}}^*_e\right] : \nabla^{*s} \left[\vec{u}^*_e\right] \, \mathrm{d}\Omega^*_e \\
&+ \left(\frac{2G^*_e}{3} - K^*_e\right) \int_{\Omega_e} \nabla^* \cdot \left[\hat{\vec{u}}^*_e\right] \, \nabla^* \cdot \left[\vec{u}^*_e\right] \, \mathrm{d}\Omega^*_e \\
&+ \int_{\partial\Omega_e} \hat{\vec{u}}^*_e \cdot \vec{\vec{p}}^*_e \, \mathrm{d}\Gamma^* = 0.
\end{aligned} \tag{4.147}$$

4.10.2 Cathode

4.10.2.1 Weak form of the cathode

From the mass balance equation (4.126a) the weak form is obtained

$$\begin{aligned}
&\frac{RT}{c_{bulk}} \int_{\Omega_c} \hat{c}_{\mathrm{Li^\oplus}} \left\{\frac{\partial c_{\mathrm{Li^\oplus}}}{\partial t} + \nabla \cdot \left[-\mathbb{D}_{\mathrm{Li^\oplus}} \nabla \left[c_{\mathrm{Li^\oplus}}\right] - \frac{\mathbb{D}_{\mathrm{Li^\oplus}}}{RT} c_{\mathrm{Li^\oplus}} \left(1 - \frac{c_{\mathrm{Li^\oplus}}}{c^{sat}_{\mathrm{Li^\oplus}}}\right) \nabla \left[\mu^{\mathrm{m}}_{\mathrm{Li^\oplus}}\right]\right]\right\} \mathrm{d}\Omega_c \\
&= \frac{RT}{c_{bulk}} \int_{\Omega_c} \hat{c}_{\mathrm{Li^\oplus}} \frac{\partial c_{\mathrm{Li^\oplus}}}{\partial t} \mathrm{d}\Omega_c + \frac{RT}{c_{bulk}} \int_{\Omega_c} \mathbb{D}_{\mathrm{Li^\oplus}} \nabla \left[\hat{c}_{\mathrm{Li^\oplus}}\right] \cdot \nabla \left[c_{\mathrm{Li^\oplus}}\right] \mathrm{d}\Omega_c \\
&+ \frac{RT}{c_{bulk}} \int_{\Omega_c} \frac{\mathbb{D}_{\mathrm{Li^\oplus}}}{RT} c_{\mathrm{Li^\oplus}} \left(1 - \frac{c_{\mathrm{Li^\oplus}}}{c^{sat}_{\mathrm{Li^\oplus}}}\right) \nabla \left[\hat{c}_{\mathrm{Li^\oplus}}\right] \cdot \nabla \left[\mu^{\mathrm{m}}_{\mathrm{Li^\oplus}}\right] \mathrm{d}\Omega_c \\
&+ \frac{RT}{c_{bulk}} \int_{\partial\Omega_c} \hat{c}_{\mathrm{Li^\oplus}} \left\{\vec{h}_{\mathrm{Li^\oplus}} \cdot \vec{n}_c\right\} \mathrm{d}\Gamma = 0.
\end{aligned} \tag{4.148}$$

The equation (4.126b) can be expressed in a weak form as follows

$$\int_{\Omega_c} \hat{\phi}_c \, \mathrm{div} \left[-\kappa_c \nabla \left[\phi_c\right]\right] \, \mathrm{d}\Omega_c = \int_{\Omega_c} \kappa_c \nabla \left[\hat{\phi}_c\right] \cdot \nabla \left[\phi_c\right] \, \mathrm{d}\Omega_c + \int_{\partial\Omega_c} \hat{\phi}_c \left\{\vec{i}_c \cdot \vec{n}_c\right\} \mathrm{d}\Gamma = 0 \tag{4.149}$$

The weak form of the equation (4.126c) is obtained

$$\begin{aligned}
&\frac{1}{\bar{t}}\int_{\Omega_c}\hat{\vec{u}}_c\cdot\nabla\cdot\left[\boldsymbol{\sigma}_c\right]\mathrm{d}\Omega_c=-\frac{2G_c}{\bar{t}}\int_{\Omega_c}\nabla^s\left[\hat{\vec{u}}_c\right]:\nabla^s\left[\vec{u}_c\right]\,\mathrm{d}\Omega_c\\
&+\frac{\left(\frac{2G_c}{3}-K_c\right)}{\bar{t}}\int_{\Omega_c}\nabla\cdot\left[\hat{\vec{u}}_c\right]\,\nabla\cdot\left[\vec{u}_c\right]\,\mathrm{d}\Omega_c\\
&+\frac{3K_c\,\omega_{Li^\oplus}}{\bar{t}}\int_{\Omega_c}\nabla\cdot\left[\hat{\vec{u}}_c\right]\left(c_{\mathrm{Li}^\oplus}-c^0_{\mathrm{Li}^\oplus}\right)\,\mathrm{d}\Omega_c\\
&+\frac{1}{\bar{t}}\int_{\partial\Omega_c}\hat{\vec{u}}_c\cdot\vec{p}_c\,\mathrm{d}\Gamma=0
\end{aligned}\tag{4.150}$$

Finally, equation (4.126d) returns

$$\frac{c_{bulk}}{RT\,\bar{t}}\int_{\Omega_c}\hat{\mu}^m_{\mathrm{Li}^\oplus}\left(\mu^m_{\mathrm{Li}^\oplus}-3K_c\omega_{\mathrm{Li}^\oplus}\left(\mathrm{tr}[\boldsymbol{\varepsilon}_\mathrm{c}]-3\omega_{\mathrm{Li}^\oplus}\left(\mathrm{c}_{\mathrm{Li}^\oplus}-\mathrm{c}^0_{\mathrm{Li}^\oplus}\right)\right)\right)\,\mathrm{d}\Omega_c=0\tag{4.151}$$

4.10.2.2 Dimensionless weak form of the cathode

Similar to the approach used for the electrolyte, it is beneficial to rewrite equations (4.148), (4.149), (4.150), and (4.151) in a dimensionless form. This is accomplished by introducing appropriate scaling factors for the governing fields, thereby transforming them into their dimensionless counterparts, denoted by starred superscripts. These scaling factors for the cathode are as follows:

$$\vec{x}^*=\frac{\vec{x}}{L},\quad t^*=\frac{t}{\bar{t}},\quad \nabla^*=L\,\nabla,\quad \mathrm{d}\Omega^*=\frac{\mathrm{d}\Omega_c}{L^3},\quad \mathrm{d}\Gamma^*=\frac{\mathrm{d}\Gamma}{L^2},$$

$$c^*_{\mathrm{Li}^\oplus}=\frac{c_{\mathrm{Li}^\oplus}}{c_{\mathrm{bulk}}},\quad \hat{c}^*_{\mathrm{Li}^\oplus}=\frac{\hat{c}_{\mathrm{Li}^\oplus}}{c_{\mathrm{bulk}}},\quad c^{0*}_{\mathrm{Li}^\oplus}=\frac{c^0_{\mathrm{Li}^\oplus}}{c_{\mathrm{bulk}}},\quad c^{\mathrm{sat}*}_{\mathrm{Li}^\oplus}=\frac{c^{\mathrm{sat}}_{\mathrm{Li}^\oplus}}{c_{\mathrm{bulk}}},\quad \mathbb{D}^*_{\mathrm{Li}^\oplus}=\frac{\mathbb{D}_{\mathrm{Li}^\oplus}\bar{t}}{L^2}$$

$$\phi^*_c=\frac{F}{RT}\,\phi_c,\quad \hat{\phi}^*_c=\frac{F}{RT}\,\hat{\phi}_c,\quad \kappa^*_c=\frac{\vec{\kappa}_c\,\bar{t}\,R\,T}{c_{\mathrm{bulk}}\,L^2F^2},\quad \vec{i}^*_c=\frac{\vec{i}_c\,\bar{t}}{c_{\mathrm{bulk}}\,L\,F},\quad \vec{h}^*_{\mathrm{Li}^\oplus}=\frac{\vec{h}_{\mathrm{Li}^\oplus}\bar{t}}{c_{\mathrm{bulk}}\,L}$$

$$\vec{u}^*_c=\frac{\vec{u}_c}{L},\quad \hat{\vec{u}}^*_c=\frac{\hat{\vec{u}}_c}{L},\quad \boldsymbol{\sigma}^*_c=\frac{\boldsymbol{\sigma}_c}{RTc_{\mathrm{bulk}}},\quad \bar{p}^*_c=\frac{\bar{p}_c}{RTc_{\mathrm{bulk}}},\quad G^*_c=\frac{G_c}{RTc_{\mathrm{bulk}}},\quad K^*_c=\frac{K_c}{RTc_{\mathrm{bulk}}}$$

$$\mu^{m*}_{\mathrm{Li}^\oplus}=\frac{\mu^m_{\mathrm{Li}^\oplus}}{RT},\quad \hat{\mu}^{m*}_{\mathrm{Li}^\oplus}=\frac{\hat{\mu}^m_{\mathrm{Li}^\oplus}}{RT},\quad \omega^*_{\mathrm{Li}^\oplus}=\omega_{\mathrm{Li}^\oplus}\,c_{\mathrm{bulk}}.$$

The weak forms of equations (4.148), (4.149), (4.150), and (4.151) are expressed over the time interval $[0,t_{\mathrm{end}}]$ as follows:

$$\begin{aligned}
&\frac{RTc_{\mathrm{bulk}}\,L^3}{\bar{t}}\int_{\Omega_c}\hat{c}^*_{\mathrm{Li}^\oplus}\frac{\partial c^*_{\mathrm{Li}^\oplus}}{\partial t}\mathrm{d}\Omega^*_c\\
&+\frac{RTc_{\mathrm{bulk}}\,L^3}{\bar{t}}\int_{\Omega_c}\mathbb{D}_{\mathrm{Li}^\oplus}\nabla^*[\hat{c}^*_{\mathrm{Li}^\oplus}]\cdot\nabla^*[c^*_{\mathrm{Li}^\oplus}]\mathrm{d}\Omega^*_c\\
&+\frac{RTc_{\mathrm{bulk}}\,L^3}{\bar{t}}\int_{\Omega_c}\mathbb{D}_{\mathrm{Li}^\oplus}c^*_{\mathrm{Li}^\oplus}\left(1-\frac{c^*_{\mathrm{Li}^\oplus}}{c^{sat*}_{\mathrm{Li}^\oplus}}\right)\nabla^*\left[\hat{c}^*_{\mathrm{Li}^\oplus}\right]\cdot\nabla^*\left[\mu^{\mathrm{m}*}_{\mathrm{Li}^\oplus}\right]\mathrm{d}\Omega^*_c\\
&+\frac{RTc_{\mathrm{bulk}}\,L^3}{\bar{t}}\int_{\partial\Omega_c}\hat{c}^*_{\mathrm{Li}^\oplus}\left\{\vec{h}^*_{\mathrm{Li}^\oplus}\cdot\vec{n}_c\right\}\mathrm{d}\Gamma^*=0.
\end{aligned}\tag{4.152}$$

$$\frac{RTc_{\mathrm{bulk}}\,L^3}{\bar{t}}\int_{\Omega_c}\kappa^*_c\,\nabla^*\left[\hat{\phi}^*_c\right]\cdot\nabla^*\left[\phi^*_c\right]\,\mathrm{d}\Omega^*_c+\frac{RTc_{\mathrm{bulk}}\,L^3}{\bar{t}}\int_{\partial\Omega_c}\hat{\phi}^*_c\left\{\vec{i}^*_\mathrm{c}\cdot\vec{n}_c\right\}\,\mathrm{d}\Gamma^*=0\tag{4.153}$$

$$
\begin{aligned}
&- \frac{2G_c^*\ RTc_{\text{bulk}}\ L^3}{\bar{t}} \int_{\Omega_c} \nabla^{s*} \left[\hat{\vec{u}}_c^*\right] : \nabla^{s*} \left[\vec{u}_c^*\right]\ \mathrm{d}\Omega_c^* \\
&+ \frac{\left(\frac{2G_c^*}{3} - K_c^*\right)\ RTc_{\text{bulk}}\ L^3}{\bar{t}} \int_{\Omega_c} \nabla^* \cdot \left[\hat{\vec{u}}_c^*\right]\ \nabla^* \cdot \left[\vec{u}_c^*\right]\ \mathrm{d}\Omega_c^* \\
&+ \frac{3K_c^*\ \omega_{Li\oplus}^*\ RTc_{\text{bulk}}\ L^3}{\bar{t}} \int_{\Omega_c} \nabla^* \cdot \left[\hat{\vec{u}}_c^*\right] \left(c_{\text{Li}\oplus}^* - c_{\text{Li}\oplus}^{0*}\right)\ \mathrm{d}\Omega_c^* \\
&+ \frac{RTc_{\text{bulk}}\ L^3}{\bar{t}} \int_{\partial\Omega_c} \hat{\vec{u}}_c^* \cdot \vec{\vec{p}}_c^*\ \mathrm{d}\Gamma^* = 0.
\end{aligned}
\tag{4.154}
$$

$$
\begin{aligned}
&\frac{RTc_{\text{bulk}}\ L^3}{\bar{t}} \int_{\Omega_c} \hat{\mu}_{\text{Li}\oplus}^{\text{m}*}\ \mu_{\text{Li}\oplus}^{\text{m}*}\ \mathrm{d}\Omega_c^* - \frac{3K_c^*\ \omega_{Li\oplus}^* RTc_{\text{bulk}}\ L^3}{\bar{t}} \int_{\Omega_c} \hat{\mu}_{\text{Li}\oplus}^{\text{m}*}\ \nabla^* \cdot \left[\vec{u}_c^*\right] \mathrm{d}\Omega_c^* \\
&+ \frac{9K_c^*\omega_{Li\oplus}^* RTc_{\text{bulk}}\ L^3}{\bar{t}} \omega_{Li\oplus}^* \int_{\Omega_c} \hat{\mu}_{\text{Li}\oplus}^{\text{m}*} \left(c_{\text{Li}\oplus}^* - c_{\text{Li}\oplus}^{0*}\right)\ \mathrm{d}\Omega_c^* = 0.
\end{aligned}
\tag{4.155}
$$

Similarly to the procedure in Section 4.10.1.2 for the electrolyte we divide Equation (4.152), (4.153), (4.154) and (4.155) by the characteristic power $\frac{RTc_{\text{bulk}}\ L^3}{\bar{t}}$.
The dimensionless weak form of the mass balance equation is given by:

$$
\begin{aligned}
&\int_{\Omega_c} \hat{c}_{\text{Li}\oplus}^* \frac{\partial c_{\text{Li}\oplus}^*}{\partial t} \mathrm{d}\Omega_c^* \\
&+ \int_{\Omega_c} \mathbb{D}_{\text{Li}\oplus} \nabla^* [\hat{c}_{\text{Li}\oplus}^*] \cdot \nabla^* [c_{\text{Li}\oplus}^*] \mathrm{d}\Omega_c^* \\
&+ \int_{\Omega_c} \mathbb{D}_{\text{Li}\oplus} c_{\text{Li}\oplus}^* \left(1 - \frac{c_{\text{Li}\oplus}^*}{c_{\text{Li}\oplus}^{sat*}}\right) \nabla^* \left[\hat{c}_{\text{Li}\oplus}\right] \cdot \nabla^* \left[\mu_{\text{Li}\oplus}^{\text{m}*}\right] \mathrm{d}\Omega_c^* \\
&+ \int_{\partial\Omega_c} \hat{c}_{\text{Li}\oplus}^* \left\{\vec{h}_{\text{Li}\oplus}^* \cdot \vec{n}_c\right\} \mathrm{d}\Gamma^* = 0.
\end{aligned}
\tag{4.156}
$$

The dimensionless weak formulation of Ohm's law in the cathode reads:

$$
\int_{\Omega_c} \kappa_c^*\ \nabla^* \left[\hat{\phi}_c^*\right] \cdot \nabla^* \left[\phi_c^*\right]\ \mathrm{d}\Omega_c^* + \int_{\partial\Omega_c} \hat{\phi}_c^* \left\{\vec{i}_{\text{c}}^* \cdot \vec{n}_c\right\}\ \mathrm{d}\Gamma^* = 0 \tag{4.157}
$$

The dimensionless weak formulation of momentum balance equation in the cathode reads:

$$
\begin{aligned}
&- 2G_c^* \int_{\Omega_c} \nabla^{s*} \left[\hat{\vec{u}}_c^*\right] : \nabla^{s*} \left[\vec{u}_c^*\right]\ \mathrm{d}\Omega_c^* + \left(\frac{2G_c^*}{3} - K_c^*\right)\ \int_{\Omega_c} \nabla^* \cdot \left[\hat{\vec{u}}_c^*\right]\ \nabla^* \cdot \left[\vec{u}_c^*\right] \mathrm{d}\Omega_c^* \\
&+ 3K_c^*\ \omega_{\text{Li}\oplus}^*\ \int_{\Omega_c} \nabla^* \cdot \left[\hat{\vec{u}}_c^*\right] \left(c_{\text{Li}\oplus}^* - c_{\text{Li}\oplus}^{0*}\right)\ \mathrm{d}\Omega_c^* + \int_{\partial\Omega_c} \hat{\vec{u}}_c^* \cdot \vec{\vec{p}}_c^*\ \mathrm{d}\Gamma^* = 0.
\end{aligned}
\tag{4.158}
$$

The dimensionless weak formulation of Equation (4.155) reads:

$$
\begin{aligned}
&\int_{\Omega_c} \hat{\mu}_{\text{Li}\oplus}^{\text{m}*}\ \mu_{\text{Li}\oplus}^{\text{m}*}\ \mathrm{d}\Omega_c^* - 3K_c^*\ \omega_{\text{Li}\oplus}^* \int_{\Omega_c} \hat{\mu}_{\text{Li}\oplus}^{\text{m}*}\ \nabla^* \cdot \left[\vec{u}_c^*\right] \mathrm{d}\Omega_c^* \\
&+ 9K_c^*\ (\omega_{\text{Li}\oplus}^*)^2 \int_{\Omega_c} \hat{\mu}_{\text{Li}\oplus}^{\text{m}*} \left(c_{\text{Li}\oplus}^* - c_{\text{Li}\oplus}^{0*}\right)\ \mathrm{d}\Omega_c^* = 0.
\end{aligned}
\tag{4.159}
$$

4.10.3 Foils

4.10.3.1 Weak form of the foils

The equation (4.127a) can be expressed in a weak form as follows

$$\int_{\Omega_f} \hat{\phi}_f \, \nabla \cdot \left[\vec{i}_f\right] \mathrm{d}\Omega_f = \int_{\Omega_f} \kappa_f \nabla \left[\hat{\phi}_f\right] \cdot \nabla \left[\phi_f\right] \, \mathrm{d}\Omega_f + \int_{\partial\Omega_f} \hat{\phi}_f \left\{\vec{i}_f \cdot \vec{n}_f\right\} \mathrm{d}\Gamma = 0. \tag{4.160}$$

The weak form of equation (4.127b) returns

$$\begin{aligned} &\frac{1}{\bar{t}} \int_{\Omega_f} \hat{\vec{u}}_f \cdot \nabla \cdot \left[\boldsymbol{\sigma}_f\right] \mathrm{d}\Omega_f = -\frac{2G_f}{\bar{t}} \int_{\Omega_f} \nabla^s \left[\hat{\vec{u}}_f\right] : \nabla^s \left[\vec{u}_f\right] \, \mathrm{d}\Omega_f \\ &+ \frac{\left(\frac{2G_f}{3} - K_f\right) \bar{\sigma}}{\bar{t}} \int_{\Omega_f} \nabla \cdot \left[\hat{\vec{u}}_f\right] \, \nabla \cdot \left[\vec{u}_f\right] \, \mathrm{d}\Omega_f + \frac{1}{\bar{t}} \int_{\partial\Omega_f} \hat{\vec{u}}_f \cdot \vec{\bar{p}}_f \, \mathrm{d}\Gamma = 0. \end{aligned} \tag{4.161}$$

4.10.3.2 Dimensionless weak form of the foils

Similar to the approach employed for the electrolyte and the cathode, we write equations (4.160), and (4.161) in a dimensionless form. This is achieved by introducing appropriate scaling factors, analogous to those previously defined for the electrolyte and the cathode. These scaling factors for the foils written as follows:

$$\begin{aligned} &\vec{x}^* = \frac{\vec{x}}{L}, \quad t^* = \frac{t}{\bar{t}}, \quad \nabla^* = L\,\nabla, \quad \mathrm{d}\Omega_f^* = \frac{\mathrm{d}\Omega_f}{L^3}, \quad \mathrm{d}\Gamma^* = \frac{\mathrm{d}\Gamma}{L^2}, \\ &\phi_f^* = \frac{F}{R\,T}\,\phi_f, \quad \hat{\phi}_f^* = \frac{F}{R\,T}\,\hat{\phi}_f, \quad \kappa_f^* = \frac{\vec{\kappa}_f\,\bar{t}\,R\,T}{c_{\text{bulk}}\,L^2F^2}, \quad \vec{i}_f^* = \frac{\vec{i}_f\,\bar{t}}{c_{\text{bulk}}\,L\,F}, \quad \vec{u}_f^* = \frac{\vec{u}_f}{L}, \\ &\hat{\vec{u}}_f^* = \frac{\hat{\vec{u}}_f}{L}, \quad \boldsymbol{\sigma}_f^* = \frac{\boldsymbol{\sigma}_f}{RTc_{\text{bulk}}}, \quad \bar{p}_f^* = \frac{\bar{p}_f}{RTc_{\text{bulk}}}, \quad {G_f}^* = \frac{G_f}{RTc_{\text{bulk}}}, \quad {K_f}^* = \frac{K_f}{RTc_{\text{bulk}}}. \end{aligned}$$

The weak forms of equations (4.160) and (4.161) are reformulated using scaling factors to ensure dimensional consistency (in units of $\frac{J}{s}$) and are expressed over the time interval $[0, t_{\text{end}}]$, respectively :

$$\frac{RTc_{\text{bulk}}\,L^3}{\bar{t}} \int_{\Omega_f} \kappa_f^* \, \nabla^* \left[\hat{\phi}_f^*\right] \cdot \nabla^* \left[\phi_f^*\right] \, \mathrm{d}\Omega_f^* + \frac{RTc_{\text{bulk}}\,L^3}{\bar{t}} \int_{\partial\Omega_f} \hat{\phi}_f^* \left\{\vec{i}_f^* \cdot \vec{n}_f\right\} \, \mathrm{d}\Gamma^* = 0 \tag{4.162}$$

$$\begin{aligned} &- \frac{2G_f^*\,RTc_{\text{bulk}}\,L^3}{\bar{t}} \int_{\Omega_f} \nabla^{*s} \left[\hat{\vec{u}}_f^*\right] : \nabla^{*s} \left[\vec{u}_f^*\right] \, \mathrm{d}\Omega_f^* \\ &+ \frac{\left(\frac{2G_f^*}{3} - K_f^*\right) RTc_{\text{bulk}}\;L^3}{\bar{t}} \int_{\Omega_f} \nabla^* \cdot \left[\hat{\vec{u}}_f^*\right] \, \nabla^* \cdot \left[\vec{u}_f^*\right] \, \mathrm{d}\Omega_f^* \\ &+ \frac{RTc_{\text{bulk}}\,L^3}{\bar{t}} \int_{\partial\Omega_f} \hat{\vec{u}}_f^* \cdot \vec{\bar{p}}_f^* \, \mathrm{d}\Gamma^* = 0. \end{aligned} \tag{4.163}$$

Following the approach used for the electrolyte and cathode, the discretized foil equations (4.162) and (4.163) are rescaled by dividing through by the characteristic power

scale $\frac{RTc_{\text{bulk}}\,L^3}{t}$. This yields the following fully dimensionless weak form of Ohm's law for the foils:

$$\int_{\Omega_f} \kappa_f^* \, \nabla^* \left[\hat{\phi}_f^*\right] \cdot \nabla^* \left[\phi_f^*\right] \, \mathrm{d}\Omega_f^* + \int_{\partial\Omega_f} \hat{\phi}_f^* \left\{\vec{i}_f^* \cdot \vec{n}_f\right\} \mathrm{d}\Gamma^* = 0. \tag{4.164}$$

On the foil domains, the mechanical equilibrium equation in dimensionless form reads:

$$\begin{aligned} &- 2G_f^* \int_{\Omega_f} \nabla^{*s} \left[\hat{\vec{u}}_f^*\right] : \nabla^{*s} \left[\vec{u}_f^*\right] \, \mathrm{d}\Omega_f^* \\ &+ \left(\frac{2G_f^*}{3} - K_f^*\right) \int_{\Omega_f} \nabla^* \cdot \left[\hat{\vec{u}}_f^*\right] \, \nabla^* \cdot \left[\vec{u}_f^*\right] \, \mathrm{d}\Omega_f^* \\ &+ \int_{\partial\Omega_f} \hat{\vec{u}}_f^* \cdot \vec{p}_f^* \, \mathrm{d}\Gamma^* = 0. \end{aligned} \tag{4.165}$$

4.10.4 Interfaces

Since the interfaces Γ_a^e and Γ_e^c are part of the boundaries of the computational domain, as described in Section 4.2.1, the corresponding weak forms and their finite element formulations will be presented in the subsequent sections.

4.10.4.1 Lithium foil-electrolyte interface

4.10.4.1.1 Weak form of the lithium foil-electrolyte interface

From Equation (4.160), the weak-form boundary contribution on the anode–electrolyte interface from the anode side, i.e., over $\Gamma_a^e \subset \partial\Omega_a$, reads:

$$\int_{\Gamma_a^e} \hat{\phi}_a \left\{\vec{i}_{\text{a}} \cdot \vec{n}_a\right\} \mathrm{d}\Gamma. \tag{4.166}$$

On the electrolyte side of the anode–electrolyte interface, by substituting the interface condition (4.108b) into the weak forms (4.139) and (4.140), restricting to $\Gamma_a^e \subset \partial\Omega_e$, the boundary contribution reads

$$\frac{RT}{c_{\text{bulk}}} \int_{\Gamma_a^e} \hat{c}_{\text{Li}^+} \left\{\vec{h}_{\text{Li}^+} \cdot \vec{n}_e\right\} \mathrm{d}\Gamma \; - \; F \int_{\Gamma_a^e} \hat{\phi}_e \left\{\vec{h}_{\text{Li}^+} \cdot \vec{n}_e\right\} \mathrm{d}\Gamma. \tag{4.167}$$

After imposing the interface conditions (4.108a) and (4.108c), the weak forms on both sides of the interface are modified as follows: Equation (4.166), corresponding the lithium foil domain becomes

$$- \int_{\Gamma_a^e} \hat{\phi}_a \, i_{BV}^a \, \mathrm{d}\Gamma, \tag{4.168}$$

while the corresponding expression for the electrolyte domain, takes the form

$$\frac{RT}{Fc_{\text{bulk}}} \int_{\Gamma_a^e} \hat{c}_{\text{Li}^+} \, i_{BV}^a \, \mathrm{d}\Gamma - \int_{\Gamma_a^e} \hat{\phi}_e \, i_{BV}^a \, \mathrm{d}\Gamma. \tag{4.169}$$

After introducing and linearizing the Butler–Volmer relation in Equation (4.104)[3]

[3]The exponential Butler–Volmer terms introduce strong nonlinearity and stiffness in the Newton system. Linearizing about the current iterate provides a consistent tangent (Jacobian), reduces residuals more effectively, and improves robustness and convergence of the Newton–Raphson solver.

Lithium-foil side from Equation (4.168) becomes:

$$-\int_{\Gamma_a^e} \hat{\phi}_a \; k_R^a \; F \; \left(c_{\mathrm{Li^+}}\right)^{\alpha_A} \; \left(c_{\mathrm{Li}}\right)^{\alpha_C} \left[\frac{(\alpha_A+\alpha_C) \; F \; (\phi_e-\phi_a)}{RT}\right] \mathrm{d}\Gamma^*. \tag{4.170}$$

The electrolyte-side contribution, obtained from Equation (4.169), reads as follows:

$$\begin{aligned} &\frac{RT}{Fc_{\mathrm{bulk}}} \int_{\Gamma_a^e} \hat{c}_{\mathrm{Li^+}} \; k_R^a \; F \; \left(c_{\mathrm{Li^+}}\right)^{\alpha_A} \; \left(c_{\mathrm{Li}}\right)^{\alpha_C} \left[\frac{(\alpha_A+\alpha_C) \; F \; (\phi_e-\phi_a)}{RT}\right] \mathrm{d}\Gamma^* \\ &-\int_{\Gamma_a^e} \hat{\phi}_e \; k_R^a \; F \; \left(c_{\mathrm{Li^+}}\right)^{\alpha_A} \; \left(c_{\mathrm{Li}}\right)^{\alpha_C} \left[\frac{(\alpha_A+\alpha_C) \; F \; (\phi_e-\phi_a)}{RT}\right] \mathrm{d}\Gamma^*. \end{aligned} \tag{4.171}$$

4.10.4.1.2 Dimensionless weak form of the lithium foil - electrolyte interface

$$\begin{aligned} \hat{c}^*_{\mathrm{Li^+}} &= \frac{\hat{c}_{\mathrm{Li^+}}}{c_{\mathrm{bulk}}}, \quad \hat{\phi}^*_e = \frac{F}{RT}\hat{\phi}_e, \quad \hat{\phi}^*_a = \frac{F}{RT}\hat{\phi}_a, \quad c^*_{\mathrm{Li}} = \frac{c_{\mathrm{Li}}}{c_{\mathrm{bulk}}}, \quad \mathrm{d}\Gamma^* = \frac{\mathrm{d}\Gamma}{L^2}, \\ c^*_{\mathrm{Li^+}} &= \frac{c_{\mathrm{Li^+}}}{c_{\mathrm{bulk}}}, \quad \phi^*_e = \frac{F}{RT}\phi_e, \quad \phi^*_a = \frac{F}{RT}\phi_a, \quad k_R^{a\,*} = \frac{\bar{t}\,k_R^a}{L} c_{\mathrm{bulk}}^{\alpha_A+\alpha_C-1}. \end{aligned}$$

After applying the dimensionless variables to equation (4.170), the weak form on the lithium foil side becomes:

$$-\left(\alpha_A+\alpha_C\right)\frac{RTc_{\mathrm{bulk}}\;L^3}{\bar{t}} \int_{\Gamma_a^e} \hat{\phi}^*_a \; k_R^{a\,*} \;\; \left(c^*_{\mathrm{Li^+}}\right)^{\alpha_A} \; \left(c^*_{\mathrm{Li}}\right)^{\alpha_C} \Big[\left(\phi^*_e-\phi^*_a\right)\Big] \mathrm{d}\Gamma^*. \tag{4.172}$$

The weak form on the electrolyte side in terms of dimensionless variables, given by Equation (4.171), is expressed as:

$$\begin{aligned} &\left(\alpha_A+\alpha_C\right)\frac{RTc_{\mathrm{bulk}}\;L^3}{\bar{t}} \int_{\Gamma_a^e} \hat{c}^*_{\mathrm{Li^+}} \; k_R^{a\,*} \;\; \left(c^*_{\mathrm{Li^+}}\right)^{\alpha_A} \; \left(c^*_{\mathrm{Li}}\right)^{\alpha_C} \Big[\left(\phi^*_e-\phi^*_a\right)\Big] \mathrm{d}\Gamma^* \\ &-\left(\alpha_A+\alpha_C\right)\frac{RTc_{\mathrm{bulk}}\;L^3}{\bar{t}} \int_{\Gamma_a^e} \hat{\phi}^*_e \; k_R^{a\,*} \;\; \left(c^*_{\mathrm{Li^+}}\right)^{\alpha_A} \; \left(c^*_{\mathrm{Li}}\right)^{\alpha_C} \Big[\left(\phi^*_e-\phi^*_a\right)\Big] \mathrm{d}\Gamma^*. \end{aligned} \tag{4.173}$$

We nondimensionalize the weak forms by dividing both sides of Equations (4.172) and (4.173) by the characteristic power scale $\frac{RTc_{\mathrm{bulk}}\;L^3}{\bar{t}}$, as in the other domains. This factor, which carries units of $(\frac{J}{s})$, is then omitted, yielding the fully dimensionless expressions below.
The dimensionless weak form of lithium foil side reads [4]:

$$-\int_{\Gamma_a^e} \hat{\phi}^*_a \; k_R^{a\,*} \;\; \left(c^*_{\mathrm{Li^+}}\right)^{\alpha_A} \; \left(c^*_{\mathrm{Li}}\right)^{\alpha_C} \Big[\left(\phi^*_e-\phi^*_a\right)\Big] \mathrm{d}\Gamma^*. \tag{4.174}$$

The dimensionless weak form regarding electrolyte side is given by:

$$\int_{\Gamma_a^e} \left(\hat{c}^*_{\mathrm{Li^+}}-\hat{\phi}^*_e\right) \; k_R^{a\,*} \;\; \left(c^*_{\mathrm{Li^+}}\right)^{\alpha_A} \; \left(c^*_{\mathrm{Li}}\right)^{\alpha_C} \Big[\left(\phi^*_e-\phi^*_a\right)\Big] \mathrm{d}\Gamma^*. \tag{4.175}$$

[4] $\alpha_A+\alpha_C$ will be taken to equal 1 (See Table 4.1).

4.10.4.2 Electrolyte-cathode interface

4.10.4.2.1 Weak form of the electrolyte-cathode interface

On the electrolyte side, we refer to the weak form given in the previous section for the lithium–electrolyte interface (see Equation 4.167).

$$\frac{RT}{c_{bulk}} \int_{\Gamma_e^c} \hat{c}_{\mathrm{Li}^+} \left\{ \vec{h}_{\mathrm{Li}^+} \cdot \vec{n}_e \right\} \mathrm{d}\Gamma - F \int_{\Gamma_e^c} \hat{\phi}_e \left\{ \vec{h}_{\mathrm{Li}^+} \cdot \vec{n}_e \right\} \mathrm{d}\Gamma. \tag{4.176}$$

Similarly, the weak-form boundary contribution on the electrolyte-cathode interface from the cathode side, i.e., over $\Gamma_e^c \subset \partial\Omega_c$, reads:

$$\frac{RT}{c_{bulk}} \int_{\Gamma_e^c} \hat{c}_{\mathrm{Li}^\oplus} \left\{ \vec{h}_{\mathrm{Li}^\oplus} \cdot \vec{n}_c \right\} \mathrm{d}\Gamma + \int_{\Gamma_e^c} \hat{\phi}_c \left\{ \vec{i}_{\mathrm{c}} \cdot \vec{n}_c \right\} \mathrm{d}\Gamma. \tag{4.177}$$

By imposing the interface conditions (4.118a), and (4.118c), the weak forms on both sides of the interface are modified as follows: Equation (4.176), corresponding to the electrolyte side, becomes

$$-\frac{RT}{F c_{\mathrm{bulk}}} \int_{\Gamma_e^c} \hat{c}_{\mathrm{Li}^+}\, i_{BV}^c \,\mathrm{d}\Gamma + \int_{\Gamma_e^c} \hat{\phi}_e\, i_{BV}^c \,\mathrm{d}\Gamma. \tag{4.178}$$

while the corresponding expression for the cathode side, Equation (4.177), takes the form

$$\frac{RT}{F c_{\mathrm{bulk}}} \int_{\Gamma_e^c} \hat{c}_{\mathrm{Li}^\oplus}\, i_{BV}^c \,\mathrm{d}\Gamma + \int_{\Gamma_e^c} \hat{\phi}_c\, i_{BV}^c \,\mathrm{d}\Gamma. \tag{4.179}$$

After introducing and linearizing the Butler–Volmer relation for electrolyte-cathode interface in Equation (4.111)

The electrolyte side contribution, obtained from Equation (4.178) becomes:

$$\begin{aligned}
&-\frac{\alpha_A + \alpha_C}{c_{\mathrm{bulk}}} \int_{\Gamma_e^c} \hat{c}_{\mathrm{Li}^+}\, k_R^c F\, (c_{\mathrm{Li}^+})^{\alpha_A} \left(c_{\mathrm{Li}^\oplus}^{sat} - c_{\mathrm{Li}^\oplus}\right)^{\alpha_A} (c_{\mathrm{Li}^\oplus})^{\alpha_C} \\
&\left[(\phi_c - \phi_e) + \frac{\mu_{\mathrm{Li}^\oplus}^0}{F} + \frac{RT}{F} \ln\!\left(\frac{c_{\mathrm{Li}^\oplus}}{c_{\mathrm{Li}^\oplus}^{\mathrm{sat}} - c_{\mathrm{Li}^\oplus}} \right) - \frac{3K_c\, \omega_{\mathrm{Li}^\oplus}}{F} \mathrm{tr}[\boldsymbol{\varepsilon}_c] + \frac{9K_c\, \omega_{\mathrm{Li}^\oplus}^2}{F} \left(c_{\mathrm{Li}^\oplus} - c_{\mathrm{Li}^\oplus}^0\right) \right] \mathrm{d}\Gamma \\
&\quad + \frac{(\alpha_A + \alpha_C) F}{RT} \int_{\Gamma_e^c} \hat{\phi}_e\, k_R^c\, F\, (c_{\mathrm{Li}^+})^{\alpha_A} \left(c_{\mathrm{Li}^\oplus}^{sat} - c_{\mathrm{Li}^\oplus}\right)^{\alpha_A} (c_{\mathrm{Li}^\oplus})^{\alpha_C} \\
&\left[(\phi_c - \phi_e) + \frac{\mu_{\mathrm{Li}^\oplus}^0}{F} + \frac{RT}{F} \ln\!\left(\frac{c_{\mathrm{Li}^\oplus}}{c_{\mathrm{Li}^\oplus}^{\mathrm{sat}} - c_{\mathrm{Li}^\oplus}} \right) - \frac{3K_c\, \omega_{\mathrm{Li}^\oplus}}{F} \mathrm{tr}[\boldsymbol{\varepsilon}_c] + \frac{9K_c\, \omega_{\mathrm{Li}^\oplus}^2}{F} \left(c_{\mathrm{Li}^\oplus} - c_{\mathrm{Li}^\oplus}^0\right) \right] \mathrm{d}\Gamma.
\end{aligned} \tag{4.180}$$

while the cathode-side contribution (4.179) is given by:

$$
\begin{aligned}
&\frac{\alpha_A+\alpha_C}{c_{\text{bulk}}}\int_{\Gamma_e^c}\hat{c}_{\text{Li}^\oplus}\;k_R^c\;F\,(c_{\text{Li}^+})^{\alpha_A}\big(c_{\text{Li}^\oplus}^{sat}-c_{\text{Li}^\oplus}\big)^{\alpha_A}(c_{\text{Li}^\oplus})^{\alpha_C}\\
&\left[(\phi_c-\phi_e)+\frac{\mu_{\text{Li}^\oplus}^0}{F}+\frac{RT}{F}\ln\!\left(\frac{c_{\text{Li}^\oplus}}{c_{\text{Li}^\oplus}^{\text{sat}}-c_{\text{Li}^\oplus}}\right)-\frac{3K_c\,\omega_{\text{Li}^\oplus}}{F}\,\text{tr}[\boldsymbol{\varepsilon}_c]+\frac{9K_c\,\omega_{\text{Li}^\oplus}^2}{F}\big(c_{\text{Li}^\oplus}-c_{\text{Li}^\oplus}^0\big)\right]\mathrm{d}\Gamma\\
&\quad+\frac{(\alpha_A+\alpha_C)F}{RT}\int_{\Gamma_e^c}\hat{\phi}_c\;k_R^c\;F\,(c_{\text{Li}^+})^{\alpha_A}\big(c_{\text{Li}^\oplus}^{sat}-c_{\text{Li}^\oplus}\big)^{\alpha_A}(c_{\text{Li}^\oplus})^{\alpha_C}\\
&\left[(\phi_c-\phi_e)+\frac{\mu_{\text{Li}^\oplus}^0}{F}+\frac{RT}{F}\ln\!\left(\frac{c_{\text{Li}^\oplus}}{c_{\text{Li}^\oplus}^{\text{sat}}-c_{\text{Li}^\oplus}}\right)-\frac{3K_c\,\omega_{\text{Li}^\oplus}}{F}\,\text{tr}[\boldsymbol{\varepsilon}_c]+\frac{9K_c\,\omega_{\text{Li}^\oplus}^2}{F}\big(c_{\text{Li}^\oplus}-c_{\text{Li}^\oplus}^0\big)\right]\mathrm{d}\Gamma.
\end{aligned}
\tag{4.181}
$$

4.10.4.2.2 Dimensionless weak form of the electrolyte - cathode interface

$$
\begin{aligned}
&\hat{c}_{\text{Li}^+}^*=\frac{\hat{c}_{\text{Li}^+}}{c_{\text{bulk}}},\quad \hat{\phi}_e^*=\frac{F}{RT}\hat{\phi}_e,\quad \hat{\phi}_c^*=\frac{F}{RT}\hat{\phi}_c,\quad \hat{c}_{\text{Li}^\oplus}^*=\frac{c_{\text{Li}^\oplus}}{c_{\text{bulk}}},\quad \mathrm{d}\Gamma^*=\frac{\mathrm{d}\Gamma}{L^2},\\
&c_{\text{Li}^+}^*=\frac{c_{\text{Li}^+}}{c_{\text{bulk}}},\quad \phi_e^*=\frac{F}{RT}\phi_e,\quad \phi_c^*=\frac{F}{RT}\phi_c,\quad c_{\text{Li}^\oplus}^*=\frac{c_{\text{Li}^\oplus}}{c_{\text{bulk}}},\quad k_R^{c*}=\frac{\bar{t}\,k_R^c}{L}c_{\text{bulk}}^{2\alpha_A+\alpha_C-1},\\
&\mu_{\text{Li}^\oplus}^{0*}=\frac{\mu_{\text{Li}^\oplus}^0}{RT},\quad \omega_{\text{Li}^\oplus}^*=\omega_{\text{Li}^\oplus}\,c_{\text{bulk}},\quad \vec{u}_c^*=\frac{\vec{u}_c}{L},\quad \nabla^*=L\,\nabla,\quad K_c^*=\frac{K_c}{RTc_{\text{bulk}}}\\
&c_{\text{Li}^\oplus}^{0*}=\frac{c_{\text{Li}^\oplus}^0}{c_{\text{bulk}}},\quad c_{\text{Li}^\oplus}^{sat*}=\frac{c_{\text{Li}^\oplus}^{sat}}{c_{\text{bulk}}}.
\end{aligned}
$$

After applying the dimensionless variables to equation (4.180), the weak form on the electrolyte side becomes:

$$
\begin{aligned}
&-(\alpha_A+\alpha_C)\,\frac{RTc_{\text{bulk}}\,L^3}{\bar{t}}\int_{\Gamma_e^c}\hat{c}_{\text{Li}^+}^*\;k_R^{c*}\;(c_{\text{Li}^+}^*)^{\alpha_A}\big(c_{\text{Li}^\oplus}^{sat*}-c_{\text{Li}^\oplus}^*\big)^{\alpha_A}(c_{\text{Li}^\oplus}^*)^{\alpha_C}\\
&\left[(\phi_c^*-\phi_e^*)+\mu_{\text{Li}^\oplus}^{0*}+\ln\!\left(\frac{c_{\text{Li}^\oplus}^*}{c_{\text{Li}^\oplus}^{sat*}-c_{\text{Li}^\oplus}^*}\right)-3K_c^*\,\omega_{\text{Li}^\oplus}^*\,\nabla^*\cdot\vec{u}_c^*+9K_c^*\,\big(\omega_{\text{Li}^\oplus}^*\big)^2\big(c_{\text{Li}^\oplus}^*-c_{\text{Li}^\oplus}^{0*}\big)\right]\mathrm{d}\Gamma^*\\
&+(\alpha_A+\alpha_C)\,\frac{RTc_{\text{bulk}}\,L^3}{\bar{t}}\int_{\Gamma_e^c}\hat{\phi}_e^*\;k_R^{c*}\;(c_{\text{Li}^+}^*)^{\alpha_A}\big(c_{\text{Li}^\oplus}^{sat*}-c_{\text{Li}^\oplus}^*\big)^{\alpha_A}(c_{\text{Li}^\oplus}^*)^{\alpha_C}\\
&\left[(\phi_c^*-\phi_e^*)+\mu_{\text{Li}^\oplus}^{0*}+\ln\!\left(\frac{c_{\text{Li}^\oplus}^*}{c_{\text{Li}^\oplus}^{sat*}-c_{\text{Li}^\oplus}^*}\right)-3K_c^*\,\omega_{\text{Li}^\oplus}^*\,\nabla^*\cdot\vec{u}_c^*+9K_c^*\,\big(\omega_{\text{Li}^\oplus}^*\big)^2\big(c_{\text{Li}^\oplus}^*-c_{\text{Li}^\oplus}^{0*}\big)\right]\mathrm{d}\Gamma^*
\end{aligned}
\tag{4.182}
$$

The weak form on the cathode side in terms of dimensionless variables, given by Equation (4.181), is expressed as:

$$
\begin{aligned}
&(\alpha_A+\alpha_C)\,\frac{RTc_{\text{bulk}}\,L^3}{\bar{t}}\int_{\Gamma_e^c}\hat{c}^*_{\text{Li}^\oplus}\;k_R^{c*}\;(c^*_{\text{Li}^+})^{\alpha_A}\big(c^{sat*}_{\text{Li}^\oplus}-c^*_{\text{Li}^\oplus}\big)^{\alpha_A}(c^*_{\text{Li}^\oplus})^{\alpha_C}\\
&\left[(\phi_c^*-\phi_e^*)+\mu^{0*}_{\text{Li}^\oplus}+\ln\!\left(\frac{c^*_{\text{Li}^\oplus}}{c^{sat*}_{\text{Li}^\oplus}-c^*_{\text{Li}^\oplus}}\right)-3K_c^*\;\omega^*_{\text{Li}^\oplus}\,\nabla^*\cdot\vec{u}_c^*+9K_c^*\;\big(\omega^*_{\text{Li}^\oplus}\big)^2\big(c^*_{\text{Li}^\oplus}-c^{0*}_{\text{Li}^\oplus}\big)\right]\mathrm{d}\Gamma^*\\
&+(\alpha_A+\alpha_C)\,\frac{RTc_{\text{bulk}}\,L^3}{\bar{t}}\int_{\Gamma_e^c}\hat{\phi}_c^*\;k_R^{c*}\;(c^*_{\text{Li}^+})^{\alpha_A}\big(c^{sat*}_{\text{Li}^\oplus}-c^*_{\text{Li}^\oplus}\big)^{\alpha_A}(c^*_{\text{Li}^\oplus})^{\alpha_C}\\
&\left[(\phi_c^*-\phi_e^*)+\mu^{0*}_{\text{Li}^\oplus}+\ln\!\left(\frac{c^*_{\text{Li}^\oplus}}{c^{sat*}_{\text{Li}^\oplus}-c^*_{\text{Li}^\oplus}}\right)-3K_c^*\;\omega^*_{\text{Li}^\oplus}\,\nabla^*\cdot\vec{u}_c^*+9K_c^*\;\big(\omega^*_{\text{Li}^\oplus}\big)^2\big(c^*_{\text{Li}^\oplus}-c^{0*}_{\text{Li}^\oplus}\big)\right]\mathrm{d}\Gamma^*
\end{aligned}
\tag{4.183}
$$

We express the weak forms in nondimensional form by dividing both sides of Equations (4.182) and (4.183) by the characteristic power scale $\frac{RTc_{\text{bulk}}\,L^3}{\bar{t}}$, consistent with the other domains. Since this factor has units of $(\frac{J}{s})$, we subsequently drop it, obtaining the fully dimensionless forms shown as following:
The dimensionless weak form of electrolyte side reads

$$
\begin{aligned}
&-\int_{\Gamma_e^c}\Big(\hat{c}^*_{\text{Li}^+}-\hat{\phi}_e^*\Big)\;k_R^{c*}\;(c^*_{\text{Li}^+})^{\alpha_A}\big(c^{sat*}_{\text{Li}^\oplus}-c^*_{\text{Li}^\oplus}\big)^{\alpha_A}(c^*_{\text{Li}^\oplus})^{\alpha_C}\\
&\left[(\phi_c^*-\phi_e^*)+\mu^{0*}_{\text{Li}^\oplus}+\ln\!\left(\frac{c^*_{\text{Li}^\oplus}}{c^{sat*}_{\text{Li}^\oplus}-c^*_{\text{Li}^\oplus}}\right)-3K_c^*\;\omega^*_{\text{Li}^\oplus}\,\nabla^*\cdot\vec{u}_c^*+9K_c^*\;\big(\omega^*_{\text{Li}^\oplus}\big)^2\big(c^*_{\text{Li}^\oplus}-c^{0*}_{\text{Li}^\oplus}\big)\right]\mathrm{d}\Gamma^*.
\end{aligned}
\tag{4.184}
$$

The dimensionless weak form regarding cathode side is given by:

$$
\begin{aligned}
&\int_{\Gamma_e^c}\Big(\hat{c}^*_{\text{Li}^\oplus}+\hat{\phi}_c^*\Big)\;k_R^{c*}\;(c^*_{\text{Li}^+})^{\alpha_A}\big(c^{sat*}_{\text{Li}^\oplus}-c^*_{\text{Li}^\oplus}\big)^{\alpha_A}(c^*_{\text{Li}^\oplus})^{\alpha_C}\\
&\left[(\phi_c^*-\phi_e^*)+\mu^{0*}_{\text{Li}^\oplus}+\ln\!\left(\frac{c^*_{\text{Li}^\oplus}}{c^{sat*}_{\text{Li}^\oplus}-c^*_{\text{Li}^\oplus}}\right)-3K_c^*\;\omega^*_{\text{Li}^\oplus}\,\nabla^*\cdot\vec{u}_c^*+9K_c^*\;\big(\omega^*_{\text{Li}^\oplus}\big)^2\big(c^*_{\text{Li}^\oplus}-c^{0*}_{\text{Li}^\oplus}\big)\right]\mathrm{d}\Gamma^*.
\end{aligned}
\tag{4.185}
$$

4.11 Numerical example

The proposed numerical LIB model is applied to various scenarios to verify its consistency and to gain deeper insight into the coupled electro-chemo-mechanical behavior, particularly in the absence of experimental data. All simulations are performed using our in-house multi-physics research code, which is based on the open-source finite element library deal.ii[23]. To visualize both the simulation geometries and resulting physical fields, we use Kitware ParaView 5.13.0 [336]. Furthermore, all plots are generated using Python 3.11 [337] with the Matplotlib library [338]. The time evolution of the simulations is conducted with a fixed time step of $\Delta t = 1$ s. The LIB cells are subjected to constant current discharge conditions corresponding to C-rates of 0.5C, 1C, and 2C. In this context, a C-rate of n implies that the full charging or discharging process is completed within a time span of $\frac{1}{n}$ hours. For example, a C-rate of 1 indicates a complete discharge in one hour,

while a C-rate of 2 corresponds to a discharge time of 30 minutes. These varying C-rates are employed to analyze how the coupled electrochemical and mechanical behavior evolves under different operational conditions.

4.11.1 Description of computational domains

In this section, we present the three-dimensional particle-resolved computational geometry of the system (Figure 4.5). Rather than a tomography-based reconstruction, the geometry is an idealized yet representative microstructure constructed by adopting the overall domain dimensions reported in [138]. The computational domain includes a lithium foil anode (red), the liquid electrolyte region, embedded within both the separator and the porous cathode structure (beige), the cathode active particles (green), and the cathode-side current collector (blue). The 3D domain spans a total thickness of 95 μm in the through (z) direction, with a square cross-section of 13.4 μm$\times$ 13.4 μm in the x–y plane. Specifically, the domain consists of a 10 μm-thick lithium anode foil, a 35 μm-thick electrolyte-filled separator, and a 36.5 μm-thick porous cathode region filled with electrolyte, extending from the separator to the cathode current collector. The porous cathode also contains randomly distributed spherical active material particles, followed by a 13.5 μm-thick aluminum current collector. While the electrolyte thicknesses in the separator and the porous cathode are slightly modified, the total electrolyte domain thickness is preserved to remain consistent with the reference model in [138]. The interfaces between the cathode and electrolyte, the electrolyte and anode, as well as the cathode and current collector, are modeled using zero-thickness interface elements. The computational geometry is constructed using NETGEN [339], whereas the high-quality tetrahedral mesh generation is carried out using Gmsh [340]. Because deal.ii is not directly compatible with the tetrahedral meshes produced by Gmsh for the element types used here, we additionally used TETHEX to convert the mesh into a hexahedral mesh compatible with deal.ii. The finite element mesh used in this study consists of 28,176 tetrahedral elements defined by 32,827 nodes, resulting in a total of 257,047 degrees of freedom across the computational domain. This finite element mesh demonstrates the applicability of the given model to practical applications.

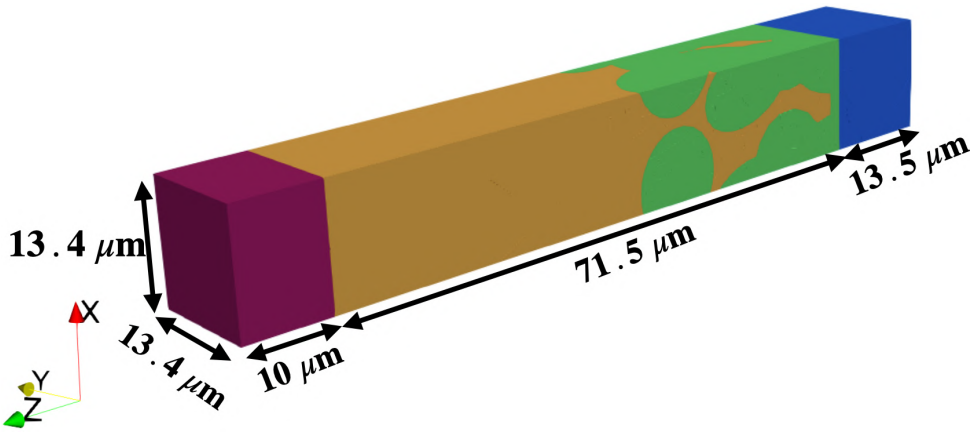

Figure 4.5: Realistic geometry of an LIB battery cell

Material Parameters				
	Symbol	Value	Unit	ref
Cathode				
Max Li Concentration	$c^{sat}_{\mathrm{Li}^{\oplus}}$	2.39×10^4	mol/m^3	[332]
Diffusivity of Lithium	$\mathbb{D}_{\mathrm{Li}^{\oplus}}$	$5.387{\times}10^{-15}$	m^2/s	[332]
Chemical Expansion coefficient	$\omega_{\mathrm{Li}^{\oplus}}$	-5.3×10^{-7}	m^3/mol	[341]
Electronic conductivity	κ_c	10	S/m	[342]
Young modulus	E_c	370	GPa	[332]
Poisson ratio	ν_c	0.2	-	[332]
Anode				
Electronic conductivity	κ_a	1.08×10^7	S/m	[260]
Young modulus	E_a	4.9	GPa	[343]
Poisson ratio	ν_a	0.36	-	[343]
Electrolyte				
Saturation limit of electrolyte	$c^{sat}_{\mathrm{Li}^{+}}$	1×10^4	mol/m^3	[252]
Diffusivity of Li^+ ions	$\mathbb{D}_{\mathrm{Li}^{+}}$	2×10^{-11}	m^2/s	[252]
Diffusivity of X^- ions	$\mathbb{D}_{\mathrm{X}^{-}}$	3×10^{-11}	m^2/s	[252]
Young modulus	E_e	450	MPa	[344]
Poisson ratio	ν_e	0.499	-	[345]
Collector				
Electronic conductivity	κ_{col}	3.77×10^7	S/m	[346]
Young Modulus	E_{cc}	70	GPa	[346]
Poisson ratio	ν_{cc}	0.35	-	[346]
Anode-Electrolyte Interface				
Forward Kinetic Constant	α_A	0.5	-	[347]
Backward Kinetic Constant	α_C	0.5	-	[347]
Anode Reactivity coefficient	k^a_R	1×10^{-5}	-	[138]
Cathode-Electrolyte Interface				
Forward Kinetic Constant	α_A	0.5	-	[347]
Backward Kinetic Constant	α_C	0.5	-	[347]
Cathode Reactivity coefficient	k^c_R	6.67×10^{-11}	-	[347]

Table 4.1: Material parameters for the computational domain.
[5]

4.11.2 Material parameters of the LIB cell

The material parameters used in all simulations are provided in Table 4.1. The materials were selected in the simulations as already stated in Section 4.2.1. The mechanical and electrochemical behavior of each battery domain is modeled with simplifications appropriate to this study. In the cathode, we do not consider lithium-ion trapping or inelastic deformations in the $LiCoO_2$ active material, in order to avoid additional complexity, as discussed in [261]. The electrolyte is modeled as an incompressible medium, reflecting the nearly incompressible nature of conventional liquid electrolytes in lithium-ion batteries; this is implemented by assigning a Poisson's ratio close to 0.5. In order to ensure dilute-solution conditions, the saturation concentration $c^{\mathrm{sat}}_{\mathrm{Li}^{+}}$ is chosen to be one order of

[5] Assuming linear elastic behavior, the shear modulus (G) and bulk modulus (K) used in simulations for each domain were computed from the provided in table Young's modulus (E) and Poisson's ratio (ν).

magnitude higher than the initial concentrations of the mobile ionic species, Li^+ and X^-, following the guidance in [252]. The anode, modeled as a lithium metal foil, is treated as an infinite lithium reservoir as described in Section 4.2.1, implying no spatial or temporal variation in lithium concentration; it is fixed at 7.64×10^4 mol/m^3, as given in Equation (4.134). The current collector is modeled as an electrochemically inert aluminum foil with high electrical conductivity (3.77×10^7 S/m), ensuring efficient electron conduction while preventing surface dissolution. Interfaces between domains are treated as ideal, with perfect contact assumed for all mechanical and electrochemical couplings. All parameters related to the interfaces are taken from the literature, as listed in Table 4.1.

4.11.3 Numerical outcomes and discussion

4.11.3.1 Electro-chemo-mechanical response at 1C

The battery voltage

In the 3D simulation of the whole battery cell, the variation in electric potential between the initial and final time steps is relatively small. Consequently, full-domain colormap visualizations are not effective, as these small changes are difficult to discern across different domains such as the anode, electrolyte, cathode, and current collector. To better illustrate the spatiotemporal evolution of the electric potential ϕ, a representative 1D line is extracted along the edge of the cell as shown in Figure 4.6, spanning the entire length from the anode to the current collector. The representative line is taken along the cell edge to avoid the geometrical irregularities of the realistic cathode structure, whose complex porous morphology could otherwise hinder a smooth and interpretable potential vs length profile. At $t = 0\,\mathrm{s}$, the system is assumed to be in thermodynamic equilibrium, and the electric potential on the lithium-foil anode is set to $\phi_a = 0$ V by taking metallic lithium as the reference electrode, as previously defined (Equation 4.137). During battery discharge, the electric potential varies approximately linearly within the electronically conductive domains (anode, cathode, and current collector), following Ohm's law. However, this linear trend is not clearly visible in the figure due to the extremely small potential gradients in these regions. A sharp potential jump is observed near $x \approx 50\,\mu$m, corresponding to the electrolyte–cathode interface Γ_c^e, which arises from electrochemical reaction kinetics described by the Butler–Volmer equation (4.111). The battery voltage, defined as the potential difference between the electrodes, gradually decreases during discharge. The overall voltage drop is primarily due to the potential drop across the cathode–electrolyte interface Γ_c^e. Figure 4.7a illustrates the battery voltage response under a 1C constant current discharge, shown as a function of time. The discharge curve reveals three distinct stages: an initial voltage drop attributed to instantaneous ohmic resistance (IR drop), a subsequent gradual and continuous decline without a well-defined plateau region, and a final rapid decrease as the discharge nears completion. This simulation terminates at $t = 2850\,\mathrm{s}$, when the lithium concentration in the cathode reaches saturation. Notably, unlike experiments that apply a voltage cutoff, this model uses a concentration-based stopping criterion. Another point of interest is the comparison between the theoretical maximum extracted charge Q_{th} and the extracted charge at 1C. To quantify Q_{th}, we define $x \in (0, 1)$ as the lithium stoichiometric ratio in the layered cathode material Li_xCoO_2, where x typically ranges from 0.5 to 1.0 under normal battery operation. Within this range, the theoretical maximum extracted charge follows from the change in lithium con-

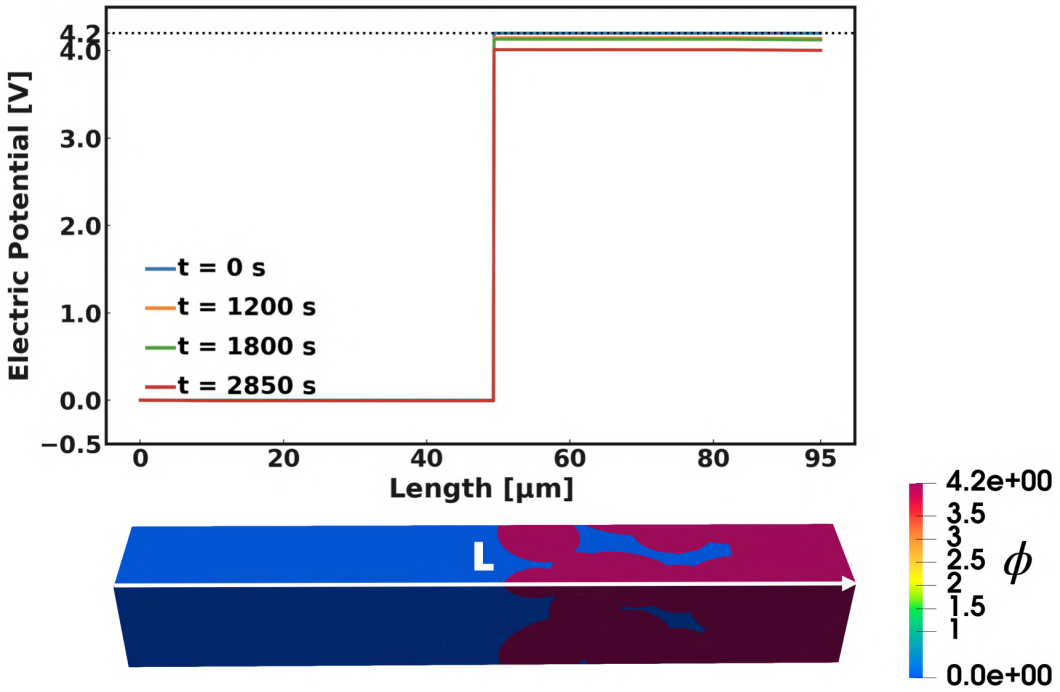

Figure 4.6: Spatial and temporal evolution of electric potential ϕ in the whole domains according to the selected edge.

centration within the active cathode volume, as given by:

$$Q_{\text{th}} = F\left(c_{\text{Li}^\oplus}^{\text{sat}} - c_{\text{Li}^\oplus}^{0}\right) V_{\text{LiCoO}_2} = 4.066 \times 10^{-6}\,\text{C} = 1.13 \times 10^{-6}\,\text{mAh}, \tag{4.186}$$

where Faraday's constant F is introduced earlier in Section 4.3.3, and $V_{\text{LiCoO}_2} = 3.52757 \times 10^{-15}\,\text{m}^3$, computed using Kitware ParaView 5.13.0 [336]. The calculation assumes a maximum lithium concentration $c_{\text{Li}^\oplus}^{\text{sat}}$, as listed in Table 4.1, and an initial concentration $c_{\text{Li}^\oplus}^{0}$, which is given in Equation (4.136). With this, the theoretical capacity range is defined. Surface open-circuit potential (OCP), which serves as a reference for comparison against the simulated battery voltage during discharge, is calculated from Equation (4.115). Figure 4.7b compares the simulated battery voltage with the idealized surface OCP given by Equation (4.115), constructed under the assumptions of a stress-free electrode and uniform lithium distribution. The OCP profile extends up to the theoretical capacity obtained in Equation (4.186), which corresponds to the complete extraction of lithium within the allowed concentration range. As observed, the simulated voltage remains consistently lower than the OCP due to dynamic effects such as overpotential η, defined as the difference between the battery voltage and OCP.

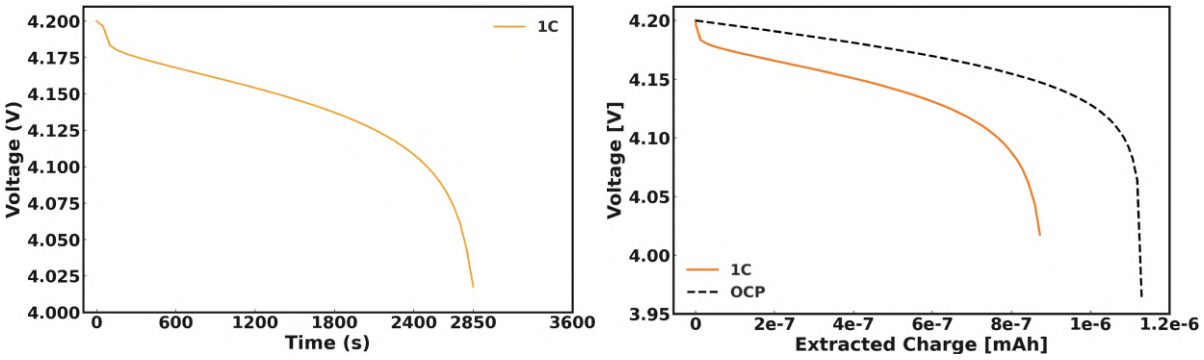

(a) (b)

Figure 4.7: (a) Simulated battery voltage at 1C. (b) Comparison between the simulated 1C battery voltage and the open-circuit potential (OCP) as a function of extracted charge.

The evolution of lithium concentration in the cathode

The simulation is carried out under galvanostatic discharge conditions at 1C, and terminates at $t = 2850\,\mathrm{s}$, once the surfaces of the active material particles reach saturation, thereby limiting the interfacial lithium flux and preventing further intercalation into the particle interiors. Figures 4.8a–4.8d illustrate the spatiotemporal evolution of lithium-ion concentration $c_{\mathrm{Li}^\oplus}$ within the cathode region at selected time instants ($t = 0\,\mathrm{s}, t = 1200\,\mathrm{s}, t = 1800\,\mathrm{s}, t = 2850\,\mathrm{s}$), with a particular focus on the intercalation process into active material particles. As specified in the initial conditions (see Section 4.9), the concentration is initially set to 11950 mol/m^3, representing a uniform initial lithium concentration equal to half of the saturation limit $c^{sat}_{\mathrm{Li}^\oplus}$ (see Table 4.1). This uniform initial state indicates that no prior intercalation has occurred before the onset of the simulation. As the discharge progresses, lithium ions begin to intercalate into the active particles via the cathode–electrolyte interface Γ^e_c, resulting in a significant increase in concentration near the particle surfaces. Over time, a pronounced concentration gradient develops within the particles, with elevated values at the particle surface and slower penetration toward the core at a given discharge rate. This behavior arises from the limited rate of lithium diffusion through the solid active material and from the particle's geometry, which lengthens or constrains the diffusion pathways. Figure 4.8 qualitatively demonstrates the evolution of lithium distribution throughout the porous cathode during 1C discharge, and reflects the progressive accumulation of lithium, with progressively stronger accumulation near particle surfaces characteristic of diffusion-limited intercalation. To give the reader a general sense of intraparticle behavior, we analyze the representative active-material particle highlighted in Figure 4.9, extracted from the cathode microstructure. Figures 4.10a-4.10d shows the lithium concentration distribution within this particle at different times, while Figure 4.10e presents the corresponding profile of $c_{\mathrm{Li}^\oplus}$ along the arc length $\mathrm{L_{ca}}$, defined from point P1 (on the electrolyte-contacting surface at the top) to point P2 (on the electrolyte-contacting surface at the bottom). This arc-based path allows us to assess how intercalation progresses spatially along the particle interior.

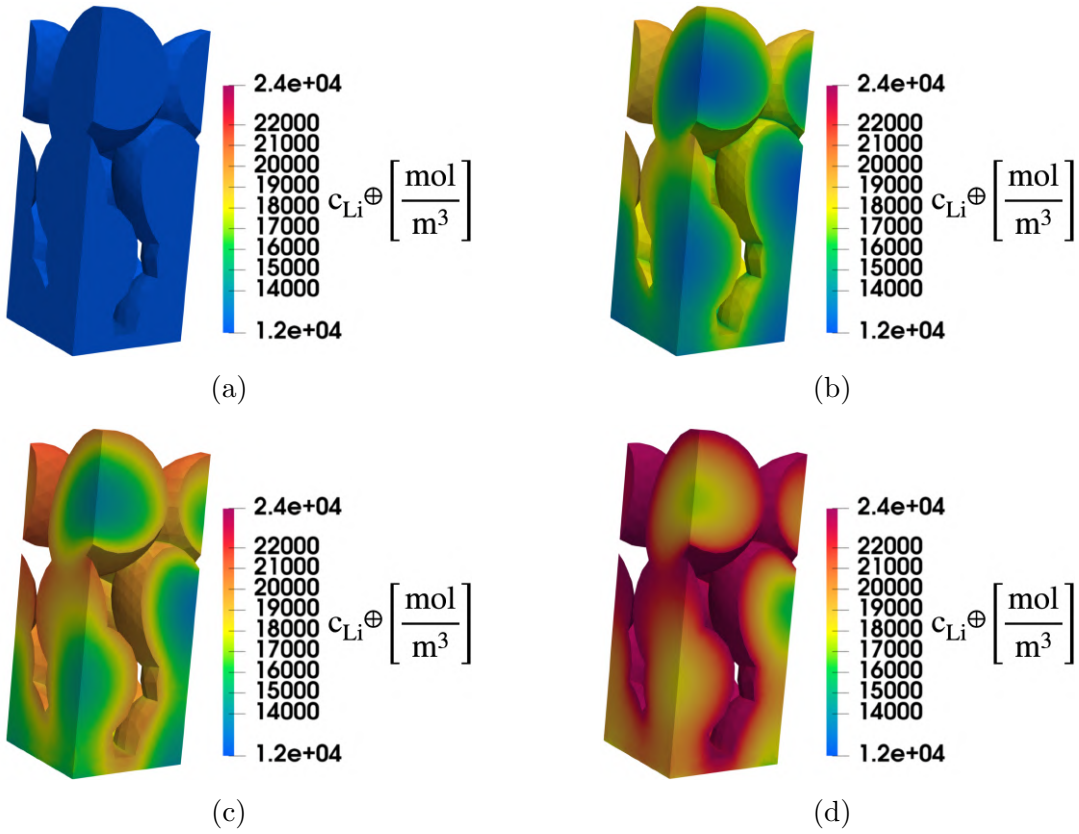

Figure 4.8: Spatial and temporal evolution of lithium-ion concentration $c_{\mathrm{Li}^\oplus}$ in the cathode active material under 1C discharge. (a–d) show 3D maps of $c_{\mathrm{Li}^\oplus}$ at $t = 0$, 1200, 1800, and 2850 s, respectively.

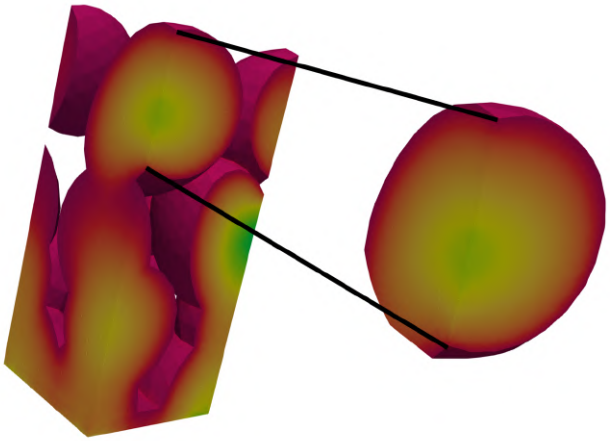

Figure 4.9: A representative cathode particle is selected from the randomly distributed active material in the cathode.

Initially, at $t = 0$ s, the concentration profile is uniform. As discharge progresses, lithium intercalates from the electrolyte-facing surface, and a gradient develops along the arc length L_{ca}. At $t = 1200$ s, $c_{\mathrm{Li}^\oplus}$ is ≈ 18173 mol/m^3 at Point P1 and ≈ 16028 mol/m^3 at Point P2; by $t = 1800$ s these become ≈ 20211 mol/m^3 at Point P1 and 18179 mol/m^3 at Point P2. At $t = 2850$ s, near the end of discharge, both approach the saturation limit $\approx$

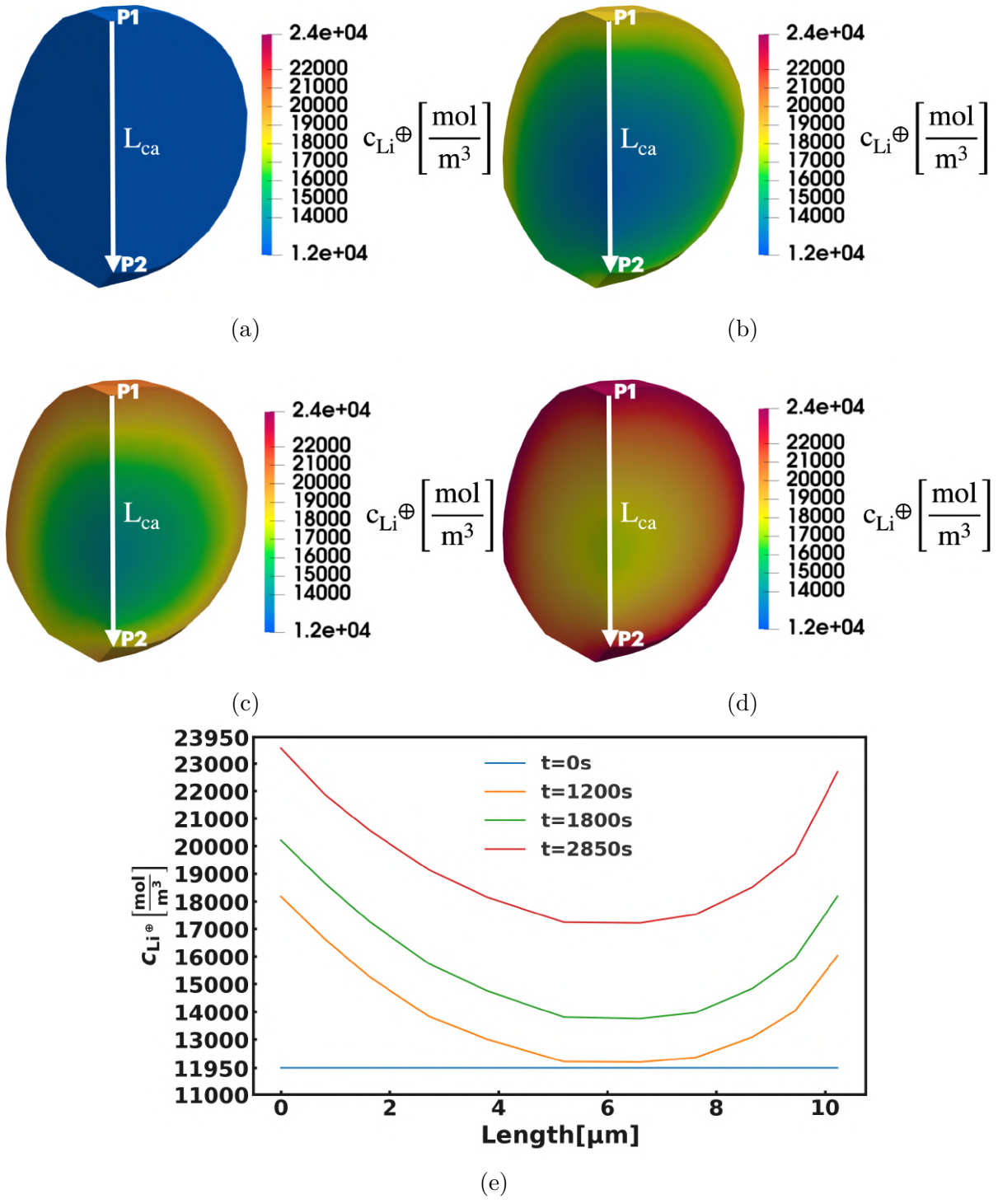

Figure 4.10: Intraparticle lithium-ion concentration in a representative cathode particle under 1C discharge. (a–d) 3D maps of $c_{\mathrm{Li}^\oplus}$ at $t = 0$, 1200, 1800, and 2850 s. (e) Concentration profiles $c_{\mathrm{Li}^\oplus}$ along L_{ca}, showing a U-shaped distribution—higher values near P1 and P2 and lower values in the core.

23900 mol/m^3, with P1 still higher at $\approx$ 23546 mol/m^3 than P2 at 22684 mol/m^3. These trends indicate diffusion-limited transport in the solid at 1 C where lithium accumulates near the surface while the interior lags. Although both P1 and P2 contact the electrolyte,

geometric asymmetries yield larger interfacial fluxes at P1, especially early on. Consequently, the profile along L_{ca} is U-shaped—higher at P1 and P2 and lower in the center 4.10e.

The evolution of lithium concentration in the electrolyte

Figures 4.11a-4.11b illustrate the spatiotemporal evolution of c_{Li^+} in the electrolyte domain during 1C discharge at selected time instants ($t = 0\,s$, $t = 2850\,s$). Initially, at $t = 0\,s$, the electrolyte exhibits a uniform c_{Li^+} distribution of $1500\,mol/m^3$. As discharge proceeds, lithium ions are released at the anode and consumed by intercalation at the porous cathode, producing enrichment near the anode/electrolyte interface and depletion near the electrolyte/cathode interface. To reveal evolution of c_{Li^+} that are not obvious at intermediate time instants, Figure 4.11c presents the evolution of c_{Li^+} along the electrolyte thickness L_e at selected time instants, based on one-dimensional profiles extracted along a single continuous section spanning the entire electrolyte from the anode/electrolyte interface to the electrolyte/cathode interface, thus showing how c_{Li^+} varies along L_e. A concentration gradient develops across the electrolyte and approaches a quasi-steady profile at later times (e.g., $t = 1200$–$2850\,s$). Within the bulk electrolyte (up to $\approx 35\,\mu m$), the gradient remains smooth and continuous. Beyond this region, inside the porous cathode, the concentration profile departs from linearity due to the heterogeneous electrode geometry (shape, size, and spatial distribution of active particles), which induces local variations in the concentration along the sampling line, despite uniform electrolyte transport parameters. Quantitatively, at $t = 1200\,s$ the concentrations are $\approx 1554.8\ mol/m^3$ at the anode/electrolyte interface and $\approx 1391.8\ mol/m^3$ at the electrolyte/porous-cathode interface; at $t = 1800\,s$ they are ≈ 1555.1 and $1389.8\ mol/m^3$; and at $t = 2850\,s \approx 1555.7$ and $1385.7\ mol/m^3$, respectively. These small changes in the interface values after $t \approx 1200\,s$ confirm the approach to quasi–steady-state behavior under galvanostatic 1C discharge.

Mechanical response of the current collector

After establishing the lithium concentration fields in the cathode and electrolyte, we now quantify the mechanical response starting at the current collector at the bottom of the domain and proceeding upward along the z-direction through the porous cathode and electrolyte to the lithium metal foil anode. Figures 4.12a–4.12c show the displacement magnitude $||\vec{u}_{cc}||$ at selected time instants ($t = 1200\,s, t = 1800\,s, t = 2850\,s$). In the current collector, the clamped bottom surface enforces a zero-displacement boundary condition ($\vec{u}_{cc} = 0$ on $\partial\Omega^B_{cc}$). At $t = 2850$ s, the displacement magnitude $||\vec{u}_{cc}||$ increases from the clamped bottom along the z-direction and peaks at the cathode-current collector interface Γ^c_{cc}, reaching $\approx 3.4 \times 10^{-8}$ m. The collector's deformation arises from intercalation-induced shrinkage in the cathode (discussed in the following section) and is transmitted to the collector via displacement continuity at the interface ($\vec{u}_c = \vec{u}_{cc}$ on Γ^c_{cc}). Figure 4.13a–4.13c show the out-of-plane displacement u_z in the current collector at the selected times. The clamped bottom keeps $u_z = 0$. During discharge, u_z increases in magnitude along z-direction toward the cathode-collector interface Γ^c_{cc}. Within the interfacial plane (x–y), the field is non-uniform and local peaks appear at some locations, while neighboring regions show smaller, occasionally slightly negative values as a result of displacement continuity. The amplitude increases over time, reaching $\approx 1.9 \times 10^{-8}\,m$ at the cathode-collector interface at $t = 2850\,s$.

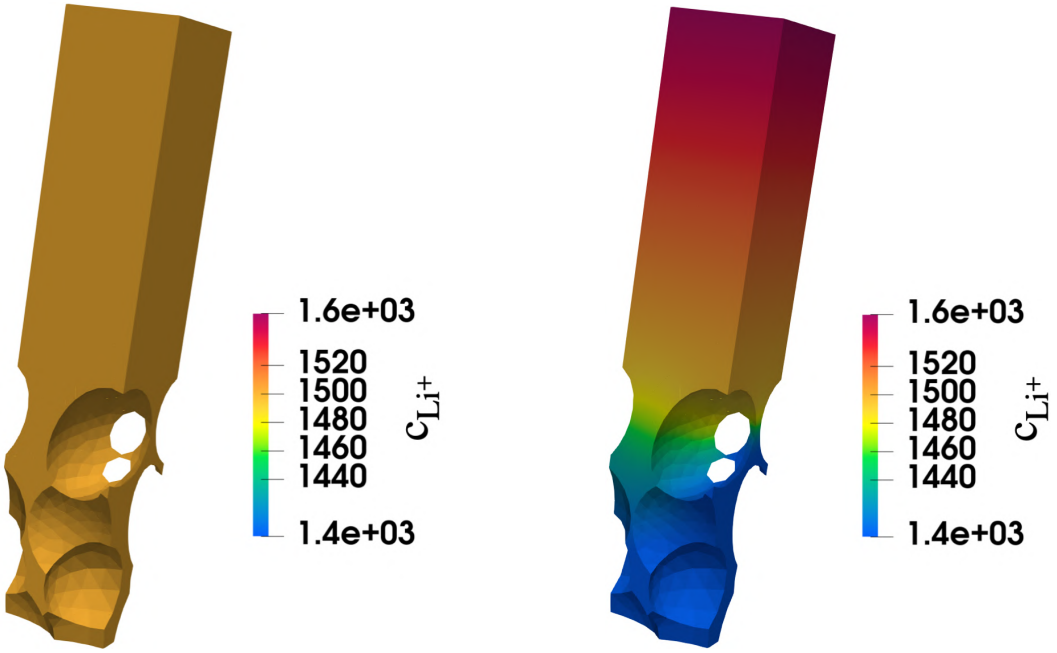

(a) (b)

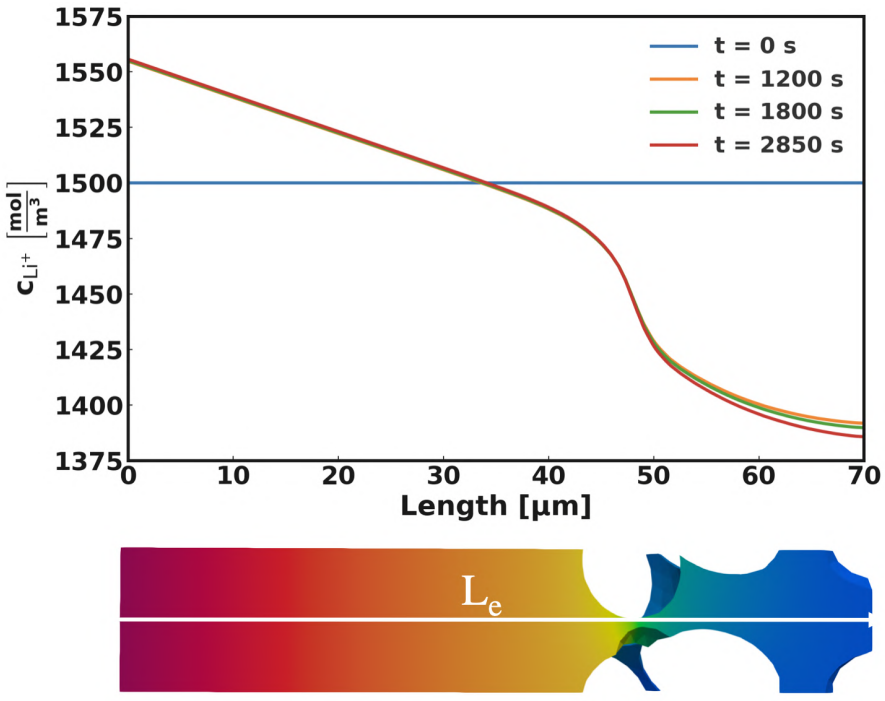

(c)

Figure 4.11: (a–b) spatiotemporal evolution of c_{Li^+} in the electrolyte domain at $t = 0\,\mathrm{s}$, and $2850\,\mathrm{s}$ respectively. (c) evolution of c_{Li^+} in the electrolyte along the thickness $\mathrm{L_e}$ at $t = 0$, 1200, 1800, and $2850\,\mathrm{s}$.

Mechanical response of the cathode

Figures 4.14a-4.14c visualizes the time evolution of the displacement magnitude $||\vec{u}_c||$ within the cathode region at selected time instants. Intercalation-induced chemical strain drives an overall increase in displacements, which localize heterogeneously across the microstructure. Larger magnitudes develop near the top of the cathode, reaching $\approx$

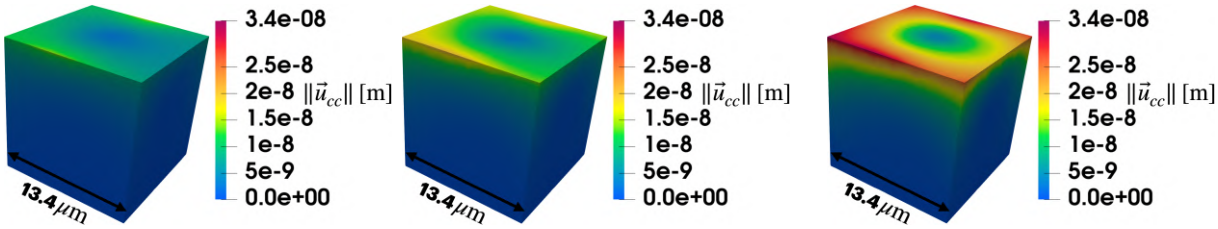

(a) (b) (c)

Figure 4.12: (a–c) show the time evolution of displacement magnitude $\|\mathbf{u}_{cc}\|$ at 1200, 1800, and 2850 s, respectively. At $t = 0$ s no displacement is present in the domain.

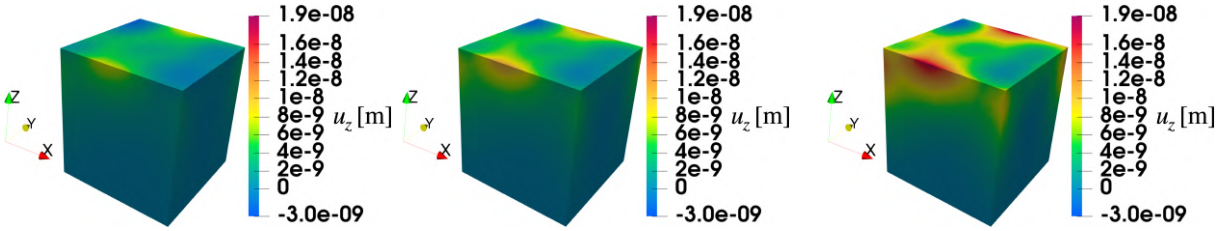

(a) (b) (c)

Figure 4.13: (a–c) show the time evolution of displacement u_z in the current collector at 1200, 1800, and 2850 s, respectively. At $t = 0$ s, $u_z = 0$ throughout the current collector.

1.8×10^{-7} m at $t = 2850$ s, whereas regions adjacent to the current collector deform less—consistent with the clamped bottom of the collector and displacement continuity at the cathode–collector interface ($\vec{u}_c = \vec{u}_{cc}$ on Γ_c^{cc}). Figures 4.15a-4.15c depict the evolu-

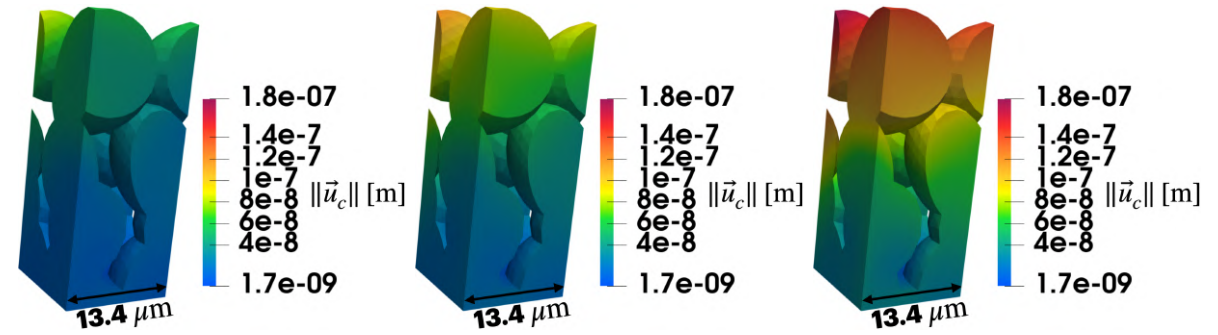

(a) (b) (c)

Figure 4.14: (a–c) show the time evolution of displacement magnitude $\|\mathbf{u}_c\|$ at 1200, 1800, and 2850 s, respectively. At $t = 0$, no lithiation has occurred yet, and thus no displacement is present in the domain.

tion of the out-of-plane displacement u_z in the cathode. During discharge, intercalation-induced chemical strain (net shrinkage in this configuration) produces a clear vertical gradient that steepens from 1200 to 2850 s. Near the cathode–collector interface Γ_c^{cc}, which is closer to the clamped bottom via the collector, vertical motion is more restricted, so u_z remains close to zero and reaches $\approx 1.9 \times 10^{-8}$ m at $t = 2850$ s. Farther from the clamp, constraints are weaker, u_z becomes increasingly negative and reaches $\approx -1.6 \times 10^{-7}$ m at $t = 2850$ s. Beyond the displacement fields, we begin to analyze the system's mechanical

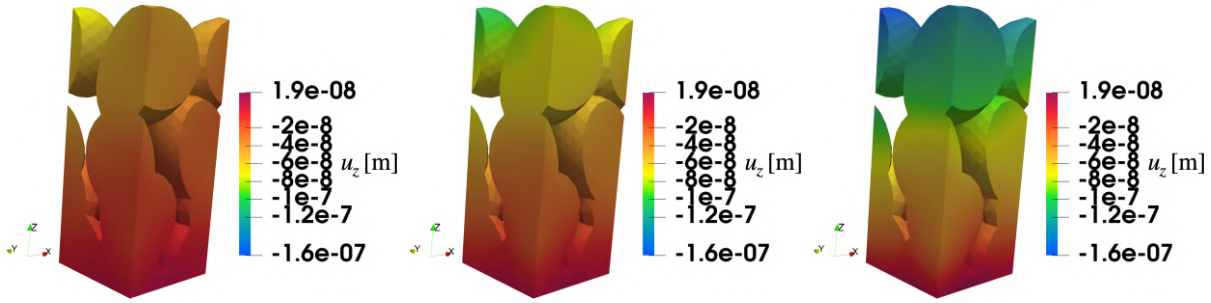

(a) (b) (c)

Figure 4.15: (a–c) show the time evolution of displacement u_z in the cathode at 1200, 1800, and 2850 s, respectively.

stress response at the baseline 1C discharge rate, quantifying stress via the von Mises (J2) equivalent. As previously discussed in [67, 332, 348], electrochemically driven lithiation alters the specific volume of $LiCoO_2$, giving rise to mechanical stresses. Figures 4.16a–

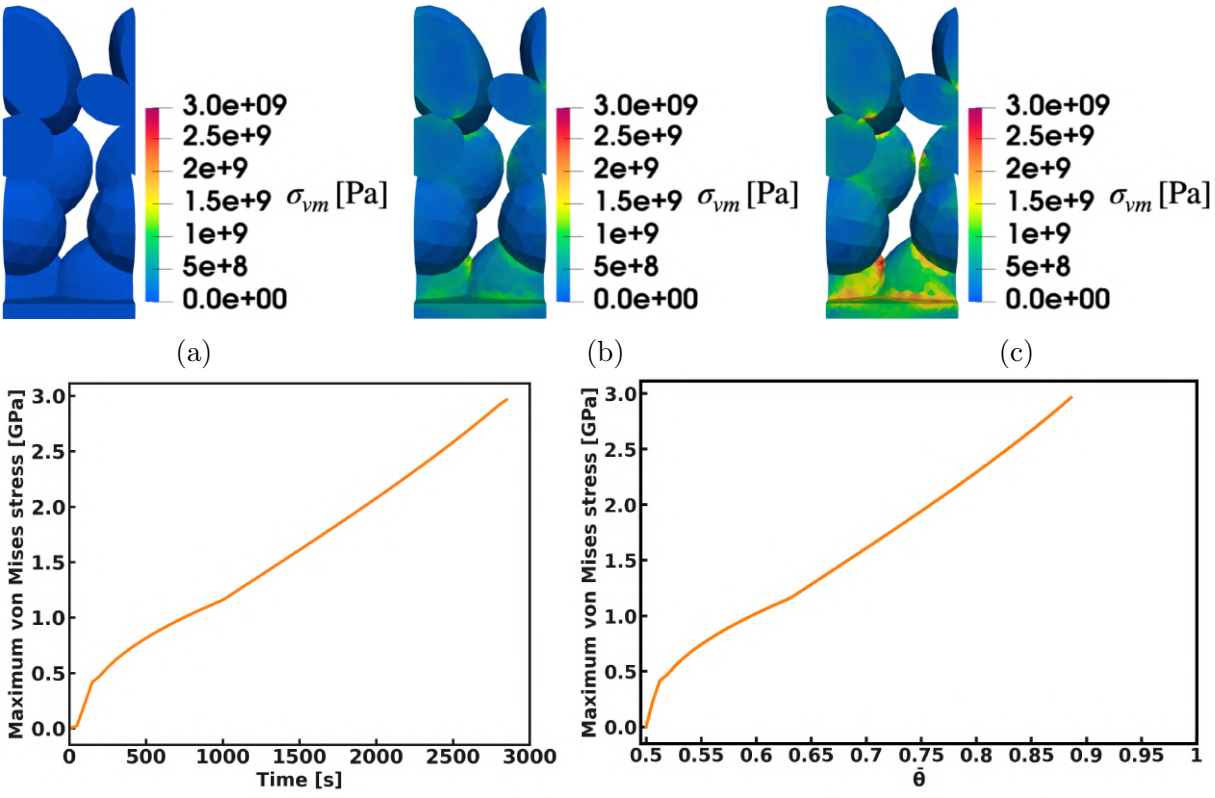

(a) (b) (c)

(d) (e)

Figure 4.16: (a–c) Evolution of von Mises stress during 1C discharge at $t = 0$, 1400, , and 2850 s, respectively, (d) the corresponding global maximum von Mises stress versus time, (e) the corresponding global maximum von Mises stress versus $\bar{\theta}$.

4.16c visualize the evolution of von Mises stress, σ_{vm}, in the cathode during 1C discharge. In order to make the interior high-stress regions visible, we apply a mid-plane clip along the z-axis and show the resulting view. As lithium intercalates, the stress-free specific volume of LCO decreases; accordingly, an isolated spherical particle under isotropic conditions would shrink uniformly and remain stress-free [349, 350, 351]. In the geometrically

confined, particle-resolved network considered here, however, this chemical contraction is constrained, generating stresses that localize at particle–particle contacts and evolve over time. Figures 4.16d-4.16e shows the global maximum σ_{vm} that develop throughout discharge at 1C over the entire cathode (i.e., the largest value attained anywhere in the domain at that time). As shown in Figure 4.16d, the maximum σ_{vm} increase throughout discharge, reaching $\approx 3\,\mathrm{GPa}$ by $t = 2850\ s$ as a consequence of lithium intercalation. We also parameterize the response by the lithiation state. Figure 4.16e presents the maximum σ_{vm}, as a function the $\bar{\theta}$ where $\bar{\theta}$ is defined as the ratio of the total moles of lithium in the cathode at a given time to the maximum moles the active cathode can host at saturation. As $\bar{\theta}$ increases, maximum σ_{vm} rises nearly monotonically and approaches $\approx 3\,\mathrm{GPa}$ near the end of discharge. The curve terminates before $\bar{\theta} = 1$ because surface regions approach saturation while particle cores remain partially unsaturated, consistent with the Figure 4.8. In addition to the von Mises stress, we evaluate the maximum principal (tensile) stress, $\sigma_{\max}$, so that our results can be compared with Malavé et al. [332]. We take the mechanical material parameters (elastic constants and related inputs) largely from that study, which reported peak stresses at geometric stress concentrators in isolated single-particle analyses. Figures 4.17a–4.17c visualize the evolution of maximum principal tensile stress, σ_{max}, in the cathode during 1C discharge. In our geometrically confined network, the peak stresses are markedly higher, reaching 4.9 GPa in maximum principal (tensile) stress , σ_{max}, at particle-particle contacts, at 1C, as shown in Figure 4.17, whereas the isolated-particle analyses by Malavé et al.[332] report peaks of only $\approx 85\,\mathrm{MPa}$–underscoring that network-level geometric confinement can elevate stresses by approximately two orders of magnitude and that full microstructural reconstructions are essential for stress analysis. With peak stresses above 1 GPa, fracture of LCO particles becomes a credible outcome. Prior work exemplified by Zhao et al. [352] uses an energy-balance framework to infer the largest particle sizes that can withstand a given discharge rate [70, 352, 353]. Renganathan et al. [342] report that ceramics typically fracture at about 1% tensile strain, which for LCO corresponds to a fracture stress of 3.7 GPa. Given that our maximum principal tensile stresses reach 4.9 GPa at last time instant as depicted in Figure 4.17d, these levels may be sufficient to initiate cracking in LCO particles, which would in turn reduce local stress and alter the microstructure.

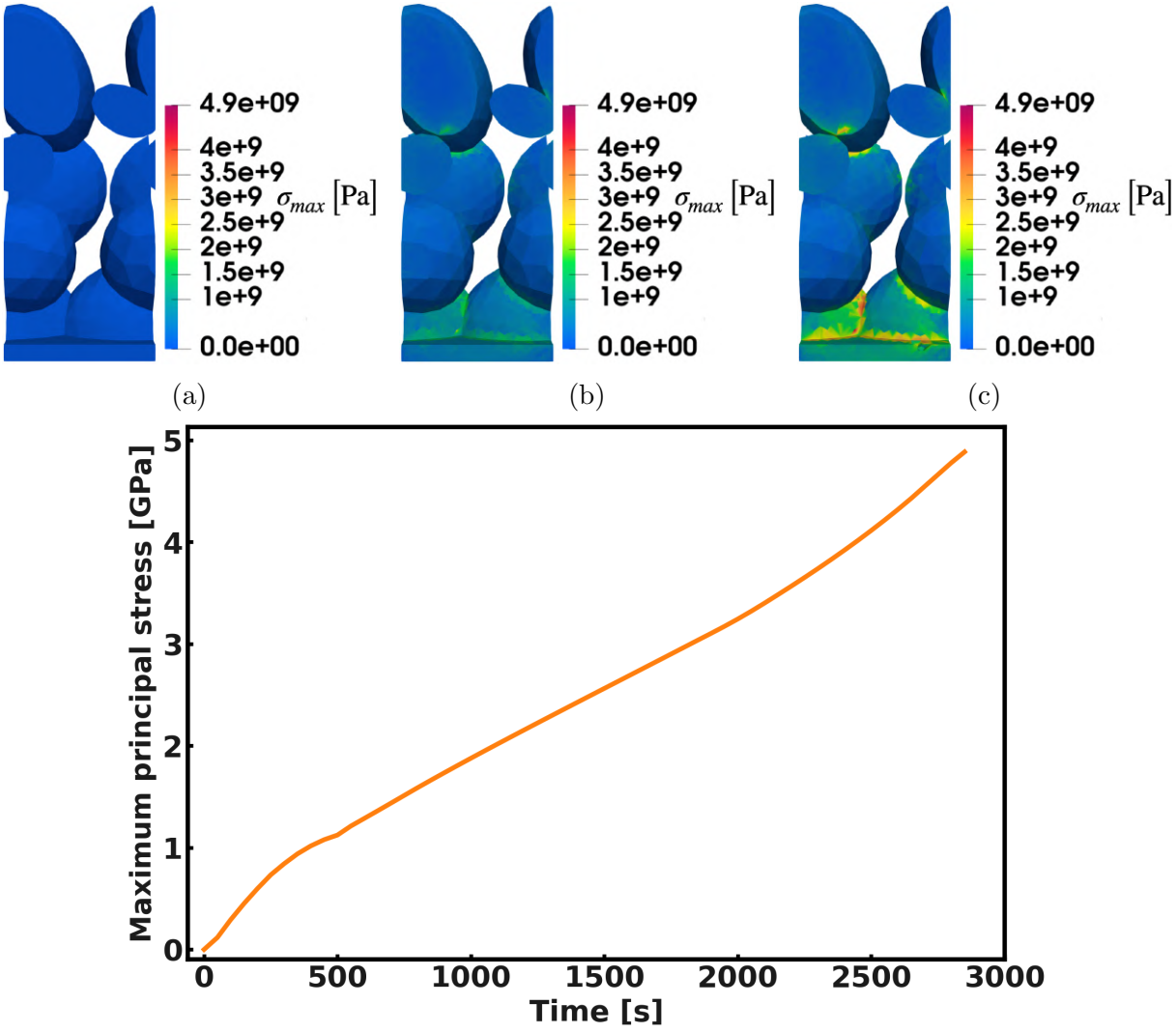

Figure 4.17: (a–c) Evolution of the maximum principal stress during 1C discharge at $t = 0$, 1400, and 2850 s, respectively, (d) the corresponding maximum principal tensile stress vs time at 1C.

Mechanical response of the electrolyte

Having established the cathode and collector response, we now examine the electrolyte. By displacement continuity at the cathode–electrolyte interface ($\vec{u}_e = \vec{u}_c$ on Γ_e^c), the cathode's downward deformation is transmitted to the adjacent electrolyte, while displacement magnitude is limited near the electrolyte–anode boundary . Figures 4.18a–4.18c show that the displacement magnitude $||\vec{u}_e||$ grows with time and is largest along particle–electrolyte contacts near Γ_e^c, while it decays with distance into the bulk and toward Γ_e^a. At $t = 2850$ s, interfacial hot spots in the electrolyte reach $\approx 1.8 \times 10^{-7}$ m, in line with the adjacent cathode peaks, as required by displacement continuity on Γ_e^c whereas values near the anode side remain much smaller.

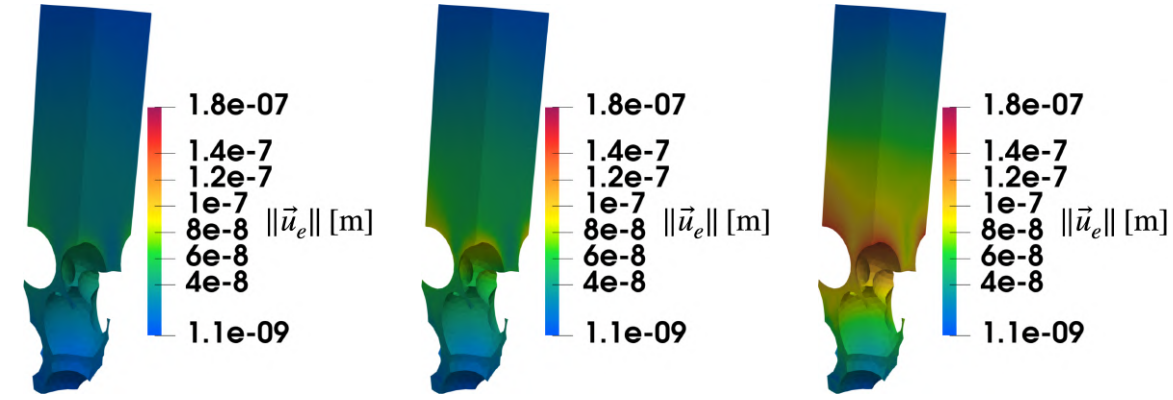

(a) (b) (c)

Figure 4.18: (a–c) show the time evolution of displacement magnitude $\|\vec{u}_e\|$ at t = 1200, 1800, and 2850 s, respectively. At $t = 0$ s, $\|\vec{u}_e\|$ throughout the electrolyte.

Figures 4.19a–4.19c show the evolution of the out-of-plane displacement u_z in the electrolyte. During discharge, a through-thickness gradient develops, such that u_z becomes most negative adjacent to the cathode–electrolyte interface Γ_e^c, being pulled downward by the cathode, and relaxes toward nearly zero as it approaches the electrolyte–anode boundary Γ_e^a. At $t = 2850$ s, the interfacial minimum of u_z in the electrolyte reaches $\approx -1.6\times10^{-7}$ m in line with adjacent cathode value as required by displacement continuity on Γ_e^c. Consequently, Figures 4.18–4.19 mirror the cathode behavior in Figures 4.14–4.15, providing a consistent picture in which cathode deformation is transmitted to the electrolyte by displacement continuity. Figure 4.20 shows the evolution of electrolyte von

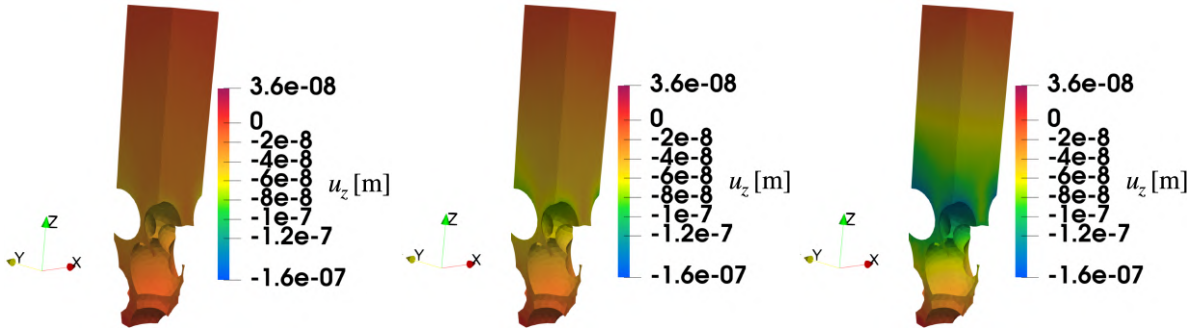

(a) (b) (c)

Figure 4.19: (a–c) show the time evolution of displacement u_z in the electrolyte at t = 1200, 1800, and 2850 s, respectively.

Mises stress. Figures 4.20a–4.20c exhibit a gradual increase in σ_{vm}, with the peak (highlighted by the zoom) remaining 115 MPa at the last instant. Stresses are largest in narrow regions adjacent to the deforming cathode and remain comparatively smooth elsewhere—well below cathode levels—because the electrolyte is much softer ($E \approx 0.45$ GPa vs. $E \approx 370$ GPa for LCO) and does not carry intercalation-induced strain. It mainly accommodates kinematically imposed displacements from the cathode hence stresses concentrates near the interfaces and decays quickly into the bulk part, with the clamped anode/collector boundaries further limiting stress build-up. Figure 4.20d shows the global maximum σ_{vm} versus time, rising nearly linearly to ≈ 115 MPa.

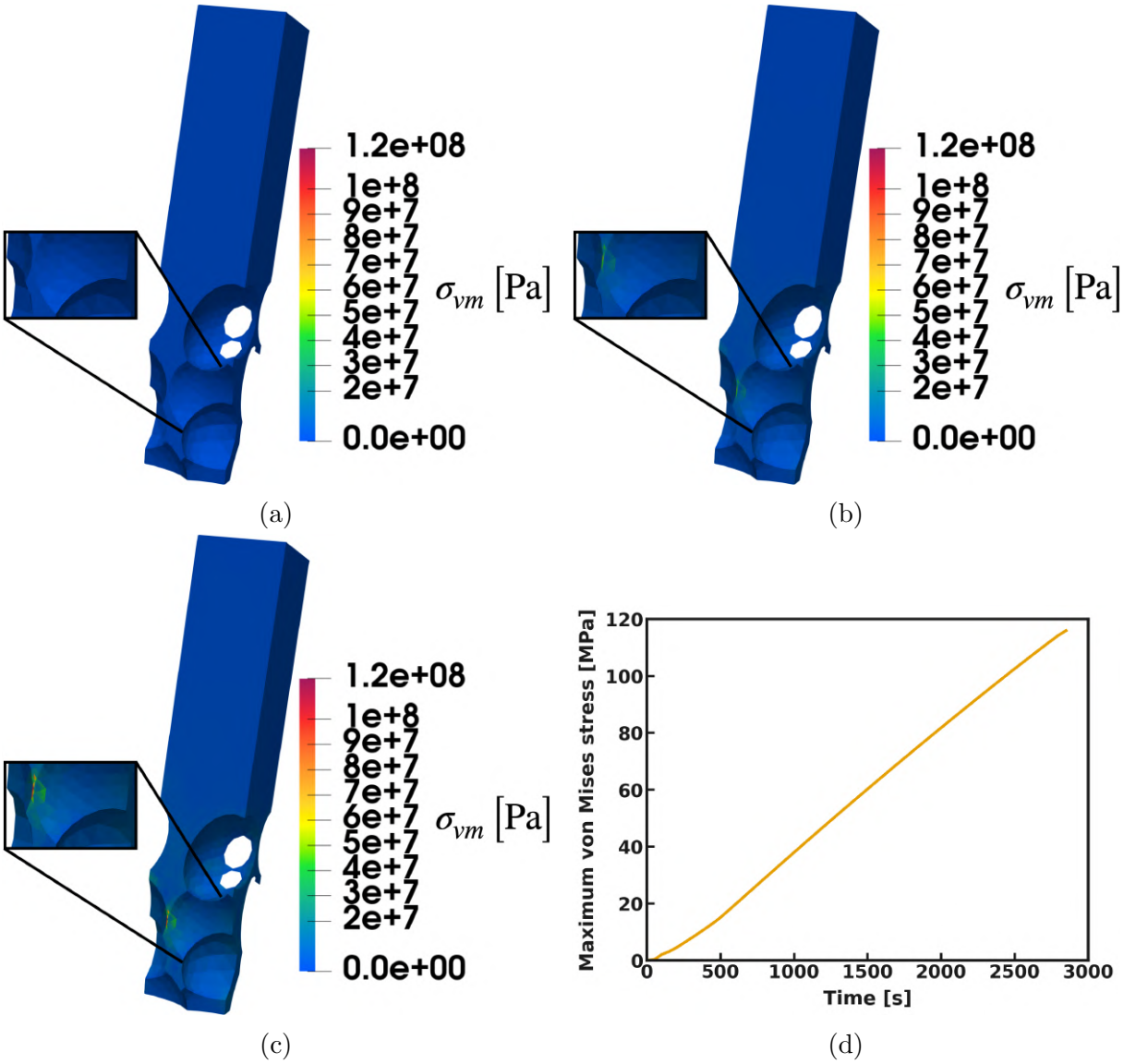

Figure 4.20: Evolution of von Mises stress in the electrolyte during 1C discharge. (a–c) show the stress field at the indicated times; the zoomed images mark the location of the global maximum at each instant. (d) plots the global maximum von Mises stress as a function of time.

Mechanical response of the lithium foil

Figures 4.21a-4.21c show the evolution of the displacement magnitude $\|\vec{u}_a\|$ in the lithium foil anode at the same selected times as for the other domains. With the top surface clamped ($\vec{u}_a = 0$ on $\partial\Omega_a^B$), displacement accumulates toward the electrolyte–anode interface Γ_e^a, where $\|\vec{u}_a\|$ is largest, and diminishes back toward the clamp. By $t = 2850\,\mathrm{s}$, the interfacial maximum reaches $\approx 7.6 \times 10^{-9}$ m. This nanometer-scale quantity represents the mechanical displacement of the lithium foil and should not be interpreted as a lithium deposition (plating) thickness, since deposition/growth is not included in the present formulation. Because the foil undergoes no chemical strain, this observed profile is a purely kinematic response transmitted from the neighboring electrolyte, and enforced by displacement continuity at the interface ($\vec{u}_e = \vec{u}_a$ on Γ_e^a). Among the all domains, the foil shows the smallest magnitudes because it is farthest from the source of deforma-

tion (intercalation-induced chemical strain in the cathode), the displacement transmitted through the electrolyte decays with distance, and the clamped top further suppresses displacement. Figures 4.22a–4.22c isolate the out-of-plane displacement u_z in the lithium

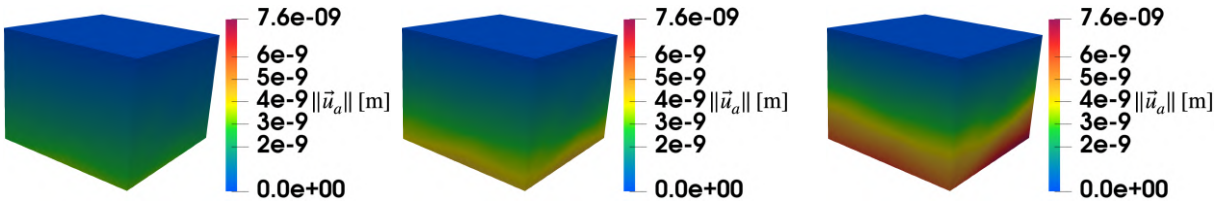

(a) (b) (c)

Figure 4.21: (a–c) show the time evolution of displacement magnitude $\|\vec{u}_a\|$ at 1200, 1800, and 2850 s, respectively. At $t = 0$ s, $\|\vec{u}_a\|$ throughout the lithium foil.

foil. As discharge proceeds, a through-thickness gradient develops with u_z most negative at the electrolyte–anode boundary Γ_e^a, and approaching zero toward the clamped top. By $t = 2850$ s, the interfacial value at Γ_e^a reaches $\approx -6 \times 10^{-9}$m , consistent in sign and location with the trends reported above.

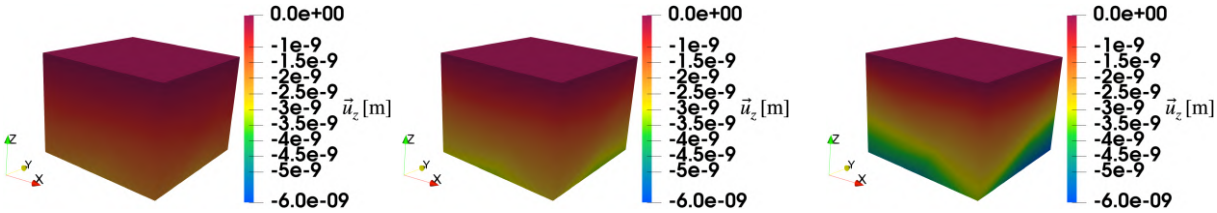

(a) (b) (c)

Figure 4.22: (a–c) show the time evolution of displacement u_z in the lithium foil at $t = 1200$, 1800, and 2850 s, respectively.

4.11.3.2 Electro-chemo-mechanical response at varying C-rates

The battery voltage

As demonstrated by experimental findings [247, 253], battery voltage is significantly affected by the applied C-rate. A quantitative analysis of the voltage–time profiles at varying C-rates, shown in Figure 4.23a, reveals an inverse relationship between the current rate and operating time. Specifically, at 0.5C, the battery operated for approximately 6400 seconds, whereas at 1C and 2C, the durations decreased to 2850 and 1100 seconds, respectively. This trend indicates that under higher loads, the battery maintains its voltage for shorter periods. Indeed, at higher discharge rates, the operating voltage tends to reach lower values due to increased overpotentials within the battery. Additionally, the amount of charge extracted during discharge is influenced by the applied C-rate (see Figure 4.23b); as the discharge rate increases, the extracted charge decreases accordingly. For a quantitative comparison, Figure 4.23b also presents the ratio of the simulated extracted charge to the theoretical capacity, indicated in brackets. This percentage represents the battery cell's utilization efficiency, providing a quantitative measure of how much of the

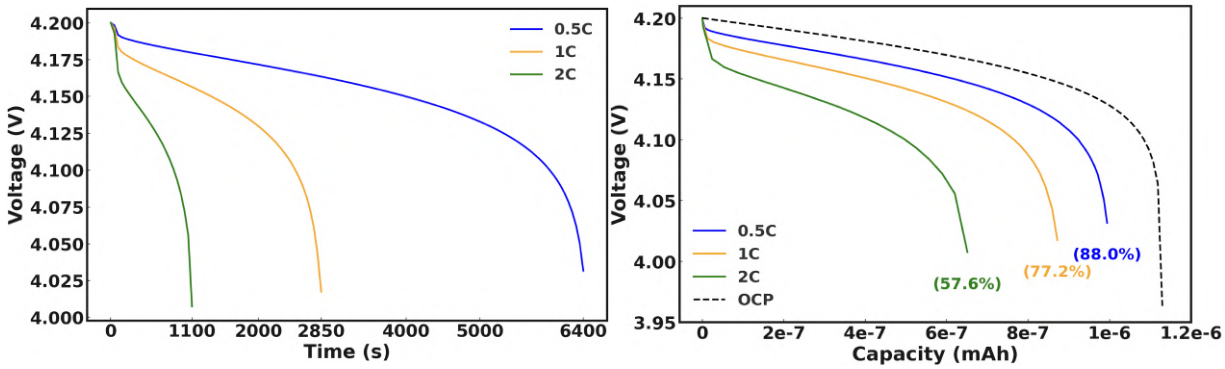

(a) (b)

Figure 4.23: (a) Terminal voltage vs time during galvanostatic discharge at 0.5C, 1C, and 2C. (b) Voltage–capacity curves for the same three rates, compared with the open-circuit potential (dashed).

theoretical capacity is accessed under different operating conditions. As illustrated in Figure 4.23b, the battery cell exhibits significant performance degradation at higher discharge rates. For instance, at a 2C rate, only 57.6% of the theoretical capacity is utilized, compared to 77.2% at 1C and 88.0% at 0.5C. These values indicate that increasing the discharge rate not only reduces the operating voltage due to higher overpotentials, but also limits the extractable charge, thereby lowering the overall efficiency of the battery cell.

The evolution of concentration in the cathode

Figures 4.24a–4.24c present the spatial distrubiton of $c_{\mathrm{Li}^{\oplus}}$ in the cathode at the end of discharge for each C-rate. At higher C-rates, such as 2C, lithium tends to accumulate near the particle surfaces due to the limited time available for diffusion, leaving the interior regions largely underutilized. In contrast, at lower C-rates such as 1C and 0.5C, the longer discharge durations allow lithium to penetrate deeper into the cathode microstructure, leading to more homogeneous concentration profiles. Although perfect uniformity is not achieved even at 0.5C, the improvement in lithiation depth is evident.

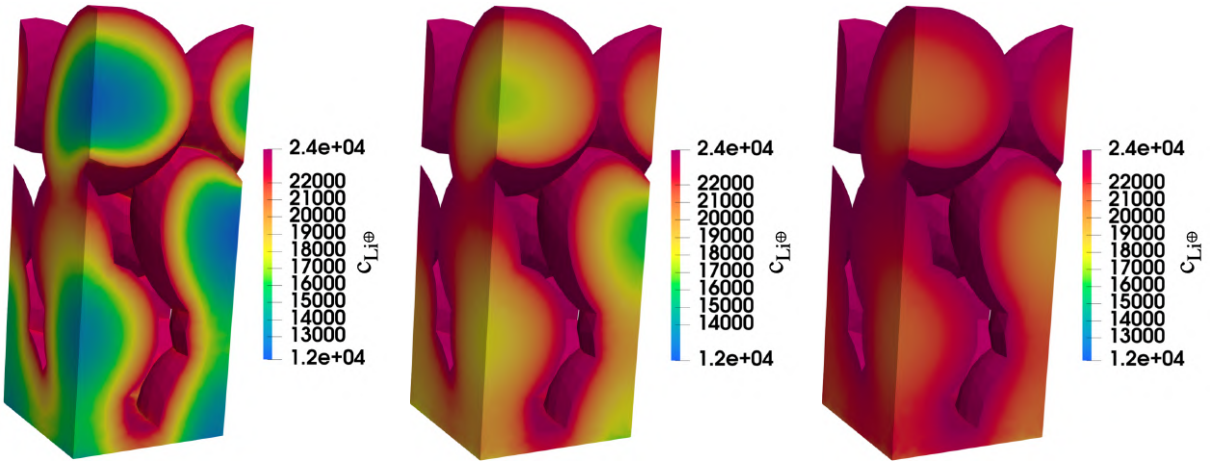

(a) (b) (c)

Figure 4.24: Lithium concentration distribution in the cathode microstructure at different C-rates upon saturation. (a-c) show the spatial distribution of $c_{\mathrm{Li}^\oplus}$ in the cathode domain at 2C (1100 s), 1C (2850 s), and 0.5C (6400 s), respectively.

Mechanical response of the cathode

Figure 4.25 summarizes the global maximum von Mises stresses that develop in the cathode during discharge at different C-rates. Figure 4.25a shows that the maximum σ_{vm} increaes monotonically with time for all C-rates, with a steeper rise at higher C-rates, and this aligns with the sharper lithium concentration gradients and stronger surface–core mismatch seen in Figure 4.24. Figure 4.25b depicts same quantity against the site-filling ratio, $\bar{\theta}$. For a given $\bar{\theta}$ within the range each C-rate actually attains, the ordering (2C > 1C > 0.5C) persists because the lithiation field is more non-uniform at higher C-rates; this spatial heterogeneity increases swelling-strain incompatibility under geometric confinement and raises the domain-wide maximum stress. However, high C-rates do not reach full filling, so their curves terminate at lower $\bar{\theta}$. In contrast, the 0.5C case evolves to higher $\bar{\theta}$ and, near the end of discharge, achieves the largest stresses.

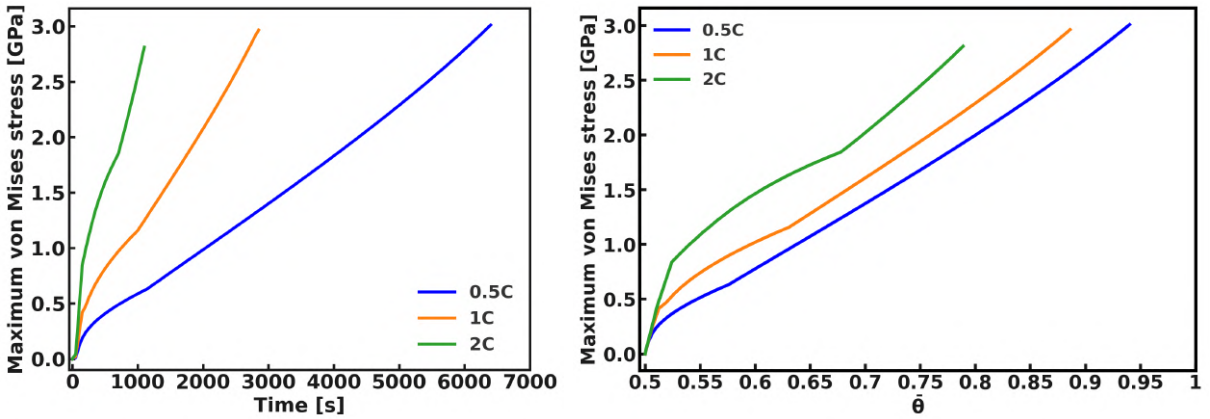

(a) (b)

Figure 4.25: Under galvanostatic discharging at 0.5C, 1C, and 2C, the cathode's maximum von Mises stress as a function of (a) time, and (b) lithium site fraction θ.

Impact of chemo-mechanical coupling on the voltage response of the battery
Figure 4.26 illustrates the effect of stress evolution on the voltage response of the battery at various C-rates. A comparison between the fully coupled model ($\omega_{Li^\oplus} \neq 0$) and the purely electrochemical case ($\omega_{Li^\oplus} = 0$) reveals that accounting for mechanical effects results in higher total discharge capacity. This behavior stems from the coupling of stress into the chemical potential definition in Equation (4.97), which subsequently influences lithium transport (4.98) and the surface open-circuit potential (4.115) through the Butler–Volmer kinetics in Equation (4.111). Notably, the difference between the voltage profiles becomes more evident at 2C, where increased current intensifies transport limitations and enhances stress-induced chemo-mechanical interactions. These findings are in agreement with the study of [354], where mechanical stresses were shown to significantly affect lithium transport and surface kinetics, thereby impacting the voltage profile.

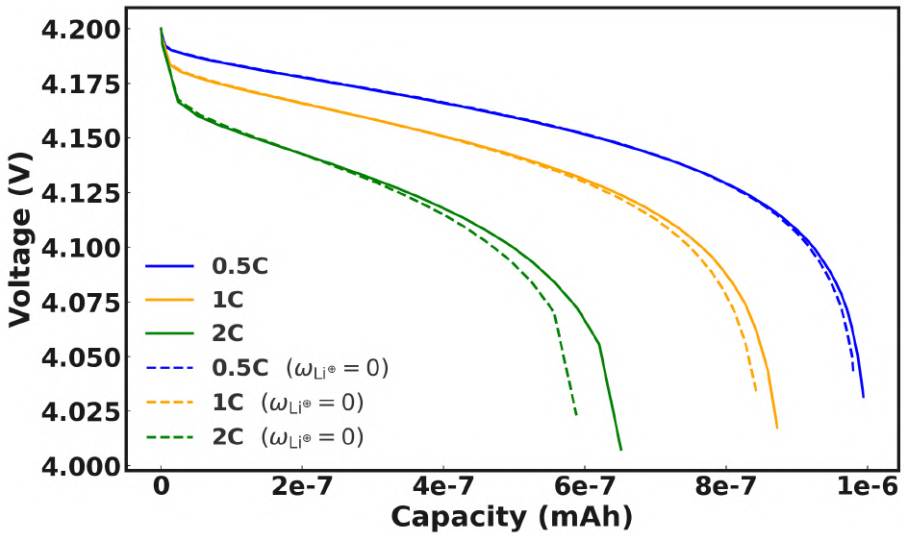

Figure 4.26: Comparison of the simulated voltage profiles obtained from a fully coupled chemo-mechanical model ($\omega_{Li^\oplus} \neq 0$) and a purely electrochemical model ($\omega_{Li^\oplus} = 0$).

4.12 Conclusions

In this work, the three-dimensional behavior of a lithium-ion half-cell has been modeled as a thermodynamically consistent initial/boundary value problem, integrating mass transport, charge transport, electrochemistry, and small-strain linear elasticity into a comprehensive multiphysics framework. The mathematical foundation of the model is built upon balance laws (mass, charge, momentum conservation), the first and second laws of thermodynamics, interface conditions between domains, and constitutive equations. Constitutive relations derived from free energy functions and constrained by thermodynamic restrictions provide the physical consistency and proper closure of the system, enabling a physically meaningful description of chemo-mechanical responses under operating conditions.

Each domain—electrolyte, cathode, anode, and current collector is governed by the relevant conservation laws, momentum equations, and explicit coupling of electrochemical and mechanical fields. The mechanical and electrochemical phenomena—including mass- and charge-transport, swelling, and reaction kinetics—are formulated in weak form, discretized, and implemented monolithically using high-performance algorithms based on the open-source finite element library deal.ii. Interface kinetics, especially between electrolyte and electrodes, are modeled with Butler-Volmer relations, introducing strong nonlinearity and stiffness into the Newton-Raphson solution process. Importantly, all equations are solved together in a fully-coupled fashion, allowing direct interaction between the different physical fields without the need for operator splitting or sequential solution procedures.

The computational domain is constructed to represent the essential features of a lithium-ion half-cell configuration. The geometry includes a lithium metal foil anode, a liquid electrolyte (embedding separator and porous cathode), a porous cathode with randomly distributed active particles, and an aluminum current collector. Mesh generation is performed with TETHEX to ensure compatibility with the requirements of deal.ii, resulting in a refined mesh containing 28,176 tetrahedral elements and 32,827 nodes, totalling 257,047 degrees of freedom. This high-fidelity discretization demonstrates the practical utility and scalability of the monolithic modeling approach.

Simulations are performed under various constant-current discharge conditions (C-rates of 0.5C, 1C, and 2C), enabling the analysis of electro-chemo-mechanical evolution across different domains and operating regimes. The main observations are as follows:

- Battery voltage declines more markedly at higher C-rates, with the IR-drop followed by a regular downward trend. The time required to reach full capacity is significantly reduced at elevated C-rates, with capacity utilization falling to 57% at 2C and rising to 88% at 0.5C.

- Lithium concentration in the cathode increases rapidly near particle surfaces and diffuses inwards; this gradient becomes more pronounced at higher C-rates, leading to surface accumulation and incomplete lithiation in particle cores. Such heterogeneities drive localized swelling and stress buildup, especially pronounced under fast discharge conditions.

- Analysis of mechanical response reveals that chemical contraction induces domain-specific displacements, most notably at interfaces. Maximum displacement at the cathode base reaches 1.8×10^{-7} m, closely correlated with lithium accumulation. The von Mises equivalent stress in the cathode increases with lithium intercalation,

reaching up to 3 GPa at full discharge, with maximum principal tensile stress approaches at 4.9 GPa, suggesting that mechanical integrity may become a relevant concern for LCO active particles.

- The fully coupled chemo-mechanical model yields higher total capacity and voltage curves compared to the purely electrochemical model. This improvement arises because mechanical stress effects are included in the chemical potential, which modifies the reaction kinetics at electrode interfaces (modeled via Butler-Volmer equations), allowing for greater lithium utilization before the discharge ends.

The deal.ii-based monolithic three-dimensional implementation provides an effective framework for the numerical solution of strongly nonlinear and coupled field equations across multiple battery domains. In this sense, the approach offers a useful computational basis for investigating capacity limitations, deformation, and coupled multiphysics interactions in lithium-ion batteries.

The present chapter should also be interpreted within its intended modeling scope. The formulation is restricted to isothermal conditions and small-strain linear elasticity, and therefore does not capture thermal effects, large-deformation phenomena, or damage evolution explicitly. In addition, the cathode domain is modeled using an idealized particle-resolved geometry based on randomly distributed active particles, rather than on an experimentally reconstructed electrode microstructure. This approximation is appropriate for investigating the coupled electro-chemo-mechanical mechanisms addressed in this work within a controlled computational setting. At the same time, tomography-based microstructural models could further improve predictive accuracy by capturing more realistically the spatial arrangement of particles, pore morphology, and local geometric heterogeneity of real electrodes. In particular, microstructural features such as particle size distribution, porosity, and tortuosity can influence ionic transport paths, reaction heterogeneity, concentration gradients, and the resulting localization of mechanical stresses within the electrode. These aspects do not affect the internal consistency of the proposed framework, but they do define the range of applicability of the present simulations and point directly to the most relevant directions for future model development.

In summary, this chapter shows how the integration of balance laws, thermodynamic principles, and constitutive equations within a monolithic and multi-domain finite element framework can provide a physically consistent and informative description of lithium-ion half-cell behavior. Although the continuum model developed in this chapter is not calibrated directly against the regenerated cathode materials examined later in the thesis, it helps identify the class of coupled mechanisms that are relevant to the behavior of LCO-based electrodes under rate loading. In particular, the simulations clarify the roles of transport limitation, interfacial polarization, concentration heterogeneity, and stress localization in shaping the electrochemical response of an idealized half-cell configuration. The experimental study presented in Chapter 5 does not investigate the same system in a directly comparable sense; rather, it provides a complementary materials-level benchmark in which regenerated and commercial LCO powders are compared under controlled half-cell conditions. In this sense, the two chapters should not be interpreted as a direct model–validation pair, but as two complementary contributions that address related aspects of the broader problem of understanding and evaluating LCO-based cathodes.

Appendix

4.A 3D Finite element implementation

4.A.1 Finite element discretization in time and space for the electrolyte domain

The governing equations in their weak form can be reformulated as a first-order Ordinary Differential Equation (ODE) in time by applying spatial discretization. This is achieved using spatial test functions $\varphi_i(\vec{x})$ and shape functions $\varphi_j(\vec{x})$, where $\vec{x} = \{x_1, x_2, x_3\}$ represents the position vector in three-dimensional space, while the nodal unknowns, which evolve over time, are incorporated.[6] We employ the Einstein summation convention: any repeated nodal index j is implicitly summed over $j = 1, \ldots, n_n$, where n_n denotes the number of nodes, whereas the test–function index i is free (also $i = 1, \ldots, n_n$). Since the displacement field $\vec{u}_e^*(\vec{x}, t)$ is vector-valued, we use vector-valued shape and test functions. Define

$$\boldsymbol{\varphi}_j^{u_e}(\vec{x}) := \varphi_j^{u_e}(\vec{x})\,\mathbb{I} \quad \text{and} \quad \boldsymbol{\varphi}^{u_e}(\vec{x}) := \left[\, \boldsymbol{\varphi}_1^{u_e}(\vec{x}) \;\cdots\; \boldsymbol{\varphi}_{n_n}^{u_e}(\vec{x}) \,\right],$$

where $\mathbb{I}$ denotes the 3×3 identity matrix, and $\boldsymbol{\varphi}^{u_e}(\vec{x})$ is a $3 \times 3n_n$ matrix in three dimensions (it collects all vector-valued basis functions into a block matrix).[7] Discritized fields for the electrolyte as follows:

$$\begin{aligned}
c_{\mathrm{Li^+}}^*(\vec{x}, t) &= \varphi_j^{\mathrm{Li^+}}(\vec{x})\; c_j^{\mathrm{Li^+}*}(t), \quad \hat{c}_{\mathrm{Li^+}}^*(\vec{x}) = \varphi_i^{\mathrm{Li^+}}(\vec{x}), \\
\phi_e^*(\vec{x}, t) &= \varphi_j^{\phi_e}(\vec{x})\; \phi_j^{e*}(t), \quad \hat{\phi}_e^*(\vec{x}) = \varphi_i^{\phi_e}(\vec{x}), \\
\vec{u}_e^*(\vec{x}, t) &= \boldsymbol{\varphi}_j^{u_e}(\vec{x})\; \vec{u}_j^{e*}(t), \quad \hat{\vec{u}}_e^*(\vec{x}) = \boldsymbol{\varphi}_i^{u_e}(\vec{x}).
\end{aligned} \tag{4.187}$$

A compact block-matrix form for the displacement field, consistent with the Einstein notation above, is written also as:

$$\vec{u}_e^*(\vec{x}, t) = \underbrace{\left[\, \boldsymbol{\varphi}_1^{u_e}(\vec{x}) \;\cdots\; \boldsymbol{\varphi}_{n_n}^{u_e}(\vec{x}) \,\right]}_{\boldsymbol{\varphi}^{u_e}(\vec{x})} \underbrace{\begin{bmatrix} \vec{u}_1^e(t) \\ \vdots \\ \vec{u}_{n_n}^e(t) \end{bmatrix}}_{\vec{u}_j^e(t)}$$

[6] In expressions involving multiple interpolations of the lithium-ion concentration field $c_{\mathrm{Li^+}}$, auxiliary dummy indices such as m and l are introduced to avoid index conflicts in Einstein summation notation. Although these indices still correspond to the nodal degrees of freedom associated with $c_{\mathrm{Li^+}}$, we prefer to ensure clarity when multiple summations appear within the same expression.

[7] Hereafter, we omit the explicit representation of the vector-valued displacement field $\vec{u}$ the same interpolation is used in the other domains.

Substituting the discretized field representations from Equation (4.187) into the fully dimensionless weak form in Equation (4.145) yields [8]:

$$\begin{aligned}
&\int_{\Omega_e} \varphi_i^{\mathrm{Li^+}}(\vec{x})\, \varphi_j^{\mathrm{Li^+}}(\vec{x})\, \frac{\partial c_j^{\mathrm{Li^+}}(t)}{\partial t}\, \mathrm{d}\Omega_e \\
&+ \mathbb{D}_{\mathrm{Li^+}} \int_{\Omega_e} \nabla\varphi_i^{\mathrm{Li^+}}(\vec{x}) \cdot \nabla\varphi_j^{\mathrm{Li^+}}(\vec{x})\, c_j^{\mathrm{Li^+}}(t)\, \mathrm{d}\Omega_e \\
&+ \mathbb{D}_{\mathrm{Li^+}} \int_{\Omega_e} \varphi_m^{\mathrm{Li^+}}(\vec{x})\, c_m^{\mathrm{Li^+}}(t)\, \nabla\varphi_i^{\mathrm{Li^+}}(\vec{x}) \cdot \nabla\varphi_j^{\phi_e}(\vec{x})\, \phi_j^e(t)\, \mathrm{d}\Omega_e \\
&- \mathbb{D}_{\mathrm{Li^+}} \int_{\Omega_e} \varphi_m^{\mathrm{Li^+}}(\vec{x})\, c_m^{\mathrm{Li^+}}(t)\, \frac{2}{c^{sat}} \varphi_l^{\mathrm{Li^+}}(\vec{x})\, c_l^{\mathrm{Li^+}}(t)\, \nabla\varphi_i^{\mathrm{Li^+}}(\vec{x}) \cdot \nabla\varphi_j^{\phi_e}(\vec{x})\, \phi_j^e(t)\, \mathrm{d}\Omega_e \\
&+ \int_{\partial\Omega_e} \varphi_i^{\mathrm{Li^+}}(\vec{x}) \left\{ \vec{h}_{\mathrm{Li^+}} \cdot \vec{n}_e \right\} \mathrm{d}\Gamma = 0.
\end{aligned} \tag{4.188}$$

Equation (4.146) returns

$$\begin{aligned}
&- (\mathbb{D}_{\mathrm{Li^+}} - \mathbb{D}_{\mathrm{X^-}}) \int_{\Omega_e} \nabla\varphi_i^{\phi_e}(\vec{x}) \cdot \nabla\varphi_j^{\mathrm{Li^+}}(\vec{x})\, c_j^{\mathrm{Li^+}}(t)\, \mathrm{d}\Omega_e \\
&- (\mathbb{D}_{\mathrm{Li^+}} + \mathbb{D}_{\mathrm{X^-}}) \int_{\Omega_e} \varphi_m^{\mathrm{Li^+}}(\vec{x})\, c_m^{\mathrm{Li^+}}(t)\, \nabla\varphi_i^{\phi_e}(\vec{x}) \cdot \nabla\varphi_j^{\phi_e}(\vec{x})\, \phi_j^e(t)\, \mathrm{d}\Omega_e \\
&+ (\mathbb{D}_{\mathrm{Li^+}} + \mathbb{D}_{\mathrm{X^-}}) \int_{\Omega_e} \varphi_m^{\mathrm{Li^+}}(\vec{x})\, c_m^{\mathrm{Li^+}}(t) \frac{2}{c^{sat}} \varphi_l^{\mathrm{Li^+}}(\vec{x})\, c_l^{\mathrm{Li^+}}(t) \nabla\varphi_i^{\phi_e}(\vec{x}) \cdot \nabla\varphi_j^{\phi_e}(\vec{x})\, \phi_j^e(t)\, \mathrm{d}\Omega_e \\
&+ \int_{\partial\Omega_e} \varphi_i^{\phi_e}(\vec{x}) \left\{ \vec{h}_{\mathrm{X^-}} \cdot \vec{n}_e \right\} \mathrm{d}\Gamma - \int_{\partial\Omega_e} \varphi_i^{\phi_e}(\vec{x}) \left\{ \vec{h}_{\mathrm{Li^+}} \cdot \vec{n}_e \right\} \mathrm{d}\Gamma = 0
\end{aligned} \tag{4.189}$$

The discretized weak form of Equation (4.147) is simply

$$\begin{aligned}
&- 2G_e \int_{\Omega_e} \nabla^{\mathrm{s}} \boldsymbol{\varphi}_i^{u_e}(\vec{x}) : \nabla^{\mathrm{s}} \boldsymbol{\varphi}_j^{u_e}(\vec{x})\, \vec{u}_j^e(t)\, \mathrm{d}\Omega_e \\
&+ \left(\frac{2G_e}{3} - K_e \right) \int_{\Omega_e} \nabla \cdot \boldsymbol{\varphi}_i^{u_e}(\vec{x})\, \nabla \cdot \boldsymbol{\varphi}_j^{u_e}(\vec{x})\, \vec{u}_j^e(t)\, \mathrm{d}\Omega_e \\
&+ \int_{\partial\Omega_e} \boldsymbol{\varphi}_i^{u_e}(\vec{x}) \cdot \bar{p}_e\, \mathrm{d}\Gamma = 0.
\end{aligned} \tag{4.190}$$

To incorporate time dependency into the entire dimensionless system, the time derivative is approximated using a first-order backward (implicit) finite difference scheme:

$$\frac{\partial c_j^{\mathrm{Li^+}}}{\partial t} \approx \frac{c_j^{\mathrm{Li^+}}(t_{n+1}) - c_j^{\mathrm{Li^+}}(t_n)}{\Delta t}$$

Here, t_{n+1} and t_n represent the current and previous time steps, respectively, within a time-stepping framework. The term $\Delta t = t_{n+1} - t_n$ denotes the time increment between two consecutive steps. The solution is updated incrementally in time using this implicit scheme. This time discretization is applied to the governing equations (4.188), (4.189), and (4.190) upon substitution, yields the time-discretized weak form equations (4.191),

[8] For improved readability, superscript $*$ will be omitted from now on in the dimensionless weak form of each domain.

(4.192), and (4.193) where all unknown fields are evaluated at the current time step t_{n+1}. After the time discretization is applied, Equation (4.188) returns,

$$\begin{aligned}
&\int_{\Omega_e} \varphi_i^{\mathrm{Li}^+}(\vec{x})\, \varphi_j^{\mathrm{Li}^+}(\vec{x})\, \frac{c_j^{\mathrm{Li}^+}(t_{n+1})}{\Delta t} \mathrm{d}\Omega_e \\
&- \int_{\Omega_e} \varphi_i^{\mathrm{Li}^+}(\vec{x})\, \varphi_j^{\mathrm{Li}^+}(\vec{x})\, \frac{c_j^{\mathrm{Li}^+}(t_n)}{\Delta t} \mathrm{d}\Omega_e \\
&+ \mathbb{D}_{\mathrm{Li}^+} \int_{\Omega_e} \nabla \varphi_i^{\mathrm{Li}^+}(\vec{x}) \cdot \nabla \varphi_j^{\mathrm{Li}^+}(\vec{x})\, c_j^{\mathrm{Li}^+}(t_{n+1})\, \mathrm{d}\Omega_e \\
&+ \mathbb{D}_{\mathrm{Li}^+} \int_{\Omega_e} \varphi_m^{\mathrm{Li}^+}(\vec{x})\, c_m^{\mathrm{Li}^+}(t_{n+1}) \nabla \varphi_i^{\mathrm{Li}^+}(\vec{x}) \cdot \nabla \varphi_j^{\phi_\mathrm{e}}(\vec{x}) \phi_j^e(t_{n+1})\, \mathrm{d}\Omega_e \\
&- \mathbb{D}_{\mathrm{Li}^+} \int_{\Omega_e} \varphi_m^{\mathrm{Li}^+}(\vec{x})\, c_m^{\mathrm{Li}^+}(t_{n+1})\, \frac{2}{c^{sat}}\, \varphi_l^{\mathrm{Li}^+}(\vec{x})\, c_l^{\mathrm{Li}^+}(t_{n+1})\, \nabla \varphi_i^{\mathrm{Li}^+}(\vec{x}) \cdot \nabla \varphi_j^{\phi_\mathrm{e}}(\vec{x})\, \phi_j^e(t_{n+1}) \mathrm{d}\Omega_e \\
&+ \int_{\partial\Omega_e} \varphi_i^{\mathrm{Li}^+}(\vec{x}) \left\{ \vec{h}_{\mathrm{Li}^+} \cdot \vec{n}_e \right\} \mathrm{d}\Gamma = 0.
\end{aligned} \tag{4.191}$$

Similarly, substituting the same time discretization into Equation (4.189) yields the updated weak form shown in the following form

$$\begin{aligned}
&- (\mathbb{D}_{\mathrm{Li}^+} - \mathbb{D}_{\mathrm{X}^-}) \int_{\Omega_e} \nabla \varphi_i^{\phi_\mathrm{e}}(\vec{x}) \cdot \nabla \varphi_j^{\mathrm{Li}^+}(\vec{x}) c_j^{\mathrm{Li}^+}(t_{n+1}) \mathrm{d}\Omega_e \\
&- (\mathbb{D}_{\mathrm{Li}^+} + \mathbb{D}_{\mathrm{X}^-}) \int_{\Omega_e} \varphi_m^{\mathrm{Li}^+}(\vec{x}) c_m^{\mathrm{Li}^+}(t_{n+1}) \nabla \varphi_i^{\phi_\mathrm{e}}(\vec{x}) \cdot \nabla \varphi_j^{\phi_\mathrm{e}}(\vec{x})\, \phi_j^e(t_{n+1}) \mathrm{d}\Omega_e \\
&+ (\mathbb{D}_{\mathrm{Li}^+} + \mathbb{D}_{\mathrm{X}^-}) \int_{\Omega_e} \varphi_m^{\mathrm{Li}^+}(\vec{x}) c_m^{\mathrm{Li}^+}(t_{n+1}) \frac{2}{c^{sat}} \varphi_l^{\mathrm{Li}^+}(\vec{x}) c_l^{\mathrm{Li}^+}(t_{n+1}) \nabla \varphi_i^{\phi_\mathrm{e}}(\vec{x}) \cdot \nabla \varphi_j^{\phi_\mathrm{e}}(\vec{x}) \phi_j^e(t_{n+1}) \mathrm{d}\Omega_e \\
&+ \int_{\partial\Omega_e} \varphi_i^{\phi_\mathrm{e}}(\vec{x}) \left\{ \vec{h}_{\mathrm{X}^-} \cdot \vec{n}_e \right\} \mathrm{d}\Gamma - \int_{\partial\Omega_e} \varphi_i^{\phi_\mathrm{e}}(\vec{x}) \left\{ \vec{h}_{\mathrm{Li}^+} \cdot \vec{n}_e \right\} \mathrm{d}\Gamma = 0
\end{aligned} \tag{4.192}$$

Lastly, applying the time discretization to the mechanical equilibrium Equation (4.190) results in the time-discretized counterpart as follows:

$$\begin{aligned}
&- 2G_e \int_{\Omega_e} \nabla^{\mathrm{s}} \boldsymbol{\varphi}_i^{u_e}(\vec{x}) : \nabla^{\mathrm{s}} \boldsymbol{\varphi}_j^{u_e}(\vec{x})\, \vec{u}_j^e(t_{n+1})\, \mathrm{d}\Omega_e \\
&+ \left(\frac{2G_e}{3} - K_e \right) \int_{\Omega_e} \nabla \cdot \boldsymbol{\varphi}_i^{u_e}(\vec{x})\, \nabla \cdot \boldsymbol{\varphi}_j^{u_e}(\vec{x})\, \vec{u}_j^e(t_{n+1})\, \mathrm{d}\Omega_e \\
&+ \int_{\partial\Omega_e} \boldsymbol{\varphi}_i^{u_e}(\vec{x}) \cdot \bar{p}_e\, \mathrm{d}\Gamma = 0.
\end{aligned} \tag{4.193}$$

4.A.2 Newton-Raphson scheme in the electrolyte domain

To solve the nonlinear system $f(a,b)$ we employ the Newton–Raphson method, which is expressed as:

$$f(a,b) \approxeq f(a^{(n)},b^{(n)}) + D^g\left[f(a^{(k)},b^{(k)})\right] = 0 \tag{4.194}$$

Following the standard approach using the Gateaux derivative D^g, the Newton–Raphson iteration at step k results in

$$D^g\left[f(a^{(k)},b^{(k)})\right] = \frac{\mathrm{d}}{\mathrm{d}\epsilon}\left[f\left(a^{(k)}+\epsilon\delta a, b^{(k)}+\epsilon\delta b\right)\right]\Big|_{\epsilon=0}. \tag{4.195}$$

In the electrolyte domain, the nonlinear residual $\mathcal{R}$, depends on multiple fields, namely the lithium-ion concentration $c_j^{\mathrm{Li}^+}$, the electric potential ϕ_j^e, and displacement $\vec{u}_j^e$. From now on, we omit the explicit spatial dependence of the shape and test functions and simply write

$$\varphi_i^I \equiv \varphi_i^I(\vec{x}), \qquad \varphi_j^I \equiv \varphi_j^I(\vec{x}),$$

where $I \in \{\mathrm{Li}^+, \phi_e, u_e\}$. Given a residual $\mathcal{R}(c_j^{\mathrm{Li}^+}, \phi_j^e, \vec{u}_j^e)$, its linearization using the Gateaux derivative yields:

$$D^g\left[\mathcal{R}\left(c_j^{\mathrm{Li}^+(k)},\, \phi_j^{e(k)},\, \vec{u}_j^{e(k)}\right)\right] = \frac{\mathrm{d}}{\mathrm{d}\epsilon}\mathcal{R}\left(c_j^{\mathrm{Li}^+(k)} + \epsilon\,\delta c_j^{\mathrm{Li}^+},\, \phi_j^{e(k)} + \epsilon\,\delta\phi_j^e,\, \vec{u}_j^{e(k)} + \epsilon\,\delta\vec{u}_j^e\right)\Big|_{\epsilon=0} \tag{4.196}$$

The Newton Raphson at iteration k yields:

$$\frac{\mathrm{d}}{\mathrm{d}\epsilon}\mathcal{R}\left(c_j^{\mathrm{Li}^+(k)} + \epsilon\,\delta c_j^{\mathrm{Li}^+},\, \phi_j^{e(k)} + \epsilon\,\delta\phi_j^e,\, \vec{u}_j^{e(k)} + \epsilon\,\delta\vec{u}_j^e\right)\Big|_{\epsilon=0} = -\mathcal{R}\left(c_j^{\mathrm{Li}^+(k)},\, \phi_j^{e(k)},\, \vec{u}_j^{e(k)}\right) \tag{4.197}$$

$$
\begin{aligned}
&\frac{\mathrm{d}}{\mathrm{d}\epsilon}\mathcal{R}\left(c_j^{\mathrm{Li}^+(k)}+\epsilon\,\delta c_j^{\mathrm{Li}^+},\ \phi_j^{e(k)}+\epsilon\,\delta\phi_j^e,\ \vec{u}_j^{e(k)}+\epsilon\,\delta\vec{u}_j^e\right)\Big|_{\epsilon=0}\\
&=\int_{\Omega_e}\frac{1}{\Delta t}\,\varphi_i^{\mathrm{Li}^+}\varphi_j^{\mathrm{Li}^+}\delta c_j^{\mathrm{Li}^+}(t_{n+1})\,\mathrm{d}\Omega_e\\
&\quad+\mathbb{D}_{\mathrm{Li}^+}\int_{\Omega_e}\nabla\varphi_i^{\mathrm{Li}^+}\cdot\nabla\varphi_j^{\mathrm{Li}^+}\delta c_j^{\mathrm{Li}^+}(t_{n+1})\,\mathrm{d}\Omega_e\\
&\quad+\mathbb{D}_{\mathrm{Li}^+}\int_{\Omega_e}\varphi_m^{\mathrm{Li}^+}\delta c_m^{\mathrm{Li}^+}(t_{n+1})\nabla\varphi_i^{\mathrm{Li}^+}\cdot\nabla\varphi_j^{\phi_e}\phi_j^{e(k)}(t_{n+1})\,\mathrm{d}\Omega_e\\
&\quad-\mathbb{D}_{\mathrm{Li}^+}\int_{\Omega_e}\varphi_m^{\mathrm{Li}^+}\delta c_m^{\mathrm{Li}^+}(t_{n+1})\frac{2}{c^{sat}}\varphi_l^{\mathrm{Li}^+}c_l^{\mathrm{Li}^+(k)}(t_{n+1})\nabla\varphi_i^{\mathrm{Li}^+}\cdot\nabla\varphi_j^{\phi_e}\phi_j^{e(k)}(t_{n+1})\,\mathrm{d}\Omega_e\\
&\quad-\mathbb{D}_{\mathrm{Li}^+}\int_{\Omega_e}\varphi_m^{\mathrm{Li}^+}c_m^{\mathrm{Li}^+(k)}(t_{n+1})\frac{2}{c^{sat}}\varphi_l^{\mathrm{Li}^+}\delta c_l^{\mathrm{Li}^+}(t_{n+1})\nabla\varphi_i^{\mathrm{Li}^+}\cdot\nabla\varphi_j^{\phi_e}\phi_j^{e(k)}(t_{n+1})\,\mathrm{d}\Omega_e\\
&\quad+\mathbb{D}_{\mathrm{Li}^+}\int_{\Omega_e}\varphi_m^{\mathrm{Li}^+}c_m^{\mathrm{Li}^+(k)}(t_{n+1})\nabla\varphi_i^{\mathrm{Li}^+}\cdot\nabla\varphi_j^{\phi_e}\delta\phi_j^e(t_{n+1})\,\mathrm{d}\Omega_e\\
&\quad-\mathbb{D}_{\mathrm{Li}^+}\int_{\Omega_e}\varphi_m^{\mathrm{Li}^+}c_m^{\mathrm{Li}^+(k)}(t_{n+1})\frac{2}{c^{sat}}\varphi_l^{\mathrm{Li}^+}c_l^{\mathrm{Li}^+(k)}(t_{n+1})\nabla\varphi_i^{\mathrm{Li}^+}\cdot\nabla\varphi_j^{\phi_e}\delta\phi_j^e(t_{n+1})\,\mathrm{d}\Omega_e\\
&\quad-(\mathbb{D}_{\mathrm{Li}^+}-\mathbb{D}_{\mathrm{X}^-})\int_{\Omega_e}\nabla\varphi_i^{\phi_e}\cdot\nabla\varphi_j^{\mathrm{Li}^+}\delta c_j^{\mathrm{Li}^+}(t_{n+1})\,\mathrm{d}\Omega_e\\
&\quad-(\mathbb{D}_{\mathrm{Li}^+}+\mathbb{D}_{\mathrm{X}^-})\int_{\Omega_e}\varphi_m^{\mathrm{Li}^+}\delta c_m^{\mathrm{Li}^+}(t_{n+1})\nabla\varphi_i^{\phi_\mathrm{e}}\cdot\nabla\varphi_j^{\phi_\mathrm{e}}\phi_j^{e(k)}(t_{n+1})\mathrm{d}\Omega_e\\
&\quad+(\mathbb{D}_{\mathrm{Li}^+}+\mathbb{D}_{\mathrm{X}^-})\int_{\Omega_e}\varphi_m^{\mathrm{Li}^+}\delta c_m^{\mathrm{Li}^+}(t_{n+1})\frac{2}{c^{sat}}\varphi_l^{\mathrm{Li}^+}c_l^{\mathrm{Li}^+(k)}(t_{n+1})\nabla\varphi_i^{\phi_\mathrm{e}}\cdot\nabla\varphi_j^{\phi_\mathrm{e}}\phi_j^{e(k)}(t_{n+1})\mathrm{d}\Omega_e\\
&\quad+(\mathbb{D}_{\mathrm{Li}^+}+\mathbb{D}_{\mathrm{X}^-})\int_{\Omega_e}\varphi_m^{\mathrm{Li}^+}c_m^{\mathrm{Li}^+(k)}(t_{n+1})\frac{2}{c^{sat}}\varphi_l^{\mathrm{Li}^+}\delta c_l^{\mathrm{Li}^+}(t_{n+1})\nabla\varphi_i^{\phi_\mathrm{e}}\cdot\nabla\varphi_j^{\phi_\mathrm{e}}\phi_j^{e(k)}(t_{n+1})\mathrm{d}\Omega_e\\
&\quad-(\mathbb{D}_{\mathrm{Li}^+}+\mathbb{D}_{\mathrm{X}^-})\int_{\Omega_e}\varphi_m^{\mathrm{Li}^+}c_m^{\mathrm{Li}^+(k)}(t_{n+1})\nabla\varphi_i^{\phi_\mathrm{e}}\cdot\nabla\varphi_j^{\phi_\mathrm{e}}\delta\phi_j^e(t_{n+1})\mathrm{d}\Omega_e\\
&\quad+(\mathbb{D}_{\mathrm{Li}^+}+\mathbb{D}_{\mathrm{X}^-})\int_{\Omega_e}\varphi_m^{\mathrm{Li}^+}c_m^{\mathrm{Li}^+(k)}(t_{n+1})\frac{2}{c^{sat}}\varphi_l^{\mathrm{Li}^+}c_l^{\mathrm{Li}^+(k)}(t_{n+1})\nabla\varphi_i^{\phi_\mathrm{e}}\cdot\nabla\varphi_j^{\phi_\mathrm{e}}\delta\phi_j^e(t_{n+1})\mathrm{d}\Omega_e\\
&\quad-2G_e\int_{\Omega_e}\nabla^{\mathrm{s}}\boldsymbol{\varphi}_i^{u_e}:\nabla^{\mathrm{s}}\boldsymbol{\varphi}_j^{u_e}\,\delta\vec{u}_j^e(t_{n+1})\,\mathrm{d}\Omega_e\\
&\quad+\left(\frac{2G_e}{3}-K_e\right)\int_{\Omega_e}\nabla\cdot\boldsymbol{\varphi}_i^{u_e}\,\nabla\cdot\boldsymbol{\varphi}_j^{u_e}\,\delta\vec{u}_j^e(t_{n+1})\,\mathrm{d}\Omega_e
\end{aligned}
\tag{4.198}
$$

and residual yields as follows:

$$
\begin{aligned}
&-\mathcal{R}\left(c_j^{\mathrm{Li}^+(k)}, \phi_j^{e(k)}, \vec{u}_j^{e(k)}\right) \\
&= -\frac{1}{\Delta t}\int_{\Omega_e} \varphi_i^{\mathrm{Li}^+}\varphi_j^{\mathrm{Li}^+} c_j^{\mathrm{Li}^+(k)}(t_{n+1})\,\mathrm{d}\Omega_e + \frac{1}{\Delta t}\int_{\Omega_e} \varphi_i^{\mathrm{Li}^+}\varphi_j^{\mathrm{Li}^+} c_j^{\mathrm{Li}^+(k)}(t_n)\,\mathrm{d}\Omega_e \\
&\quad - \mathbb{D}_{\mathrm{Li}^+}\int_{\Omega_e} \nabla\varphi_i^{\mathrm{Li}^+}\nabla\varphi_j^{\mathrm{Li}^+} c_j^{\mathrm{Li}^+(k)}(t_{n+1})\,\mathrm{d}\Omega_e \\
&\quad - \mathbb{D}_{\mathrm{Li}^+}\int_{\Omega_e} \varphi_m^{\mathrm{Li}^+} c_m^{\mathrm{Li}^+(k)}(t_{n+1})\,\nabla\varphi_i^{\mathrm{Li}^+}\cdot\nabla\varphi_j^{\phi_\mathrm{e}}\,\phi_j^{e(k)}(t_{n+1})\,\mathrm{d}\Omega_e \\
&\quad + \mathbb{D}_{\mathrm{Li}^+}\int_{\Omega_e} \varphi_m^{\mathrm{Li}^+} c_m^{\mathrm{Li}^+(k)}(t_{n+1})\,\frac{2}{c^{sat}}\varphi_l^{\mathrm{Li}^+} c_l^{\mathrm{Li}^+(k)}(t_{n+1})\,\nabla\varphi_i^{\mathrm{Li}^+}\cdot\nabla\varphi_j^{\phi_\mathrm{e}}\,\phi_j^{e(k)}(t_{n+1})\,\mathrm{d}\Omega_e \\
&\quad + (\mathbb{D}_{\mathrm{Li}^+} - \mathbb{D}_{\mathrm{X}^-})\int_{\Omega_e} \nabla\varphi_i^{\phi_\mathrm{e}}\cdot\nabla\varphi_j^{\mathrm{Li}^+} c_j^{\mathrm{Li}^+(k)}(t_{n+1})\mathrm{d}\Omega_e \\
&\quad + (\mathbb{D}_{\mathrm{Li}^+} + \mathbb{D}_{\mathrm{X}^-})\int_{\Omega_e} \varphi_m^{\mathrm{Li}^+} c_m^{\mathrm{Li}^+(k)}(t_{n+1})\nabla\varphi_i^{\phi_\mathrm{e}}\cdot\nabla\varphi_j^{\phi_\mathrm{e}}\phi_j^{e(k)}(t_{n+1})\mathrm{d}\Omega_e \\
&\quad - (\mathbb{D}_{\mathrm{Li}^+} + \mathbb{D}_{\mathrm{X}^-})\int_{\Omega_e} \varphi_m^{\mathrm{Li}^+} c_m^{\mathrm{Li}^+(k)}(t_{n+1})\frac{2}{c^{sat}}\varphi_l^{\mathrm{Li}^+} c_l^{\mathrm{Li}^+(k)}(t_{n+1})\nabla\varphi_i^{\phi_\mathrm{e}}\cdot\nabla\varphi_j^{\phi_\mathrm{e}}\phi_j^{e(k)}(t_{n+1})\mathrm{d}\Omega_e \\
&\quad + 2G_e\int_{\Omega_e} \nabla^{\mathrm{s}}\boldsymbol{\varphi}_i^{u_e} : \nabla^{\mathrm{s}}\boldsymbol{\varphi}_j^{u_e}\,\vec{u}_j^{e(k)}(t_{n+1})\,\mathrm{d}\Omega_e \\
&\quad - \left(\frac{2G_e}{3} - K_e\right)\int_{\Omega_e} \nabla\cdot\boldsymbol{\varphi}_i^{u_e}\,\nabla\cdot\boldsymbol{\varphi}_j^{u_e}\,\vec{u}_j^{e(k)}(t_{n+1})\,\mathrm{d}\Omega_e \\
&\quad + \int_{\partial\Omega_e}\varphi_i^{\phi_e}\left\{\vec{h}_{\mathrm{Li}^+}\cdot\vec{n}_e\right\}\mathrm{d}\Gamma - \int_{\partial\Omega_e}\boldsymbol{\varphi}_i^{u_e}\,\bar{p}_e\;\mathrm{d}\Gamma
\end{aligned}
\tag{4.199}
$$

4.A.3 Finite element discretization for the cathode domain

The finite element formulation in the cathode region follows the same spatial discretization used for the electrolyte in Section 4.A.1. The corresponding nodal unknowns, defined at discrete spatial locations and evolving in time, are interpolated as

$$
\begin{aligned}
&c^*_{\mathrm{Li}^\oplus}(\vec{x},t) = \varphi_j^{\mathrm{Li}^\oplus}(\vec{x})\,c_j^{\mathrm{Li}^{\oplus *}}(t), \quad \hat{c}^*_{\mathrm{Li}^\oplus}(\vec{x}) = \varphi_i^{\mathrm{Li}^\oplus}(\vec{x}),\\
&\phi^*_c(\vec{x},t) = \varphi_j^{\phi_\mathrm{c}}(\vec{x})\,\phi_j^{c*}(t), \quad \hat{\phi}^*_c(\vec{x}) = \varphi_i^{\phi_\mathrm{c}}(\vec{x}),\\
&\vec{u}^*_c(\vec{x},t) = \boldsymbol{\varphi}_j^{u_c}(\vec{x})\,\vec{u}_j^{c*}(t), \quad \hat{\vec{u}}^*_c(\vec{x}) = \boldsymbol{\varphi}_i^{u_c}(\vec{x}),\\
&\mu^{\mathrm{m}*}_{\mathrm{Li}^\oplus}(\vec{x},t) = \varphi_j^{\mu}(\vec{x})\,\mu_j^{\mathrm{Li}^{\oplus *}}(t), \quad \hat{\mu}^{\mathrm{m}*}_{\mathrm{Li}^\oplus}(\vec{x}) = \varphi_i^{\mu}(\vec{x}).
\end{aligned}
\tag{4.200}
$$

By substituting the discretized field expressions from Equation (4.200) into the weak form given in Equation (4.156), the resulting expression becomes:

$$
\begin{aligned}
&\int_{\Omega_c}\varphi_i^{\mathrm{Li}^\oplus}(\vec{x})\,\varphi_j^{\mathrm{Li}^\oplus}(\vec{x})\,\frac{\partial c_j^{\mathrm{Li}^\oplus}(t)}{\partial t}\,\mathrm{d}\Omega_c \\
&+ \mathbb{D}_{\mathrm{Li}^\oplus}\int_{\Omega_c}\nabla\varphi_i^{\mathrm{Li}^\oplus}(\vec{x})\cdot\nabla\varphi_j^{\mathrm{Li}^\oplus}(\vec{x})\,c_j^{\mathrm{Li}^\oplus}(t)\,\mathrm{d}\Omega_c \\
&+ \mathbb{D}_{\mathrm{Li}^\oplus}\int_{\Omega_c}\varphi_m^{\mathrm{Li}^\oplus}(\vec{x})\,c_m^{\mathrm{Li}^\oplus}(t)\left(1 - \frac{\varphi_l^{\mathrm{Li}^\oplus}(\vec{x})\,c_l^{\mathrm{Li}^\oplus}(t)}{c^{sat}_{\mathrm{Li}^\oplus}}\right)\nabla\varphi_i^{\mathrm{Li}^\oplus}(\vec{x})\cdot\nabla\varphi_j^{\mu}(\vec{x})\,\mu_j^{\mathrm{Li}^\oplus}(t)\,\mathrm{d}\Omega_c \\
&+ \int_{\partial\Omega_c}\varphi_i^{\mathrm{Li}^\oplus}(\vec{x})\left(\vec{h}_{\mathrm{Li}^\oplus}\cdot\vec{n}_c\right)\mathrm{d}\Gamma = 0.
\end{aligned}
\tag{4.201}
$$

The dimensionless weak form of Ohm's law in the cathode domain, obtained from Equation (4.157), is discretized as:

$$\int_{\Omega_c} \kappa_c \, \nabla\varphi_i^{\phi_c}(\vec{x}) \cdot \nabla\varphi_j^{\phi_c}(\vec{x})\phi_j^c(t) \, \mathrm{d}\Omega_c + \int_{\partial\Omega_c} \varphi_i^{\phi_c}(\vec{x}) \left\{ \vec{i}_c \cdot \vec{n}_c \right\} \, \mathrm{d}\Gamma = 0. \tag{4.202}$$

The dimensionless weak form of the mechanical equilibrium equation in the cathode domain, obtained from Equation (4.158), is discretized as:

$$\begin{aligned} &- 2G_c \int_{\Omega_c} \nabla^{\mathrm{s}}\boldsymbol{\varphi}_i^{u_c}(\vec{x}) : \nabla^{\mathrm{s}}\boldsymbol{\varphi}_j^{u_c}(\vec{x}) \, \vec{u}_j^c(t) \, \mathrm{d}\Omega_c \\ &+ \left(\frac{2G_c}{3} - K_c \right) \int_{\Omega_c} \nabla \cdot \boldsymbol{\varphi}_i^{u_c}(\vec{x}) \, \nabla \cdot \boldsymbol{\varphi}_j^{u_c}(\vec{x}) \, \vec{u}_j^c(t) \, \mathrm{d}\Omega_c \\ &+ 3K_c \, \omega_{\mathrm{Li}^\oplus} \int_{\Omega_c} \nabla \cdot \boldsymbol{\varphi}_i^{u_c}(\vec{x}) \, \varphi_j^{\mathrm{Li}^\oplus}(\vec{x}) \, c_j^{\mathrm{Li}^\oplus}(t) \, \mathrm{d}\Omega_c \\ &+ \int_{\partial\Omega_c} \boldsymbol{\varphi}_i^{u_c}(\vec{x}) \cdot \bar{p}_c \, \mathrm{d}\Gamma = 0. \end{aligned} \tag{4.203}$$

The dimensionless weak form of the equation (4.159)

$$\begin{aligned} &\int_{\Omega_c} \varphi_i^{\mu}(\vec{x}) \, \varphi_j^{\mu}(\vec{x}) \, \mu_j^{\mathrm{Li}^\oplus}(t) \, \mathrm{d}\Omega_c \\ &- 3K_c \, \omega_{\mathrm{Li}^\oplus} \int_{\Omega_c} \varphi_i^{\mu}(\vec{x}) \, \nabla \cdot \boldsymbol{\varphi}_j^{u_c}(\vec{x}) \, \vec{u}_j^c(t) \, \mathrm{d}\Omega_c \\ &+ 9K_c \, (\omega_{\mathrm{Li}^\oplus})^2 \int_{\Omega_c} \varphi_i^{\mu}(\vec{x}) \, \varphi_j^{\mathrm{Li}^\oplus}(\vec{x}) \, c_j^{\mathrm{Li}^\oplus}(t) \, \mathrm{d}\Omega_c = 0. \end{aligned} \tag{4.204}$$

The implicit Backward Euler method presented for the electrolyte in 4.A.1 is applied in the same manner to the cathode. After time discretization, equation (4.201) becomes:

$$\begin{aligned} &\int_{\Omega_c} \varphi_i^{\mathrm{Li}^\oplus}(\vec{x}) \, \varphi_j^{\mathrm{Li}^\oplus}(\vec{x}) \, \frac{c_j^{\mathrm{Li}^\oplus}(t_{n+1})}{\Delta t} \, \mathrm{d}\Omega_c \\ &- \int_{\Omega_c} \varphi_i^{\mathrm{Li}^\oplus}(\vec{x}) \varphi_j^{\mathrm{Li}^\oplus}(\vec{x}) \, \frac{c_j^{\mathrm{Li}^\oplus}(t_n)}{\Delta t} \mathrm{d}\Omega_c \\ &+ \mathbb{D}_{\mathrm{Li}^\oplus} \int_{\Omega_c} \nabla\varphi_i^{\mathrm{Li}^\oplus}(\vec{x}) \cdot \nabla\varphi_j^{\mathrm{Li}^\oplus}(\vec{x}) \, c_j^{\mathrm{Li}^\oplus}(t_{n+1}) \, \mathrm{d}\Omega_c \\ &+ \mathbb{D}_{\mathrm{Li}^\oplus} \int_{\Omega_c} \varphi_m^{\mathrm{Li}^\oplus}(\vec{x}) \, c_m^{\mathrm{Li}^\oplus}(t_{n+1}) \left(1 - \frac{\varphi_l^{\mathrm{Li}^\oplus}(\vec{x}) \, c_l^{\mathrm{Li}^\oplus}(t_{n+1})}{c_{\mathrm{Li}^\oplus}^{sat}} \right) \nabla\varphi_i^{\mathrm{Li}^\oplus}(\vec{x}) \cdot \nabla\varphi_j^{\mu}(\vec{x}) \, \mu_j^{\mathrm{Li}^\oplus}(t_{n+1}) \, \mathrm{d}\Omega_c \\ &+ \int_{\partial\Omega_c} \varphi_i^{\mathrm{Li}^\oplus}(\vec{x}) \left\{ \vec{h}_{\mathrm{Li}^\oplus} \cdot \vec{n}_c \right\} \mathrm{d}\Gamma = 0. \end{aligned} \tag{4.205}$$

Similarly, substituting the same time discretization into equation (4.202) gives the following updated weak form:

$$\int_{\Omega_c} \kappa_c \, \nabla\varphi_i^{\phi_c}(\vec{x}) \cdot \nabla\varphi_j^{\phi_c}(\vec{x})\phi_j^c(t_{n+1}) \, \mathrm{d}V_c + \int_{\partial\Omega_c} \varphi_i^{\phi_c}(\vec{x}) \left\{ \vec{i}_c \cdot \vec{n}_c \right\} \, \mathrm{d}\Gamma = 0. \tag{4.206}$$

Equation (4.203) stems from the mechanical equilibrium is rearranged as follows:

$$
\begin{aligned}
&- 2G_c \int_{\Omega_c} \nabla^{\mathrm{s}} \boldsymbol{\varphi}_i^{u_c}(\vec{x}) : \nabla^{\mathrm{s}} \boldsymbol{\varphi}_j^{u_c}(\vec{x})\, \vec{u}_j^{c}(t_{n+1})\, \mathrm{d}V_c \\
&+ \left(\frac{2G_c}{3} - K_c \right) \int_{\Omega_c} \nabla \cdot \boldsymbol{\varphi}_i^{u_c}(\vec{x})\, \nabla \cdot \boldsymbol{\varphi}_j^{u_c}(\vec{x})\, \vec{u}_j^{c}(t_{n+1})\, \mathrm{d}V_c \\
&+ \int_{\partial\Omega_c} \boldsymbol{\varphi}_i^{u_c}(\vec{x}) \cdot \bar{p}_c\, \mathrm{d}\Gamma = 0.
\end{aligned}
\tag{4.207}
$$

Lastly, applying the time discretization to the mechanical equilibrium equation (4.204) results in the following time-discretized form in the cathode region :

$$
\begin{aligned}
&\int_{\Omega_c} \varphi_i^{\mu}(\vec{x})\, \varphi_j^{\mu}(\vec{x})\, \mu_j^{\mathrm{Li}^{\oplus}}(t_{n+1})\, \mathrm{d}\Omega_c \\
&- 3K_c\, \omega_{\mathrm{Li}^{\oplus}} \int_{\Omega_c} \varphi_i^{\mu}(\vec{x})\, \nabla \cdot \boldsymbol{\varphi}_j^{u_c}(\vec{x})\, \vec{u}_j^{c}(t_{n+1})\, \mathrm{d}\Omega_c \\
&+ 9K_c\, (\omega_{\mathrm{Li}^{\oplus}})^2 \int_{\Omega_c} \varphi_i^{\mu}(\vec{x})\ \ \varphi_j^{\mathrm{Li}^{\oplus}}(\vec{x})\, c_j^{\mathrm{Li}^{\oplus}}(t_{n+1})\, \mathrm{d}\Omega_c = 0.
\end{aligned}
\tag{4.208}
$$

4.A.4 Newton-Raphson scheme in the cathode domain

In order to solve the resulting nonlinear system in the cathode domain, we apply the Newton–Raphson method following the same procedure outlined for the electrolyte in Section 4.A.2. In the cathode domain, as in the electrolyte, the explicit spatial dependence of the shape and test functions is omitted, and we simply write:

$$\varphi_i^I \equiv \varphi_i^I(\vec{x}), \qquad \varphi_j^I \equiv \varphi_j^I(\vec{x}),$$

where $I \in \{\mathrm{Li}^{\oplus}, \phi_c, u_c, \mu\}$. At iteration step k, the residual $\mathcal{R}(c_j^{\mathrm{Li}^{\oplus}}, \phi_j^c, \vec{u}_j^c, \mu_j^{\mathrm{Li}^{\oplus}})$ is linearized using the Gateaux derivative and the Newton-Raphson yields:

$$\frac{\mathrm{d}}{\mathrm{d}\epsilon}\mathcal{R}\left(c_j^{\mathrm{Li}^{\oplus}} + \epsilon\,\delta c_j^{\mathrm{Li}^{\oplus}},\, \phi_j^c + \epsilon\,\delta\phi_j^c,\, \vec{u}_j^c + \epsilon\,\delta\vec{u}_j^c,\, \mu_j^{\mathrm{Li}^{\oplus}} + \epsilon\,\delta\mu_j^{\mathrm{Li}^{\oplus}}\right)\Big|_{\epsilon=0}^{(k)} = -\mathcal{R}\left(c_j^{\mathrm{Li}^{\oplus}(k)},\, \phi_j^{c(k)},\, \vec{u}_j^{c(k)},\, \mu_j^{\mathrm{Li}^{\oplus}(k)}\right) \tag{4.209}$$

where Gateaux derivative is written explicitly as:

$$\begin{aligned}
&\frac{\mathrm{d}}{\mathrm{d}\epsilon}\mathcal{R}\left(c_j^{\mathrm{Li}^{\oplus}(k)} + \epsilon\,\delta c_j^{\mathrm{Li}^{\oplus}},\, \phi_j^{c(k)} + \epsilon\,\delta\phi_j^c,\, \vec{u}_j^{c(k)} + \epsilon\,\delta\vec{u}_j^c,\, \mu_j^{\mathrm{Li}^{\oplus}(k)} + \epsilon\,\delta\mu_j^{\mathrm{Li}^{\oplus}}\right)\Big|_{\epsilon=0} \\
&= \int_{\Omega_c} \frac{1}{\Delta t}\,\varphi_i^{\mathrm{Li}^{\oplus}}\varphi_j^{\mathrm{Li}^{\oplus}}\delta c_j^{\mathrm{Li}^{\oplus}}(t_{n+1})\,\mathrm{d}\Omega_c \\
&\quad + \mathbb{D}_{\mathrm{Li}^{\oplus}}\int_{\Omega_c} \nabla\varphi_i^{\mathrm{Li}^{\oplus}}\cdot\nabla\varphi_j^{\mathrm{Li}^{\oplus}}\delta c_j^{\mathrm{Li}^{\oplus}}(t_{n+1})\,\mathrm{d}\Omega_c \\
&\quad + \mathbb{D}_{\mathrm{Li}^{\oplus}}\int_{\Omega_c} \varphi_m^{\mathrm{Li}^{\oplus}}\,\delta c_m^{\mathrm{Li}^{\oplus}}(t_{n+1})\nabla\varphi_i^{\mathrm{Li}^{\oplus}}\cdot\nabla\varphi_j^{\mu}\,\mu_j^{\mathrm{Li}^{\oplus}}(t_{n+1})\,\mathrm{d}\Omega_c \\
&\quad - \mathbb{D}_{\mathrm{Li}^{\oplus}}\int_{\Omega_c} \varphi_m^{\mathrm{Li}^{\oplus}}\,\delta c_m^{\mathrm{Li}^{\oplus}}(t_{n+1})\frac{\varphi_l^{\mathrm{Li}^{\oplus}}c_l^{\mathrm{Li}^{\oplus}}(t_{n+1})}{c_{\mathrm{Li}^{\oplus}}^{sat}}\nabla\varphi_i^{\mathrm{Li}^{\oplus}}\cdot\nabla\varphi_j^{\mu}\,\mu_j^{\mathrm{Li}^{\oplus}}(t_{n+1})\,\mathrm{d}\Omega_c \\
&\quad - \mathbb{D}_{\mathrm{Li}^{\oplus}}\int_{\Omega_c} \varphi_m^{\mathrm{Li}^{\oplus}}\,c_m^{\mathrm{Li}^{\oplus}}(t_{n+1})\frac{\varphi_l^{\mathrm{Li}^{\oplus}}\delta c_l^{\mathrm{Li}^{\oplus}}(t_{n+1})}{c_{\mathrm{Li}^{\oplus}}^{sat}}\nabla\varphi_i^{\mathrm{Li}^{\oplus}}\cdot\nabla\varphi_j^{\mu}\,\mu_j^{\mathrm{Li}^{\oplus}}(t_{n+1})\,\mathrm{d}\Omega_c \\
&\quad + \mathbb{D}_{\mathrm{Li}^{\oplus}}\int_{\Omega_c} \varphi_m^{\mathrm{Li}^{\oplus}}\,c_m^{\mathrm{Li}^{\oplus}}(t_{n+1})\nabla\varphi_i^{\mathrm{Li}^{\oplus}}\cdot\nabla\varphi_j^{\mu}\,\delta\mu_j^{\mathrm{Li}^{\oplus}}(t_{n+1})\,\mathrm{d}\Omega_c \\
&\quad - \mathbb{D}_{\mathrm{Li}^{\oplus}}\int_{\Omega_c} \varphi_m^{\mathrm{Li}^{\oplus}}\,c_m^{\mathrm{Li}^{\oplus}}(t_{n+1})\frac{\varphi_l^{\mathrm{Li}^{\oplus}}c_l^{\mathrm{Li}^{\oplus}}(t_{n+1})}{c_{\mathrm{Li}^{\oplus}}^{sat}}\nabla\varphi_i^{\mathrm{Li}^{\oplus}}\cdot\nabla\varphi_j^{\mu}\,\delta\mu_j^{\mathrm{Li}^{\oplus}}(t_{n+1})\,\mathrm{d}\Omega_c \\
&\quad + \int_{\Omega_c} \kappa_c\,\nabla\varphi_i^{\phi_c}\cdot\nabla\varphi_j^{\phi_c}\delta\phi_j^c(t_{n+1})\,\mathrm{d}\Omega_c \\
&\quad - 2G_c\int_{\Omega_c} \nabla^{\mathrm{s}}\boldsymbol{\varphi}_i^{u_c} : \nabla^{\mathrm{s}}\boldsymbol{\varphi}_j^{u_c}\,\delta\vec{u}_j^c(t_{n+1})\,\mathrm{d}\Omega_c \\
&\quad + \left(\frac{2G_c}{3} - K_c\right)\int_{\Omega_c} \nabla\cdot\boldsymbol{\varphi}_i^{u_c}\,\nabla\cdot\boldsymbol{\varphi}_j^{u_c}\,\delta\vec{u}_j^c(t_{n+1})\,\mathrm{d}\Omega_c \\
&\quad + 3K_c\,\omega_{\mathrm{Li}^{\oplus}}\int_{\Omega_c} \nabla\cdot\boldsymbol{\varphi}_i^{u_c}\varphi_j^{\mathrm{Li}^{\oplus}}\,\delta c_j^{\mathrm{Li}^{\oplus}}(t_{n+1})\mathrm{d}\Omega_c \\
&\quad + \int_{\Omega_c} \varphi_i^{\mu}\,\varphi_j^{\mu}\,\delta\mu_j^{\mathrm{Li}^{\oplus}}(t_{n+1})\,\mathrm{d}\Omega_c \\
&\quad - 3K_c\,\omega_{\mathrm{Li}^{\oplus}}\int_{\Omega_c} \varphi_i^{\mu}\,\nabla\cdot\boldsymbol{\varphi}_j^{u_c}\,\delta\vec{u}_j^c(t_{n+1})\,\mathrm{d}\Omega_c \\
&\quad + 9K_c\,(\omega_{\mathrm{Li}^{\oplus}})^2\int_{\Omega_c} \varphi_i^{\mu}\,\varphi_j^{\mathrm{Li}^{\oplus}}\,\delta c_j^{\mathrm{Li}^{\oplus}}(t_{n+1})\,\mathrm{d}\Omega_c.
\end{aligned} \tag{4.210}$$

and residual yields as follows:

$$
\begin{aligned}
&- \mathcal{R}\left(c_j^{\mathrm{Li}^\oplus(k)},\, \phi_j^{c(k)},\, \vec{u}_j^{c(k)},\, \mu_j^{\mathrm{Li}^\oplus(k)}\right) \\
&= -\frac{1}{\Delta t}\int_{\Omega_c} \varphi_i^{\mathrm{Li}^\oplus}\varphi_j^{\mathrm{Li}^\oplus} c_j^{\mathrm{Li}^\oplus}(t_{n+1})\,\mathrm{d}\Omega_c + \frac{1}{\Delta t}\int_{\Omega_c} \varphi_i^{\mathrm{Li}^\oplus}\varphi_j^{\mathrm{Li}^\oplus} c_j^{\mathrm{Li}^\oplus}(t_n)\,\mathrm{d}\Omega_c \\
&\quad - \mathbb{D}_{\mathrm{Li}^\oplus}\int_{\Omega_c} \nabla\varphi_i^{\mathrm{Li}^\oplus}\cdot\nabla\varphi_j^{\mathrm{Li}^\oplus} c_j^{\mathrm{Li}^\oplus}(t_{n+1})\,\mathrm{d}\Omega_c \\
&\quad - \mathbb{D}_{\mathrm{Li}^\oplus}\int_{\Omega_c} \varphi_m^{\mathrm{Li}^\oplus}\, c_m^{\mathrm{Li}^\oplus}(t_{n+1})\,\nabla\varphi_i^{\mathrm{Li}^\oplus}\cdot\nabla\varphi_j^{\mu}\,\mu_j^{\mathrm{Li}^\oplus}(t_{n+1})\,\mathrm{d}\Omega_c \\
&\quad + \mathbb{D}_{\mathrm{Li}^\oplus}\int_{\Omega_c} \varphi_m^{\mathrm{Li}^\oplus}\, c_m^{\mathrm{Li}^\oplus}(t_{n+1})\frac{\varphi_l^{\mathrm{Li}^\oplus} c_l^{\mathrm{Li}^\oplus}(t_{n+1})}{c_{\mathrm{Li}^\oplus}^{sat}}\,\nabla\varphi_i^{\mathrm{Li}^\oplus}\cdot\nabla\varphi_j^{\mu}\,\mu_j^{\mathrm{Li}^\oplus}(t_{n+1})\,\mathrm{d}\Omega_c \\
&\quad - \int_{\Omega_c}\kappa_c\,\nabla\varphi_i^{\phi_c}\cdot\nabla\varphi_j^{\phi_c}\phi_j^c(t_{n+1})\,\mathrm{d}\Omega_c \\
&\quad + 2G_c\int_{\Omega_c}\nabla^{\mathrm{s}}\boldsymbol{\varphi}_i^{u_c}:\nabla^{\mathrm{s}}\boldsymbol{\varphi}_j^{u_c}\,\vec{u}_j^c(t_{n+1})\,\mathrm{d}\Omega_c \\
&\quad - \left(\frac{2G_c}{3}-K_c\right)\int_{\Omega_c}\nabla\cdot\boldsymbol{\varphi}_i^{u_c}\,\nabla\cdot\boldsymbol{\varphi}_j^{u_c}\,\vec{u}_j^c(t_{n+1})\,\mathrm{d}\Omega_c \\
&\quad - 3K_c\,\omega_{\mathrm{Li}^\oplus}\int_{\Omega_c}\nabla\cdot\boldsymbol{\varphi}_i^{u_c}\varphi_j^{\mathrm{Li}^\oplus}\, c_j^{\mathrm{Li}^\oplus}(t_{n+1})\mathrm{d}\Omega_c \\
&\quad - \int_{\Omega_c}\varphi_i^{\mu}\,\varphi_j^{\mu}\,\mu_j^{\mathrm{Li}^\oplus}(t_{n+1})\,\mathrm{d}\Omega_c \\
&\quad + 3K_c\,\omega_{\mathrm{Li}^\oplus}\int_{\Omega_c}\varphi_i^{\mu}\,\nabla\cdot\boldsymbol{\varphi}_j^{u_c}\,\vec{u}_j^c(t_{n+1})\,\mathrm{d}\Omega_c \\
&\quad - 9K_c\,(\omega_{\mathrm{Li}^\oplus})^2\int_{\Omega_c}\varphi_i^{\mu}\,\varphi_j^{\mathrm{Li}^\oplus}\, c_j^{\mathrm{Li}^\oplus}(t_{n+1})\,\mathrm{d}\Omega_c \\
&\quad - \int_{\partial\Omega_c}\varphi_i^{\mathrm{Li}^\oplus}\left\{\vec{h}_{\mathrm{Li}^\oplus}\cdot\vec{n}_c\right\}\mathrm{d}\Gamma - \int_{\partial\Omega_c}\varphi_i^{\phi_c}\left\{\vec{i}_{\mathrm{c}}\cdot\vec{n}_c\right\}\,\mathrm{d}\Gamma - \int_{\partial\Omega_c}\boldsymbol{\varphi}_i^{u_c}\cdot\bar{p}_c\,\mathrm{d}\Gamma.
\end{aligned}
\tag{4.211}
$$

4.A.5 Finite element discretization for the foil domains

We use the same finite-element framework as in the electrolyte (see Section 4.A.1) and the cathode (see Section 4.A.3). The associated nodal unknowns, which are defined at discrete spatial points and vary in time, are interpolated as

$$
\begin{aligned}
\phi_f^*(\vec{x},t) &= \varphi_j^{\phi_f}(\vec{x})\,\phi_j^{f*}(t), \quad \hat{\phi}_f^*(\vec{x}) = \varphi_i^{\phi_f}(\vec{x}), \\
\vec{u}_f^*(\vec{x},t) &= \boldsymbol{\varphi}_j^{u_f}(\vec{x})\,\vec{u}_j^{f*}(t), \quad \hat{\vec{u}}_f^*(\vec{x}) = \boldsymbol{\varphi}_i^{u_f}(\vec{x}).
\end{aligned}
\tag{4.212}
$$

Incorporating the discretized field expressions from Equation (4.212) into the weak form of Equation (4.164) results in the following form:

$$
\int_{\Omega_f}\kappa_f\,\nabla\varphi_i^{\phi_f}(\vec{x})\cdot\nabla\varphi_j^{\phi_f}(\vec{x})\,\phi_j^f(t)\,\mathrm{d}\Omega_f + \int_{\partial\Omega_f}\varphi_i^{\phi_f}(\vec{x})\left\{\vec{i}_f\cdot\vec{n}_f\right\}\mathrm{d}\Gamma = 0. \tag{4.213}
$$

The discretized weak form of equation (4.165) is simply

$$\begin{aligned}
&- 2G_f \int_{\Omega_f} \nabla^{\mathrm{s}} \boldsymbol{\varphi}_i^{u_f}(\vec{x}) : \nabla^{\mathrm{s}} \boldsymbol{\varphi}_j^{u_f}(\vec{x})\, \vec{u}_j^f(t)\, \mathrm{d}\Omega_f \\
&+ \left(\frac{2G_f}{3} - K_f\right) \int_{\Omega_f} \nabla \cdot \boldsymbol{\varphi}_i^{u_f}(\vec{x})\, \nabla \cdot \boldsymbol{\varphi}_j^{u_f}(\vec{x})\, \vec{u}_j^f(t)\, \mathrm{d}\Omega_f \\
&+ \int_{\partial\Omega_f} \boldsymbol{\varphi}_i^{u_f}(\vec{x}) \cdot \bar{p}_f\, \mathrm{d}\Gamma = 0.
\end{aligned} \tag{4.214}$$

Unlike the cathode and electrolyte, which include an evolutionary equation for the lithium-ion concentration, the foil contains no time-dependent equation; therefore, no time discretization is required. The electric potential and displacement are solved quasi-statically at each time step, with data evaluated at t_{n+1} We solve quasi-static boundary-value problems on Ω_a and Ω_{cc}, enforcing boundary data on $\partial\Omega_a$ and $\partial\Omega_{cc}$. The contributions assembled in (4.213) and (4.214) define the foil residual, which will be linearized and solved at t_{n+1} via a Newton–Raphson iteration in Section 4.A.6.

4.A.6 Newton-Raphson scheme in the foils domain

We solve the nonlinear problem in the foil domains by applying the Newton–Raphson scheme, following the strategy described for the electrolyte in Section 4.A.2, and for the cathode in Section 4.A.4. In the foil domains, the shape and test functions are likewise used without writing their explicit spatial dependence; we simply denote them by

$$\varphi_i^I \equiv \varphi_i^I(\vec{x}), \qquad \varphi_j^I \equiv \varphi_j^I(\vec{x}),$$

where $I \in \{\phi_f, u_f\}$, and $f \in \{a, cc\}$ as already mentioned before. At iteration k, the residual $\mathcal{R}(\phi_j^f, \vec{u}_j^f)$ is linearized using the Gateaux derivative within the Newton-Raphson scheme and written as following form:

$$\frac{\mathrm{d}}{\mathrm{d}\epsilon} \mathcal{R}\left(\phi_j^f + \epsilon\, \delta\phi_j^f,\ \vec{u}_j^f + \epsilon\, \delta\vec{u}_j^f\right)\Big|_{\epsilon=0}^{(k)} = -\mathcal{R}\left(\phi_j^{f(k)},\ \vec{u}_j^{f(k)}\right) \tag{4.215}$$

where Gateaux derivative is written expilicitly as:

$$\begin{aligned}
&\frac{\mathrm{d}}{\mathrm{d}\epsilon} \mathcal{R}\left(\phi_j^{f(k)} + \epsilon\, \delta\phi_j^f,\ \vec{u}_j^{f(k)} + \epsilon\, \delta\vec{u}_j^f\right)\Big|_{\epsilon=0} \\
&= \int_{\Omega_f} \kappa_f\, \nabla\varphi_i^{\phi_f} \cdot \nabla\varphi_j^{\phi_f}\, \delta\phi_j^f(t_{n+1})\, \mathrm{d}\Omega_f \\
&\quad - 2G_f \int_{\Omega_f} \nabla^{\mathrm{s}} \boldsymbol{\varphi}_i^{u_f} : \nabla^{\mathrm{s}} \boldsymbol{\varphi}_j^{u_f}\, \delta\vec{u}_j^f(t_{n+1})\, \mathrm{d}\Omega_f \\
&\quad + \left(\frac{2G_f}{3} - K_f\right) \int_{\Omega_f} \nabla \cdot \boldsymbol{\varphi}_i^{u_f}\, \nabla \cdot \boldsymbol{\varphi}_j^{u_f}\, \delta\vec{u}_j^f(t_{n+1})\, \mathrm{d}\Omega_f.
\end{aligned} \tag{4.216}$$

and residual yields as follows:

$$
\begin{aligned}
&-\mathcal{R}\left(\phi_j^{f(k)}, \vec{u}_j^{f(k)}\right) \\
&= -\int_{\Omega_f} \kappa_f \, \nabla\varphi_i^{\phi_f} \cdot \nabla\varphi_j^{\phi_f} \, \phi_j^{f(k)}(t_{n+1}) \, \mathrm{d}\Omega_f \\
&\quad + 2G_f \int_{\Omega_f} \nabla^{\mathrm{s}}\varphi_i^{u_f} : \nabla^{\mathrm{s}}\varphi_j^{u_f} \, \vec{u}_j^{f(k)}(t_{n+1}) \, \mathrm{d}\Omega_f \\
&\quad - \left(\frac{2G_f}{3} - K_f\right) \int_{\Omega_f} \nabla \cdot \varphi_i^{u_f} \, \nabla \cdot \varphi_j^{u_f} \, \vec{u}_j^{f(k)}(t_{n+1}) \, \mathrm{d}\Omega_f \\
&\quad - \int_{\partial\Omega_f} \varphi_i^{\phi_f} \left\{\vec{i}_f \cdot \vec{n}_f\right\} \mathrm{d}\Gamma - \int_{\partial\Omega_f} \varphi_i^{u_f} \cdot \bar{p}_f \, \mathrm{d}\Gamma.
\end{aligned}
\tag{4.217}
$$

4.A.7 Finite element discretization for the lithium foil-electrolyte interface domain

The corresponding nodal unknowns, defined at discrete spatial locations and evolving over time, are interpolated similarly. The Einstein summation convention is likewise adopted, and it results in the following expressions:

$$
\begin{aligned}
&c^*_{\mathrm{Li}^+}(\vec{x}, t) = \varphi_j^{\mathrm{Li}^+}(\vec{x}) \, c_j^{\mathrm{Li}^+}(t), \quad \hat{c}^*_{\mathrm{Li}^+}(\vec{x}) = \varphi_i^{\mathrm{Li}^+}(\vec{x}), \\
&\phi^*_e(\vec{x}, t) = \varphi_j^{\phi_{\mathrm{e}}}(\vec{x}) \, \phi_j^e(t), \quad \hat{\phi}^*_e(\vec{x}) = \varphi_i^{\phi_{\mathrm{e}}}(\vec{x}), \\
&\phi^*_a(\vec{x}, t) = \varphi_j^{\phi_{\mathrm{a}}}(\vec{x}) \, \phi_j^a(t), \quad \hat{\phi}^*_a(\vec{x}) = \varphi_i^{\phi_{\mathrm{a}}}(\vec{x}).
\end{aligned}
\tag{4.218}
$$

Incorporating the discretized field expressions from Equation (4.218) into the weak form of Equation (4.174) results in the following form[9]:

$$
-\int_{\Gamma_a^e} \varphi_i^{\phi_{\mathrm{a}}}(\vec{x}) \, k_R^a \, (c_{\mathrm{Li}})^{\alpha_C} \left(\varphi_j^{\mathrm{Li}^+}(\vec{x}) \, c_j^{\mathrm{Li}^+}(t)\right)^{\alpha_A} \left(\varphi_j^{\phi_{\mathrm{e}}}(\vec{x}) \, \phi_j^e(t) - \varphi_j^{\phi_{\mathrm{a}}}(\vec{x}) \, \phi_j^a(t)\right) \mathrm{d}\Gamma.
\tag{4.219}
$$

The discretized weak form of equation (4.173) is simply

$$
\int_{\Gamma_a^e} \left(\varphi_i^{\mathrm{Li}^+}(\vec{x}) - \varphi_i^{\phi_{\mathrm{e}}}(\vec{x})\right) \, k_R^a \, (c_{\mathrm{Li}})^{\alpha_C} \left(\varphi_j^{\mathrm{Li}^+}(\vec{x}) \, c_j^{\mathrm{Li}^+}(t)\right)^{\alpha_A} \left(\varphi_j^{\phi_{\mathrm{e}}}(\vec{x}) \, \phi_j^e(t) - \varphi_j^{\phi_{\mathrm{a}}}(\vec{x}) \, \phi_j^a(t)\right) \mathrm{d}\Gamma.
\tag{4.220}
$$

Although the discretized interface weak forms in Equations (4.219) and (4.220) contain no explicit time derivatives—just as the foil equations in Section 4.A.5—we adopt a fully implicit (Backward Euler, $\theta = 1$) scheme: the interface fields c_{Li^+}, ϕ_e, and ϕ_a are all evaluated at t_{n+1} at the current Newton iterate. Equation (4.219) becomes

$$
-\int_{\Gamma_a^e} \varphi_i^{\phi_{\mathrm{a}}}(\vec{x}) \, k_R^a \, (c_{\mathrm{Li}})^{\alpha_C} \left(\varphi_j^{\mathrm{Li}^+}(\vec{x}) \, c_j^{\mathrm{Li}^+}(t_{n+1})\right)^{\alpha_A} \left(\varphi_j^{\phi_{\mathrm{e}}}(\vec{x}) \, \phi_j^e(t_{n+1}) - \varphi_j^{\phi_{\mathrm{a}}}(\vec{x}) \, \phi_j^a(t_{n+1})\right) \mathrm{d}\Gamma.
\tag{4.221}
$$

The electrolyte-side expression in equation (4.220) is reformulated as:

$$
\int_{\Gamma_a^e} \left(\varphi_i^{\mathrm{Li}^+}(\vec{x}) - \varphi_i^{\phi_{\mathrm{e}}}(\vec{x})\right) \, k_R^a \, (c_{\mathrm{Li}})^{\alpha_C} \left(\varphi_j^{\mathrm{Li}^+}(\vec{x}) \, c_j^{\mathrm{Li}^+}(t_{n+1})\right)^{\alpha_A} \left(\varphi_j^{\phi_{\mathrm{e}}}(\vec{x}) \, \phi_j^e(t_{n+1}) - \varphi_j^{\phi_{\mathrm{a}}}(\vec{x}) \, \phi_j^a(t_{n+1})\right) \mathrm{d}\Gamma.
\tag{4.222}
$$

[9]Since the lithium concentration in the foil is unchanged, c^*_{Li} is taken as constant and is not discretized.

4.A.8 Newton-Raphson scheme in the lithium foil-electrolyte interface domain

The Newton–Raphson method is also employed to solve the nonlinear problem at the lithium foil–electrolyte interface. At iteration k, the residual $\mathcal{R}(c_j^{\mathrm{Li}^+}, \phi_j^a, \phi_j^e)$ is linearized via the Gateaux derivative as part of the Newton–Raphson procedure, and is expressed in the following form:

$$\frac{\mathrm{d}}{\mathrm{d}\epsilon}\mathcal{R}\left(c_j^{\mathrm{Li}^+} + \epsilon\,\delta c_j^{\mathrm{Li}^+},\, \phi_j^a + \epsilon\,\delta\phi_j^a,\, \phi_j^e + \epsilon\,\delta\phi_j^e\right)\Big|_{\epsilon=0}^{(k)} = -\mathcal{R}\left(c_j^{\mathrm{Li}^+(k)},\, \phi_j^{a(k)},\, \phi_j^{e(k)}\right) \tag{4.223}$$

where Gateaux derivative is described as:

$$\begin{aligned}
&\frac{\mathrm{d}}{\mathrm{d}\epsilon}\mathcal{R}\left(c_j^{\mathrm{Li}^+(k)} + \epsilon\,\delta c_j^{\mathrm{Li}^+},\, \phi_j^{a(k)} + \epsilon\,\delta\phi_j^a,\, \phi_j^{e(k)} + \epsilon\,\delta\phi_j^e\right)\Big|_{\epsilon=0} \\
&= -\int_{\Gamma_a^e} \varphi_i^{\phi_a}\, k_R^a\,(c_{\mathrm{Li}})^{\alpha_C}\Big\{\alpha_A\big(\varphi_j^{\mathrm{Li}^+} c_j^{\mathrm{Li}^+}(t_{n+1})\big)^{\alpha_A-1}\big(\varphi_j^{\mathrm{Li}^+}\,\delta c_j^{\mathrm{Li}^+}(t_{n+1})\big)\big(\varphi_j^{\phi_e}\phi_j^e(t_{n+1}) - \varphi_j^{\phi_a}\phi_j^a(t_{n+1})\big) \\
&\quad + \big(\varphi_j^{\mathrm{Li}^+} c_j^{\mathrm{Li}^+}(t_{n+1})\big)^{\alpha_A}\big(\varphi_j^{\phi_e}\,\delta\phi_j^e(t_{n+1}) - \varphi_j^{\phi_a}\,\delta\phi_j^a(t_{n+1})\big)\Big\}\,\mathrm{d}\Gamma \\
&\quad + \int_{\Gamma_a^e} \varphi_i^{\mathrm{Li}^+}\, k_R^a\,(c_{\mathrm{Li}})^{\alpha_C}\Big\{\alpha_A\big(\varphi_j^{\mathrm{Li}^+} c_j^{\mathrm{Li}^+}(t_{n+1})\big)^{\alpha_A-1}\big(\varphi_j^{\mathrm{Li}^+}\,\delta c_j^{\mathrm{Li}^+}(t_{n+1})\big)\big(\varphi_j^{\phi_e}\phi_j^e(t_{n+1}) - \varphi_j^{\phi_a}\phi_j^a(t_{n+1})\big) \\
&\quad + \big(\varphi_j^{\mathrm{Li}^+} c_j^{\mathrm{Li}^+}(t_{n+1})\big)^{\alpha_A}\big(\varphi_j^{\phi_e}\,\delta\phi_j^e(t_{n+1}) - \varphi_j^{\phi_a}\,\delta\phi_j^a(t_{n+1})\big)\Big\}\,\mathrm{d}\Gamma \\
&\quad - \int_{\Gamma_a^e} \varphi_i^{\phi_e}\, k_R^a\,(c_{\mathrm{Li}})^{\alpha_C}\Big\{\alpha_A\big(\varphi_j^{\mathrm{Li}^+} c_j^{\mathrm{Li}^+}(t_{n+1})\big)^{\alpha_A-1}\big(\varphi_j^{\mathrm{Li}^+}\,\delta c_j^{\mathrm{Li}^+}(t_{n+1})\big)\big(\varphi_j^{\phi_e}\phi_j^e(t_{n+1}) - \varphi_j^{\phi_a}\phi_j^a(t_{n+1})\big) \\
&\quad + \big(\varphi_j^{\mathrm{Li}^+} c_j^{\mathrm{Li}^+}(t_{n+1})\big)^{\alpha_A}\big(\varphi_j^{\phi_e}\,\delta\phi_j^e(t_{n+1}) - \varphi_j^{\phi_a}\,\delta\phi_j^a(t_{n+1})\big)\Big\}\,\mathrm{d}\Gamma
\end{aligned} \tag{4.224}$$

and residual yields as follows:

$$\begin{aligned}
&-\mathcal{R}\left(c_j^{\mathrm{Li}^+(k)},\, \phi_j^{a(k)},\, \phi_j^{e(k)}\right) \\
&= \int_{\Gamma_a^e} \varphi_i^{\phi_{\mathrm{a}}}\, k_R^a\,(c_{\mathrm{Li}})^{\alpha_C}\left(\varphi_j^{\mathrm{Li}^+}\, c_j^{\mathrm{Li}^+}(t_{n+1})\right)^{\alpha_A}\left(\varphi_j^{\phi_{\mathrm{e}}}\,\phi_j^e(t_{n+1}) - \varphi_j^{\phi_{\mathrm{a}}}\,\phi_j^a(t_{n+1})\right)\mathrm{d}\Gamma \\
&- \int_{\Gamma_a^e} \varphi_i^{\mathrm{Li}^+}\, k_R^a\,(c_{\mathrm{Li}})^{\alpha_C}\left(\varphi_j^{\mathrm{Li}^+}\, c_j^{\mathrm{Li}^+}(t_{n+1})\right)^{\alpha_A}\left(\varphi_j^{\phi_{\mathrm{e}}}\,\phi_j^e(t_{n+1}) - \varphi_j^{\phi_{\mathrm{a}}}\,\phi_j^a(t_{n+1})\right)\mathrm{d}\Gamma \\
&+ \int_{\Gamma_a^e} \varphi_i^{\phi_{\mathrm{e}}}\, k_R^a\,(c_{\mathrm{Li}})^{\alpha_C}\left(\varphi_j^{\mathrm{Li}^+}\, c_j^{\mathrm{Li}^+}(t_{n+1})\right)^{\alpha_A}\left(\varphi_j^{\phi_{\mathrm{e}}}\,\phi_j^e(t_{n+1}) - \varphi_j^{\phi_{\mathrm{a}}}\,\phi_j^a(t_{n+1})\right)\mathrm{d}\Gamma.
\end{aligned} \tag{4.225}$$

4.A.9 Finite element discretization for the electrolyte-cathode interface domain

The corresponding nodal unknowns—defined at discrete spatial points and evolving in time—are interpolated in the same manner. Adopting the Einstein summation convention, we obtain the following expressions

$$\begin{aligned}
&c_{\mathrm{Li}^+}^*(\vec{x},t) = \varphi_j^{\mathrm{Li}^+}(\vec{x})\; c_j^{\mathrm{Li}^+}(t), \quad \hat{c}_{\mathrm{Li}^+}^*(\vec{x}) = \varphi_i^{\mathrm{Li}^+}(\vec{x}), \\
&c_{\mathrm{Li}^\oplus}^*(\vec{x},t) = \varphi_j^{\mathrm{Li}^\oplus}(\vec{x})\; c_j^{\mathrm{Li}^\oplus}(t), \quad \hat{c}_{\mathrm{Li}^\oplus}^*(\vec{x}) = \varphi_i^{\mathrm{Li}^\oplus}(\vec{x}), \\
&\phi_e^*(\vec{x},t) = \varphi_j^{\phi_{\mathrm{e}}}(\vec{x})\; \phi_j^e(t), \quad \hat{\phi}_e^*(\vec{x}) = \varphi_i^{\phi_{\mathrm{e}}}(\vec{x}), \\
&\phi_c^*(\vec{x},t) = \varphi_j^{\phi_c}(\vec{x})\; \phi_j^c(t), \quad \hat{\phi}_c^*(\vec{x}) = \varphi_i^{\phi_c}(\vec{x}), \\
&\vec{u}_c^*(\vec{x},t) = \boldsymbol{\varphi}_j^{u_c}(\vec{x})\; \vec{u}_j^c(t).
\end{aligned} \tag{4.226}$$

Incorporating the discretized field expressions from Equation (4.226) into the weak form of Equation (4.184) results in the following form:

$$\int_{\Gamma_e^c} \left(\varphi_i^{\phi_e}(\vec{x}) - \varphi_i^{\mathrm{Li}^+}(\vec{x})\right) k_R^{c*} \left(\varphi_j^{\mathrm{Li}^+}(\vec{x})\, c_j^{\mathrm{Li}^+}(t)\right)^{\alpha_A} \left(c_{\mathrm{Li}^\oplus}^{\mathrm{sat}*} - \varphi_j^{\mathrm{Li}^\oplus}(\vec{x})\, c_j^{\mathrm{Li}^\oplus}(t)\right)^{\alpha_A} \left(\varphi_j^{\mathrm{Li}^\oplus}(\vec{x})\, c_j^{\mathrm{Li}^\oplus}(t)\right)^{\alpha_C}$$
$$\Bigg[\left(\varphi_j^{\phi_c}(\vec{x})\, \phi_j^c(t) - \varphi_j^{\phi_e}(\vec{x})\, \phi_j^e(t)\right) + \mu_{\mathrm{Li}^\oplus}^{0*} + \ln\left(\frac{\varphi_j^{\mathrm{Li}^\oplus}(\vec{x})\, c_j^{\mathrm{Li}^\oplus}(t)}{c_{\mathrm{Li}^\oplus}^{\mathrm{sat}*} - \varphi_j^{\mathrm{Li}^\oplus}(\vec{x})\, c_j^{\mathrm{Li}^\oplus}(t)}\right)$$
$$- 3K_c^*\, \omega_{\mathrm{Li}^\oplus}^*\, \nabla^* \cdot \left(\boldsymbol{\varphi}_j^{u_c}(\vec{x})\, \vec{u}_j^c(t)\right) + 9K_c^*\, (\omega_{\mathrm{Li}^\oplus}^*)^2 \left(\varphi_j^{\mathrm{Li}^\oplus}(\vec{x})\, c_j^{\mathrm{Li}^\oplus}(t) - c_{\mathrm{Li}^\oplus}^{0*}\right) \Bigg] \, \mathrm{d}\Gamma \tag{4.227}$$

The discretized weak form of equation (4.185) is simply

$$\int_{\Gamma_e^c} \left(\varphi_i^{\mathrm{Li}^\oplus}(\vec{x}) + \varphi_i^{\phi_c}(\vec{x})\right) k_R^{c*} \left(\varphi_j^{\mathrm{Li}^+}(\vec{x})\, c_j^{\mathrm{Li}^+}(t)\right)^{\alpha_A} \left(c_{\mathrm{Li}^\oplus}^{\mathrm{sat}*} - \varphi_j^{\mathrm{Li}^\oplus}(\vec{x})\, c_j^{\mathrm{Li}^\oplus}(t)\right)^{\alpha_A} \left(\varphi_j^{\mathrm{Li}^\oplus}(\vec{x})\, c_j^{\mathrm{Li}^\oplus}(t)\right)^{\alpha_C}$$
$$\Bigg[\left(\varphi_j^{\phi_c}(\vec{x})\, \phi_j^c(t) - \varphi_j^{\phi_e}(\vec{x})\, \phi_j^e(t)\right) + \mu_{\mathrm{Li}^\oplus}^{0*} + \ln\left(\frac{\varphi_j^{\mathrm{Li}^\oplus}(\vec{x})\, c_j^{\mathrm{Li}^\oplus}(t)}{c_{\mathrm{Li}^\oplus}^{\mathrm{sat}*} - \varphi_j^{\mathrm{Li}^\oplus}(\vec{x})\, c_j^{\mathrm{Li}^\oplus}(t)}\right)$$
$$- 3K_c^*\, \omega_{\mathrm{Li}^\oplus}^*\, \nabla^* \cdot \left(\boldsymbol{\varphi}_j^{u_c}(\vec{x})\, \vec{u}_j^c(t)\right) + 9K_c^*\, (\omega_{\mathrm{Li}^\oplus}^*)^2 \left(\varphi_j^{\mathrm{Li}^\oplus}(\vec{x})\, c_j^{\mathrm{Li}^\oplus}(t) - c_{\mathrm{Li}^\oplus}^{0*}\right) \Bigg] \, \mathrm{d}\Gamma \tag{4.228}$$

After adopting a fully implicit (Backward Euler, $\theta = 1$) scheme, the cathode–electrolyte interface fields c_{Li^+}, $c_{\mathrm{Li}^\oplus}$, ϕ_e, ϕ_c, and $\vec{u}_c$ are evaluated at t_{n+1} at the current Newton iterate, and the interface contribution takes the following form for the Equation (4.227):

$$\int_{\Gamma_e^c} \left(\varphi_i^{\phi_e}(\vec{x}) - \varphi_i^{\mathrm{Li}^+}(\vec{x})\right) k_R^{c*} \left(\varphi_j^{\mathrm{Li}^+}(\vec{x}) c_j^{\mathrm{Li}^+}(t_{n+1})\right)^{\alpha_A} \left(c_{\mathrm{Li}^\oplus}^{\mathrm{sat}*} - \varphi_j^{\mathrm{Li}^\oplus}(\vec{x}) c_j^{\mathrm{Li}^\oplus}(t_{n+1})\right)^{\alpha_A} \left(\varphi_j^{\mathrm{Li}^\oplus}(\vec{x}) c_j^{\mathrm{Li}^\oplus}(t_{n+1})\right)^{\alpha_C}$$
$$\Bigg[\left(\varphi_j^{\phi_c}(\vec{x})\, \phi_j^c(t_{n+1}) - \varphi_j^{\phi_e}(\vec{x})\, \phi_j^e(t_{n+1})\right) + \mu_{\mathrm{Li}^\oplus}^{0*} + \ln\left(\frac{\varphi_j^{\mathrm{Li}^\oplus}(\vec{x})\, c_j^{\mathrm{Li}^\oplus}(t_{n+1})}{c_{\mathrm{Li}^\oplus}^{\mathrm{sat}*} - \varphi_j^{\mathrm{Li}^\oplus}(\vec{x})\, c_j^{\mathrm{Li}^\oplus}(t_{n+1})}\right)$$
$$- 3K_c^*\, \omega_{\mathrm{Li}^\oplus}^*\, \nabla^* \cdot \left(\boldsymbol{\varphi}_j^{u_c}(\vec{x}) \vec{u}_j^c(t_{n+1})\right) + 9K_c^*\, (\omega_{\mathrm{Li}^\oplus}^*)^2 \left(\varphi_j^{\mathrm{Li}^\oplus}(\vec{x}) c_j^{\mathrm{Li}^\oplus}(t_{n+1}) - c_{\mathrm{Li}^\oplus}^{0*}\right) \Bigg] \, \mathrm{d}\Gamma \tag{4.229}$$

Equation (4.228) becomes

$$\int_{\Gamma_e^c} \left(\varphi_i^{\mathrm{Li}^\oplus}(\vec{x}) + \varphi_i^{\phi_c}(\vec{x})\right) k_R^{c*} \left(\varphi_j^{\mathrm{Li}^+}(\vec{x})\, c_j^{\mathrm{Li}^+}(t_{n+1})\right)^{\alpha_A} \left(c_{\mathrm{Li}^\oplus}^{\mathrm{sat}*} - \varphi_j^{\mathrm{Li}^\oplus}(\vec{x})\, c_j^{\mathrm{Li}^\oplus}(t_{n+1})\right)^{\alpha_A} \left(\varphi_j^{\mathrm{Li}^\oplus}(\vec{x})\, c_j^{\mathrm{Li}^\oplus}(t_{n+1})\right)^{\alpha_C}$$
$$\Bigg[\left(\varphi_j^{\phi_c}(\vec{x})\, \phi_j^c(t_{n+1}) - \varphi_j^{\phi_e}(\vec{x})\, \phi_j^e(t_{n+1})\right) + \mu_{\mathrm{Li}^\oplus}^{0*} + \ln\left(\frac{\varphi_j^{\mathrm{Li}^\oplus}(\vec{x})\, c_j^{\mathrm{Li}^\oplus}(t_{n+1})}{c_{\mathrm{Li}^\oplus}^{\mathrm{sat}*} - \varphi_j^{\mathrm{Li}^\oplus}(\vec{x})\, c_j^{\mathrm{Li}^\oplus}(t_{n+1})}\right)$$
$$- 3K_c^*\, \omega_{\mathrm{Li}^\oplus}^*\, \nabla^* \cdot \left(\boldsymbol{\varphi}_j^{u_c}(\vec{x})\, \vec{u}_j^c(t_{n+1})\right) + 9K_c^*\, (\omega_{\mathrm{Li}^\oplus}^*)^2 \left(\varphi_j^{\mathrm{Li}^\oplus}(\vec{x})\, c_j^{\mathrm{Li}^\oplus}(t_{n+1}) - c_{\mathrm{Li}^\oplus}^{0*}\right) \Bigg] \, \mathrm{d}\Gamma \tag{4.230}$$

4.A.10 Newton-Raphson scheme in the electrolyte-cathode interface domain

The Newton–Raphson scheme is also employed to solve the nonlinear problem at the electrolyte-cathode interface. The residual $\mathcal{R}\left(c_j^{\mathrm{Li}^+(k)}, c_j^{\mathrm{Li}^\oplus(k)}, \phi_j^{e(k)}, \phi_j^{c(k)}, \vec{u}_j^{c(k)}\right)$ is linearized via the Gateaux derivative as part of the Newton–Raphson procedure at iteration

k, and is expressed in the following form:

$$\begin{aligned}&\frac{\mathrm{d}}{\mathrm{d}\epsilon}\mathcal{R}\left(c_j^{\mathrm{Li}^+}+\epsilon\,\delta c_j^{\mathrm{Li}^+},\, c_j^{\mathrm{Li}^\oplus}+\epsilon\,\delta c_j^{\mathrm{Li}^\oplus},\, \phi_j^e+\epsilon\,\delta\phi_j^e,\, \phi_j^c+\epsilon\,\delta\phi_j^c,\, \vec{u}_j^c+\epsilon\,\delta\vec{u}_j^c\right)\Big|_{\epsilon=0}^{(k)}\\&=-\mathcal{R}\left(c_j^{\mathrm{Li}^+(k)},\, c_j^{\mathrm{Li}^\oplus(k)},\phi_j^{e(k)},\, \phi_j^{c(k)},\, \vec{u}_j^{c(k)}\right)\end{aligned}\tag{4.231}$$

As the electrolyte–cathode interface contribution is algebraically much more involved than the lithium-foil counterpart, we introduce the following abbreviations in order to simplify the presentation of the Newton–Raphson linearization.

$$\begin{aligned}A &:= \varphi_j^{\mathrm{Li}^+}(\vec{x})\, c_j^{\mathrm{Li}^+}(t_{n+1}),\\B &:= c_{\mathrm{Li}^\oplus}^{\mathrm{sat}*} - \varphi_j^{\mathrm{Li}^\oplus}(\vec{x})\, c_j^{\mathrm{Li}^\oplus}(t_{n+1}),\\C &:= \varphi_j^{\mathrm{Li}^\oplus}(\vec{x})\, c_j^{\mathrm{Li}^\oplus}(t_{n+1}),\\G &:= \left(\varphi_j^{\phi_c}(\vec{x})\,\phi_j^c(t_{n+1}) - \varphi_j^{\phi_e}(\vec{x})\,\phi_j^e(t_{n+1})\right) + \mu_{\mathrm{Li}^\oplus}^{0*} + \ln\left(\frac{C}{B}\right)\\&\quad - 3K_c^*\omega_{\mathrm{Li}^\oplus}^*\,\nabla^*\cdot\left(\boldsymbol{\varphi}_j^{u_c}(\vec{x})\,\vec{u}_j^c(t_{n+1})\right) + 9K_c^*(\omega_{\mathrm{Li}^\oplus}^*)^2\left(C - c_{\mathrm{Li}^\oplus}^{0*}\right),\\S &:= -\alpha_A\,\frac{G}{B} + \alpha_C\,\frac{G}{C} + \frac{1}{C} + \frac{1}{B} + 9K_c^*(\omega_{\mathrm{Li}^\oplus}^*)^2.\end{aligned}$$

where Gateaux derivative is described as:

$$
\begin{aligned}
&\frac{\mathrm{d}}{\mathrm{d}\epsilon}\mathcal{R}\Big(c_j^{\mathrm{Li}^+(k)}+\epsilon\,\delta c_j^{\mathrm{Li}^+},c_j^{\mathrm{Li}^\oplus(k)}+\epsilon\,\delta c_j^{\mathrm{Li}^\oplus},\phi_j^{e(k)}+\epsilon\,\delta\phi_j^e,\phi_j^{c(k)}+\epsilon\,\delta\phi_j^c,\vec{u}_j^{\,c(k)}+\epsilon\,\delta\vec{u}_j^{\,c}\Big)\Big|_{\epsilon=0}\\
&=\int_{\Gamma_e^c}\varphi_i^{\phi_e}\,k_R^c\,\Big\{\alpha_A A^{\alpha_A-1}B^{\alpha_A}C^{\alpha_C}\,G\,\varphi_j^{\mathrm{Li}^+}\,\delta c_j^{\mathrm{Li}^+}(t_{n+1})\\
&\qquad+A^{\alpha_A}B^{\alpha_A}C^{\alpha_C}\,S\,\big(\varphi_j^{\mathrm{Li}^\oplus}\,\delta c_j^{\mathrm{Li}^\oplus}(t_{n+1})\big)\\
&\qquad+A^{\alpha_A}B^{\alpha_A}C^{\alpha_C}\,\big(-\varphi_j^{\phi_e}\,\delta\phi_j^e(t_{n+1})+\varphi_j^{\phi_c}\,\delta\phi_j^c(t_{n+1})\big)\\
&\qquad+A^{\alpha_A}B^{\alpha_A}C^{\alpha_C}\,\big(-3K_c\,\omega_{\mathrm{Li}^\oplus}\big)\,\nabla\cdot\big(\boldsymbol{\varphi}_j^{u_c}\,\delta\vec{u}_j^{\,c}(t_{n+1})\big)\Big\}\,\mathrm{d}\Gamma\\
&-\int_{\Gamma_e^c}\varphi_i^{\mathrm{Li}^+}\,k_R^c\,\Big\{\alpha_A A^{\alpha_A-1}B^{\alpha_A}C^{\alpha_C}\,G\,\varphi_j^{\mathrm{Li}^+}\,\delta c_j^{\mathrm{Li}^+}(t_{n+1})\\
&\qquad+A^{\alpha_A}B^{\alpha_A}C^{\alpha_C}\,S\,\big(\varphi_j^{\mathrm{Li}^\oplus}\,\delta c_j^{\mathrm{Li}^\oplus}(t_{n+1})\big)\\
&\qquad+A^{\alpha_A}B^{\alpha_A}C^{\alpha_C}\,\big(-\varphi_j^{\phi_e}\,\delta\phi_j^e(t_{n+1})+\varphi_j^{\phi_c}\,\delta\phi_j^c(t_{n+1})\big)\\
&\qquad+A^{\alpha_A}B^{\alpha_A}C^{\alpha_C}\,\big(-3K_c\,\omega_{\mathrm{Li}^\oplus}\big)\,\nabla\cdot\big(\boldsymbol{\varphi}_j^{u_c}\,\delta\vec{u}_j^{\,c}(t_{n+1})\big)\Big\}\,\mathrm{d}\Gamma\\
&+\int_{\Gamma_e^c}\varphi_i^{\mathrm{Li}^\oplus}\,k_R^{c*}\,\Big\{\alpha_A A^{\alpha_A-1}B^{\alpha_A}C^{\alpha_C}\,G\,\big(\varphi_j^{\mathrm{Li}^+}\,\delta c_j^{\mathrm{Li}^+}(t_{n+1})\big)\\
&\qquad+A^{\alpha_A}B^{\alpha_A}C^{\alpha_C}\,S\,\big(\varphi_j^{\mathrm{Li}^\oplus}\,\delta c_j^{\mathrm{Li}^\oplus}(t_{n+1})\big)\\
&\qquad+A^{\alpha_A}B^{\alpha_A}C^{\alpha_C}\,\big(-\varphi_j^{\phi_e}\,\delta\phi_j^e(t_{n+1})+\varphi_j^{\phi_c}\,\delta\phi_j^c(t_{n+1})\big)\\
&\qquad+A^{\alpha_A}B^{\alpha_A}C^{\alpha_C}\,\big(-3K_c\,\omega_{\mathrm{Li}^\oplus}\big)\,\nabla\cdot\big(\boldsymbol{\varphi}_j^{u_c}\,\delta\vec{u}_j^{\,c}(t_{n+1})\big)\Big\}\,\mathrm{d}\Gamma\\
&+\int_{\Gamma_e^c}\varphi_i^{\phi_c}\,k_R^c\,\Big\{\alpha_A A^{\alpha_A-1}B^{\alpha_A}C^{\alpha_C}\,G\,\big(\varphi_j^{\mathrm{Li}^+}\,\delta c_j^{\mathrm{Li}^+}(t_{n+1})\big)\\
&\qquad+A^{\alpha_A}B^{\alpha_A}C^{\alpha_C}\,S\,\big(\varphi_j^{\mathrm{Li}^\oplus}\,\delta c_j^{\mathrm{Li}^\oplus}(t_{n+1})\big)\\
&\qquad+A^{\alpha_A}B^{\alpha_A}C^{\alpha_C}\,\big(-\varphi_j^{\phi_e}\,\delta\phi_j^e(t_{n+1})+\varphi_j^{\phi_c}\,\delta\phi_j^c(t_{n+1})\big)\\
&\qquad+A^{\alpha_A}B^{\alpha_A}C^{\alpha_C}\,\big(-3K_c\,\omega_{\mathrm{Li}^\oplus}\big)\,\nabla\cdot\big(\boldsymbol{\varphi}_j^{u_c}\,\delta\vec{u}_j^{\,c}(t_{n+1})\big)\Big\}\,\mathrm{d}\Gamma
\end{aligned}
\tag{4.232}
$$

and residual yields as follows:

$$
\begin{aligned}
&-\mathcal{R}\left(c_j^{\mathrm{Li}^+(k)},\,c_j^{\mathrm{Li}^\oplus(k)},\phi_j^{e(k)},\,\phi_j^{c(k)},\,\vec{u}_j^{\,c(k)}\right)\\
&=-\int_{\Gamma_e^c}\varphi_i^{\phi_e}\,k_R^c\,A^{\alpha_A}B^{\alpha_A}C^{\alpha_C}\,G\,\mathrm{d}\Gamma\\
&+\int_{\Gamma_e^c}\varphi_i^{\mathrm{Li}^+}\,k_R^c\,A^{\alpha_A}B^{\alpha_A}C^{\alpha_C}\,G\,\mathrm{d}\Gamma\\
&-\int_{\Gamma_e^c}\varphi_i^{\mathrm{Li}^\oplus}\,k_R^c\,A^{\alpha_A}B^{\alpha_A}C^{\alpha_C}\,G\,\mathrm{d}\Gamma\\
&-\int_{\Gamma_e^c}\varphi_i^{\phi_c}\,k_R^c\,A^{\alpha_A}B^{\alpha_A}C^{\alpha_C}\,G\,\mathrm{d}\Gamma.
\end{aligned}
\tag{4.233}
$$

Chapter 5

Commercial versus hybrid thermochemical regenerated $LiCoO_2$ cathodes: A comparative electrochemical study

5.1 Introduction

Thanks to their high energy density and reliable electrochemical performance, lithium-ion batteries (LIBs) have become among the most prominent and cost-efficient energy storage solutions, advancing portable electronics, electric vehicles, and grid-scale energy storage systems [355, 356, 357]. However, the widespread use of LIBs brings significant environmental challenges, including improper disposal leading to soil and water contamination, as well as the resource-intensive and environmentally detrimental mining of critical raw materials such as lithium, cobalt, and nickel [358, 359, 360, 361]. While Chapter 4 focused on the continuum modeling of coupled electro-chemo-mechanical behavior in an idealized LCO-based half-cell, the present chapter examines the same material family from an experimental perspective by comparing commercial and regenerated $LiCoO_2$ cathodes under identical half-cell conditions. The aim is not to validate the continuum model directly, but to assess whether regeneration-induced differences in microstructure and impurity content are reflected in measurable differences in rate capability, voltage response, and Coulombic efficiency. In this sense, the experimental analysis provides a complementary materials-level benchmark for the broader evaluation of $LiCoO_2$ cathodes. Motivated by these challenges and building on the hybrid thermochemical strategy described in [28]—comprising selective leaching, a glucose-assisted self-sustaining reaction (SSR), and a brief oxidative annealing step—this study presents a comparative assessment of the electrochemical behavior of $LiCoO_2$ (LCO) materials regenerated by Armenuhi Yeghishyan, Dr. Khachatur Manukyan, and their colleagues at the Nuclear Science Laboratory, Department of Physics and Astronomy, University of Notre Dame. Specifically, this work benchmarks regenerated LCO materials against a commercial LCO reference under identical testing protocols, focusing on relative differences in charge–discharge behavior, rate capability, and Coulombic efficiency. In addition to electrochemical testing, morphological and microstructural characterization (scanning electron microscopy (SEM), and porosity analysis) are employed to rationalize performance differences between regenerated and commercial LCO powders. Among commercial LIBs, LCO remains particularly signif-

icant due to its high energy density and stable performance, making it widely used in consumer electronics [362]. Developing sustainable recycling methods to recover and regenerate LCO is therefore essential to reduce the environmental footprint of LIBs while advancing a circular economy. Accordingly, the present study does not aim at an absolute certification of cathode performance; rather, it reports side-by-side comparisons with a commercial baseline under controlled conditions. Within this comparative scope, the chapter evaluates whether the hybrid thermochemical recycling route can produce regenerated LCO materials whose short-term electrochemical response approaches that of commercial references.

5.2 Experimental procedures

5.2.1 List of the samples

As summarized in Table 5.1, all regenerated cathode active materials (LCO-M, LCO-R, and LCO-S) were produced using the same method reported in [28]. To demonstrate the method's applicability, LCO-M was first obtained from commercial powder using the identical workflow. Subsequently, spent lithium-ion battery packs (10.8 V, 5.2 Ah, 57 Wh; six cells per pack) provided by the University of Notre Dame Office of Sustainability were used to produce LCO-R and LCO-S. Following disassembly and laminate separation, the cathode/Al pieces were thermally pre-treated at 350 °C (N_2, then air) to remove electrolyte residues, and the active material was separated from the Al current collector using an HNO_3/H_2O_2 solution at 75 °C; the resulting solution was purified by stepwise precipitation with NH_4HCO_3 (pH $\approx 5 \rightarrow 6.35$). Glucose monohydrate was then added to obtain a gel-like precursor; when ICP–OES indicated Li deficiency, Li_2CO_3 was supplemented. The precursor underwent a glucose-assisted self-sustaining reaction (SSR), followed by brief oxidative annealing ($\approx$ 850 °C for $\sim$ 10 min) to complete the conversion to phase-pure $LiCoO_2$. LCO-R denotes the first recycled batch from the spent batteries, and LCO-S a subsequent batch from the same source produced after correcting the Li : Co stoichiometry (via Li_2CO_3 adjustment) and optimizing the brief oxidative annealing step within the same method. In addition to these regenerated powders, a commercially supplied LCO powder from MSE Supplies Inc. was used as the reference material (hereafter LCO-C). All regenerated materials (LCO-M, LCO-R, and LCO-S) were benchmarked against LCO-C under identical electrochemical testing conditions.

Material	Source	Regeneration Process
LCO-C	Commercial Lithium Cobalt Oxide Powder	Commercial Product (MSE Supplies Inc.)
LCO-M	Regenerated from commercial powder	Regenerated via hybrid thermochemical method
LCO-R	Spent Batteries	Regenerated via hybrid thermochemical method
LCO-S	Spent Batteries	Regenerated via hybrid thermochemical method

Table 5.1: Summary of LCO materials with their sources and regeneration processes.

5.2.2 Scanning electron microscopy images (SEM)

In Figure 5.1, Scanning Electron Microscopy (SEM) was employed to investigate the surface morphology, particle size distribution, and agglomeration behavior of LCO-C, LCO-M, LCO-R, and LCO-S samples. These SEM images were not conducted by the author but were performed at the Department of Physics and Astronomy at the University of Notre Dame by Dr. Khachatur Manukyan, ensuring precise and standardized imaging conditions. A Magellan 400 Scanning Electron Microscope (SEM) was used for surface characterization of the cathode materials. The powders were compacted into small discs (1 mm thick, 5 mm in diameter) and attached to an Al stub for imaging. The SEM was operated at an accelerating voltage of 5.00 kV, which is suitable for capturing fine surface details while minimizing sample damage. A beam current of 25 pA was used to reduce charging effects on non-conductive materials, ensuring high-quality imaging. The images were captured at a magnification of 25,000x, allowing detailed analysis of the particle size, morphology, and agglomeration behavior. The scale bar in the images represents 5 μm, providing a clear reference for estimating feature sizes.

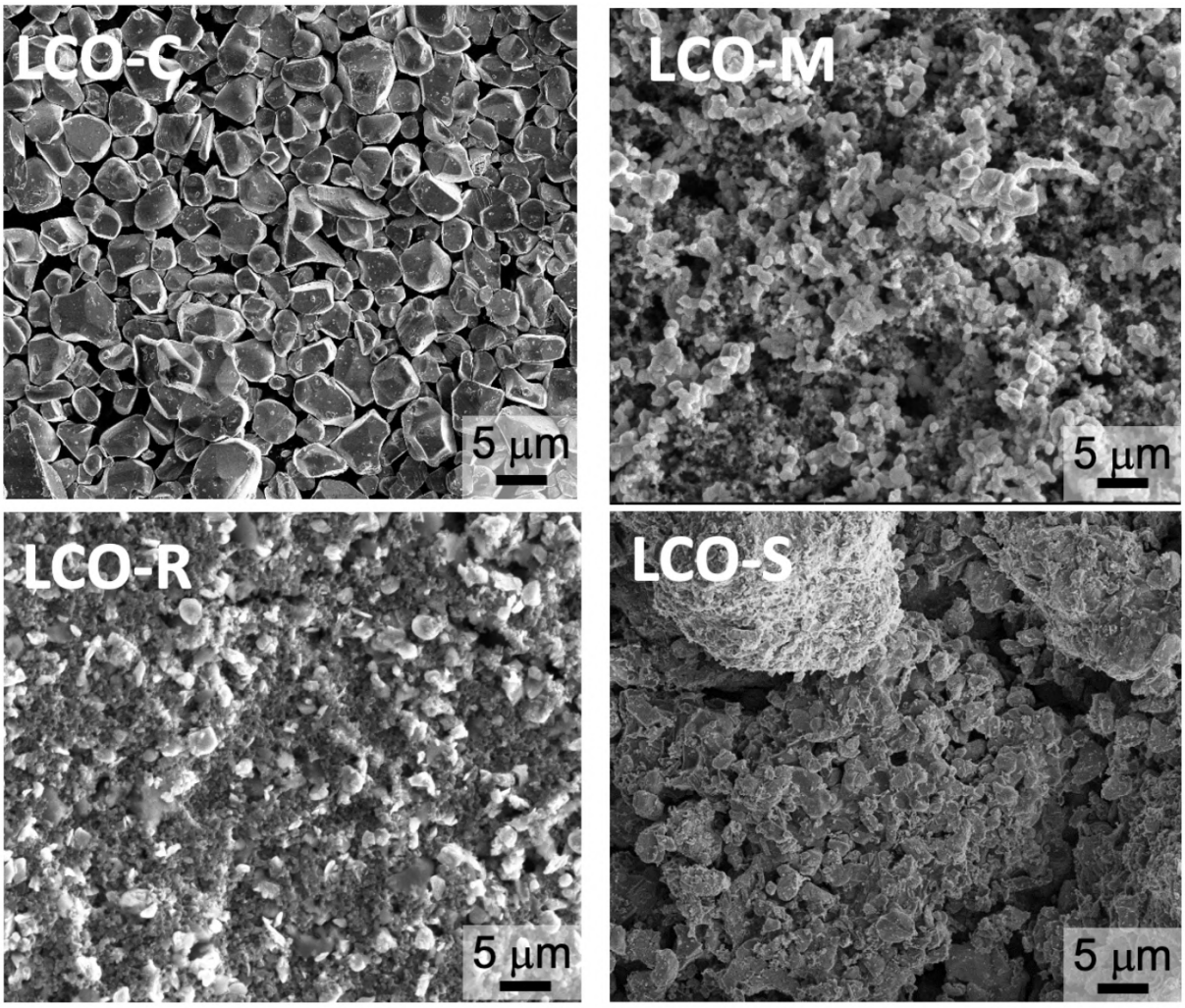

Figure 5.1: SEM images of four different sample

5.2.3 Cathode preparation

To remove moisture, LCO cathode powders were heat-treated in a vacuum oven at 120°C for two hours. After heat treatment, the cathode active particles and Super P carbon black (MTI Corp) were ground together using a ball mill (MTI-MSK-SFM-3) to achieve a fine and uniform particle size. Simultaneously, N-methyl-2-pyrrolidone (NMP, Sigma Aldrich) was heated to 80°C, and polyvinylidene difluoride binder (PVDF, Kynar HSV 900, Arkema) was gradually dissolved into the solvent with continuous stirring for approximately 30 minutes to create a homogeneous solution. The mixture of active and conductive powders obtained after ball milling was gradually added to the PVDF solution in two batches, with each batch stirred for 30 minutes to ensure uniform mixing. The LCO powders, carbon black, and PVDF were dissolved in NMP solvent with a 94:3:3 weight ratio. The resulting slurry (see Figure 5.2a) was stirred on a hot plate before being transferred to a stir plate, where it was mixed overnight to achieve complete homogeneity. Once the slurry was ready, it was evenly coated onto aluminum foil (see Figure 5.2b) using a doctor blade to achieve a uniform thickness of 300 μm. The coated cathode sheet was then dried in a vacuum oven at 90°C under high vacuum for 12 hours to remove residual NMP and water.

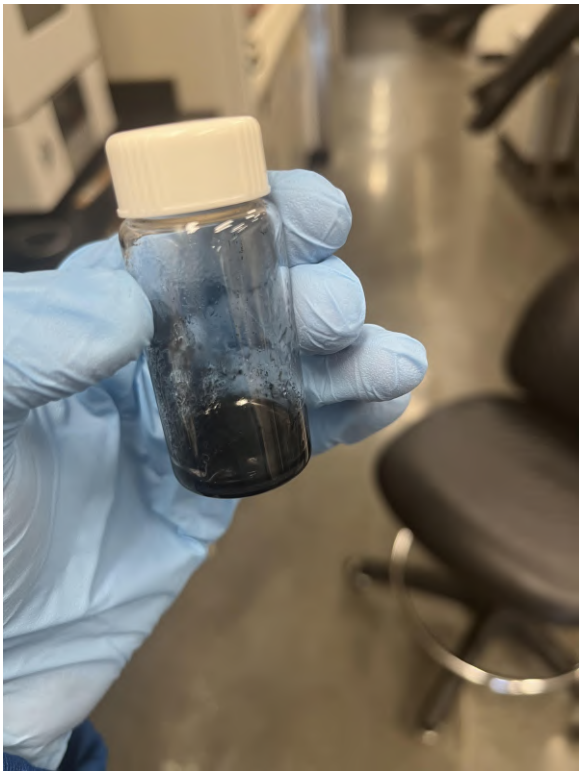

(a) An example of LCO slurry

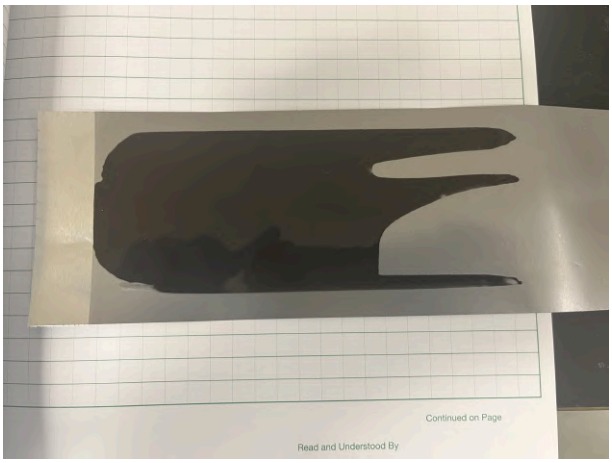

(b) LCO coated aluminum foil

5.2.4 Determination of the mass loading

Mass loading is defined as the weight of the electrode slurry deposited per unit area of the current collector. In laboratory-scale cells, electrodes are commonly prepared with a relatively low mass loading, typically around 2 mg/cm^2 [363]. In these experiments, the mass loading of the punched cathodes varied, with some electrodes having an active material loading was around 2 mg/cm^2, while others exhibited different loadings, as presented in later sections (see Section 5.3.1, 5.3.2, 5.3.3, and 5.3.4). As the areal loading increases, the electrode film thickness also increases. Thicker electrodes are more prone to mechanical issues such as fracturing and delamination from the current collector during the coating and drying processes, making the fabrication of high-loading electrodes more challenging [364].

5.2.4.1 Steps for determining mass loading

In the following sections, the mass loading of each material under comparison has been carefully determined using the specified formulas and methodologies. This approach ensures reliable comparisons and maintains a consistent framework for accurate analysis.

$$\text{Mass loading (mg/cm}^2) = \frac{\text{Mass of coating (mg)}}{\text{Electrode area (cm}^2)}$$

1. **Weighing the bare disc before coating:** The mass of the current collector, serving as the bare electrode substrate was measured [1].

[1]The weight of a 10 mm diameter current collector was measured to be 3.3 mg

2. **Weighing the electrode disc after coating:** The mass of the coated electrode disc was measured.

3. **Calculation of the mass of coating:**

$$\text{Mass of coating} = \text{Total mass of coated disc} - \text{Total mass of bare disc}$$

4. **Determination of the surface area of the electrode:** Area of the coated region was measured.

$$\text{Surface area of the electrode} = A = \pi r^2$$

5. **Calculation of mass loading:**

$$\text{Mass loading} = \frac{\text{Mass of coating}}{\text{Electrode area}}$$

5.2.5 Determination of porosity

Porosity is a crucial factor influencing the electrochemical performance of lithium-ion battery cathode materials. It refers to the fraction of void space within a material and plays a significant role in electrolyte penetration, ion diffusion, and overall battery performance [365].

5.2.5.1 Steps for determining the porosity

1. **Given Data[2].**

   - Total mass of coated disc: 5.1 mg
   - Mass of bare disc: 3.3 mg
   - Thickness of bare disc: 16 μm
   - Thickness of coated disc: 32 μm
   - Mass of LCO (active material): 470 mg
   - Mass of PVDF: 15 mg
   - Mass of Super P: 15 mg
   - Density of LCO: 5050 mg/cm^3
   - Density of PVDF: 1780 mg/cm^3
   - Density of Super P: 1600 mg/cm^3

2. **Determination of the coating Mass**

$$\text{Mass of coating} = \text{Total mass of coated disc} - \text{Mass of bare disc} \tag{5.1}$$

$$\text{Mass of coating} = 5.1 \text{ mg} - 3.3 \text{ mg} = 1.8 \text{ mg} \tag{5.2}$$

[2]These calculations were performed for the LCO-C1 sample, and the same steps were applied to the other samples as well, but for the sake of simplicity, each is not shown individually.

3. **Calculation of the effective coating thickness**

$$\text{Effective coating thickness} = \text{Thickness of coated disc} - \text{Thickness of bare disc} \tag{5.3}$$

$$\text{Effective coating thickness} = 32\ \mu\text{m} - 16\ \mu\text{m} = 16\mu\text{m} = 0.0016\text{cm} \tag{5.4}$$

4. **Calculation of the surface area of the electrode**

$$A = \pi r^2 = \pi(0.5\ \text{cm})^2 = 0.785\ \text{cm}^2 \tag{5.5}$$

5. **Calculation of the coating volume**

$$V_{\text{coating}} = A \times \text{Coating thickness} = 0.785 \times 0.0016 = 0.001257\ \text{cm}^3 \tag{5.6}$$

6. **Determination of the total mass of solid components in the slurry**

$$M_{\text{total solids}} = 470 + 15 + 15 = 500\ \text{mg} \tag{5.7}$$

7. **Calculation of the individual solid component volumes**

$$V_{\text{LCO}} = \frac{470}{5050} \approx 0.09307\ \text{cm}^3 \tag{5.8}$$

$$V_{\text{Super P}} = \frac{15}{1600} \approx 0.009375\ \text{cm}^3 \tag{5.9}$$

$$V_{\text{PVDF}} = \frac{15}{1780} \approx 0.00843\ \text{cm}^3 \tag{5.10}$$

8. **Scaling the Solid Component Volumes to Match the Coating Mass**

$$V_{\text{LCO, scaled}} = V_{\text{LCO}} \times \frac{1.8}{500} \approx 0.000335\ \text{cm}^3 \tag{5.11}$$

$$V_{\text{Super P, scaled}} = V_{\text{Super P}} \times \frac{1.8}{500} \approx 0.00003375\ \text{cm}^3 \tag{5.12}$$

$$V_{\text{PVDF, scaled}} = V_{\text{PVDF}} \times \frac{1.8}{500} \approx 0.0000304\ \text{cm}^3 \tag{5.13}$$

9. **Determination of the Total Volume of Solid Components in the Coating**

$$V_{\text{total solids}} = V_{\text{LCO, scaled}} + V_{\text{Super P, scaled}} + V_{\text{PVDF, scaled}} \tag{5.14}$$

$$V_{\text{total solids}} \approx 0.000335 + 0.0000304 + 0.00003375 \approx 0.00039915\ \text{cm}^3 \tag{5.15}$$

10. **Calculation of the Coating Porosity**

$$\text{Porosity} = 1 - \frac{V_{\text{total solids}}}{V_{\text{coating}}} \tag{5.16}$$

$$\text{Porosity} = 1 - \frac{0.00039915}{0.001257} \approx 1 - 0.3175 \approx 0.6825 \tag{5.17}$$

$$\text{Porosity} \approx 68.3\% \tag{5.18}$$

In the present work, porosity was estimated from electrode mass, coating thickness, geometrical area, and the densities of the solid constituents, and should therefore be regarded as a geometric/density-based estimate of the void fraction within the coating. The values reported here were not independently validated by mercury intrusion porosimetry, nor was a pore-size distribution measured. Consequently, the porosity results are used primarily as comparative descriptors of the electrode architecture across the investigated samples, rather than as a complete pore-network characterization. A more comprehensive assessment of electrode porosity and transport pathways would require dedicated techniques such as Hg porosimetry or three-dimensional imaging-based analysis, which were beyond the scope of the present experimental investigation.

5.2.6 Coin cell assembly

Cathodes were punched into circular discs with a diameter of 10 mm, which were then assembled into 2032-type coin cells in a half-cell configuration. Lithium metal (Alfa Aesar, 0.75 mm thick) was mechanically scraped to remove surface layers, pressed to achieve a shiny surface and reduce anode thickness, and punched into circular discs with a diameter of 14 mm. A separator (polyolefin, from MTI Corp) was placed between the cathode and lithium metal anode to avoid short-circuiting. The separator and cathodes were wet with 25 μL of a 1.0 M $LiPF_6$ electrolyte solution in a 50:50 EC/DEC solvent mixture (Sigma Aldrich). The assembly also included two stainless steel spacers (15.5 mm in diameter and 0.2 mm thick) and a wave spring, all sealed using an electronic crimper. The coin cells were assembled in a precise order as seen in Figure 5.3:

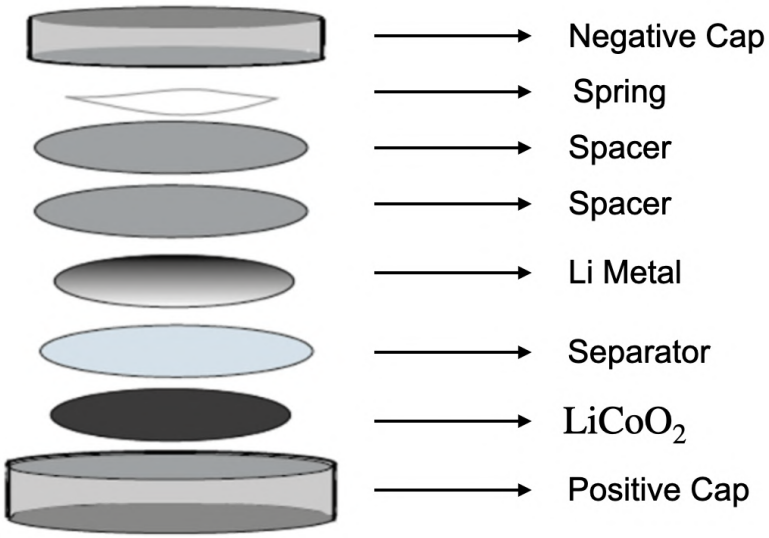

Figure 5.3: A sketch of coin cell configuration during assembly

5.2.7 Half cell cycling performance

The performance and C-rate capabilities of each $LiCoO_2$ sample were assessed using a lithium metal/$LiCoO_2$ half-cell configuration. Galvanostatic charge-discharge tests were conducted in the potential range of 3.0-4.2 V vs. Li^+/Li at various C-rates 0.1, 0.2, 0.5, 1, 2, and 5 on a BTS-5 V 10 mA battery tester (NEWARE, China). The theoretical discharge capacity of $LiCoO_2$ is around 274 mAh/g; however, a more restrictive discharge capacity of 140 mAh/g is commonly employed in practical applications. This constraint stems from inherent structural stability issues and the requirement for cycling durability. In its fully lithiated state, $LiCoO_2$ exhibits a stable layered hexagonal structure. During charging, the removal of lithium ions leads to the formation of non-stoichiometric $Li_{1-x}CoO_2$ substances, which need the undergo oxidation of Co^{3+} ions for compensation of charge. The increasing extraction of lithium modifies the crystallographic structure according to lithium concentration, and when over % 50 of lithium is extracted, the structure experiences a phase shift from hexagonal to monoclinic. This transition markedly destabilizes the material, hence constraining the maximum attainable discharge capacity in practice. Functioning at maximum theoretical capacity would accelerate structural deterioration and capacity decline over successive cycles, so undermining both longevity and dependability. Thus, restricting lithium extraction to around 0.5 per formula unit—and thereby capping the capacity at 140 mAh/g—facilitates enhanced stability and durability throughout charge and discharge cycles [366, 367]. For this reason, discharge capacity of $LiCoO_2$ was taken as 140 mAh/g in these experiments.

5.3 Results and Discussion

5.3.1 Cycling protocol and general rate trend

All cells were cycled according to the rate-capability protocol described in Section 5.2.7: five cycles at each of 0.1, 0.2, 0.5, 1, 2, and 5C (cycles 1–30), followed by five cycles at 0.1C (cycles 31–35) to evaluate reversible capacity recovery after the high-rate steps. All cells were tested under identical conditions (voltage window and protocol), enabling a direct comparison across materials. In general, electrodes with higher areal loading show a modest capacity advantage at low C-rates, whereas thinner (lower-loading) electrodes perform better at higher C-rates, where transport and polarization limitations dominate. As a result, the discharge capacity decreases systematically with C-rate and partially recovers when the current is reduced back to 0.1C. The subsections below report only material-specific observations.

5.3.2 Morphological comparison of commercial and regenerated LCO powders (SEM)

Figure 5.1 compares the particle morphology and agglomeration of LCO-C, LCO-M, LCO-R, and LCO-S (see Section 5.2.2 for imaging conditions). LCO-C, the commercial reference powder, exhibits a notably uniform distribution of well-faceted, equiaxed particles with sharp edges and minimal agglomeration. The particle size is typically on the micron scale (average sizes order of $5 - 10$ μm), consistent with an industrially produced powder, where high-temperature calcination commonly yields larger, faceted grains [368,

369]. Such a morphology offers good structural stability and predictable packing behaviour, but a more modest specific surface area, which tends to favour robust cycling at moderate rates while limiting high-rate performance. In contrast, LCO-M, regenerated from commercial $LiCoO_2$ powder using the hybrid thermochemical route, consists of fine/sub-micron particles (< 1 μm) with a rough surface texture and occasional secondary agglomerates. This morphology may increase the accessible surface area, shorten solid-state diffusion pathways, and facilitate electrolyte access at elevated C-rates; this expectation is evaluated in Section 5.3.7. The first recycled batch from spent cells, LCO-R, displays a fine, texturally irregular particle morphology that is superficially comparable to LCO-M. Although no large secondary agglomerates comparable to those observed in LCO-S are evident, the powder appears heterogeneous and poorly faceted, with a compact fine-particle matrix in several regions. Notably, despite this comparably fine particle size, LCO-R exhibits markedly inferior electrochemical performance, indicating that particle size alone does not control the rate response. This discrepancy suggests that factors beyond bulk morphology, including surface-chemical limitations, imperfect particle connectivity, and electrode-level packing effects, may contribute significantly to the poor electrochemical response of LCO-R. Given the synthesis history of LCO-R, residual surface phases or processing by-products, possibly including Li_2CO_3 from incomplete or inhomogeneous Li compensation, represent a plausible working hypothesis. However, because no direct surface-chemical analysis such as XPS was performed in this work, this interpretation should be regarded as tentative rather than confirmed. The corresponding electrochemical behaviour is discussed in Section 5.3.5. By contrast, the second recycled batch, LCO-S, regenerated under refined Li:Co compensation and annealing conditions, displays a distinctly bimodal particle size distribution. While a significant fraction of the powder consists of fine, sub-micron particles, a number of considerably larger agglomerated clusters — on the order of several micrometres — are also clearly visible. Together with the improved electrochemical response discussed below, this morphology suggests that the refined synthesis conditions may have reduced transport-limiting residual phases relative to LCO-R; however, this cannot be confirmed by SEM alone. At the same time, the broad particle-size distribution indicates that full control over particle growth and agglomeration was not achieved within the present processing window. Compared with LCO-C, the size distribution is broader and the particle packing less uniform; compared with LCO-R, however, the finer matrix fraction appears more connected and the surface texture less irregular. This intermediate morphological character is consistent with the electrochemical observation that LCO-S outperforms LCO-R markedly while falling short of LCO-C and LCO-M at the highest C-rates, as discussed in Section 5.3.6 and Section 5.3.7. It should be emphasised that SEM alone cannot resolve crystal structure, phase purity, or subtle compositional inhomogeneities; these aspects were characterised in detail in the work of Yeghishyan *et al.* [28]. Nonetheless, the morphological trends observed here from the highly uniform, well-faceted commercial grains (LCO-C), through the fine, rough-textured regenerated particles (LCO-M), to the irregular first recycled batch (LCO-R) and the bimodally distributed second recycled batch (LCO-S) — which represents a partial but incomplete recovery of morphological quality — provide a coherent qualitative framework for interpreting the electrochemical performance differences analysed in Sections 5.3.3–5.3.7.

5.3.3 Rate capability of LCO-C

We began with the commercial powders (LCO-C) listed in Table 5.1. The two electrodes from Table 5.2 compared have areal loadings of 2.29 (LCO-C1) and 5.22 mg/cm^2 (LCO-C2). Figure 5.4 shows their specific discharge capacities at the C-rates defined in the cycling protocol. At 0.1–0.2C, the higher-loading electrode delivers a slightly higher capacity; from 0.5C onward, the lower-loading electrode becomes superior, with the performance gap widening at 1–5C. Upon returning to 0.1C, the capacity largely recovers, consistent with reversible rate limitations noted in Section 5.3.1.[3]

Sample ID	Total Mass	Mass Loading	Effective Coating Thickness	Porosity
LCO-C1	5.1 mg	2.29 mg/cm^2	16 μm	%68.3
LCO-C2	7.4 mg	5.22 mg/cm^2	36 μm	%67.8

Table 5.2: Summary of LCO-C samples with their identity, total mass, mass loading, coating thickness, and porosity.

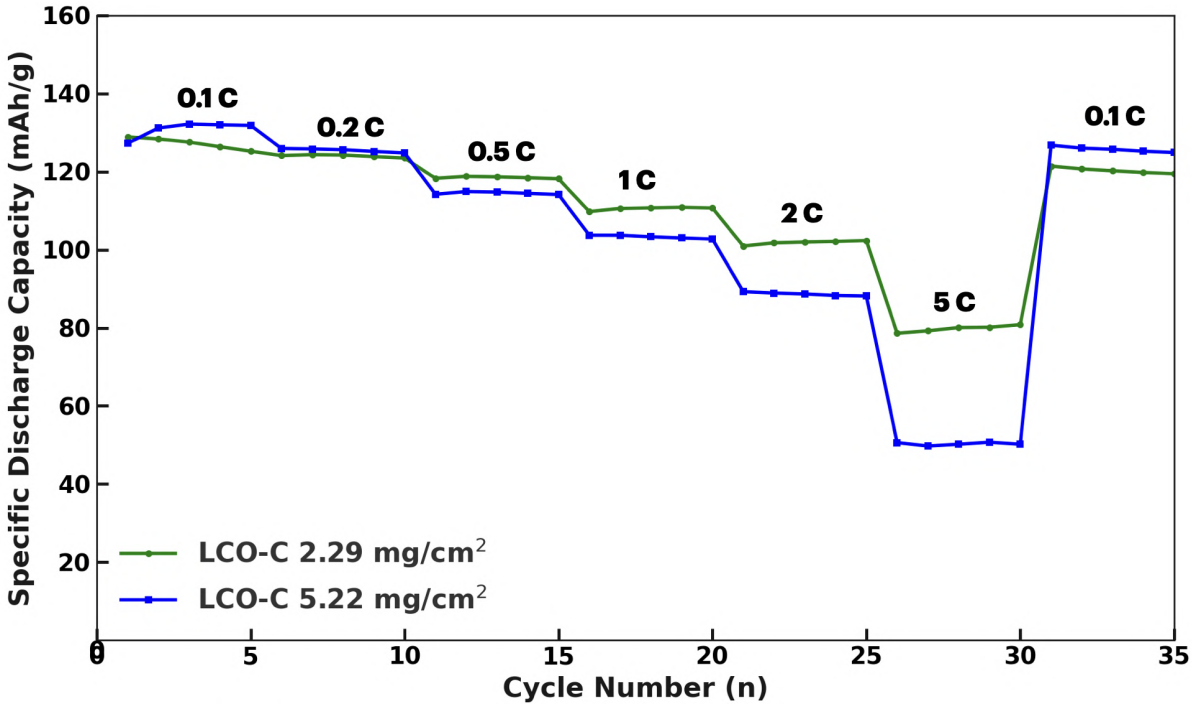

Figure 5.4: Comparison of LCO-C samples among themselves

5.3.4 Rate capability of LCO-M

After completing the rate-capability tests on the commercial material LCO-C, attention shifted to the regenerated batch LCO-M, as shown in Table 5.1. The primary aim of this

[3]Starting with these samples, the mass-loading and porosity calculation steps in Sections 5.2.4.1 and 5.2.5.1 are applied to all subsequent samples.

step was to test the material regenerated using the recyling method and conduct electrochemical analyses as a preliminary phase before applying this method to recycling spent lithium-ion batteries. Consequently, the samples listed in the Table 5.3 were subjected to electrochemical testing. Figure 5.5 compares the two LCO-M electrodes from Table

Sample ID	Total Mass	Mass Loading	Effective Coating Thickness	Porosity
LCO-M1	4.8 mg	1.91 mg/cm^2	15 μm	%71.7
LCO-M2	5.7 mg	3.06 mg/cm^2	25 μm	%72.8

Table 5.3: Summary of LCO-M samples with their identity, total mass, mass loading, and coating thickness.

5.3, with areal loadings 1.91 (LCO-M1) and 3.06 mg/cm^2 (LCO-M2). Minor fluctuations during the first few cycles at 0.1 C are most likely related to electrode wetting effects during cell assembly. At 0.2–0.5C, the lower-loading LCO-M1 exhibits a slightly higher specific discharge capacity than LCO-M2. From 1C upward, the divergence grows, with the higher-loading LCO-M2 dropping more steeply such that the lower-loading LCO-M1 maintains the advantage at 1–5C. After the high-rate steps, both samples show near-initial capacities when cycled again at 0.1C, as described in the cycling protocol.

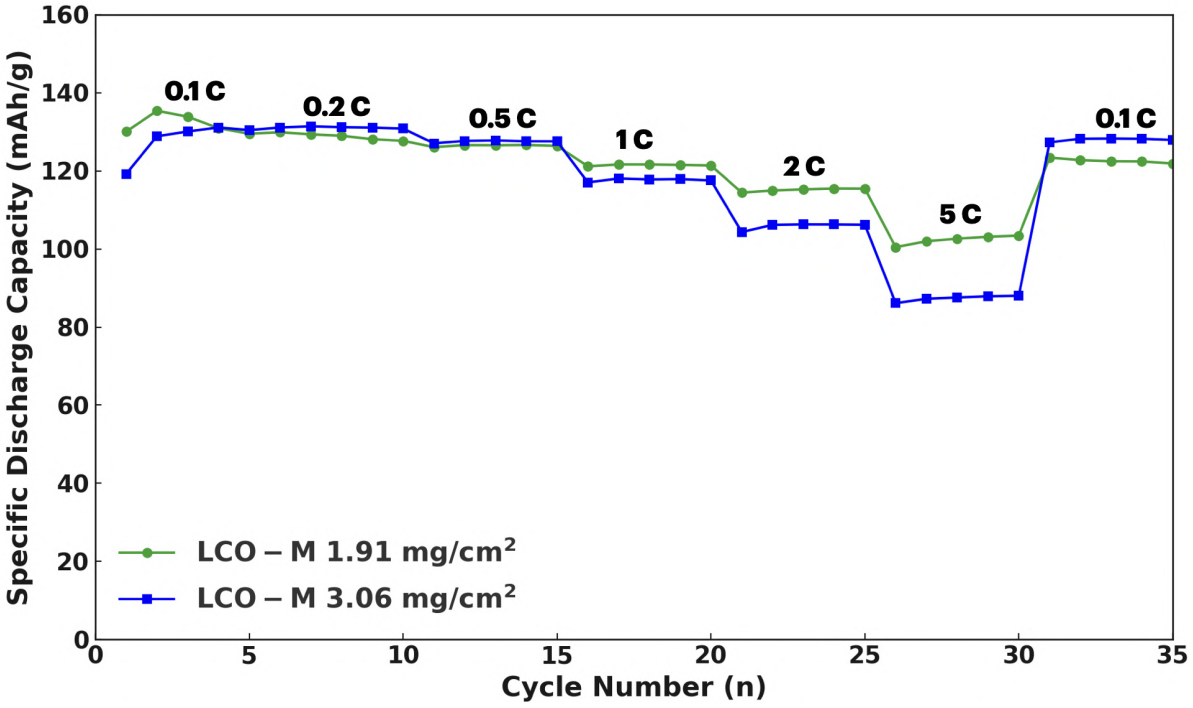

Figure 5.5: Comparison of LCO-M samples among themselves

5.3.5 Rate capability of LCO-R

The electrochemical performance of the regenerated-from-commercial-powder batch LCO-M was found to be consistent with that of the commercial reference LCO-C, confirming

that the hybrid thermochemical route can deliver high-quality $LiCoO_2$ from a clean feedstock. Building on these promising results, the next step was to test cathodes recovered from spent lithium-ion battery packs, in line with the overall recycling objective of this work. As summarized in Table 5.1, the first such recycled batch is denoted LCO-R and was synthesized from the spent-cell leachate using the same hybrid thermochemical route; in that synthesis, Li_2CO_3 was added to the purified leachate as needed to compensate Li losses and to target an overall Li:Co ratio close to 1:1 (see Section 5.2.1).

Sample ID	Total Mass	Mass Loading	Effective Coating Thickness	Porosity
LCO-R1	4.8 mg	1.91 mg/cm^2	16 μm	% 73.5
LCO-R2	4.4 mg	1.4 mg/cm^2	12 μm	% 74.1

Table 5.4: Summary of LCO-R samples with their identity, total mass, mass loading, coating thickness, and porosity.

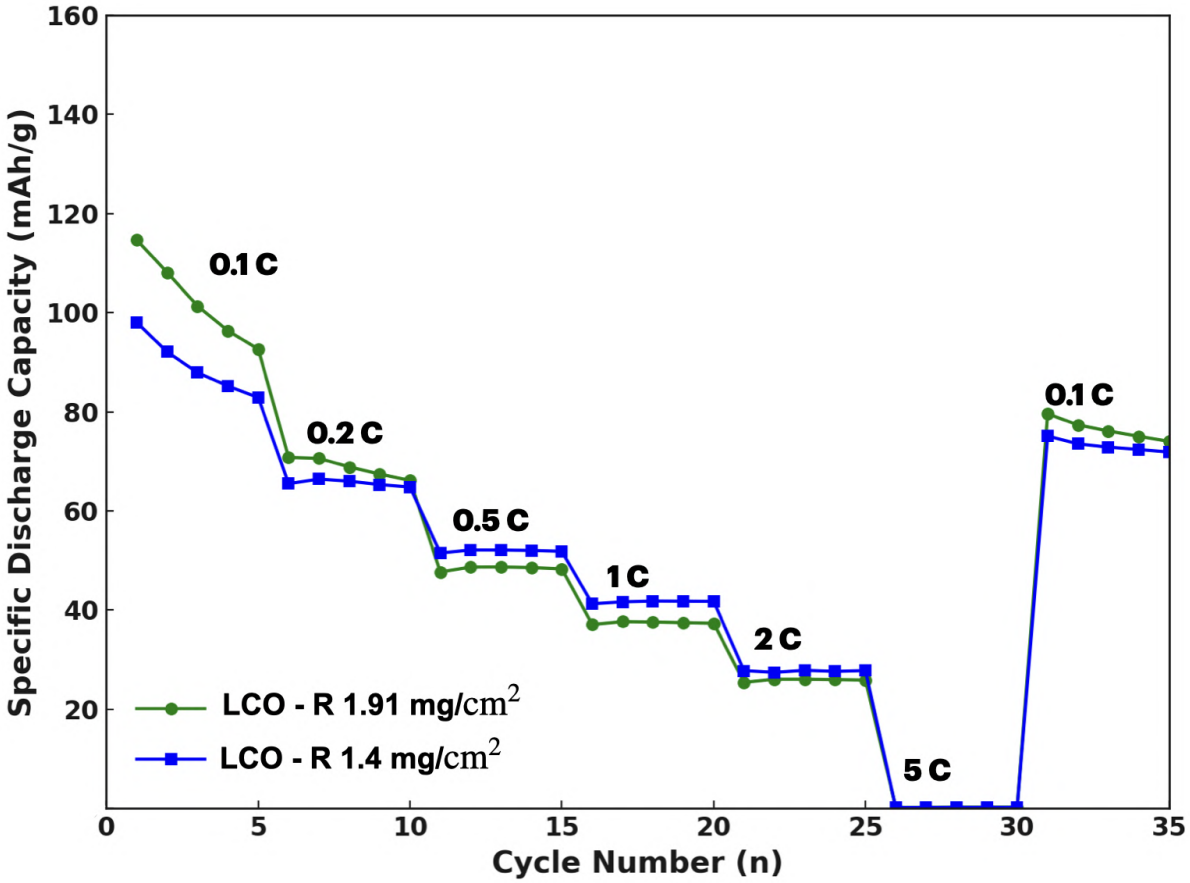

Figure 5.6: Comparison of LCO-R samples among themselves

Figure 5.6 presents the two regenerated electrodes from Table 5.4, with areal loadings 1.91 (LCO-R1) and 1.40 mg/cm^2 (LCO-R2). Both LCO-R samples start with lower initial capacities than the commercial references (LCO-C, LCO-M), and exhibit an early decline. At 0.1–0.2C, LCO-R1 (higher loading) performs slightly better than LCO-R2, but at 1–5C both samples suffer marked drops, with LCO-R1 degrading most severely and

showing negligible capacity at 5C. These trends indicate that the electrochemical response of LCO-R is not controlled by particle size alone. As shown by the SEM observations in Section 5.2.2, LCO-R displays a fine, texturally irregular particle morphology that is superficially comparable to LCO-M. However, although no large secondary agglomerates comparable to those observed in LCO-S are evident, the powder appears heterogeneous and poorly faceted, with a compact fine-particle matrix in several regions. In addition, LCO-R exhibits the highest electrode-level porosity among the four materials (Table 5.4), suggesting less efficient electrode packing and possibly weaker particle connectivity under the present fabrication conditions. These electrode-level features may exacerbate polarization and transport limitations at elevated C-rates. Given the synthesis route described in Section 5.2.1, a plausible working hypothesis is that residual or inhomogeneously distributed Li_2CO_3 and/or other impurity-related surface species contributed to increased interfacial resistance and rate sensitivity. Residual Li_2CO_3 species at the $LiCoO_2$ particle surface have been reported to impede lithium-ion transport and increase interfacial resistance, thereby depressing capacity and rate capability [370, 371]. However, because these surface species were not directly quantified in this work, this explanation should be treated as tentative rather than confirmed. Therefore, the poor rate capability of LCO-R is most consistently interpreted as the combined effect of an irregular fine-particle morphology, high electrode-level porosity, imperfect particle connectivity, and possible transport-limiting surface species. These electrochemical observations motivated a refinement of Li:Co stoichiometry control and annealing conditions in subsequent synthesis runs, leading to the improved second recycled batch LCO-S discussed in Section 5.3.6.

5.3.6 Rate capability of LCO-S

After the challenges encountered in the previous regeneration batch, a new material was regenerated from the same spent cells using refined Li:Co stoichiometry and annealing conditions designed to minimise residual Li_2CO_3, this optimised recycled powder is denoted LCO-S (see Table 5.1). Figure 5.7 compares the two LCO-S electrodes from Table 5.5 with areal loadings 2.16 (LCO-S1) and 5.09 mg/cm^2 (LCO-S2) under the rate-capability protocol defined in Section 5.3.1. At 0.1–0.2C, the higher-loading LCO-S2 delivers a slightly

Sample ID	**Total Mass**	**Mass Loading**	**Effective Coating Thickness**	**Porosity**
LCO-S1	5.0 mg	2.16 mg/cm^2	15 μm	%68.1
LCO-S2	7.3 mg	5.09 mg/cm^2	35 μm	%67.7

Table 5.5: Summary of LCO-S samples with their identity, total mass, mass loading, coating thickness, and porosity.

higher capacity. With increasing rate, both samples decline, but the higher-loading electrode drops more sharply: by 2C a clear separation appears, and at 5C the thicker electrode shows a pronounced loss, consistent with transport and polarization penalties in thicker structures. Upon returning to 0.1C, both samples recover a substantial fraction of capacity, indicating that the high-rate losses are largely reversible and dominated by rate limitations rather than permanent degradation. The more pronounced rate sensitivity of the higher-loading electrode is consistent with the bimodal particle size distribution

observed for LCO-S by SEM (Section 5.2.2): the presence of larger agglomerated clusters within the fine matrix is expected to introduce local transport heterogeneities that become more detrimental as electrode thickness — and therefore effective diffusion path length — increases. To accurately compare the electrochemical performance of the four

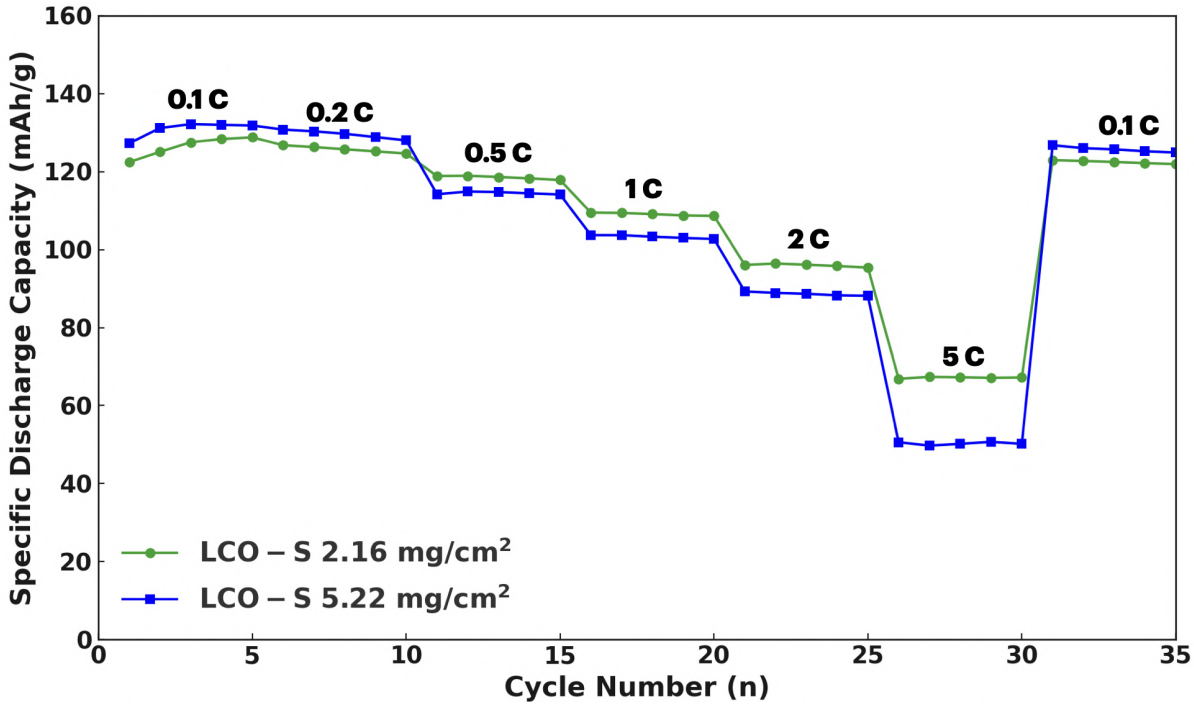

Figure 5.7: Comparison of LCO-S samples among themselves

samples presented in Table 5.1, LCO-C1, LCO-M1, LCO-R1, and LCO-S1 were selected from Tables 5.2-5.5, respectively, based on their similar or closely matched mass loadings. In this study, specific charge and discharge capacities were normalized with respect to mass, as substantial differences in mass loading could lead to inconsistencies and hinder the reliability of the results obtained during the analysis. For the sake of clarity and brevity in subsequent discussions, selected samples—LCO-C1, LCO-M1, LCO-R1, and LCO-S1—will be discussed and referred to by their generalized names: LCO-C, LCO-M, LCO-R, and LCO-S.

5.3.7 Rate capability comparison of LCO materials

Figure 5.8 summarizes the rate-capability response of the four representative electrodes (LCO-C, LCO-M, LCO-R, and LCO-S) over 0.1–5C using the common protocol described in Section 5.3.1. This consolidated comparison provides a direct overview of the relative performance of the commercial reference and the regenerated powders across the full C-rate window. Across all rates, LCO-M delivers the highest specific capacities, with the performance advantage becoming most pronounced at 1–5C. LCO-C and LCO-S follow closely and remain similar at low and intermediate rates, with a clearer separation only emerging at the highest rates. In contrast, LCO-R exhibits the weakest rate capability and approaches negligible capacity at 5C. In summary, LCO-M maintains the strongest capacity retention as the rate increases, LCO-C and LCO-S remain close over most of the window, and LCO-R shows the most pronounced deterioration toward high-rate operation. Consistent with the material-specific observations discussed in Sections 5.3.3-5.3.6,

Figure 5.8 indicates that the optimized regenerated powder (LCO-S) can achieve a rate response comparable to the commercial benchmark under the present fabrication and test conditions, whereas the first recycled batch (LCO-R) highlights the sensitivity of recycled-material performance to regeneration quality. Overall, the results support that the hybrid thermochemical regeneration route can yield regenerated $LiCoO_2$ with commercially competitive rate capability when synthesis and post-processing conditions are properly controlled. The porosity values calculated in Section 5.2.5 and reported in Tables 5.2-5.5 provide additional electrode-level descriptors that are consistent with, but do not by themselves prove, the observed rate trends. Specifically, LCO-S (68.1% and 67.7%) and LCO-C (68.3% and 67.8%) exhibit comparable porosity, consistent with their similar rate response over most of the tested window. It is noteworthy that despite the bimodal particle size distribution observed for LCO-S by SEM, the electrode-level porosity converges toward that of LCO-C. This is consistent with a gap-filling effect, in which the fine particle fraction of the bimodal distribution occupies the interstitial space between larger agglomerated clusters, yielding a comparable overall packing density to the well-faceted LCO-C particles. LCO-M shows slightly higher porosity (71.7% and 72.8%), which may facilitate electrolyte access under the present fabrication conditions. By contrast, LCO-R presents the highest porosity (73.5% and 74.1%), indicating less efficient electrode-level packing under the present calendering conditions, which may exacerbate transport limitations and rate sensitivity. It should be noted, however, that industrial electrodes typically target porosity levels of around 30% [372]; despite attempts in this work (e.g., calendering), a substantial reduction toward this benchmark was not achieved, and further process optimization is therefore warranted.

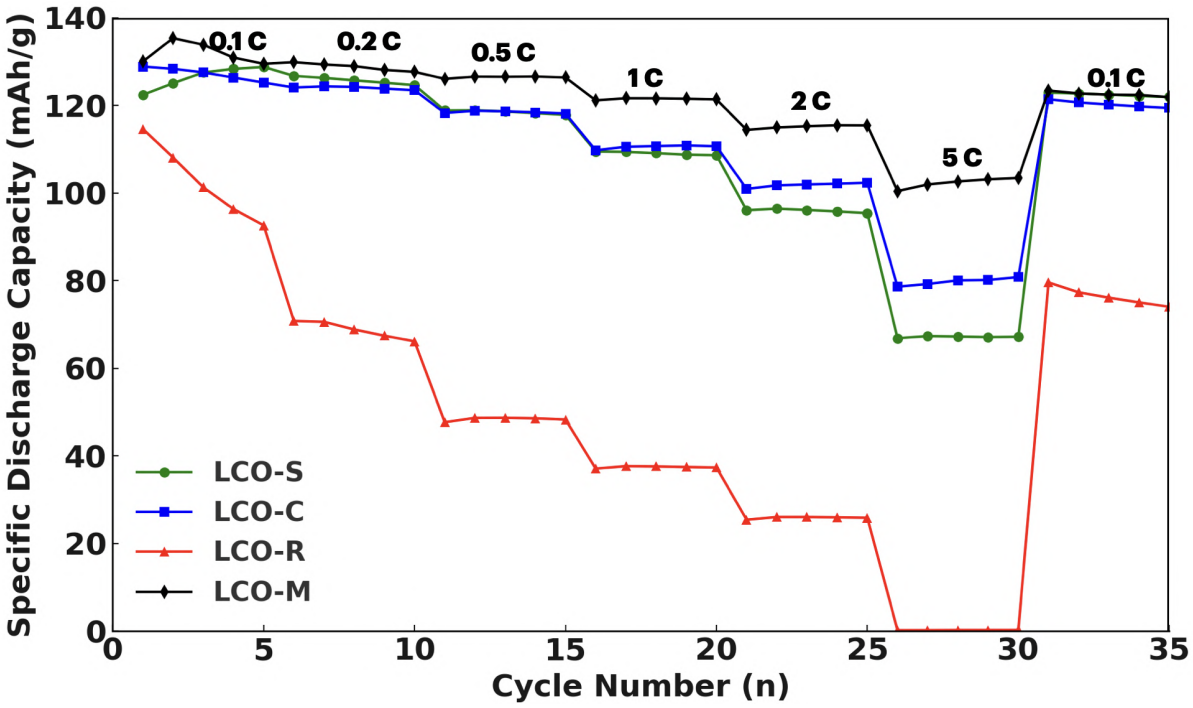

Figure 5.8: Rate capability curves at C-rates from 0.1 to 5 C.

5.3.8 Voltage-capacity profiles at different C-rates for each LCO material

As shown in Figure 5.9a, LCO-C achieves a discharge capacity of around 125.24 mAh g^{-1} at a discharge rate of 0.1 C, close to the practical upper limit of $\sim$ 140 mAh g^{-1} for $LiCoO_2$, indicating high active-material utilization at this low rate. As the C-rate increases, capacity declines steadily: 123.49 mAh g^{-1} at 0.2 C, 118.18 mAh g^{-1} at 0.5 C, 110.70 mAh g^{-1} at 1 C, and 102.37 mAh g^{-1} at 2 C. By 5 C, capacity is reduced to 80.82 mAh g^{-1}, reflecting nearly a 35 % decrease from the capacity at 0.1 C. This trend reveals LCO-C's limitations in rate capability, as higher discharge rates restrict the time available for lithium ions to fully intercalate, thereby reducing overall capacity. The discharge curve exhibits a stable plateau near 3.9 V at 0.1–0.2C, which progressively shortens and becomes more sloped at 0.5–1C. At 2C and above, the plateau collapses into a steep drop and is essentially absent at 5C, consistent with strong polarization contributions that limit high-rate utilization. Figure 5.9b shows that LCO-M achieves a

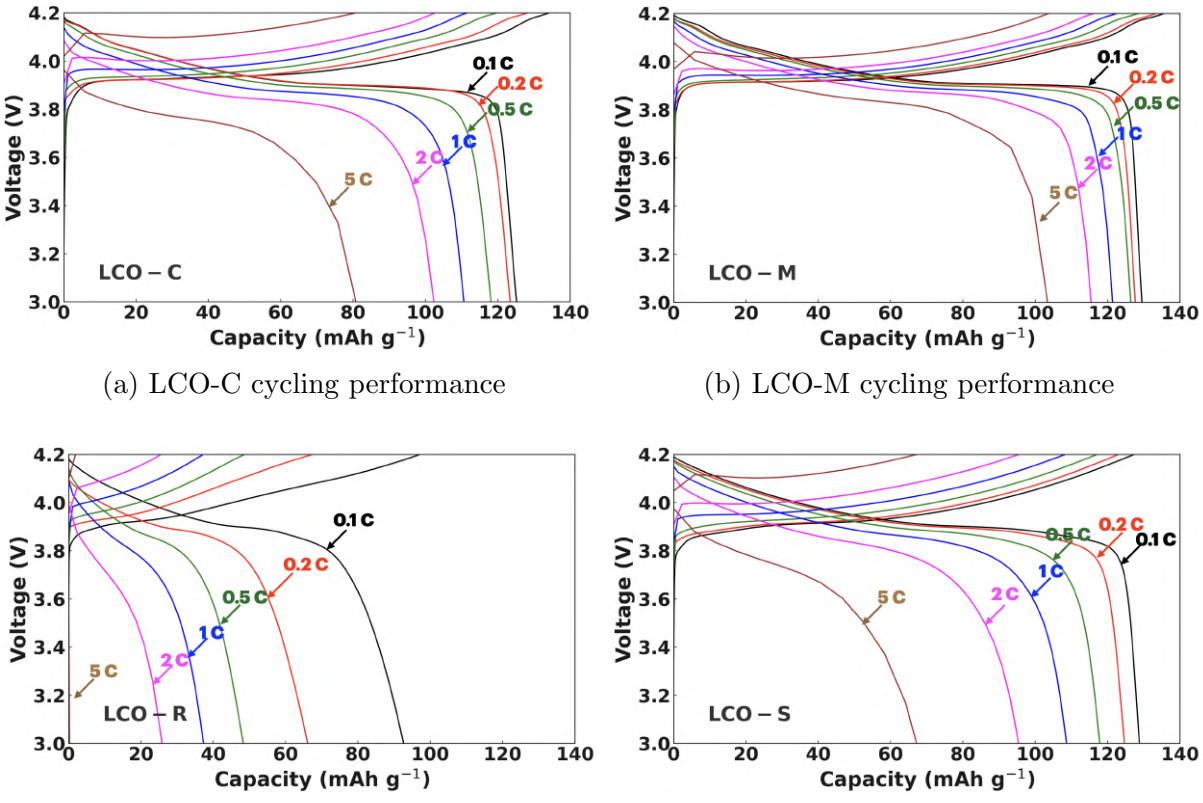

(a) LCO-C cycling performance

(b) LCO-M cycling performance

(c) LCO-R cycling performance

(d) LCO-S cycling performance

Figure 5.9: Voltage-capacity profiles for LCO-C, LCO-M, LCO-R, and LCO-S at various C-rates (0.1C to 5C). The curves correspond to the final cycle of each C-rate (cycles 5, 10, 15, 20, 25, and 30).

discharge capacity of 129.54 mAh g^{-1} at 0.1C, i.e., near the practical upper-capacity limit for $LiCoO_2$ ($\sim$ 140 mAh g^{-1}). This indicates a high degree of active-material utilization at this low current rate. As the C-rate increases, a gradual reduction in specific capacity is observed, with values decreasing to 127.70 mAh g^{-1} at 0.2 C, 126.41 mAh g^{-1} at 0.5 C, 121.41 mAh g^{-1} at 1 C, and 115.47 mAh g^{-1} at 2 C. At a C-rate of 5 C, the specific capacity drops further to 103.46 mAh g^{-1}, representing an approximately 20 % decline compared

to its capacity at 0.1 C. Compared with LCO-C, the 3.9 V plateau remains more extended up to 0.5–1C, indicating improved voltage stability at intermediate rates. This behavior is qualitatively consistent with the finer and more uniform particle morphology observed by SEM (Figure 5.1), which is expected to facilitate transport and reduce polarization under the present electrode fabrication conditions. Figure 5.9c shows that LCO-R exhibits the strongest rate-induced distortion in the voltage–capacity profiles. With increasing C-rate, the characteristic plateau region becomes rapidly compressed and the discharge curves develop a steep, continuously sloped shape, indicating pronounced polarization. At 1C–2C, the discharge voltage drops quickly toward the lower cut-off, limiting the accessible capacity, and at 5C the curve reaches the cut-off almost immediately, yielding negligible discharge capacity. This behavior is consistent with severe transport and/or interfacial limitations in the first recycled batch and may be exacerbated by electrode-level connectivity effects (e.g., high porosity) and/or residual surface species associated with lithium compensation (e.g., Li_2CO_3), although such surface phases were not directly quantified in this work. Figure 5.9d illustrates the electrochemical performance of LCO-S. Relative to LCO-R in Figure 5.9c, LCO-S shows improved capacity retention and more stable voltage behavior, consistent with the refined regeneration conditions designed to better control residual Li_2CO_3. At 0.1 C, LCO-S delivers approximately 128.82 mAh g^{-1}, and exhibits a clear plateau near 3.9 V with limited polarization, similar in shape to the commercial reference at low rates. With increasing C-rate, the plateau progressively shortens and the profiles become more sloped, indicating increasing polarization effects: LCO-S retains 117.86 mAh g^{-1} at 0.5C and 108.66 mAh g^{-1} at 1C, before decreasing to 95.42 mAh g^{-1} at 2C and 67.20 mAh g^{-1} at 5C. Despite the expected high-rate losses, the voltage profiles remain clearly less degraded than those of LCO-R at the same rates, highlighting the improvement achieved in the second recycled batch.

5.3.9 Comparison of coulombic efficiency of LCO materials

Coulombic efficiency (CE) is defined as the ratio of discharge capacity to charge capacity for each cycle:

$$\mathrm{CE}(\%) = \frac{Q_{\mathrm{discharge}}}{Q_{\mathrm{charge}}} \times 100. \tag{5.19}$$

Here, $Q_{\mathrm{discharge}}$ and Q_{charge} denote the discharge and charge capacities measured in the same cycle, respectively. In an ideal cell without side reactions, CE approaches 100%. In practical cells, parasitic reactions at electrode/electrolyte interfaces lead to deviations from 100%. In addition, because the present measurements were performed in Li-metal half-cells, the Li-metal counter electrode acts as an excess lithium reservoir; therefore, CE does not directly quantify full-cell cyclable-lithium inventory loss and is strongly influenced by interfacial parasitic processes at the Li-metal surface, particularly during the early cycles [373]. Coulombic efficiency (CE) is used in this section as an indicator of cycle-to-cycle reversibility during the rate-capability protocol, rather than as a long-term capacity-retention metric. Figure 5.10 provides the full-scale CE evolution for LCO-C, LCO-M, LCO-R, and LCO-S over the entire stepped-rate (rate capability) protocol (cycles 1–5: 0.1C; cycles 6–10: 0.2C; cycles 11–15: 0.5C; cycles 16–20: 1C; cycles 21–25: 2C; cycles 26–30: 5C). All cells show CE values below 100% in the first cycle, which is commonly attributed to initial interfacial side reactions (formation processes) in Li-metal half-cells. After this initial conditioning, LCO-C, LCO-M, and LCO-S stabilize and remain close to 100% with only minor fluctuations throughout the subsequent cycles. In

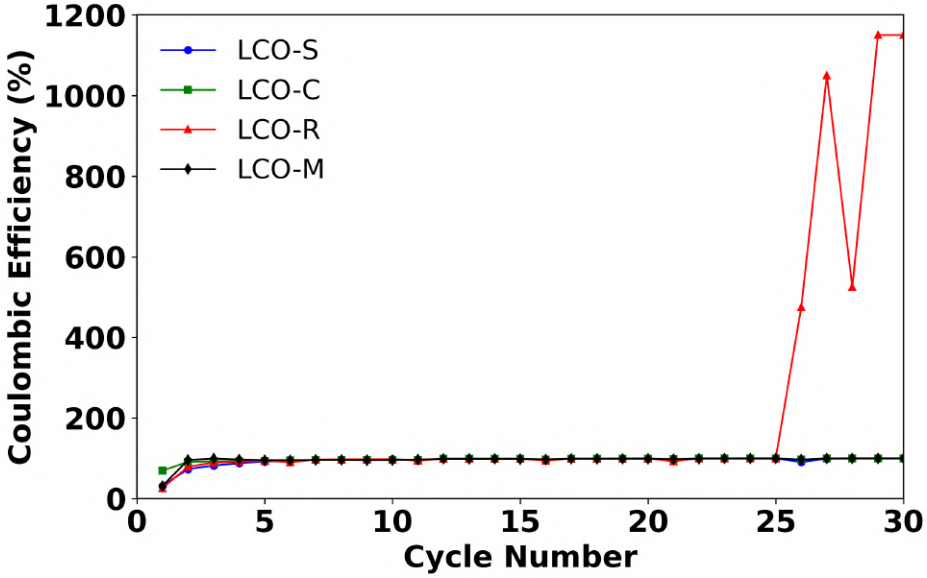

Figure 5.10: Comparison of coulombic efficiency for four different cells.

contrast, LCO-R shows irregular behavior during the final high-rate segment (5C), where the CE displays anomalously large spikes exceeding 1000% (cycles ∼26–30). These spikes should be interpreted in the context of the severe polarization observed for LCO-R at high rates. Under very high current, the cell can reach the voltage cut-off rapidly and the measured Q_{charge} becomes exceptionally small; consequently, if $Q_{\text{discharge}}$ remains finite, the ratio $Q_{\text{discharge}}/Q_{\text{charge}}$ can increase disproportionately. This interpretation is consistent with the LCO-R voltage–capacity response at 5C, where the discharge curve reaches the cut-off almost immediately and the accessible capacity collapses. Such severe polarization may also be influenced by surface residues (e.g., Li_2CO_3) that can form during synthesis, which could increase interfacial resistance and accelerate reaching the voltage cut-off under high current. Because the full-scale plot is dominated by the large CE spikes of LCO-R, Figure 5.11 replots the same CE data using a limited y-axis window (50–105%) to enable a clearer comparison of the stabilization behavior and the high-efficiency regime. In this zoomed view, LCO-C and LCO-M show nearly identical performance, maintaining CE values close to the 99–100% band across the stepped-rate sequence, including at higher C-rates. LCO-S exhibits a gradual improvement after the early cycles and approaches the same 99–100% range, remaining largely comparable to the commercial benchmark. By comparison, LCO-R displays larger cycle-to-cycle scatter and intermittent deviations in CE, consistent with less stable interfacial/transport behavior under the stepped-rate protocol. Overall, the CE trends corroborate the rate-performance observations: LCO-C, LCO-M, and LCO-S exhibit stable and highly reversible cycling across the stepped-rate sequence, whereas LCO-R demonstrates unstable behavior under high-rate operation. This interpretation is consistent with the LCO-R voltage–capacity response at 5C, where the accessible discharge capacity collapses in Figure 5.9c.

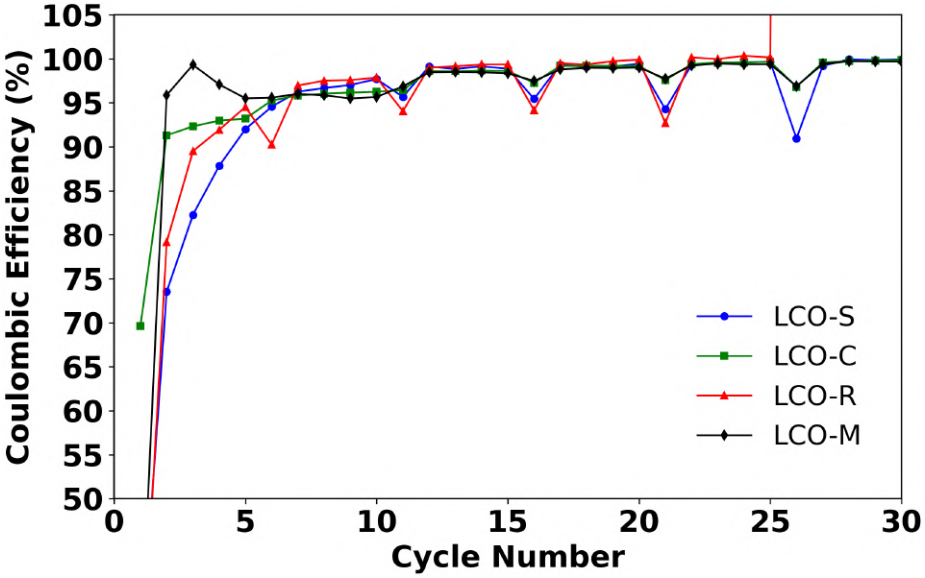

Figure 5.11: Detailed comparison of coulombic efficiency for four different samples (zoomed in)

5.4 Conclusion

This chapter presented a comparative electrochemical evaluation of commercial and hybrid thermochemically regenerated $LiCoO_2$ cathodes, including the commercial benchmark LCO-C and the regenerated samples LCO-M, LCO-R, and LCO-S, under identical electrode-preparation and Li-metal half-cell testing conditions. By comparing charge–discharge profiles, rate capability, and coulombic-efficiency trends, the relative electrochemical performance of regenerated and commercial materials was assessed. Among the regenerated samples, LCO-M showed the strongest overall response and outperformed LCO-C particularly at intermediate-to-high C-rates, consistent with its finer sub-micron particle morphology reducing solid-state diffusion length scales relative to the larger commercial grains. LCO-S achieved performance close to that of the commercial reference at low and moderate C-rates, with only a modest shortfall at the highest rates. In contrast, LCO-R exhibited the weakest rate capability and unstable behavior under high-rate operation, consistent with severe polarization and cut-off-limited cycling. Overall, these results indicate that hybrid thermochemical regeneration can yield $LiCoO_2$ cathode materials approaching the performance of commercial references, provided that regeneration and post-processing conditions are sufficiently well controlled.

The observed differences among the regenerated samples are consistent with variations in microstructure and processing history. In particular, the strong performance of LCO-M is consistent with its fine/sub-micron particle morphology and rough surface texture observed by SEM, which may reduce solid-state diffusion length scales and improve electrolyte accessibility. In contrast, the inferior behavior of LCO-R is plausibly associated with a combination of irregular fine-particle morphology, high electrode-level porosity, imperfect particle connectivity, and possible transport-limiting surface species, including residual or inhomogeneously distributed Li_2CO_3. Since these surface species were not directly quantified in this work, this interpretation should be regarded as tentative rather than confirmed. At the same time, the conclusions of the present experimental campaign

should be interpreted within the limits of the adopted methodology. Owing to the limited experimental time window available during the research period at the University of Notre Dame, the study was conceived as a short-term comparative benchmark rather than as a full long-term durability assessment. Extended cycling experiments and advanced diagnostics such as EIS, GITT, or systematic structural confirmation by complementary techniques were not carried out within the scope of this work. Therefore, the mechanistic interpretation of the present results remains limited to trends that are consistent with the observed electrochemical behavior and microstructural evidence.

Within these limits, the electrochemical benchmarking framework established in this thesis also provided the basis for the electrochemical section of Yeghisyan *et al.* [28], where subsequent process refinements were pursued to obtain more consistent and higher-performing regenerated materials. From a broader perspective, the present results support the continued development of sustainable regeneration routes for LCO cathodes and provide a comparative foundation for future optimization of synthesis, electrode fabrication, porosity control, and long-term electrochemical validation.

Chapter 6

Conclusions and outlook

In this final chapter, the main outcomes of the thesis are synthesized and placed in the broader context of the literature on lithium-ion batteries, electro-chemo-mechanical modeling, and cathode recycling. Lithium-ion batteries (LIBs) have become the dominant technology for portable electronics, electric vehicles and grid-scale storage because of their high energy density and long cycle life [142, 307, 374]. At the same time, advanced continuum and electro-chemo-mechanical models have been developed to better understand performance and degradation of lithium-ion cells, with the aim of improving lifetime and safety [375, 376]. In parallel, their rapid deployment raises concerns about resource availability, environmental impacts, and end-of-life management, spurring intensive research into physics-based continuum models for degradation prediction and lifetime extension, as well as effective recycling and circular-economy strategies [377, 378, 379].

Against this background, the work presented in this thesis addresses these issues in two main parts. On the modeling side, the thermodynamically consistent continuum multiphysics framework proposed by Magri et al. [278] is adopted and implemented within a high-performance computing environment using the open-source finite element library deal.ii. This implementation extends previous work by enabling fully three-dimensional simulations of a realistic lithium-ion cell geometry, resolving the coupled electro-chemo-mechanical response within a Li/LCO half-cell. On the experimental side, a comparative study of commercial and hybrid thermochemically regenerated $LiCoO_2$ (LCO) cathodes is carried out, in order to assess the performance of regenerated materials obtained from different feedstocks and processing routes, and to evaluate the potential of direct regeneration as a route towards more sustainable battery materials.

6.1 Summary of main contributions

This thesis brings together two related lines of work on $LiCoO_2$-based lithium-ion half-cells. The first part develops a thermodynamically consistent continuum model to study the coupled electro-chemo-mechanical behavior of the cell during operation. The second part presents an experimental comparison between regenerated and commercial $LiCoO_2$ cathodes under controlled half-cell conditions. These two parts are not combined into a fully calibrated model–experiment framework. However, they are connected by a common objective: to improve the understanding and evaluation of LCO-based cathodes from both a modeling and an experimental point of view. In this way, the thesis contributes both to the study of coupled battery behavior and to the assessment of cathode regeneration as a possible route for cathode recovery.

The main scientific contributions of the thesis can be summarized as follows. First, a three-dimensional, multi-domain, thermodynamically consistent electro-chemo-mechanical continuum model for an LCO-based lithium-ion half-cell has been formulated and implemented in a finite-element framework based on deal.II. Second, the numerical results clarify how mechanical coupling modifies lithium redistribution, overpotential fields, and stress localization under different C-rates, thereby providing mechanistic insight into rate-dependent battery response. Third, a controlled comparative electrochemical study has shown that selected regenerated $LiCoO_2$ powders can approach the short-term performance of commercial references, while also identifying the limiting roles of microstructural heterogeneity and impurity-related effects in less successful regenerated samples. Finally, by placing these modeling and experimental contributions within a common $LiCoO_2$-centered framework, the thesis establishes a basis for future model-guided evaluation and optimization of regenerated cathode materials.

6.1.1 Continuum electro-chemo-mechanical modeling

Chapters 3 and 4 of this thesis addressed the problem of modeling the coupled electro-chemo-mechanical behavior of lithium-ion batteries from a continuum perspective. In Chapter 3, the focus was restricted to all-solid-state lithium-ion batteries (ASSLIBs), and a targeted critical review was conducted in the spirit of the recent comparative study by Yildiz et al. [226], to highlight the modeling choices most relevant to the present work. Particular attention was given to one-dimensional single-ion-conduction models for thin-film ASSLIBs [245], advanced frameworks for solid electrolyte intercalation batteries [246], and all-solid-state cell models featuring two-mechanism ionic transport and multiscale-compatible formulations [247, 248]. Taken together, these contributions illustrate how charge transport and interfacial kinetics in ASSLIBs can be cast into thermodynamically consistent continuum formulations and provide the mathematical tools that underpin the multi-physics modeling strategy adopted later in this thesis. Building on this foundation, Chapter 4 implemented a thermodynamically consistent continuum model [249, 278] rooted in the Larché–Cahn framework [261], posed as an initial- and boundary-value problem over a realistic three-dimensional cell geometry. The model simultaneously accounts for

- lithium mass transport in the electrolyte and cathode,
- electric potential in the electrolyte, cathode, and metallic foils,
- small-strain elastic deformation in all solid constituents, including volumetric shrinkage due to intercalation.

The governing equations were derived systematically from balance laws and thermodynamic restrictions, and then recast in weak form for each domain (electrolyte, cathode, foils, and interfaces). The resulting coupled system was discretized in space via finite elements and in time via an implicit scheme, and solved through a Newton–Raphson procedure implemented in a high-performance computing environment using deal.ii.

The numerical study in Chapter 4 demonstrated that the model:

- Exhibits the expected electrochemical trends, namely a lower terminal voltage and a reduced accessible capacity as the C-rates increase,

- Predicts highly non-uniform lithium concentration and stress fields within the cathode microstructure, with near-surface lithium accumulation and strong stress localization at particle–particle contacts and in regions close to the cathode–electrolyte interface. The growth of the global maximum stress is steeper at higher C-rates and, for a given lithiation state, the maximum von Mises stress follows the ordering 2C > 1C > 0.5C, even though the deeply lithiated 0.5C case attains the largest stresses near the end of discharge,
- Indicates that chemo-mechanical coupling, incorporated via the stress-dependent Larché–Cahn chemical potential and the surface OCP modifies the overpotential and stress fields and, leads to a measurable increase in dischargeable capacity and a change in the voltage profile compared with a purely electrochemical model, especially at 2C.

Rather than proposing an entirely new theoretical framework, the present modeling work therefore contributes a fully coupled, multi-domain finite element implementation of this thermodynamically consistent electro-chemo-mechanical formulation for a realistic three-dimensional Li/LCO half-cell. In this sense, it sits between classical one-dimensional cell-level descriptions and purely cathode-microstructure-focused simulations by resolving both the porous $LiCoO_2$ microstructure and the entire Li/LCO half-cell configuration (lithium metal anode, separator-embedded electrolyte and metallic current collectors) within a single consistent framework.

6.1.2 Comparative electrochemical study of commercial and regenerated $LiCoO_2$ cathodes

Chapter 5 presented an experimental study carried out at the University of Notre Dame, where commercial LCO powders (LCO-C), regenerated-from-commercial powders (LCO-M), and recycled powders from spent lithium-ion batteries (LCO-R, LCO-S) were compared under identical electrode fabrication and coin-cell testing conditions.

The hybrid thermochemical regeneration method developed in the Nuclear Science Laboratory of the University of Notre Dame was first applied to a commercial LCO feedstock to produce the regenerated batch LCO-M. Under the present fabrication protocol, the electrochemical performance of LCO-M was found to be broadly consistent with that of the commercial reference LCO-C across C-rates from 0.1C to 5C, confirming that the route can deliver high-quality $LiCoO_2$ when starting from a clean feedstock.

The next step extended the method to precursors recovered from spent battery packs. The first recycled batch, LCO-R, was synthesized from spent-cell leachate using the same hybrid thermochemical route, with Li_2CO_3 addition to compensate lithium losses and target a Li:Co ratio near 1:1. Nevertheless, LCO-R exhibited

- lower initial discharge capacities than LCO-C and LCO-M,
- pronounced capacity decay with increasing C-rate,
- nearly negligible capacity at 5C, particularly for the higher-loading electrode.

Morphological inspection via SEM revealed that LCO-R displays a fine, texturally irregular particle morphology superficially comparable to LCO-M, with no obvious large agglomerates apparent from the images. Nonetheless, LCO-R presents the highest electrode-level porosity among the four materials, indicating less efficient packing under the present

fabrication conditions, which is expected to exacerbate polarization at elevated C-rates. Notably, the discrepancy between the relatively fine particle morphology and the markedly inferior electrochemical performance suggests that surface-chemical limitations are the primary performance-determining factor, with high electrode-level porosity providing a secondary contributing effect. In this regard, the synthesis route suggests that residual Li_2CO_3 at the particle surface may impede lithium-ion transport and increase interfacial resistance, in line with literature reports on carbonate surface layers on LCO cathodes [370, 371, 380], although such surface species were not directly quantified in this work.

A second recycled batch, LCO-S, regenerated from the same spent-cell feedstock but under refined Li:Co compensation and annealing conditions, showed a bimodal particle size distribution — with a fine sub-micron matrix alongside larger agglomerated clusters — representing a partial but incomplete recovery of morphological quality relative to LCO-R. Although the electrochemical data set was not as extensive as initially planned due to time constraints, the available results indicate that LCO-S narrows the performance gap with commercial material, particularly at moderate C-rates, supporting the notion that careful tuning of synthesis parameters and impurity control enables the regeneration of cathodes with competitive rate capability.

In summary, the experimental work demonstrates that:

- The hybrid thermochemical route developed at the Nuclear Science Laboratory of the University of Notre Dame can regenerate commercial $LiCoO_2$ (LCO-M) with electrochemical performance broadly comparable to that of the commercial reference LCO-C when a clean feedstock is used.

- Applying the same route directly to spent-cell-derived precursors (LCO-R) under insufficiently optimized regeneration conditions led to a fine but texturally irregular, highly porous electrode structure together with poor high-rate performance.

- The combination of elevated electrode porosity and surface-chemical inhomogeneity arising from the synthesis route given in [28], which involves Li_2CO_3 addition, provides a plausible mechanistic explanation for the inferior behavior of LCO-R in terms of interfacial resistance and rate sensitivity. Although XPS measurements were not available in this work to directly confirm the surface chemistry, this interpretation is consistent with literature reports on carbonate-containing surface layers on LCO cathodes [370, 371].

- Refinement of the Li:Co compensation and annealing conditions partially recovered the electrochemical response of LCO-S and may have reduced transport-limiting residual surface species relative to LCO-R, although this was not directly confirmed by surface-chemical analysis.

These laboratory-scale results also served as a precursor to the subsequent optimization and scale-up study of the same hybrid thermochemical route reported by Yeghishyan et al. [28]. In that work, regenerated $LiCoO_2$ materials with electrochemical performance even more closely comparable to commercial powders were obtained by refining the synthesis conditions on the basis of insights gained from the LCO-M, LCO-R and LCO-S batches tested in this thesis.

6.2 Limitations of the present work

While the thesis makes progress on both modeling and experimental fronts, several limitations must be acknowledged.

On the modeling side, the following simplifying assumptions were introduced:

- The analysis was restricted to isothermal conditions, hence thermal gradients and heat generation due to ohmic (Joule) losses and electrochemical processes (irreversible and reversible/entropic heat) were neglected. Consequently, temperature-dependent feedback on transport properties, reaction kinetics, thermodynamics (e.g., OCP), and mechanical response could not be captured.

- All solid constituents (LCO cathode, electrolyte-soaked separator, and metal foils) were modeled using small-strain linear elasticity. Swelling (chemical expansion) was considered only in the LCO cathode, where it was introduced as a concentration-dependent eigenstrain. Large-strain deformations, plastic deformation, and fracture were not included, although they can be relevant for high-capacity materials or under severe operating conditions.

- Interfacial degradation mechanisms such as solid–electrolyte interphase growth, loss of active surface area, delamination and crack propagation were not modeled explicitly. Interface conditions were enforced by Butler–Volmer-type relations with prescribed kinetic parameters and did not evolve with damage.

- The microstructure of the cathode was represented by idealized particle-resolved geometries, generated to reflect realistic volume fractions and particle size distributions but not reconstructed from tomography or imaging. This restricts the model's ability to capture microstructural features such as particle connectivity, binder distribution and tortuosity with full fidelity.

On the experimental side, the main limitations are linked to the finite duration of the research stay in the host laboratory:

- The electrochemical study lasted only about five months, which limited the scope of the test plan and the duration of cycling protocols. As a result, mainly short-term rate-capability tests were performed, along with only a limited number of cycling experiments. Long-term aging behavior was outside the scope of this work.

- Advanced electrochemical diagnostics such as cyclic voltammetry (CV), electrochemical impedance spectroscopy (EIS) or intermittent titration techniques were not systematically employed. This restricts the ability to deconvolute charge-transfer, transport and interfacial contributions to performance and to identify degradation modes in a quantitative way.

- A comprehensive model–experiment cross-validation and parameter identification campaign was beyond the scope of the available time. As a result, the continuum model was not calibrated directly against the coin-cell data generated in this work, and the two parts of the thesis remain methodologically independent.

These limitations do not undermine the main findings, they simply define the scope in which the results apply and point to the future work discussed in the next section.

6.3 Perspectives and future research directions

Building on the modeling and experimental contributions of this thesis, several avenues for future research can be identified.

6.3.1 Model development and extensions

Several directions appear promising for extending the modeling framework developed in this work:

- Incorporating thermo–electro–chemo–mechanical coupling by adding an energy balance equation would enable the simulation of temperature evolution and its feedback on reaction kinetics, transport coefficients, and mechanical response. This is essential for studying fast charging, high-power operation, and thermal-runaway precursors within a unified framework.
- Moving beyond small-strain elasticity by adopting finite-strain kinematics and introducing inelastic mechanisms (e.g., viscoelasticity, plasticity, and fracture) would enable the analysis of high-volume-change materials and large deformations in composite electrodes and polymeric separators. Such extensions would also provide a pathway to modeling crack initiation, particle pulverization, and interfacial delamination under repeated cycling.
- Achieving more realistic microstructural representation by replacing idealized, randomly generated particle packings with tomography-based geometries reconstructed from actual electrodes would allow a more accurate assessment of microstructural effects on performance and degradation. This would also facilitate direct comparison with experimentally characterized samples.
- Improving the interface description beyond the Butler–Volmer relations used in this work by accounting for concentration- and stress-dependent kinetics, evolving interfacial resistance (e.g., film growth), and loss of active area would help bridge the gap between continuum fields and observed degradation patterns. Coupling these effects with mechanical damage variables would further strengthen the link between electrochemical response and mechanically driven degradation.

6.3.2 Strengthening the link between modeling and experiments

A second major direction is the integration of the continuum model with targeted experiments:

- Designing electrochemical tests based on model sensitivity (e.g., short high-current pulses, controlled relaxation periods, or multistep rate sequences) can generate data that isolates the influence of specific transport and kinetic parameters, improving parameter identifiability during calibration.
- Calibrating key transport and kinetic parameters against coin-cell voltage–capacity data for both commercial and regenerated LCO cathodes would allow the model to make material and process specific quantitative predictions (e.g., rate capability and polarization trends) rather than only reproducing qualitative behavior.

- Combining simulations with complementary electrochemical diagnostics (e.g. EIS and operando methods) could help attribute deviations between regenerated and commercial materials to specific mechanisms such as ionic transport limitations, increased charge-transfer resistance, or altered mechanical constraints.

In this broader context, once systematically calibrated and benchmarked against targeted experiments, the continuum modeling framework developed in this thesis could serve as the basis for a digital-twin-type tool to virtually test regenerated cathodes under various designs and operating conditions before large-scale experimental campaigns are launched.

6.3.3 Implications for recycling and cathode regeneration

From an application standpoint, the experimental results indicate that hybrid thermochemical regeneration of LCO is a promising pathway for closing the materials loop in lithium-ion batteries.

Future work could explore:

- Extending the comparative framework to other cathode chemistries (NMC, NCA, high-voltage spinels) to evaluate how regeneration strategies and performance recovery depend on crystal chemistry and microstructure.
- Integrating regenerated materials into full-cell configurations and evaluating their performance under realistic duty cycles for consumer electronics or electric-vehicle applications.
- Establishing links between synthesis parameters, microstructural features (particle size distribution, porosity, crack density) and electrochemical performance, for example by combining advanced characterization (e.g. tomography) with continuum-scale modeling.
- Investigating the long-term durability of regenerated cathodes under severe operating conditions, including fast charging, elevated temperatures and extended cycling, with particular attention to impedance growth, mechanical degradation and loss of active material.

6.4 Final remarks

This thesis has combined advanced continuum modeling with targeted electrochemical experiments to gain insight into the behavior of $LiCoO_2$-based lithium-ion cells and the potential of regenerated cathode materials. The three-dimensional electro–chemo–mechanical model provides a practical basis for studying complex multi-physics interactions in realistic cell architectures, while the experimental benchmarking study indicates that under the present electrode fabrication and short-term testing conditions, regenerated LCO powders can approach the performance of commercial references.

Although the two parts were not fully coupled through calibration or validation, together they highlight complementary insights and motivate a future integrated workflow in which modeling and experiments can inform each other in the design of more sustainable, reliable and resource-efficient battery systems. The limitations identified in this

work point to promising directions for further research, ranging from thermo–electro–chemo–mechanically coupled simulations and microstructure-resolved modeling to long-term cycling studies and advanced diagnostics on regenerated materials.

In conclusion, the results presented here contribute to ongoing efforts to develop quantitative, physics-based models and circular-economy strategies for lithium-ion batteries. They also highlight that electrochemistry, transport, and mechanics must be considered together when interpreting cell behavior and evaluating regenerated cathodes.

Bibliography

[1] MM Hasan et al. "Advancing energy storage: The future trajectory of lithium-ion battery technologies". *J ENERGY STORAGE* 120, 2025, p. 116511.

[2] George G Njema, Russel Ben O Ouma, and Joshua K Kibet. "A review on the recent advances in battery development and energy storage technologies". *J. RENEW. ENERGY* 20241, 2024, p. 2329261.

[3] Tuhibur Rahman and Talal Alharbi. "Exploring lithium-Ion battery degradation: A concise review of critical factors, impacts, data-driven degradation estimation techniques, and sustainable directions for energy storage systems". *Batteries* 107, 2024, p. 220.

[4] Ridha Ali Ben Saleh, Nicola Faccilongo, and Roberto Leonardo Rana. "The role of renewable energy production on greenhouse gas emission reduction in international petroleum companies under energy transition policy". *DISCOV. SUSTAIN.* 61, 2025, p. 979.

[5] Kitalu Ricin Ngoy et al. "Lithium-ion batteries and the future of sustainable energy: A comprehensive review". *Renewable and Sustainable Energy Reviews* 223, 2025, p. 115971.

[6] Ganna Kostenko and Artur Zaporozhets. "Transition from electric vehicles to energy storage: review on targeted lithium-ion battery diagnostics". *Energies* 1720, 2024, p. 5132.

[7] Statista. *Lithium-Ion Battery Demand*. `https://www.statista.com/chart/23808/lithium-ion-battery-demand/`. 2023.

[8] Francesco Montana et al. "Assessing Critical Raw Materials and Their Supply Risk in Energy Technologies—A Literature Review". *Energies* 181, 2024, p. 86.

[9] Marm Dixit et al. "Insights into the critical materials supply chain of the battery market for enhanced energy security". *ACS Energy Letters* 98, 2024, pp. 3780–3789.

[10] Joshua P Pender et al. "Electrode degradation in lithium-ion batteries". *ACS nano* 142, 2020, pp. 1243–1295.

[11] Francesca Pistorio et al. "Review on the numerical modeling of fracture in active materials for lithium ion batteries". *Journal of Power Sources* 566, 2023, p. 232875.

[12] Francesca Pistorio et al. "Review on the experimental characterization of fracture in active material for lithium-ion batteries". *Energies* 1523, 2022, p. 9168.

[13] Hüsnü Dal and Christian Miehe. "Computational electro-chemo-mechanics of lithium-ion battery electrodes at finite strains". *Computational Mechanics* 552, 2015, pp. 303–325.

[14] Tobias Hofmann et al. “Electro-chemo-mechanical simulation for lithium ion batteries across the scales”. *International Journal of Solids and Structures* 184, 2020, pp. 24–39.

[15] Ting Hei Wan and Francesco Ciucci. “Electro-chemo-mechanical modeling of solid-state batteries”. *Electrochimica Acta* 331, 2020, p. 135355.

[16] M. Ganser et al. “A finite strain electro-chemo-mechanical theory for ion transport with application to binary solid electrolytes”. *J MECH PHYS SOLIDS* 125, 2019, pp. 681–713.

[17] Kasra Taghikhani et al. “Modeling coupled electro-chemo-mechanical phenomena within all-solid-state battery composite cathodes”. *Journal of the Mechanics and Physics of Solids* 198, 2025, p. 106060.

[18] Christoph P Schmidt et al. “A three-dimensional finite element formulation coupling electrochemistry and solid mechanics on resolved microstructures of all-solid-state lithium-ion batteries”. *Computer Methods in Applied Mechanics and Engineering* 417, 2023, p. 116468.

[19] Francesca Pistorio et al. “Coupled electrochemical–mechanical model for fracture analysis in active materials of lithium ion batteries”. *Journal of Power Sources* 580, 2023, p. 233378.

[20] Donald Bistri and Claudio V Di Leo. “A continuum electro-chemo-mechanical gradient theory coupled with damage: Application to Li-metal filament growth in all-solid-state batteries”. *Journal of the Mechanics and Physics of Solids* 174, 2023, p. 105252.

[21] Jaime Mora-Paz. “High-order transient multidimensional simulation of a thermo-electro-chemo-mechanical model for Lithium-ion batteries”. *Journal of Computational Physics* 519, 2024, p. 113392.

[22] Yunlei Zhong et al. “Understanding and unveiling the electro-chemo-mechanical behavior in solid-state batteries”. *SusMat* 42, 2024, e190.

[23] Daniel Arndt et al. “The `deal.II` Library, Version 9.5”. *J NUMER MATH* 313, 2023, pp. 231–246.

[24] Isabella Bianco, Eng Elisa Accorsi, and Saeideh Heydari. “Social-LCA and Sustainable Strategies of Critical Raw Material Supply Chains in the Battery Sector”, 2025.

[25] Lingyu Kong et al. “Sustainable regeneration of high-performance LiCoO2 from completely failed lithium-ion batteries”. *Journal of Colloid and Interface Science* 640, 2023, pp. 1080–1088.

[26] Jin Feng et al. “Recovery of LiCoO2 and graphite from spent lithium-ion batteries by molten-salt electrolysis”. *Iscience* 2611, 2023.

[27] Hehe Nie et al. “LiCoO 2: recycling from spent batteries and regeneration with solid state synthesis”. *Green chemistry* 172, 2015, pp. 1276–1280.

[28] Armenuhi Yeghishyan et al. “Scalable ultrafast regeneration of cathodes from battery waste”. *Chemical Engineering Journal*, 2025, p. 166888.

[29] Mattia Serpelloni et al. “4.14 - Mechanics of Batteries”. *Comprehensive Mechanics of Materials (First Edition)*. Ed. by Vadim Silberschmidt. First Edition. Oxford: Elsevier, 2024, pp. 335–354. ISBN: 978-0-323-90647-0.

[30] Miquel Martí-Florences, Andreu Cecilia, and Ramon Costa-Castelló. "Modelling and Estimation in Lithium-Ion Batteries: A Literature Review". *Energies* 1619, 2023, p. 6846.

[31] Muhammad-Sadeeq Balogun et al. "A review of carbon materials and their composites with alloy metals for sodium ion battery anodes". *Carbon* 98, 2016, pp. 162–178.

[32] Sen Xin, Yu-Guo Guo, and Li-Jun Wan. "Nanocarbon networks for advanced rechargeable lithium batteries". *Accounts of chemical research* 4510, 2012, pp. 1759–1769.

[33] Peichao Lian et al. "Large reversible capacity of high quality graphene sheets as an anode material for lithium-ion batteries". *Electrochimica Acta* 5512, 2010, pp. 3909–3914.

[34] Michel Armand et al. "Lithium-ion batteries–Current state of the art and anticipated developments". *Journal of Power Sources* 479, 2020, p. 228708.

[35] Hui Cheng et al. "Recent progress of advanced anode materials of lithium-ion batteries". *Journal of Energy Chemistry* 57, 2021, pp. 451–468.

[36] Tatsuki Hiraoka et al. "Synthesis of single-and double-walled carbon nanotube forests on conducting metal foils". *Journal of the American Chemical Society* 12841, 2006, pp. 13338–13339.

[37] H Zhang, GP Cao, and YS Yang. "Using a cut–paste method to prepare a carbon nanotube fur electrode". *Nanotechnology* 1819, 2007, p. 195607.

[38] Mingwen Zhao, Yueyuan Xia, and Liangmo Mei. "Diffusion and condensation of lithium atoms in single-walled carbon nanotubes". *Physical Review B—Condensed Matter and Materials Physics* 7116, 2005, p. 165413.

[39] Masato Senami et al. "Theoretical study of adsorption of lithium atom on carbon nanotube". *AIP Advances* 14, 2011.

[40] Ruopian Fang et al. "The regulating role of carbon nanotubes and graphene in lithium-ion and lithium–sulfur batteries". *Advanced Materials* 319, 2019, p. 1800863.

[41] Seung Woo Lee et al. "Layer-by-layer assembly of all carbon nanotube ultrathin films for electrochemical applications". *Journal of the American Chemical Society* 1312, 2009, pp. 671–679.

[42] Shiyan Xiao et al. "Enhancing the efficiency of lithium intercalation in carbon nanotube bundles using surface functional groups". *Physical Chemistry Chemical Physics* 1630, 2014, pp. 16003–16012.

[43] Sau Yen Chew et al. "Flexible free-standing carbon nanotube films for model lithium-ion batteries". *Carbon* 4713, 2009, pp. 2976–2983.

[44] Brian J Landi et al. "Lithium ion capacity of single wall carbon nanotube paper electrodes". *The Journal of Physical Chemistry C* 11219, 2008, pp. 7509–7515.

[45] Fang Zhao et al. "Directly grown carbon nanotube based hybrid electrodes with enhanced thermo-cell performances". *RSC advances* 738, 2017, pp. 23890–23895.

[46] Sicong Che et al. "Three-dimensional porous N-doped graphitic carbon framework with embedded CoO for ultrahigh and stable lithium storage". *Journal of Alloys and Compounds* 965, 2023, p. 171493.

[47] Guangzhe Li et al. “Advances in three-dimensional graphene-based materials: configurations, preparation and application in secondary metal (Li, Na, K, Mg, Al)-ion batteries”. *Energy & Environmental Science* 127, 2019, pp. 2030–2053.

[48] Ming-Hui Sun et al. “Applications of hierarchically structured porous materials from energy storage and conversion, catalysis, photocatalysis, adsorption, separation, and sensing to biomedicine”. *Chemical society reviews* 4512, 2016, pp. 3479–3563.

[49] Yan Lu, Le Yu, and Xiong Wen David Lou. “Nanostructured conversion-type anode materials for advanced lithium-ion batteries”. *Chem* 45, 2018, pp. 972–996.

[50] Yang Zhao et al. “Recent developments and understanding of novel mixed transition-metal oxides as anodes in lithium ion batteries”. *Advanced Energy Materials* 68, 2016, p. 1502175.

[51] Guangxun Zhang et al. “Transition metal oxides with one-dimensional/one-dimensional-analogue nanostructures for advanced supercapacitors”. *Journal of Materials Chemistry A* 518, 2017, pp. 8155–8186.

[52] Kangzhe Cao et al. “3D hierarchical porous α-Fe2O3 nanosheets for high-performance lithium-ion batteries”. *Advanced Energy Materials* 54, 2015, p. 1401421.

[53] Guo Gao et al. “CNTs in situ attached to α-Fe2O3 submicron spheres for enhancing lithium storage capacity”. *ACS Applied Materials & Interfaces* 71, 2015, pp. 340–350.

[54] Kangzhe Cao et al. “Ultra-high capacity lithium-ion batteries with hierarchical CoO nanowire clusters as binder free electrodes”. *Advanced Functional Materials* 257, 2015, pp. 1082–1089.

[55] Xianhong Rui et al. “Template-free synthesis of urchin-like Co3O4 hollow spheres with good lithium storage properties”. *Journal of power sources* 222, 2013, pp. 97–102.

[56] Yake Wu et al. “The coaxial MnO2/CNTs nanocomposite freestanding membrane on SSM substrate as anode materials in high performance lithium ion batteries”. *Journal of Electroanalytical Chemistry* 834, 2019, pp. 161–166.

[57] Shao-Zhuan Huang et al. “Three-dimensional (3D) bicontinuous hierarchically porous Mn2O3 single crystals for high performance lithium-ion batteries”. *Scientific Reports* 51, 2015, p. 14686.

[58] Buket Boz et al. “Evaluating Polyacrylic Acid as a Universal Aqueous Binder for Ni-Rich Cathodes NMC811 and Si Anodes in Full Cell Lithium-ion Batteries”. *ChemPlusChem*, 2024, e202400195.

[59] Glaydson Simoes dos Reis et al. “Biomass-derived carbon–silicon composites (C@ Si) as anodes for lithium-ion and sodium-ion batteries: A promising strategy towards long-term cycling stability: A mini review”. *Electrochemistry Communications*, 2023, p. 107536.

[60] Chenyuan Zhu et al. “Achieving high-performance silicon anodes of lithium-ion batteries via atomic and molecular layer deposited surface coatings: an overview”. *Electrochimica Acta* 251, 2017, pp. 710–728.

[61] Bo Liang, Yanping Liu, and Yunhua Xu. "Silicon-based materials as high capacity anodes for next generation lithium ion batteries". *Journal of Power sources* 267, 2014, pp. 469–490.

[62] Arūnas Meščeriakovas et al. "Influence of induction-annealing temperature on the morphology of barley-straw-derived Si@ C and SiC@ graphite for potential application in Li-ion batteries". *Nanotechnology* 3133, 2020, p. 335709.

[63] J. Christensen and J. Newman. "A Mathematical Model of Stress Generation and Fracture in Lithium Manganese Oxide". *J ELECTROCHEM SOC* 1536, 2006, A1019–A1030.

[64] J. Christensen and J. Newman. "Stress generation and fracture in Lithium insertion materials". *J SOLID STATE ELECTR* 10, 2006, pp. 293–319.

[65] Y.T. Cheng and M.W. Verbrugge. "Evolution of stress within a spherical insertion electrode particle under potentiostatic and galvanostatic operation". *J POWER SOURCES* 190, 2009, pp. 453–460.

[66] Y.T. Cheng and M.W. Verbrugge. "The influence of surface mechanics on diffusion induced stresses within spherical nanoparticles". *J APPL PHYS* 104, 2008, p. 083521.

[67] X. Zhang, A.M. Sastry, and W. Shyy. "Intercalation-Induced Stress and Heat Generation within Single Lithium-Ion Battery Chatode Particles". *J ELECTROCHEM SOC* 1557, 2008, A542–A552.

[68] R. Deshpande, Y.T. Cheng, and M.W. Verbrugge. "Modeling diffusion-induced stress in nanowire electrode structures". *J POWER SOURCES* 195, 2010, pp. 5081–5088.

[69] T.K. Bhandakkar and H. Gao. "Cohesive modeling of crack nucleation in a cylindrical electrode under axisymmetric diffusion induced stresses". *INT J SOLIDS STRUCT* 48, 2011, pp. 2304–2309.

[70] H. Woodford, Y.M. Chiang, and W.C. Carter. "Electrochemical Shock of Intercalation Electrodes: A Fracture Mechanics Analysis". *J ELECTROCHEM SOC* 15710, 2010, A1052–A1059.

[71] Mark J Armstrong et al. "Evaluating the performance of nanostructured materials as lithium-ion battery electrodes". *Nano Research* 7, 2014, pp. 1–62.

[72] Liangbiao Wang et al. "Chemical synthesis of germanium nanoparticles with uniform size as anode materials for lithium ion batteries". *Dalton Transactions* 457, 2016, pp. 2814–2817.

[73] Hyungki Kim et al. "Catalyst-free direct growth of a single to a few layers of graphene on a germanium nanowire for the anode material of a lithium battery". *Angewandte Chemie International Edition* 5223, 2013, pp. 5997–6001.

[74] Kyu T Lee, Yoon S Jung, and Seung M Oh. "Synthesis of tin-encapsulated spherical hollow carbon for anode material in lithium secondary batteries". *Journal of the American Chemical Society* 12519, 2003, pp. 5652–5653.

[75] Martin Winter and Jürgen O Besenhard. "Electrochemical lithiation of tin and tin-based intermetallics and composites". *Electrochimica Acta* 451-2, 1999, pp. 31–50.

[76] L. Y. Beaulieu et al. "Colossal Reversible Volume Changes in Lithium Alloys". *ELECTROCHEM SOLID ST* 49, 2001, A137–A140. DOI: 10.1149/1.1388178.

[77] Yang Zhao et al. "Significant impact of 2D graphene nanosheets on large volume change tin-based anodes in lithium-ion batteries: a review". *Journal of Power Sources* 274, 2015, pp. 869–884.

[78] Lei Wen, Feng Li, and Hui-Ming Cheng. "Carbon nanotubes and graphene for flexible electrochemical energy storage: from materials to devices". *Advanced Materials* 2822, 2016, pp. 4306–4337.

[79] Hoang X Dang et al. "Tin microparticles for a lithium ion battery anode with enhanced cycling stability and efficiency derived from Se-doping". *Journal of Materials Chemistry A* 325, 2015, pp. 13500–13506.

[80] Jian Qin et al. "One-step synthesis of SnCo nanoconfined in hierarchical carbon nanostructures for lithium ion battery anode". *Nanoscale* 941, 2017, pp. 15856–15864.

[81] Leigang Xue et al. "Three-dimensional porous Sn–Cu alloy anode for lithium-ion batteries". *Electrochimica Acta* 5524, 2010, pp. 7310–7314.

[82] Jun Yang et al. "Sub-Microcrystalline Sn and Sn-SnSb powders as lithium storage materials for Lithium-ion batteries". *Electrochemical and Solid-State Letters* 24, 1999, p. 161.

[83] Sukeun Yoon et al. "An Sn–Fe/carbon nanocomposite as an alternative anode material for rechargeable lithium batteries". *Electrochimica acta* 5410, 2009, pp. 2699–2705.

[84] Meng-Yuan Li et al. "Nanostructure Sn–Co–C composite lithium ion battery electrode with unique stability and high electrochemical performance". *Electrochimica acta* 568, 2011, pp. 3023–3028.

[85] N Tamura et al. "Mechanical stability of Sn–Co alloy anodes for lithium secondary batteries". *Electrochimica Acta* 4912, 2004, pp. 1949–1956.

[86] ADW Todd, RA Dunlap, and JR Dahn. "Mössbauer effect studies of sputter-deposited tin–cobalt and tin–cobalt–carbon alloys". *Journal of alloys and compounds* 4431-2, 2007, pp. 114–120.

[87] D Larcher et al. "In situ X-ray study of the electrochemical reaction of Li with η-Cu6Sn5". *Journal of the Electrochemical Society* 1475, 2000, p. 1658.

[88] Lynn Trahey et al. "High-capacity, microporous Cu6Sn5–Sn anodes for Li-ion batteries". *Journal of The Electrochemical Society* 1565, 2009, A385.

[89] Wei-Jun Zhang. "A review of the electrochemical performance of alloy anodes for lithium-ion batteries". *Journal of Power Sources* 1961, 2011, pp. 13–24.

[90] T. Richard Jow et al. *Electrolytes for Lithium and Lithium-Ion Batteries*. Springer, 2014.

[91] E. Quartarone and P. Mustarelli. "Review-Emerging Trends in the Design of Electrolytes for Lithium and Post-Lithium Batteries." *J ELECTROCHEM SOC* 1675, 2020, p. 50508.

[92] Z. Zhang et al. "Review on composite solid electrolytes for solid-state lithium-ion batteries". *MATER TODAY SUS* 21, 2023, p. 100316.

[93] D. Zhou et al. “Polymer Electrolytes for Lithium-Based Batteries: Advances and Prospects”. *CHEM* 59, 2019, pp. 2326–2352.

[94] H. Wang et al. “Liquid electrolyte: The nexus of practical lithium metal batteries”. *JOULE* 63, 2022, pp. 588–616.

[95] Qi Li et al. “Progress in electrolytes for rechargeable Li-based batteries and beyond”. *GREEN ENERGY ENV* 11, 2016, pp. 18–42.

[96] R. Younesi et al. “Lithium salts for advanced lithium batteries: Li–metal, Li–O_2, and Li–S”. *ENERGY ENVIRON SCI* 8, 2015, pp. 1905–1922.

[97] Y. Qian et al. “How electrolyte additives work in Li-ion batteries”. *ENERGY STORAGE MATERIALS* 20, 2019, pp. 208–215. ISSN: 2405-8297.

[98] A. Yao. *The Li(ttle) ion that could*. `https://honestenergy.substack.com/p/the-little-ion-that-could`. 2023.

[99] F. Cheng et al. “Electrolyte Salts for Sodium-Ion Batteries: $NaPF_6$ or $NaClO_4$?” *ACS NANO* 1718, 2023, pp. 18608–18615.

[100] X. Chen et al. “Ion–solvent chemistry in lithium battery electrolytes: From mono-solvent to multi-solvent complexes”. *FUNDAMENTAL RESEARCH* 14, 2021, pp. 393–398. ISSN: 2667-3258.

[101] G. Sikha, B. N. Popov, and R. E. White. “Effect of Porosity on the Capacity Fade of a Lithium-Ion Battery: Theory”. *J ELECTROCHEM SOC* 1517, 2004, A1104.

[102] B. Ghanbarian et al. “Tortuosity in Porous Media: A Critical Review”. *SOIL SCI SOC AM J* 775, 2013, pp. 1461–1477.

[103] M. Pasta et al. “2020 roadmap on solid-state batteries”. *J PHYS ENERGY* 23, 2020, p. 032008.

[104] Y. Chen et al. “A review of lithium-ion battery safety concerns: The issues, strategies, and testing standards”. *J ENERGY CHEM* 59, 2021, pp. 83–99. ISSN: 2095-4956.

[105] N. Boaretto et al. “Lithium solid-state batteries: State-of-the-art and challenges for materials, interfaces and processing”. *J POWER SOURCES* 502, 2021, p. 229919. ISSN: 0378-7753.

[106] R. Chen et al. “The Thermal Stability of Lithium Solid Electrolytes with Metallic Lithium”. *JOULE* 44, 2020, pp. 812–821. ISSN: 2542-4351.

[107] A. M. Bates et al. “Are solid-state batteries safer than lithium-ion batteries?” *JOULE* 64, 2022, pp. 742–755. ISSN: 2542-4351.

[108] L.P. Hou et al. “Improved interfacial electronic contacts powering high sulfur utilization in all-solid-state lithium–sulfur batteries”. *ENERGY STORAGE MATERIALS* 25, 2020, pp. 436–442. ISSN: 2405-8297.

[109] Y. Zhou et al. “Quasi-solid-state polymer plastic crystal electrolyte for subzero lithium-ion batteries”. *J ENERGY CHEM* 46, 2020, pp. 87–93. ISSN: 2095-4956.

[110] J. Tippens et al. “Visualizing Chemomechanical Degradation of a Solid-State Battery Electrolyte”. *ACS ENERGY LETT* 46, 2019, pp. 1475–1483.

[111] J. Gao, Q. Shao, and J. Chen. “Lithiated Nafion-garnet ceramic composite electrolyte membrane for solid-state lithium metal battery”. *J ENERGY CHEM* 46, 2020, pp. 237–247. ISSN: 2095-4956.

[112] M. Irfan et al. "Recent advances in high performance conducting solid polymer electrolytes for lithium-ion batteries". *J POWER SOURCES* 486, 2021, p. 229378. ISSN: 0378-7753.

[113] R. Xu et al. "The reduction of interfacial transfer barrier of Li ions enabled by inorganics-rich solid-electrolyte interphase". *ENERGY STORAGE MATERIALS* 28, 2020, pp. 401–406.

[114] Z. Hou et al. "Towards high-performance lithium metal anodes via the modification of solid electrolyte interphases". *J ENERGY CHEM* 45, 2020, pp. 7–17. ISSN: 2095-4956.

[115] T. Yu et al. "Progress and perspectives on typical inorganic solid-state electrolytes". *J ALLOY COMPD* 885, 2021, p. 161013. ISSN: 0925-8388.

[116] L. Cabras et al. "A two-mechanism and multiscale compatible approach for solid state electrolytes of (Li-ion) batteries". *Journal of Energy Storage* 48, 2022, p. 103842. ISSN: 2352-152X.

[117] Janis K. Eckhardt et al. "Influence of Microstructure on the Material Properties of LLZO Ceramics Derived by Impedance Spectroscopy and Brick Layer Model Analysis". *ACS Applied Materials & Interfaces* 1540, 2023, pp. 47260–47277. DOI: 10.1021/acsami.3c10060. URL: https://doi.org/10.1021/acsami.3c10060.

[118] S. B. Aziz et al. "A conceptual review on polymer electrolytes and ion transport models". *J SCI ADV MAT DEV* 31, 2018, pp. 1–17. ISSN: 2468-2179.

[119] L. C. De Jonghe. "Transport number gradients and solid electrolyte degradation". *J ELECTROCHEM SOC* 1294, 1982, p. 752.

[120] J. C. Bachman et al. "Inorganic solid-state electrolytes for lithium batteries: mechanisms and properties governing ion conduction". *CHEM REV* 1161, 2016, pp. 140–162.

[121] R. Kanno and M. Murayama. "Lithium ionic conductor thio-LISICON: the $Li_2SGeS_2P_2S_5$ system". *J ELECTROCHEM SOC* 1487, 2001, A742.

[122] Q. Liu et al. "Challenges and perspectives of garnet solid electrolytes for all solid-state lithium batteries". *J POWER SOURCES* 389, 2018, pp. 120–134.

[123] C. Chen S .and Wu et al. "Challenges and perspectives for NASICON-type electrode materials for advanced sodium-ion batteries". *ADV MAT* 2948, 2017, p. 1700431.

[124] X. Han et al. "Negating interfacial impedance in garnet-based solid-state Li metal batteries". *NAT MATER* 165, 2017, pp. 572–579.

[125] R. Murugan, V. Thangadurai, and W. Weppner. "Fast lithium ion conduction in garnet-type $Li_7La_3Zr_2O_{12}$". *ANGEW CHEM INT EDIT* 4641, 2007, pp. 7778–7781.

[126] Y. Seino et al. "A sulphide lithium super ion conductor is superior to liquid ion conductors for use in rechargeable batteries". *ENERGY ENVIRON SCI* 72, 2014, pp. 627–631.

[127] J. S. Thokchom, N. Gupta, and B. Kumar. "Superionic conductivity in a lithium aluminum germanium phosphate glass–ceramic". *J ELECTROCHEM SOC* 15512, 2008, A915.

[128] S. Zhang et al. “Designing all-solid-state batteries by theoretical computation: A review”. *ELECTROCHEM ENERGY REV* 61, 2023, p. 4.

[129] A. Sharafi et al. “Characterizing the Li–$Li_7La_3Zr_2O_{12}$ interface stability and kinetics as a function of temperature and current density”. *J POWER SOURCES* 302, 2016, pp. 135–139.

[130] E. J. Cheng, A. Sharafi, and J. Sakamoto. “Intergranular Li metal propagation through polycrystalline $Li_{6.25}Al_{0.25}La_3Zr_2O_{12}$ ceramic electrolyte”. *ELECTROCHIM ACTA* 223, 2017, pp. 85–91.

[131] F. Aguesse et al. “Investigating the dendritic growth during full cell cycling of garnet electrolyte in direct contact with Li metal”. *ACS APPL MATER INTER* 94, 2017, pp. 3808–3816.

[132] D. Bistri, A. Afshar, and C.V. Di Leo. “Modeling the chemo-mechanical behavior of all-solid-state batteries: a review.” *MECCANICA* 56, 2021, pp. 1523–1554.

[133] A. A. Kornyshev and M. A. Vorotyntsev. “Conductivity and space charge phenomena in solid electrolytes with one mobile charge carrier species, a review with original material”. *ELECTROCHIM ACTA* 263, 1981, pp. 303–323.

[134] L. Long et al. “Polymer electrolytes for lithium polymer batteries”. *J MAT CHEM A* 426, 2016, pp. 10038–10069.

[135] E. Quartarone and P. Mustarelli. “Electrolytes for solid-state lithium rechargeable batteries: recent advances and perspectives”. *CHEM SOC REV* 405, 2011, pp. 2525–2540.

[136] T. Vu et al. “Hybrid electrolytes for solid-state lithium batteries: Challenges, progress, and prospects”. *ENERGY STORAGE MATERIALS* 61, 2023, p. 102876.

[137] T. Dev, J.L. Schaefer, and A. Salvadori. “The impact of ionomeric active binder on Li-ion battery charge–discharge and rate capability, Part I: Electrolyte”. *J ENERGY STORAGE* 68, 2023, p. 107581.

[138] T. Dev, J.L. Schaefer, and A. Salvadori. “The impact of lithiated active binder on Li-ion battery charge–discharge and rate capability, Part II: Mesoscale modeling of LCO based Half-cell”. *J ENERGY STORAGE* 73, 2023, p. 108927.

[139] Jeevan Jyoti, Bhanu Pratap Singh, and Surya Kant Tripathi. “Recent advancements in development of different cathode materials for rechargeable lithium ion batteries”. *Journal of Energy Storage* 43, 2021, p. 103112.

[140] Xingyu Qu et al. “Enhanced electrochemical performance of Ni-rich cathode materials with Li1. 3Al0. 3Ti1. 7 (PO4) 3 coating”. *ACS Sustainable Chemistry & Engineering* 815, 2020, pp. 5819–5830.

[141] Xianhong Rui et al. “Li3V2 (PO4) 3 cathode materials for lithium-ion batteries: A review”. *Journal of Power Sources* 258, 2014, pp. 19–38.

[142] N. Nitta et al. “Li-ion battery materials: present and future”. *MATER TODAY* 185, 2015, pp. 252–264. ISSN: 1369-7021. DOI: http://dx.doi.org/10.1016/j.mattod.2014.10.040. URL: http://www.sciencedirect.com/science/article/pii/S1369702114004118.

[143] N Bensalah and H Dawood. “Review on synthesis, characterizations, and electrochemical properties of cathode materials for lithium ion batteries”, 2016.

[144] Ermete Antolini. "LiCoO2: formation, structure, lithium and oxygen nonstoichiometry, electrochemical behaviour and transport properties". *Solid state ionics* 1703-4, 2004, pp. 159–171.

[145] Zeyuan Li et al. "Multi-scale stabilization of high-voltage LiCoO2 enabled by nanoscale solid electrolyte coating". *Energy Storage Materials* 29, 2020, pp. 71–77.

[146] Gerbrand Ceder et al. "Identification of cathode materials for lithium batteries guided by first-principles calculations". *Nature* 3926677, 1998, pp. 694–696.

[147] R Alcantara et al. "X-ray diffraction, 57Fe Mössbauer and step potential electrochemical spectroscopy study of LiFeyCo1- yO2 compounds". *Journal of power sources* 81, 1999, pp. 547–553.

[148] Isaac D Scott et al. "Ultrathin coatings on nano-LiCoO2 for Li-ion vehicular applications". *Nano letters* 112, 2011, pp. 414–418.

[149] Lawrence D Dyer, Bernard S Borie Jr, and G Pedro Smith. "Alkali metal-nickel oxides of the type MNiO2". *Journal of the American Chemical Society* 766, 1954, pp. 1499–1503.

[150] Gaurav Assat and Jean-Marie Tarascon. "Fundamental understanding and practical challenges of anionic redox activity in Li-ion batteries". *Nature Energy* 35, 2018, pp. 373–386.

[151] S Venkatraman, Y Shin, and Arumugam Manthiram. "Phase relationships and structural and chemical stabilities of charged Li1- x CoO2- δ and Li1- x Ni0. 85Co0. 15 O 2- δ cathodes". *Electrochemical and solid-state letters* 61, 2002, A9.

[152] Doron Aurbach et al. "The study of surface phenomena related to electrochemical lithium intercalation into Li x MO y host materials (M= Ni, Mn)". *Journal of The Electrochemical Society* 1474, 2000, p. 1322.

[153] Tsutomu Ohzuku, Atsushi Ueda, and Masatoshi Nagayama. "Electrochemistry and structural chemistry of LiNiO2 (R3m) for 4 volt secondary lithium cells". *Journal of the Electrochemical Society* 1407, 1993, p. 1862.

[154] A Robert Armstrong and Peter G Bruce. "Synthesis of layered LiMnO2 as an electrode for rechargeable lithium batteries". *Nature* 3816582, 1996, pp. 499–500.

[155] Brett Ammundsen and Jens Paulsen. "Novel lithium-ion cathode materials based on layered manganese oxides". *Advanced Materials* 1312-13, 2001, pp. 943–956.

[156] G Ceder and SK Mishra. "The stability of orthorhombic and monoclinic-layered LiMnO2". *Electrochemical and solid-state letters* 211, 1999, p. 550.

[157] Myung-Hyoon Kim et al. "Synthesis and electrochemical properties of Li [Ni0. 8Co0. 1Mn0. 1] O2 and Li [Ni0. 8Co0. 2] O2 via co-precipitation". *Journal of Power Sources* 1592, 2006, pp. 1328–1333.

[158] Jing Li et al. "Study of the failure mechanisms of LiNi0. 8Mn0. 1Co0. 1O2 cathode material for lithium ion batteries". *Journal of The Electrochemical Society* 1627, 2015, A1401.

[159] Joo Hyeong Lee et al. "High-energy-density lithium-ion battery using a carbon-nanotube–Si composite anode and a compositionally graded Li [Ni 0.85 Co 0.05 Mn 0.10] O 2 cathode". *Energy & Environmental Science* 96, 2016, pp. 2152–2158.

[160] Irmgard Buchberger et al. “Aging analysis of graphite/LiNi1/3Mn1/3Co1/3O2 cells using XRD, PGAA, and AC impedance”. *Journal of The Electrochemical Society* 16214, 2015, A2737.

[161] J Kasnatscheew et al. “The truth about the 1st cycle Coulombic efficiency of LiNi 1/3 Co 1/3 Mn 1/3 O 2 (NCM) cathodes”. *Physical chemistry chemical physics* 185, 2016, pp. 3956–3965.

[162] Jing Li et al. “In-situ neutron diffraction study of a high voltage Li (Ni0. 42Mn0. 42Co0. 16) O2/graphite pouch cell”. *Electrochimica Acta* 180, 2015, pp. 234–240.

[163] Jian Xia et al. “Fluorinated electrolyte for 4.5 V Li (Ni0. 4Mn0. 4Co0. 2) O2/graphite Li-ion cells”. *Journal of Power Sources* 307, 2016, pp. 340–350.

[164] Do Kyung Kim et al. “Spinel LiMn2O4 nanorods as lithium ion battery cathodes”. *Nano letters* 811, 2008, pp. 3948–3952.

[165] Jeevan Jyoti et al. “Recent advancement in three dimensional graphene-carbon nanotubes hybrid materials for energy storage and conversion applications”. *Journal of Energy Storage* 50, 2022, p. 104235.

[166] J Marzec et al. “Conduction mechanism in operating a LiMn2O4 cathode”. *Solid State Ionics* 1463-4, 2002, pp. 225–237.

[167] D Guyomard and JM Tarascon. “The carbon/Li1+ xMn2O4 system”. *Solid State Ionics* 693-4, 1994, pp. 222–237.

[168] Ting-Feng Yi et al. “A literature review and test: Structure and physicochemical properties of spinel LiMn2O4 synthesized by different temperatures for lithium ion battery”. *Synthetic Metals* 15913, 2009, pp. 1255–1260.

[169] Navjot K Sidhu and AC Rastogi. “Bifacial carbon nanofoam-fibrous PEDOT composite supercapacitor in the 3-electrode configuration for electrical energy storage”. *Synthetic Metals* 219, 2016, pp. 1–10.

[170] LI Tao et al. “Effect of lithium content on the electrochemical properties of solid-state-synthesized spinel LixMn2O4”. *Rare metals* 263, 2007, pp. 280–285.

[171] Peifeng ZHANG et al. “Synthesis and electrochemical properties of sol-gel derived LiMn2O4 cathode for lithium-ion batteries”. *Rare Metals* 256, 2006, pp. 100–104.

[172] P Arora, BN Popov, and Ralph E White. “Electrochemical Investigations of Cobalt-Doped LiMn2 O 4 as Cathode Material for Lithium-Ion Batteries”. *Journal of the electrochemical society* 1453, 1998, p. 807.

[173] Sung-Wook Kim et al. “Electrochemical performance and ex situ analysis of ZnMn 2 O 4 nanowires as anode materials for lithium rechargeable batteries”. *Nano Research* 4, 2011, pp. 505–510.

[174] YI Tingfeng et al. “Powder electrochemical properties with different particle sizes of spinel LiAl0. 05Mn1. 95O4 synthesized by sol-gel method”. *Rare Metals* 264, 2007, pp. 330–334.

[175] FX Wang et al. “Spinel LiNixMn2- xO4 as cathode material for aqueous rechargeable lithium batteries”. *Electrochimica Acta* 93, 2013, pp. 301–306.

[176] Agnieszka Chojnacka et al. “An influence of carbon matrix origin on electrochemical behaviour of carbon-tin anode nanocomposites”. *Electrochimica Acta* 209, 2016, pp. 7–16.

[177] Haowen Liu, Cuixia Cheng, Keli Zhang, et al. "The effect of ZnO coating on LiMn2O4 cycle life in high temperature for lithium secondary batteries". *Materials chemistry and physics* 1012-3, 2007, pp. 276–279.

[178] Xiaohong Liu et al. "Sol–gel-template synthesis of ZnO nanotubes and its coaxial nanocomposites of LiMn2O4/ZnO". *Materials Science and Engineering: A* 4301-2, 2006, pp. 248–253.

[179] Yunhai Ding et al. "Direct growth of LiMn2O4 on carbon nanotubes as cathode materials for lithium ion batteries". *Materials Letters* 68, 2012, pp. 197–200.

[180] M Saiful Islam et al. "Atomic-scale investigation of defects, dopants, and lithium transport in the LiFePO4 olivine-type battery material". *Chemistry of Materials* 1720, 2005, pp. 5085–5092.

[181] Sukesh Kumar et al. "Effect of different aqueous electrolytes on electrochemical behavior of LiFePO4 as a cathode material: Lithium ion battery and renewable energy nexus". *Energy Nexus* 1, 2021, p. 100005.

[182] Seung-Ho Yu et al. "Understanding conversion-type electrodes for lithium rechargeable batteries". *Accounts of chemical research* 512, 2018, pp. 273–281.

[183] Feixiang Wu and Gleb Yushin. "Conversion cathodes for rechargeable lithium and lithium-ion batteries". *Energy & Environmental Science* 102, 2017, pp. 435–459.

[184] Jordi Cabana et al. "Beyond intercalation-based Li-ion batteries: the state of the art and challenges of electrode materials reacting through conversion reactions". *Advanced materials* 2235, 2010, E170–E192.

[185] Ruijie Wu et al. "Transition Metal Fluorides as Advanced Cathodes for Lithium/Sodium-Ion Batteries: Rational Enhancement Strategies and Underlying Electrochemical Mechanisms". *Advanced Functional Materials*, 2025, p. 2424603.

[186] Zibing Pan et al. *Fluorine chemistry in lithium-ion and sodium-ion batteries*. OAE Publishing Inc., 2023.

[187] Lidong Sun, Yu Li, and Wei Feng. "Metal fluoride cathode materials for lithium rechargeable batteries: focus on iron fluorides". *Small Methods* 72, 2023, p. 2201152.

[188] Linsen Li, Fei Meng, and Song Jin. "High-capacity lithium-ion battery conversion cathodes based on iron fluoride nanowires and insights into the conversion mechanism". *Nano letters* 1211, 2012, pp. 6030–6037.

[189] Lorenz F Olbrich, Albert W Xiao, and Mauro Pasta. "Conversion-type fluoride cathodes: Current state of the art". *Current Opinion in Electrochemistry* 30, 2021, p. 100779.

[190] Wentian Gu et al. "Metal fluorides nanoconfined in carbon nanopores as reversible high capacity cathodes for Li and Li-Ion rechargeable batteries: FeF2 as an example". *Advanced Energy Materials* 54, 2015, p. 1401148.

[191] Georg F Dewald et al. "Influence of Iron Sulfide Nanoparticle Sizes in Solid-State Batteries". *Angewandte Chemie* 13333, 2021, pp. 18096–18100.

[192] David S Ashby et al. "Understanding the electrochemical performance of FeS2 conversion cathodes". *ACS Applied Materials & Interfaces* 1423, 2022, pp. 26604–26611.

[193] Zhendong Li et al. “Unlocking cycling longevity in micro-sized conversion-type FeS2 cathodes”. *Joule* 711, 2023, pp. 2609–2621.

[194] Arumugam Manthiram et al. “Rechargeable lithium–sulfur batteries”. *Chemical reviews* 11423, 2014, pp. 11751–11787.

[195] Patrick Schön, Frederik Hintz, and Ulrike Krewer. “Electrochemical analysis of the reaction mechanism of sulfur reduction as a function of state of charge”. *Electrochimica Acta* 295, 2019, pp. 926–933.

[196] Qinjun Shao, Shengdong Zhu, and Jian Chen. “A review on lithium-sulfur batteries: Challenge, development, and perspective”. *Nano Research* 166, 2023, pp. 8097–8138.

[197] Ze-Chen Lv et al. “Key challenges, recent advances and future perspectives of rechargeable lithium-sulfur batteries”. *Journal of Industrial and Engineering Chemistry* 124, 2023, pp. 68–88.

[198] G.A. Nazri and G. Pistoia, eds. *Lithium batteries science and technology*. Dordrecht: Kluwer Academic, 2003.

[199] Fausto Croce et al. “Advanced electrolyte and electrode materials for lithium polymer batteries”. *Journal of power sources* 119, 2003, pp. 399–402.

[200] Yeru Liang et al. “A review of rechargeable batteries for portable electronic devices”. *InfoMat* 11, 2019, pp. 6–32.

[201] Weidong Chen et al. “A review of lithium-ion battery for electric vehicle applications and beyond”. *Energy Procedia* 158, 2019, pp. 4363–4368.

[202] Huixin Tian et al. “A review of the state of health for lithium-ion batteries: Research status and suggestions”. *Journal of Cleaner Production* 261, 2020, p. 120813.

[203] Tianmei Chen et al. “Applications of lithium-ion batteries in grid-scale energy storage systems”. *Transactions of Tianjin University* 263, 2020, pp. 208–217.

[204] Chao Hu et al. “Remaining useful life assessment of lithium-ion batteries in implantable medical devices”. *Journal of Power Sources* 375, 2018, pp. 118–130.

[205] David C Bock et al. “Batteries used to power implantable biomedical devices”. *Electrochimica acta* 84, 2012, pp. 155–164.

[206] Henok Ayele Behabtu et al. “A review of energy storage technologies’ application potentials in renewable energy sources grid integration”. *sustainability* 1224, 2020, p. 10511.

[207] Chun Sing Lai and Giorgio Locatelli. “Economic and financial appraisal of novel large-scale energy storage technologies”. *Energy* 214, 2021, p. 118954.

[208] Zhang Wei, Byung Young Moon, and Young Hoon Joo. “Smooth wind power fluctuation based on battery energy storage system for wind farm”. *Journal of Electrical Engineering and Technology* 96, 2014, pp. 2134–2141.

[209] Boucar Diouf and Christophe Avis. “The potential of Li-ion batteries in ECOWAS solar home systems”. *Journal of Energy Storage* 22, 2019, pp. 295–301.

[210] Nor Izzati Ahmad et al. “Impacts of lightning-induced overvoltage on a hybrid solar PV–battery energy storage system”. *Applied Sciences* 118, 2021, p. 3633.

[211] Lucian Ungurean et al. “Battery state of health estimation: a structured review of models, methods and commercial devices”. *International Journal of Energy Research* 412, 2017, pp. 151–181.

[212] MS Hossain Lipu et al. “A review of state of health and remaining useful life estimation methods for lithium-ion battery in electric vehicles: Challenges and recommendations”. *Journal of cleaner production* 205, 2018, pp. 115–133.

[213] Yangtao Liu et al. “Current and future lithium-ion battery manufacturing”. *IScience* 244, 2021.

[214] Shabbir Ahmed et al. “Energy impact of cathode drying and solvent recovery during lithium-ion battery manufacturing”. *Journal of Power Sources* 322, 2016, pp. 169–178.

[215] Tao Li et al. “Fluorinated solid-electrolyte interphase in high-voltage lithium metal batteries”. *Joule* 311, 2019, pp. 2647–2661.

[216] David L Wood, Jianlin Li, and Seong Jin An. “Formation challenges of lithium-ion battery manufacturing”. *Joule* 312, 2019, pp. 2884–2888.

[217] Maeva Philippot et al. “Eco-efficiency of a lithium-ion battery for electric vehicles: Influence of manufacturing country and commodity prices on ghg emissions and costs”. *Batteries* 51, 2019, p. 23.

[218] Zachary J Baum et al. *Lithium-ion battery recycling overview of techniques and trends*. 2022.

[219] PM Tembo, C Dyer, and V Subramanian. “Lithium-ion battery recycling—a review of the material supply and policy infrastructure”. *NPG Asia Materials* 161, 2024, p. 43.

[220] Yaocai Bai et al. “Energy and environmental aspects in recycling lithium-ion batteries: Concept of Battery Identity Global Passport”. *Materials Today* 41, 2020, pp. 304–315.

[221] Yuchen Hu et al. “Development tendency and future response about the recycling methods of spent lithium-ion batteries based on bibliometrics analysis”. *Journal of Energy Storage* 27, 2020, p. 101111.

[222] Seoa Kim et al. “A comprehensive review on the pretreatment process in lithium-ion battery recycling”. *Journal of Cleaner Production* 294, 2021, p. 126329.

[223] Xuehu Zhong et al. “Pretreatment for the recovery of spent lithium ion batteries: theoretical and practical aspects”. *Journal of Cleaner Production* 263, 2020, p. 121439.

[224] Lingxi Kong et al. “Li-ion battery fire hazards and safety strategies”. *Energies* 119, 2018, p. 2191.

[225] Binghe Liu et al. “Safety issues and mechanisms of lithium-ion battery cell upon mechanical abusive loading: A review”. *Energy Storage Materials* 24, 2020, pp. 85–112.

[226] Erkin Yildiz et al. “A comparative review of models for all-solid-state li-ion batteries”. *Batteries* 105, 2024, p. 150.

[227] J. Schnell et al. “All-solid-state lithium-ion and lithium metal batteries – paving the way to large-scale production”. *J POWER SOURCES* 382, 2018, pp. 160–175.

[228] F. Zheng et al. “Review on solid electrolytes for all-solid-state lithium-ion batteries”. *J POWER SOURCES* 389, 2018, pp. 198–213.

[229] David E Arreaga-Salas et al. “Progression of solid electrolyte interphase formation on hydrogenated amorphous silicon anodes for lithium-ion batteries”. *J PHYS CHEM C* 11616, 2012, pp. 9072–9077.

[230] M. Pasta et al. “2020 roadmap on solid-state batteries”. *J PHYS ENERGY* 23, 2020, p. 032008.

[231] D. Santhanagopalan et al. “Interface limited lithium transport in solidstate batteries”. *J PHYS CHEM LETT* 52, 2014, pp. 298–303.

[232] C. Chen et al. “Interface Aspects in All-Solid-State Li-Based Batteries Reviewed”. *ADV ENERGY MATER*, 2021, p. 2003939.

[233] F. Zhang et al. “A review of mechanics-related material damages in all-solid-state batteries: Mechanisms, performance impacts and mitigation strategies”. *NANO ENERGY* 70, 2020, p. 104545.

[234] H.-K. Tian and Y. Qi. “Simulation of the Effect of Contact Area Loss in All-Solid-State Li-Ion Batteries”. *J ELECTROCHEM SOC* 16411, 2017, pp. 3512–3521.

[235] T. Waldmann, B. Hogg, and M. Wohlfahrt-Mehrens. “Li plating as unwanted side reaction in commercial Li-ion cells – A review”. *J POWER SOURCES* 384, 2018, pp. 107–124.

[236] L. Porz et al. “Mechanism of Lithium Metal Penetration through Inorganic Solid Electrolytes”. *ADV ENERGY MATER* 720, 2017, p. 1701003.

[237] S.S. Shishvan et al. “Growth rate of lithium filaments in ceramic electrolytes”. *ACTA MATER* 196, 2020, pp. 444–455.

[238] L. Fan et al. “Recent Progress of the Solid-State Electrolytes for High-Energy Metal-Based Batteries”. *ADV ENERGY MATER* 811, 2018, p. 1702657.

[239] H. Yuan et al. “Single Lithium-Ion Conducting Solid Polymer Electrolyte with Superior Electrochemical Stability and Interfacial Compatibility for Solid-State Lithium Metal Batteries”. *ACS APPL MATER INTER* 126, 2020, pp. 7249–7256.

[240] Y. Zheng et al. “A review of composite solid-state electrolytes for lithium batteries: fundamentals, key materials and advanced structures”. *CHEM SOC REV* 49, 2020, pp. 8790–8839.

[241] A. Bielefeld, D.A. Weber, and J. Janek. “Microstructural modeling of composite cathodes for all solid state batteries”. *J PHYS CHEM C* 123, 2019, pp. 1626–1634.

[242] C. Cao et al. “Recent advances in inorganic solid electrolytes for lithium batteries”. *FRONT ENERGY RES* 2, 2014, pp. 25–35.

[243] D. Grazioli, M. Magri, and A. Salvadori. “Computational modeling of Li-ion batteries”. *COMPUT MECH* 586, 2016, pp. 889–909.

[244] G. Li and C. W. Monroe. “Multiscale Lithium-Battery Modeling from Materials to Cells”. *ANNU REV CHEM BIOMOL* 111, 2020, pp. 277–310.

[245] S.D. Fabre et al. “Charge/Discharge Simulation of an All-Solid-State Thin-Film Battery Using a One-Dimensional Model”. *J ELECTROCHEM SOC* 1592, 2012, A104–A115.

[246] M. Landstorfer, S. Funken, and T. Jacob. "An advanced model framework for solid electrolyte intercalation batteries". *PHYS CHEM CHEM PHYS* 13, 2011, pp. 12817–12825.

[247] L.H.J. Raijmakers et al. "An advanced all-solid-state Li-ion battery model". *ELECTROCHIM ACTA* 330135147, 2020.

[248] L. Cabras et al. "A two-mechanism and multiscale compatible approach for solid state electrolytes of (Li-ion) batteries". *J ENERGY STORAGE* 48, 2022, p. 103842.

[249] A. Salvadori, D. Grazioli, and M.G.D. Geers. "Governing equations for a two-scale analysis of Li-ion battery cells". *INT J SOLIDS STRUCT* 59, 2015, pp. 90–109.

[250] M. Mykhaylov et al. "An elementary 1-dimensional model for a solid state lithium-ion battery with a single ion conductor electrolyte and a lithium metal negative electrode". *J MECH PHYS SOLIDS* 123, 2019, pp. 207–221.

[251] A. Salvadori et al. "A multiscale-compatible approach in modeling ionic transport in the electrolyte of (Lithium ion) batteries". *J POWER SOURCES* 293, 2015, pp. 892–911.

[252] A. Salvadori et al. "On the role of saturation in modeling ionic transport in the electrolyte of (Li-ion) batteries." *J POWER SOURCES* 294, 2015, pp. 696–710.

[253] D. Danilov, R.A.H. Niessen, and P.H.L. Notten. "Modeling All-Solid-State Li-Ion Batteries". *J ELECTROCHEM SOC* 1583, 2011, A215–A222.

[254] M. Doyle and J. Newman. "The use of mathematical modeling in the design of Lithium/polymer battery systems". *ELECTROCHIM ACTA* 4013, 1995, pp. 2191–2196.

[255] T.F. Fuller, M. Doyle, and J. Newman. "Simulation and Optimization of the Dual Lithium Ion Insertion Cell". *J ELECTROCHEM SOC* 1411, 1994, pp. 1–10.

[256] A. Salvadori, E. Bosco, and D. Grazioli. "A computational homogenization approach for Li-ion battery cells. Part 1 - Formulation". *J MECH PHYS SOLIDS* 65, 2014, pp. 114–137.

[257] A.A. Franco. "Multiscale modelling and numerical simulation of rechargeable Lithium ion batteries: concepts, methods and challenges". *RSC ADVANCES* 313027, 2013.

[258] S. Lee, A.M. Sastry, and J. Park. "Study on microstructures of electrodes in Lithium-ion batteries using variational multi-scale enrichment". *J POWER SOURCES* 315, 2016, pp. 96–110. ISSN: 0378-7753. DOI: http://dx.doi.org/10.1016/j.jpowsour.2016.02.086. URL: http://www.sciencedirect.com/science/article/pii/S0378775316301938.

[259] A.A. Franco et al. "Boosting Rechargeable Batteries R&D by Multiscale Modeling: Myth or Reality?" *CHEM REV* 119, 2019, p. 4569.

[260] R.T. Purkayastha and R.M. McMeeking. "An integrated 2-D model of a Lithium ion battery: the effect of material parameters and morphology on storage particle stress". *COMPUT MECH* 50, 2012, pp. 209–227.

[261] A. Salvadori et al. "A coupled model of transport-reaction-mechanics with trapping. Part I - small strain analysis." *J MECH PHYS SOLIDS* 114, 2018, pp. 1–30.

[262] Matteo Arricca et al. “A coupled model of transport-reaction-mechanics with trapping, Part II: Large strain analysis”. *J MECH PHYS SOLIDS* 181, 2023, p. 105425.

[263] L. Anand. “A Cahn-Hilliard-type theory for species diffusion coupled with large elastic-plastic deformations”. *J MECH PHYS SOLIDS* 6012, 2012, pp. 1983–2002.

[264] R. DeHoff. *Thermodynamic in material science*. CRC Press - Taylor and Francis, 2006.

[265] S. Shell. *Thermodynamics and statistical mechanics: an integrated approach*. Cambridge University Press, 2015.

[266] E. Bohn et al. “A Model for Lithium Diffusion and Stress Generation in an Intercalation Storage Particle with Phase Change”. *J ELECTROCHEM SOC* 16010, 2013, A1638–A1652. DOI: 10.1149/2.011310jes.

[267] C. Di Leo, E. Rejovitzky, and L. Anand. “A Cahn-Hilliard-type phase-field theory for species diffusion coupled with large elastic deformations: Application to phase-separating Li-ion electrode materials”. *J MECH PHYS SOLIDS* 70, 2014, pp. 1–29.

[268] A.F. Bower, P.R. Guduru, and E. Chason. “Analytical solutions for composition and stress in spherical elastic–plastic Lithium-ion electrode particles containing a propagating phase boundary”. *INT J SOLIDS STRUCT* 69-70, 2015, pp. 328–342.

[269] A. Bonnefont, F. Argoul, and M.Z. Bazant. “Analysis of diffuse-layer effects on time-dependent interfacial kinetics”. *J ELECTROANAL CHEM* 5001, 2001, pp. 52–61.

[270] M.Z. Bazant, K.T. Chu, and B.J. Bayly. “Current-voltage relations for elecrochemical thin films”. *SIAM J APPL MATH* 65, 2005, pp. 1463–1484.

[271] D. Li et al. “Degradation mechanisms of C6/LiFePO4 batteries: experimental analyses of calendar aging”. *ELECTROCHIM ACTA* 190, 2016, pp. 1124–1133.

[272] D. Li et al. “Degradation mechanisms of C6/LiFePO4 batteries: experimental analyses of cycling-induced aging”. *ELECTROCHIM ACTA* 210, 2016, pp. 445–455.

[273] A.J Bard and L.R. Faulkner. *Electrochemical Methods: Fundamentals and Applications*. 2nd. Wiley, 2000.

[274] T. Famprikis et al. “Fundamentals of inorganic solid-state electrolytes for batteries”. *NAT MATER* 1812, 2019, pp. 1278–1291.

[275] L. Cabras, M. Serpelloni, and A. Salvadori. “Electro-chemo-mechanics of solid state batteries with lithium plating and stripping.” *FRONT MATER* 9, 2022, p. 1052617.

[276] A.F. Bower, P.R. Guduru, and E. Chason. “A continuum model of deformation, transport and irreversible changes in atomic structure in amorphous Lithium–silicon electrodes”. *ACTA MATER* 98, 2015, pp. 229–241.

[277] G. Bucci et al. “Measurement and modeling of the mechanical and electrochemical response of amorphous Si thin film electrodes during cyclic lithiation”. *J MECH PHYS SOLIDS* 62, 2014, pp. 276–294.

[278] M. Magri et al. “Quantitative investigation of the influence of electrode morphology in the electro-chemo-mechanical response of li-ion batteries.” *ELECTROCHIM ACTA* 405, 2022, p. 139778.

[279] A. Latz and J. Zausch. "Multiscale modeling of Li-ion batteries: thermal aspects." *BEILSTEIN J NANOTECHNOL* 6, 2015, pp. 987–1007.

[280] Jiale Ma and Zhenyu Li. "Computational Design of Inorganic Solid-State Electrolyte Materials for Lithium-Ion Batteries". *ACC MATER RES*, 2024.

[281] Dheeraj K Maurya et al. "Composite polymer electrolytes: progress, challenges, and future outlook for sodium-ion batteries". *ADV COMPOS HYBRID MA* 54, 2022, pp. 2651–2674.

[282] Yubin Liao et al. "Recent progress in flame-retardant polymer electrolytes for solid-state lithium metal batteries". *BATTERIES* 99, 2023, p. 439.

[283] Philippe Knauth and Harry L Tuller. "Solid-state ionics: roots, status, and future prospects". *J AM CERAM SOC* 857, 2002, pp. 1654–1680.

[284] Kazunori Takada. "Progress in solid electrolytes toward realizing solid-state lithium batteries". *J POWER SOURCES* 394, 2018, pp. 74–85.

[285] RC Xu et al. "Interfacial challenges and progress for inorganic all-solid-state lithium batteries". *ELECTROCHIM ACTA* 284, 2018, pp. 177–187.

[286] Xiaona Li et al. "Water-mediated synthesis of a superionic halide solid electrolyte". *ANGEW CHEM* 13146, 2019, pp. 16579–16584.

[287] Prashun Gorai et al. "Devil is in the defects: electronic conductivity in solid electrolytes". *CHEM MATER* 3318, 2021, pp. 7484–7498.

[288] Kazunori Takada and Takahisa Ohno. "Experimental and computational approaches to interfacial resistance in solid-state batteries". *FRONT ENERGY RES* 4, 2016, p. 10.

[289] Narumi Ohta et al. "LiNbO3-coated LiCoO2 as cathode material for all solid-state lithium secondary batteries". *ELECTROCHEM COMMUN* 97, 2007, pp. 1486–1490.

[290] Kazunori Takada et al. "Interfacial phenomena in solid-state lithium battery with sulfide solid electrolyte". *SOLID STATE IONICS* 225, 2012, pp. 594–597.

[291] Geoffroy Hautier et al. "Novel mixed polyanions lithium-ion battery cathode materials predicted by high-throughput ab initio computations". *J MATER CHEM* 2143, 2011, pp. 17147–17153.

[292] Zhuoying Zhu, Iek-Heng Chu, and Shyue Ping Ong. "Li3Y (PS4) 2 and Li5PS4Cl2: new lithium superionic conductors predicted from silver thiophosphates using efficiently tiered ab initio molecular dynamics simulations". *CHEM MATER* 296, 2017, pp. 2474–2484.

[293] Xingyu Guo et al. "Machine-Learning Assisted High-Throughput Discovery of Solid-State Electrolytes for Li-ion Batteries". *J MATER CHEM A*, 2024.

[294] Lei Xi et al. "Interface Engineering of All-Solid-State Batteries Based on Inorganic Solid Electrolytes". *CHEMSUSCHEM* 169, 2023, e202202158.

[295] Guoliang Li et al. "Modeling of an all-solid-state battery with a composite positive electrode". *ETRANSPORTATION*, 2024, p. 100315.

[296] Jürgen Janek and Wolfgang G Zeier. "Challenges in speeding up solid-state battery development". *NAT ENERGY* 83, 2023, pp. 230–240.

[297] H. Haftbaradaran, S. Esmizadeh, and A. Salvadori. “Competing effects of current density and viscoplastic deformation on the critical conditions for dendrite growth into solid-state lithium battery electrolytes”. *International Journal of Solids and Structures* 254-255, 2022, p. 111852.

[298] C.V. Di Leo, E. Rejovitzky, and L. Anand. “Diffusion-deformation theory for amorphous silicon anodes: the role of plastic deformation on elecrochemical performance.” *INT J SOLIDS STRUCT* 67-68, 2015, pp. 283–296.

[299] H. Fathiannasab et al. “Three-Dimensional Modeling of All-Solid-State Lithium-Ion Batteries Using Synchrotron Transmission X-ray Microscopy Tomography”. *J ELECTROCHEM SOC* 16710, 2020, p. 100558.

[300] H. Fathiannasab, L. Zhu, and Z. Chen. “Chemo-mechanical modeling of stress evolution in all-solid-state lithium-ion batteries using synchrotron transmission X-ray microscopy tomography”. *J POWER SOURCES* 483, 2021, p. 229028.

[301] John B Goodenough and Youngsik Kim. “Challenges for rechargeable Li batteries”. *CHEM MATER* 223, 2010, pp. 587–603.

[302] Henry Adenusi et al. “Lithium batteries and the solid electrolyte interphase (SEI)—progress and outlook”. *ADV ENERGY MATER* 1310, 2023, p. 2203307.

[303] Seama Koohi-Fayegh and Marc A Rosen. “A review of energy storage types, applications and recent developments”. *J ENERGY STORAGE* 27, 2020, p. 101047.

[304] Mohammed Bin Jassar et al. “A Perspective on the Molecular Modeling of Electrolyte Decomposition Reactions for Solid Electrolyte Interphase Growth in Lithium-Ion Batteries”. *ADV FUNCT MATER* n/an/a, p. 2313188.

[305] Diddo Diddens et al. “Modeling the Solid Electrolyte Interphase: Machine Learning as a Game Changer?” *ADV MATER INTERFACES* 98, 2022, p. 2101734.

[306] M. Landstorfer. “A Discussion of the Cell Voltage during Discharge of an Intercalation Electrode for Various C-Rates Based on Non-Equilibrium Thermodynamics and Numerical Simulations”. *J ELECTROCHEM SOC* 1671, 2019, p. 013518.

[307] J.M. Tarascon and M. Armand. “Issues and challenges facing rechargeable Lithium batteries”. *NATURE* 414, 2001, pp. 359–367.

[308] B. Scrosati and J. Garche. “Lithium batteries: status, prospects and future”. *J POWER SOURCES* 195, 2010, pp. 2419–2430.

[309] A. Salvadori and D. Grazioli. “Computer simulation for battery design and lifetime prediction”. *Advances in battery technologies for electric vehicles*. Ed. by B. Scrosati, J. Garche, and W. Tillmetz. Woodhead Publishing, 2015. Chap. 16, pp. 417–442.

[310] Alejandro A Franco. “Multiscale modelling and numerical simulation of rechargeable lithium ion batteries: concepts, methods and challenges”. *Rsc Advances* 332, 2013, pp. 13027–13058.

[311] D. Doerffel and S.A. Sharkh. “A critical review of using the Peukert equation for determining the remaining capacity of lead-acid and Lithium-ion batteries.” *J POWER SOURCES* 1552, 2006, pp. 395–400.

[312] M.T. von Srbik et al. "A physically meaningful equivalent circuit network model of a Lithium-ion battery accounting for local electrochemical and thermal behaviour, variable double layer capacitance and degradation". *J POWER SOURCES* 325, 2016, pp. 171–184.

[313] W.D. Widanage et al. "Design and use of multisine signals for Li-ion battery equivalent circuit modelling. Part II: Model estimation". *J POWER SOURCES* 324, 2016, pp. 61–69.

[314] V. Ramadesigan et al. "Modeling and Simulation of Lithium-Ion Batteries from a Systems Engineering Perspective". *J ELECTROCHEM SOC* 1593, 2012, R31–R45. DOI: 10.1149/2.018203jes.

[315] Lidan Xing et al. "Electrode/electrolyte interface in sulfolane-based electrolytes for Li ion batteries: a molecular dynamics simulation study". *J. Phys. Chem. C* 11645, 2012, pp. 23871–23881.

[316] H. Haftbaradaran et al. "Continuum and atomistic models of strongly coupled diffusion, stress, and solute concentration". *J POWER SOURCES* 196, 2011, pp. 361–370.

[317] Alain C Ngandjong et al. "Multiscale simulation platform linking lithium ion battery electrode fabrication process with performance at the cell level". *J. Phys. Chem. Lett.* 823, 2017, pp. 5966–5972.

[318] Fridolin Röder, Richard D Braatz, and Ulrike Krewer. "Multi-scale simulation of heterogeneous surface film growth mechanisms in lithium-ion batteries". *J ELECTROCHEM SOC* 16411, 2017, E3335.

[319] S.R. De Groot and P. Mazur. *Non-Equilibrium Thermodynamics*. Dover, 1984.

[320] M.E. Gurtin, E. Fried, and L. Anand. *The Mechanics and Thermodynamics of Continua*. Cambridge University Press, 2010.

[321] G. Holzapfel. *Nonlinear Solid Mechanics: A Continuum Approach for Engineering*. John Wiley & Sons, Ltd., 2001.

[322] E.B. Tadmor, R.E. Miller, and R.S. Elliott. *Continuum Mechanics and Thermodynamics: From Fundamental Concepts to Governing Equations*. Cambridge University Press, 2011.

[323] A.F. Bower, P.M. Guduru, and V.A. Sethuraman. "A finite strain model of stress, diffusion, plastic flow and electrochemical reactions in a Lithium-ion half-cell". *J MECH PHYS SOLIDS* 59, 2011, pp. 804–828.

[324] Duo Zhang et al. "Progress in 3D electrode microstructure modelling for fuel cells and batteries: transport and electrochemical performance". *Progress in Energy* 11, 2019, p. 012003.

[325] F. Larche and J.W. Cahn. "A linear theory of thermochemical equilibrium under stress". *ACTA METALL MATER* 21, 1973, pp. 1051–1063.

[326] J. Larsson. "Electromagnetics from a quasistatic perspective". *AM J PHYS* 753, 2007, pp. 230–239.

[327] A. Kovetz. *The principles of electromagnetic theory*. Cambridge University Press, 1989.

[328] Yang-Tse Cheng and Mark W Verbrugge. “Evolution of stress within a spherical insertion electrode particle under potentiostatic and galvanostatic operation”. *Journal of Power Sources* 1902, 2009, pp. 453–460.

[329] D. Danilov and P.H.L. Notten. “Mathematical modeling of ionic transport in the electrolyte of Li-ion batteries.” *ELECTROCHIM ACTA* 53, 2008, pp. 5569–5578.

[330] L.H.J. Raijmakers et al. “An advanced all-solid-state Li-ion battery model”. *ELECTROCHIM ACTA* 330135147, 2020.

[331] W. Dreyer, C. Guhlke, and R. Muller. “A new perspective on the electron transfer: recovering the Butler-Volmer equation in non-equilibrium thermodynamics”. *PHYS CHEM CHEM PHYS* 18, 2016, pp. 24966–24983.

[332] V. Malave et al. “A Computational Model of the Mechanical Behavior within Reconstructed Li_xCoO_2 Li-ion Battery Cathode Particles”. *ELECTROCHIM ACTA* 130, 2014, pp. 707–717.

[333] R.T. Purkayastha and R.M. McMeeking. “A linearized model for Lithium ion batteries and maps for their performance and failure”. *J APPL MECH* 79, 2012, pp. 1–16.

[334] Jan Naess Reimers and Jeff R. Dahn. “Electrochemical and In Situ X-Ray Diffraction Studies of Lithium Intercalation in Li x CoO2”. *Journal of The Electrochemical Society* 139, 1992, pp. 2091–2097.

[335] V. Malave, J.R. Berger, and P.A. Martin. “Concentration-Dependent Chemical Expansion in Lithium-Ion Battery Cathode Particles”. *J APPL MECH* 819, 2014.

[336] Utkarsh Ayachit. *The paraview guide: a parallel visualization application*. Kitware, Inc., 2015.

[337] Python Software Foundation. *Python Language Reference, version 3.11*. `https://www.python.org`. Python Software Foundation. 2023.

[338] John D Hunter. “Matplotlib: A 2D graphics environment”. *Computing in science & engineering* 903, 2007, pp. 90–95.

[339] Joachim Schöberl. “NETGEN An advancing front 2D/3D-mesh generator based on abstract rules”. *Computing and visualization in science* 11, 1997, pp. 41–52.

[340] C. Geuzaine and J.-F. Remacle. “Gmsh: a three-dimensional finite element mesh generator with built-in pre- and post-processing facilities.” *INT J NUMER METH ENG* 7911, 2009, pp. 1309–1331.

[341] A. Mukhopadhyay and B.V. Sheldon. “Deformation and stress in electrode materials for Li-ion batteries”. *PROG MATER SCI* 63, 2014, pp. 58–116.

[342] S. Renganathan et al. “Theoretical Analysis of Stresses in a Lithium Ion Cell”. *J ELECTROCHEM SOC* 157, 2010, pp. 155–163.

[343] E. A. Brandes and G. B. Brook. *Smithells Metals Reference Book*. Butterworth Einemann, 1998.

[344] J. Chen et al. “Evolution of mechanical properties of polypropylene separator in liquid electrolytes for lithium ion batteries”. *J APPL POLYM SCI* 13527, 2018, p. 46441. DOI: `10.1002/app.46441`.

[345] Danghe Shi et al. “Modeling stresses in the separator of a pouch lithium-ion cell”. *Journal of Power Sources* 19619, 2011, pp. 8129–8139.

[346] L.B. Freund and S. Suresh. *Thin film materials: stress, defect formation and surface evolution*. Cambridge University Press, 2004.

[347] M. Guo and R.E. White. "Thermal Model for Lithium Ion Battery Pack with Mixed Parallel and Series Configuration". *J ELECTROCHEM SOC* 15810, 2011, A1166–A1176.

[348] Jan N. Reimers and J. R. Dahn. "Electrochemical and In Situ X-Ray Diffraction Studies of Lithium Intercalation in Li_xCoO_2". *J ELECTROCHEM SOC* 1398, 1992, pp. 2091–2097. DOI: 10.1149/1.2221184.

[349] Xiangchun Zhang, Ann Marie Sastry, and Wei Shyy. "Intercalation-induced stress and heat generation within single lithium-ion battery cathode particles". *Journal of The Electrochemical Society* 1557, 2008, A542.

[350] J. Park, W. Lu, and A.M. Sastry. "Numerical Simulation of Stress Evolution in Lithium Manganese Dioxide Particles due to Coupled Phase Transition and Intercalation". *J ELECTROCHEM SOC* 1582, 2011, A201–A206. DOI: 10.1149/1.3526597.

[351] X. Zhang, W. Shyy, and A.M. Sastry. "Numerical Simulation of Intercalation-Induced Stress in Li-Ion Battery Electrode Particles". *J ELECTROCHEM SOC* 154, 2007, A910–A916.

[352] K. Zhao et al. "Fracture of electrodes in Lithium-ion batteries caused fast charging". *J APPL PHYS* 108, 2010, p. 073517.

[353] M. Zhu, J. Park, and A.M. Sastry. "Fracture analysis of the cathode in Li-ion batteries: a simulation study". *J ELECTROCHEM SOC* 1594, 2012, A492–A498.

[354] M. Magri et al. "Quantitative investigation of the influence of electrode morphology in the electro-chemo-mechanical response of li-ion batteries." *ELECTROCHIM ACTA* 405, 2022, p. 139778.

[355] Jang Wook Choi and Doron Aurbach. "Promise and reality of post-lithium-ion batteries with high energy densities". *Nature reviews materials* 14, 2016, pp. 1–16.

[356] Arumugam Manthiram. "A reflection on lithium-ion battery cathode chemistry". *Nature communications* 111, 2020, p. 1550.

[357] Yongling An et al. "Green, scalable, and controllable fabrication of nanoporous silicon from commercial alloy precursors for high-energy lithium-ion batteries". *ACS nano* 125, 2018, pp. 4993–5002.

[358] George Wei et al. "Direct recycling of spent Li-ion batteries: Challenges and opportunities toward practical applications". *iScience* 269, 2023, pp. 107676–107676.

[359] Stefanie Arnold et al. "Electrochemical recycling of lithium-ion batteries: Advancements and future directions". *EcoMat* 611, 2024, e12494.

[360] Sangyoon Lee et al. "Sustainable method for disposing of ceramic-coated battery separator via carbon dioxide-assisted thermochemical process". *Journal of Analytical and Applied Pyrolysis* 179, 2024, p. 106466.

[361] Marita Pigłowska et al. "Novel recycling technologies and safety aspects of lithium ion batteries for electric vehicles". *Journal of Material Cycles and Waste Management* 265, 2024, pp. 2656–2669.

[362] Alex K Koech et al. “Lithium-ion battery fundamentals and exploration of cathode materials: A review”. *South African Journal of Chemical Engineering*, 2024.

[363] Dongping Lv et al. “High energy density lithium–sulfur batteries: challenges of thick sulfur cathodes”. *Advanced Energy Materials* 516, 2015, p. 1402290.

[364] Zhan Lin et al. “Aligning academia and industry for unified battery performance metrics”. *Nature communications* 91, 2018, p. 5262.

[365] Philip Minnmann et al. “Designing cathodes and cathode active materials for solid-state batteries”. *Advanced Energy Materials* 1235, 2022, p. 2201425.

[366] Shuaipeng Hao et al. “Achieving structural stability of LiCoO2 at high-voltage by gadolinium decoration”. *MATER. TODAY ENERGY* 25, 2022, p. 100980.

[367] M Stanley Whittingham. “Lithium batteries and cathode materials”. *CHEM. REV.* 10410, 2004, pp. 4271–4302.

[368] Jean-Pierre Brog et al. “Characteristics and properties of nano-LiCoO2 synthesized by pre-organized single source precursors: Li-ion diffusivity, electrochemistry and biological assessment”. *Journal of nanobiotechnology* 151, 2017, p. 58.

[369] Kincaid Graff et al. “Synthesis strategies and in situ characterization of layered transition metal oxide materials for sodium-ion batteries”. *Journal of Materials Research*, 2025, pp. 1–23.

[370] Nicholas V Faenza et al. “Growth of ambient induced surface impurity species on layered positive electrode materials and impact on electrochemical performance”. *Journal of the Electrochemical Society* 16414, 2017, A3727.

[371] Yujing Bi et al. “Stability of Li 2 CO 3 in cathode of lithium ion battery and its influence on electrochemical performance”. *Rsc Advances* 623, 2016, pp. 19233–19237.

[372] Pengcheng Zhu, Peter R Slater, and Emma Kendrick. “Insights into architecture, design and manufacture of electrodes for lithium-ion batteries”. *Materials & Design* 223, 2022, p. 111208.

[373] Jie Xiao et al. “Understanding and applying coulombic efficiency in lithium metal batteries”. *Nat. Energy* 58, 2020, pp. 561–568.

[374] Bruce Dunn, Haresh Kamath, and Jean-Marie Tarascon. “Electrical energy storage for the grid: a battery of choices”. *Science* 3346058, 2011, pp. 928–935.

[375] Luize Scalco de Vasconcelos et al. “Chemomechanics of rechargeable batteries: status, theories, and perspectives”. *Chemical Reviews* 12215, 2022, pp. 13043–13107.

[376] Ying Zhao et al. “A review on modeling of electro-chemo-mechanics in lithium-ion batteries”. *Journal of Power Sources* 413, 2019, pp. 259–283.

[377] G. Harper et al. “Recycling lithium-ion batteries from electric vehicles”. *NATURE* 5757781, 2019, pp. 75–86.

[378] Mina Rezaei et al. “A review of lithium-ion battery recycling for enabling a circular economy”. *Journal of Power Sources* 630, 2025, p. 236157.

[379] Yuping Liu et al. “Recycling and direct regeneration of valuable cathode materials from spent Li-ion batteries: a comprehensive review”. *Journal of Materials Chemistry A* 1313, 2025, pp. 8968–9004.

[380] Xinyi Dai et al. “Extending the high-voltage capacity of LiCoO2 cathode by direct coating of the composite electrode with Li2CO3 via magnetron sputtering”. *The Journal of Physical Chemistry C* 1201, 2016, pp. 422–430.